Developing P(MMA-co-NVP) hydrogels for use in self-inflating, anisotropic tissue expanders

Thesis submitted for the degree of Doctor of Philosophy

Jessica Rose Smith
Trinity Term 2015

ST ANNE'S COLLEGE

Abstract

Developing P(MMA-co-NVP) hydrogels for use in self-inflating, anisotropic tissue expanders

Thesis submitted for the degree of Doctor of Philosophy, Trinity Term 2015

Jessica Rose Smith, St Anne's College

Artificial tissue expansion is required to generate new skin prior to reconstructive surgery, in order to compensate for a deficit of healthy tissue. Hydrogel tissue expanders, which expand anisotropically, show great promise in overcoming clinical limitations in the field, thus allowing the technique to be used in a wider range of surgeries. These devices consist of pellets of dry poly(methyl methacrylate-co-vinylpyrrolidone), compressed into discs through a hot compression moulding process. However, a number of significant problems still exist in these devices, and this thesis aims to address these issues.

To date, there has been a lack of investigation of the factors governing the behaviour of anisotropic swelling. For this reason, a range of different compression ratios have been investigated, with particular focus on the relationship between the material flow during compression and the swelling behaviour of the resulting device. It was found that samples of the same initial size expand to the same reference swelling dimensions, regardless of compression ratio. During hot pressing, the material flow was found to be governed by slip-stick behaviour at the interface between the hot press and the device, affecting the properties and swelling behaviour of the devices.

Based on these findings, devices were developed which could expand from a disc into a non-prismatic shape (dome or wedge). Such devices could reduce complication rates and allow the growth of new tissue with anisotropic resting tension. The devices were tested in a small *in vivo* trial, where it was shown that there were no adverse effects on the tissue produced, and that the shape of the expander (dome) was retained.

As devices are being produced for medical use, understanding the effect of sterilization by γ-irradiation is essential, but to date this has been overlooked in the literature. It was found that γ-irradiation caused an increase in cross-linking in the P(MMA-co-NVP). Whilst this produced little change in swelling behaviour for isotropic devices, in the case of anisotropic devices it caused a change in the shape of expansion, reducing the area of new skin which could be generated by the device. It was found that by reducing the concentration of impurities (residual molecules from the polymer synthesis) the impact of γ-irradiation could be greatly reduced.

Finally, controlling the rate of expansion is essential in order to avoid clinical complications. In order to control the rate of expansion, particularly during the initial period of swelling, semi-permeable PDMS coatings were applied to the compressed devices. Coatings of thickness greater than 0.375mm were found to effectively control the rate of swelling, for both cylindrical and non-prismatic shapes. As the coating thickness increased, the maximum swelling size decreased. However, it has been shown that change in height (the parameter which governs the area of skin produced) is affected less than the change in mass or diameter.

Declaration

This thesis is an account of the work conducted by the author within the Department of Materials, University of Oxford (2011-2015) under the supervision of Professor Jan T Czernuszka. The project was funded by Oxtex Ltd.

No part of this work has been previously submitted for a degree at this or any other university. The work is entirely original, and where the work of others is included it has been clearly acknowledged and references. A full list of references is included at the end of this thesis.

Below is a list of the publications and presentations of the work resulting from this thesis (as of the date of submission):

J. R. Smith, Z. Radzi, J. T. Czernuszka. “The effect of hot pressing on the swelling behaviour of P(MMA-co-NVP) hydrogel discs” Journal of Polymer Engineering and Science, 2015, doi: 10.1002/pen.24067

TMS 2015, Florida, symposium for advanced materials in dental and orthopaedic applications : "Animal models of PMMA-NVP hydrogels for orthotropic, self-inflating tissue expanders" J.R. Smith, Z. Radzi, J.T. Czernuszka

TMS 2014, San Diego, symposium for advanced materials in dental and orthopaedic applications: "Optimising PMMA-NVP hydrogels for orthotropic, self-inflating tissue expanders" J.R. Smith, Z. Radzi, J.T. Czernuszka

BioTrinity 2014, London, UK Innovation Poster Presentations: "Optimising P(MMA-NVP) hydrogels for orthotropic, self-inflating tissue expanders" J.R. Smith, Z. Radzi, J.T. Czernuszka

British Equine Veterinary Association (BEVA) 2014, Birmingham, Oxtex Ltd Expo stand

ECVS Annual Scientific Meeting 2014, Copenhagen, Oxtex Ltd Expo stand

Acknowledgements

There are countless people I wish to thank on completion of my thesis, without whom the last four years would not have been so productive nor enjoyable.

Firstly, I would like to thank my supervisor, Professor Jan Czernuszka for his encouragement, support and advice throughout my project. I have sincerely valued being a part of the biomaterials group and have enjoyed working with so many ambitious and creative people. In particular I wish to thank the soft tissue subgroup of Yun, Michelle, Kerem and Sheen.

I am so grateful to the Department of Materials for giving me the opportunity to conduct this research. In particular I thank; Laurie Walton for his help with machining samples and moulds; Kyriakos Porfyrakis for his help with UV-VIS; David Collins for his help with UTS and for providing a lot of good advice throughout my degree; and all of the support and administrative staff who have helped me in countless ways over the years.

The project would not exist without Oxtex, who have been a fantastic sponsor, providing me with many incredible opportunities. I especially want to thank Dave Jackson for all of his help and insight, Justine McQuillan, and Carly Lovell, without whom large parts of this work would have been impossible. Furthermore, the collaboration with the University of Malaya and the University of Putra Malaya has been valuable to the project and I would like to thank Dr Zamri Radzi and Professor Noor Hayaty Abu Kasim who gave me the opportunity to travel to the University of Malaya during my PhD to work closely with the group, as well as to the research students and vets who carried out the animal model work of my samples. I would also like to thank Tharini Gunawardena for her help and friendship during my visit to Malaysia.

St Anne's has played a significant role in my life over the last eight years, and I couldn't have produced this thesis without the college's support and encouragement. In particular Dr Anne Mullen, Tim Gardam and Professor Chris Grovenor all played very important roles in helping me develop my academic and professional skills during my time at Oxford. It was under their suggestion that I worked with Jane Clark, who taught me more about how I work than I will ever be able to thank her for.

And now I would like to thank my friends, who have made the last four years so much brighter. To Sophie, Emma and Caroline, you have been such fun and patient housemates and ensured that I am leaving Oxford with some knowledge beyond science! To Jude and Dave, your friendships have been invaluable and I'm sure will continue to be for years to come. To George, Louise, Emma, Dave, Sandy and Tom who were there since the beginning- what a journey! I couldn't have wished to spend it with more excellent people.

Finally, I will be ever grateful to Matt and to my family for their emotional and practical support, and their tolerance and love over the last 4 years. In particular to my parents, who started me on this journey- thank you.

List of Abbreviations

AIBN	Azobisisobutyronitrile
DMA	Dynamic mechanical analysis
DSC	Differential scanning calorimetry
EWC	Equilibrium water content
H&E	Haematoxylin and eosin
MMA	Methyl methacrylate
NVP	N-vinylpyrrolidone
P(MMA-co-NVP)	Poly(methyl methacrylate-co-vinylpyrrolidone)
PAM	Poly(acrylamide)
PDMS	Poly(dimethylsiloxane)
PEO	Poly(ethylene oxide)
PMMA	Poly(methyl methacrylate)
PTFE	Poly(tetrafluoroethylene)
PVA	Poly(vinyl alcohol)
PVP	Poly(vinylpyrrolidone)
SAL	Sterility assurance level
TGA	Thermogravimetric analysis
UTS	Ultimate tensile stress
UV-VIS	Ultra-violet-visible spectroscopy

List of Symbols

Equation 2.1

A_B	The area of the skin required to cover both fingers individually (case B)
A_A	The area of skin required to cover both fingers fused together (case A)
l	The length of the finger
r	The radius of each finger

Equation 2.2 – Equation 2.7

V_{cube}	The volume of the initial (dry) cube
A_{cube}	The area of the initial (dry) cube which is in contact with skin
x	The length of the sides of the initial (dry) cube
$V_{cube,\,iso}$	The volume of the isotropically expanded cube
$A_{cube,iso}$	The area of the isotropically expanded cube which is in contact with skin
$V_{cube,\,ani}$	The volume of the anisotropically expanded cube
$A_{cube,ani}$	The area of the anisotropically expanded cube which is in contact with skin
V_{cyl}	The volume of the initial (dry) cylinder
A_{cyl}	The area of the initial (dry) cylinder which is in contact with skin
$V_{cyl,\,iso}$	The volume of the isotropically expanded cylinder
$A_{cyl,iso}$	The area of the isotropically expanded cylinder which is in contact with skin
$V_{cyl,\,ani}$	The volume of the anisotropically expanded cylinder
$A_{cyl,ani}$	The area of the anisotropically expanded cylinder which is in contact with skin
r	The initial (dry) radius of the cylinder
h	The initial (dry) height of the cylinder

Equation 2.14-2.15

A_c	The area of new skin generated by a cylinder
A_d	The area of new skin generated by a dome
r	The radius of the disc, and the height of the cylinder

Equation 2.16-2.21

t	The time at which the measurement is taken
M_t	The mass of the hydrogel at time t
d_t	The diameter of the hydrogel at time t
h_t	The height of the hydrogel at time t
d_0	The diameter of the hydrogel at time $t = 0$
h_0	The height of the hydrogel at time $t = 0$

S_t	The mass of solvent absorbed by the hydrogel at time t
S_∞	The mass of the solvent absorbed by the hydrogel at equilibrium
k	The equilibrium rate constant
n	The diffusion exponent
l	The thickness (disc) or radius (cylinder) of the hydrogel
D	The diffusion coefficient

Equation 2.22-2.27

$R^{(.)}$	The polymer chain (radical)
$H^{(.)}$	A hydrogen atom (radical)
$O^{(.)}$	An oxygen atom (radical)

Equation 3.1

C	The compression ratio
h_i	The initial height of the dry hydrogel pellet (pre compression)
h_f	The height of the pressed hydrogel disc

Equation 3.2

Y_A	The larger mean value of compared data sets
Y_B	The smaller mean value of compared data sets
SE	The standard error of the compared data sets
q_s	The value to be compared to the critical value

Equation 3.3-3.4, and 4.2

$h_{\%}$	Percentage change in height at equilibrium
C	Compression ratio
h_s	Height of the swollen hydrogel
h_i	The initial height of the dry hydrogel pellet (pre compression)

Equation 3.5-3.8

R	The radius of the hydrogel disc
r	The distance from the centre of the hydrogel disc to an annulus
h	The height of the hydrogel disc
P	The stress applied to the hydrogel during hot pressing
K	The yield stress of the disc in pure shear
Y	The yield strength of the disc
μ	The interfacial friction

R_c The distance from the centre of the hydrogel disc to the boundary edge

σ_r The radial stress

σ_θ The stress in Θ direction

Equation 4.1

$m_{t=0}$ The mass of water at time 0

$m_{t=t}$ The mass of water at time t

$m_{t=\infty}$ The mass of water at equilibrium

Equation 4.3

M_W The mass of water absorbed by the gel

M_x The mass of the P(MMA-co-NVP) network

M_r The mass of the residual molecules in the P(MMA-co-NVP) network

Equation 5.1

t_1 The time at which the first height was measured

t_2 The time at which the second height was measured

h_{t_1} The height measured at t_1

h_{t_2} The height measured at t_2

Equation 5.2-5.6

$h_{\%}$ The percentage change in height after six weeks

$m_{\%}$ The percentage change in mass after six weeks

t The PDMS coating thickness

n The coating thickness

Equation 5.7-5.8

σ_θ Hoop stress

σ_z Axial stress

P Pressure exerted by the hydrogel

r Radius of the hydrogel

t Thickness of the PDMS coating

Equation 6.1-6.3

$t_{v=1mm}$ The time (in hours) required to remove the residual molecules from 1mm^3 of P(MMA-co-NVP)

t_c The time required to wash a single rod of P(MMA-co-NVP)

v_c	The volume of a single rod of P(MMA-co-NVP)
t_d	The time required to wash a dome pellet
v_d	The volume of a dome pellet
t_w	The time required to wash a wedge pellet
v_w	The volume of a wedge pellet

List of Figures

List of Tables

Contents

Chapter 1: Introduction

1 Introduction

The use of tissue expansion in plastic and reconstructive surgery is common and well documented (1–4). Whilst there are a number of different devices available, this thesis will focus on the advancement of rate controlled, anisotropic, hydrogel tissue expanders.

These devices have been chosen because they offer significant advantages over the traditional balloon expanders, and the more recently developed isotropic hydrogel expanders. For example, balloon expanders are inflated via saline injections which necessitates regular hospital visits, increasing the cost of the surgery and the risk of infection. This issue is addressed by using a hydrogel device, which inflates by absorbing local tissue fluids. Anisotropic devices are of greater interest than isotropic devices as they increase the area of tissue gained per unit volume of device, and can be used in a wider range of anatomical locations (allowing tissue expansion to be used in new surgical applications).

Few studies have been carried out on anisotropic hydrogel tissue expanders (5,6). It is therefore important to establish the limits of manufacturing anisotropic devices, and to determine how to predict and control the expansion of devices. Of particular interest are devices which can expand from a disc into non-prismatic geometry, as these may reduce complications rates, and allow for greater control over the shape of the resulting tissue (for example, variation in the resting tension of the skin).

The thesis will begin with a literature review, which will provide justification for this research from both the clinical and materials science view-points. Following this, there will be four experimental chapters; the key points of each will be briefly described below. The thesis will conclude with a summary of the work presented and suggestions of key areas for further research.

In the first experimental chapter, “Anisotropic swelling of P(MMA-co-NVP) hydrogels”, the compression of cylindrical pellets of P(MMA-co-NVP) into discs will be investigated, in order

to generate anisotropically expanding hydrogels. In particular, emphasis will be placed on understanding how the movement of the polymer network during compression moulding affects the swelling behaviour of the expanded devices. This chapter will culminate in the development of novel devices, which expand anisotropically from disc shapes into shapes with non-prismatic cross-sections (domes and wedges).

The second experimental chapter, “Processing a viable tissue expander using P(MMA-co-NVP)” will determine the effect of medical sterilisation (using γ-irradiation) on the compressed devices (with cylindrical cross-sections). The focus of this chapter will be the presence of residual molecules (remaining from synthesis of the co-polymer) which alter the reactions occurring during sterilisation, and cause changes to the expansion geometry of compressed, γ-irradiated samples. Different methods of washing and drying the P(MMA-co-NVP) will be investigated in order to remove the residual molecules, thus creating a viable medical device.

It will be shown in the literature review that the rate of swelling is an important consideration for tissue expanders, and if overlooked can result in pain and tissue rupture at the surgery site. The third experimental chapter “Controlling the swelling rate”, will address these concerns by coating compressed samples (with cylindrical cross-sections) with semi-permeable PDMS coatings. It will be shown that these devices have reduced expansion rates, but that this gain comes at the cost of the final expansion dimensions (and therefore area of new tissue growth per device).

Finally, in the fourth experimental chapter, “Animal model”, the findings of chapter two and chapter three will be applied to samples with non-prismatic cross-sections. The swelling properties of these samples will first be considered *in vitro*, before using two expanders in a small-scale animal model. This model will act as a proof of concept, by determining whether samples with non-prismatic cross-sections are able to retain their shapes during expansion *in vivo.* The expansion of the devices under the sheep dermis, as well as the histology of the

expanded tissue, will be compared to the results of a commercially produced, cylindrical device.

The results presented in this thesis help to identify how to reliably produce anisotropically expanding tissue expanders, which inflate gradually after insertion and are not adversely affected by the sterilization process. Furthermore, the work identifies the next generation of tissue expanders; devices which inflate from a flat disc into a non-prismatic shape (wedge or dome). These novel devices may allow for fewer complications during surgery, a greater area of generate skin, and an increase in the control over the shape of the new tissue.

Chapter 2

Literature Review

2 Literature Review

In order give context and justification for the research questions which will be posed in section 2.3, a survey of the current literature is given in this chapter. The review will begin by considering the merits and limitations of different devices used in tissue expansion, before moving on to hydrogels and their potential as the base material for such devices.

2.1 Tissue Expansion

This section will begin by giving a brief overview of the history of tissue expansion, before reviewing the role of anisotropic expansion and finally expansion rate control of devices.

2.1.1 The history of tissue expansion

Tissue expansion occurs when the skin is stretched; this mechanical strain causes initial alignment of the collagen fibrils and stimulates replication of the cells, generating new, healthy tissue (7–10). Figure 2.1 shows this process schematically. Tissue expansion occurs naturally (e.g. during growth, weight gain and pregnancy), but can also be generated artificially by a tissue expander. The expander is implanted beneath the dermis and is subsequently inflated, creating tension within the tissue, and therefore causing growth (11–13). Once enough excess skin has been cultivated, the device is removed, and the excess skin is used in the reconstructive surgery (4). The excess skin could be used to cover a new prosthetic (e.g. otoplasty), or to replace excised skin (e.g. removal of skin cancer). Within this section, an account of the historical development of tissue expanders, the potential clinical applications and the role of device geometry on tissue growth will be given.

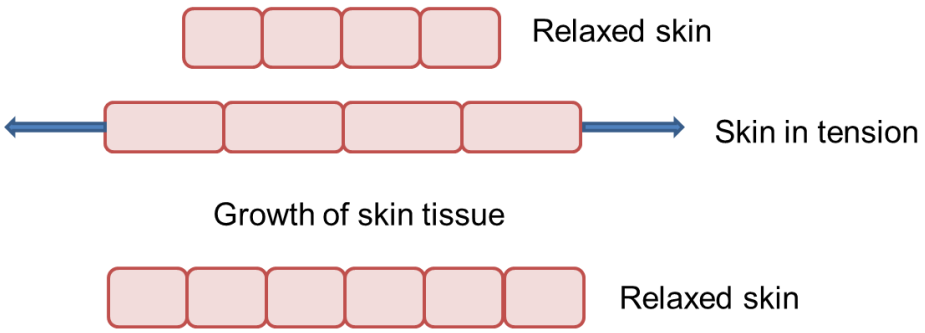

Figure 2.1 A schematic showing the process of skin growth in response to an applied tensile force

There are three basic designs of tissue expander which will be compared within this review. Photographs of each of these can be seen in Figure 2.2, and they will be discussed in turn. A traditional expander consists of a silicone balloon, connected to a metal backed filling port. The entire device is implanted under the skin, and is inflated with saline on a weekly basis via the filing port (4). Whilst this method of tissue expansion revolutionised plastic surgery, limitations such as the need for regular hospital visits, the bulk of the initial device, and the potential for infection at the port site are still a cause for concern (1,3,14,15). As a response to these limitations, self-inflating devices made of the hydrogel Poly(methyl methacrylate-co-vinylpyrrolidone), P(MMA-co-NVP), were developed (16,17). These devices are inserted in their dehydrated state, and expand isotropically by absorbing fluids from the surrounding tissue. The third type of expander is also made using P(MMA-co-NVP), but the device has been manufactured so that it expands anisotropically when implanted (5). The expansion rate of both of the hydrogel based expanders can be controlled by encapsulating the devices in perforated silicone (18,6). Figure 2.3 schematically describes the *in vivo* expansion of the devices.

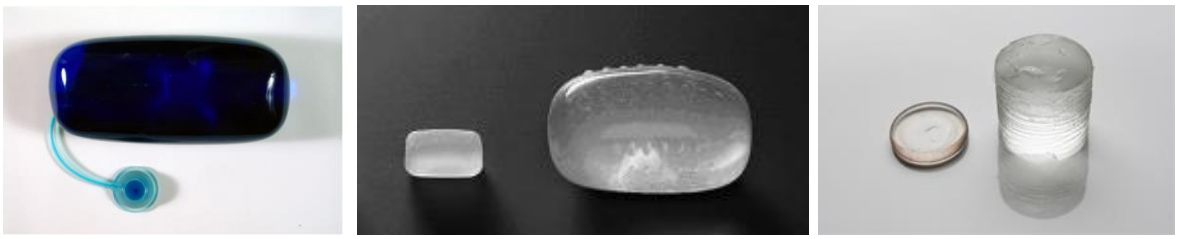

Figure 2.2 A comparison of different types of tissue expander. From left to right: A traditional silicone balloon expander, hydrated with a blue dye; an isotropic hydrogel expander; an anisotropic hydrogel expander

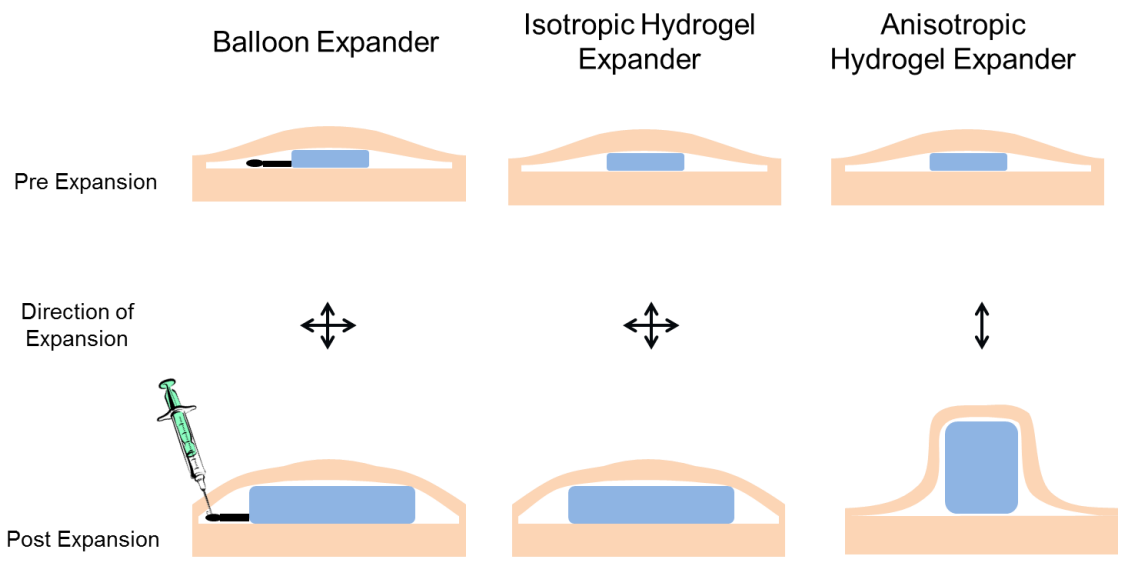

Figure 2.3 A schematic comparing the expansion of balloon, isotropic hydrogel and anisotropic hydrogel expanders under the skin

2.1.2 Anisotropy in tissue expansion

Device development has progressed in response to clinical demands. One of the key advances has been anisotropically inflating tissue expanders. Two justifications for anisotropic expansion have been proposed; firstly that being able to control the direction of expansion increases the range of surgical applications in which tissue expansion can be used; and secondly, that it increases the area of skin generated per unit volume of the device. Both of these assertions will be discussed in turn in this section. Applications in the dermis and the mucosa will be considered.

Surgical applications

The two main surgeries on the dermis are syndactyly correction and defect excision. Syndactyly is a condition where digits are fused together by soft tissue from birth, occurring in approximately 1 in 2,500 births (19). The surgical procedure to correct syndactyly is to sever between the digits, then stretch the surrounding tissue around to meet the deficit (19). However, if there is insufficient additional tissue at the time of surgery, this can cause short-term problems such as wound opening, and long-term problems such as causing the skin to creep up between the digits in the months and years after surgery (20). Syndactyly can be seen schematically in Figure 2.4 where two fingers have been modelled as cylinders. The (A)

case describes the situation for total syndactyly where the cylinders model the underlying fingers and the black line represents the skin which has fused the fingers together. Case (B) shows the desired surgical outcome of two fingers which are both surrounded in skin. The additional area of skin required in case (B) compared to case (A) is shown in Equation 2.1. Where A_B is the area of the skin required to cover both fingers individually (case B), A_A is the area of skin required to cover both fingers fused together (case A), l is the length of the finger, and r is the radius of each finger. If typical values for the length, $l = 7cm$ and finger radius, $r = 0.8cm$ are used, and it is assumed that the skin is only stretched perpendicular to the length of the finger, then this gives a strain of approximately 0.25 (not taking into account any additional tissue required to suture). The value for strain at the ultimate tensile stress of skin, depending on the strain rate (between 50mm/min and 2m/s) and angle of testing relative to the Langer lines, lies between 0.3 and 0.5, with the elastic region starting at approximately 0.1 strain (21). Therefore, a strain of 0.25 required to repair the case given in Figure 2.4 (as calculated above) would be towards the end of the linear elastic portion of the stress strain curve. This high strain may be the cause of complications such as wound opening and tissue creep. Creating excess skin using tissue expansion may eliminate these complications without the need for grafting or multiple flap creation. However, anisotropic expansion is vital if this is to be considered, as otherwise there is a risk of expansion beyond the fingertip, or into the knuckle joint.

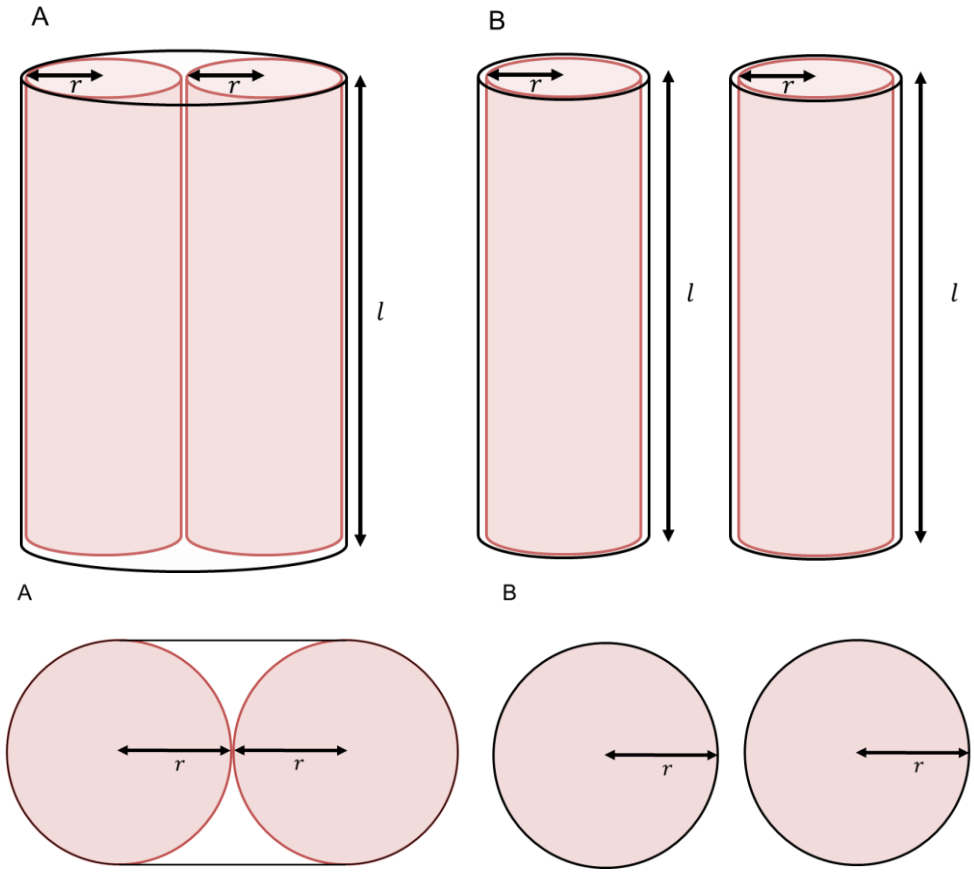

Figure 2.4 A schematic of fingers modelled as cylinders with surround skin modelled as sheets. Case A: Syndactyly case, where two adjacent fingers are covered by the same sheet of skin. Case B: Healthy case where two fingers are separate and covered in separate sheets of skin

$$A_B - A_A = 2lr(\pi - 2)$$

Equation 2.1

Defect excision refers to the removal of nevi, and the replacement of burn, scar or cancerous tissue. Nevi are regions of abnormal skin on the body, such as birthmarks and moles. Birthmarks occur in one in ten of the population, whilst moles are almost ubiquitous (2,22). Surgery for nevi is normally elective (and does not always require tissue expansion prior to surgery), but not purely cosmetic, as a region of skin with nevi is 50% more likely to develop skin cancer than an unaffected region of skin (22). Surgeries for the removal of burn, scar, cancerous or otherwise defected tissue may be either life-saving or elective. In excision surgeries, the device must be located such that it will not expand into the defected skin (and in the case of some soft tissue sarcomas, a pseudocapsule surrounds the tumour which must also be removed to prevent new tumour growth (23)) necessitating a minimal distance

(dependent on the lateral expansion of the device and the size of the exclusion zone) between the device and the defected skin. As shown schematically in Figure 2.5, if the device is anisotropic, this distance can be greatly reduced, thereby increasing the number of cases where tissue expansion is a feasible surgical option, as well as increasing the efficiency of current surgeries.

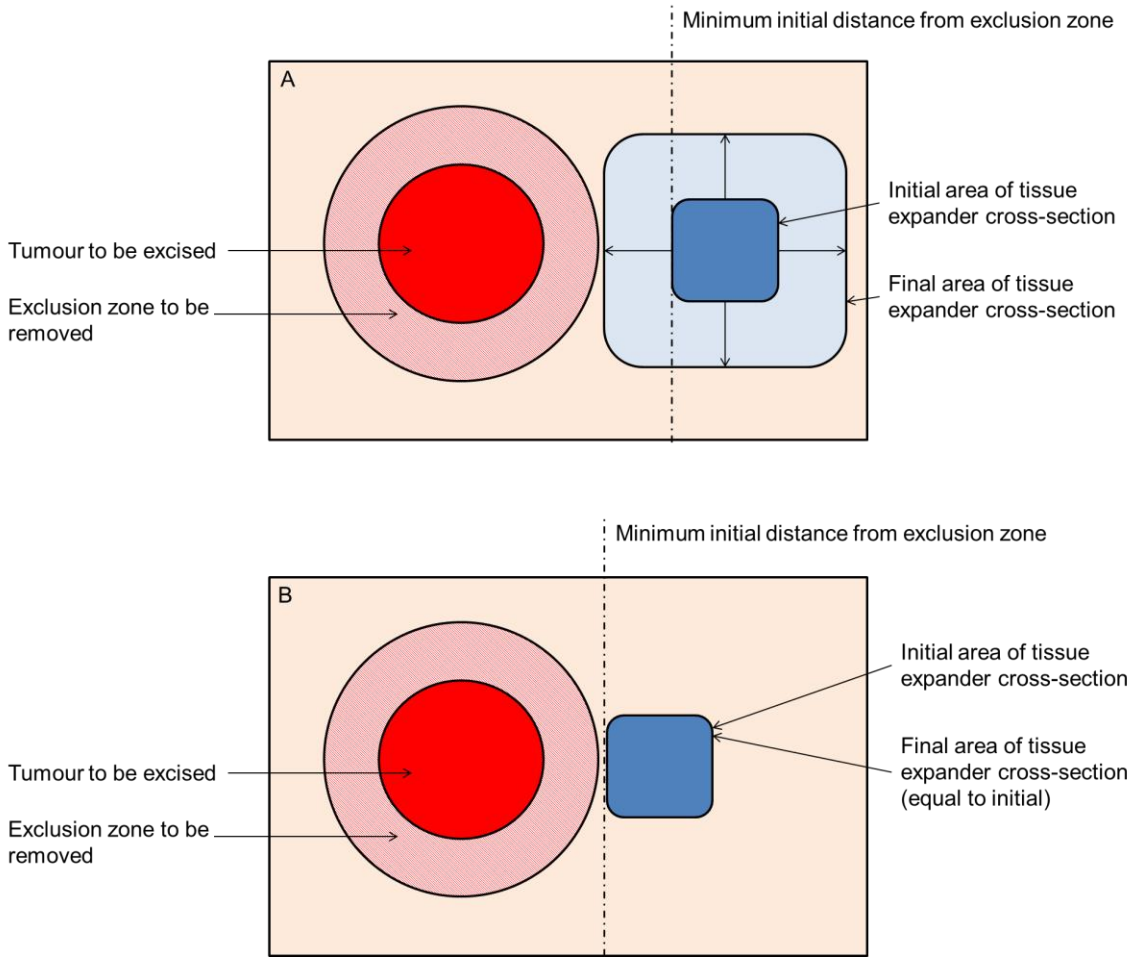

Figure 2.5 A schematic showing the minimum distances of a tissue expansion device from an exclusion zone when removing a tumour for A) isotropic expanders and B) anisotropic expanders

There are a number of maxillofacial surgeries where expansion of the mucosa is desirable, including repair of a cleft palate, alveolar ridge reconstruction and cross-bite restoration. In alveolar ridge reconstruction, additional soft tissue is needed for the implantation of a hard tissue prosthetic (24). A cleft palate occurs in approximately 1 in 750 babies, and it is frequently seen in conjunction with a cleft lip (25,26). The condition results from a failure of the palate to fuse during gestation. A cleft palate also leads to difficulties in speech development, eating, drinking and in some cases can cause psychological trauma (27–29).

Around 20% of cleft palates can be repaired by a single operation between the ages of 6 months and 12 months through stretching the existing soft tissue across the gap (30–32). However, the majority of cases require further surgeries as the patient grows, due to regression of the palate. This regression is thought to be due to insufficient soft tissue at the time of surgery, which creates tension at the closure site and in turn detrimentally effects the biological function of the mucosa (30,33). Therefore, generating excess skin prior to surgery may improve the long-term outcomes. Silicone balloon expanders are too large to be used oral applications, particularly in paediatric cases, and therefore hydrogel based expanders are of most interest. Due to the close proximity of the teeth and throat, anisotropic expanders are of much greater interest for mucosa applications that isotropic expanders.

Tissue generation

The area of skin per unit volume must be compared for isotropic vs anisotropic expanders. Duits (34) showed that for isotropic tissue expanders of identical volumes, expansion perpendicular to the skin surface has the biggest impact on the area of tissue generated. This work can be adapted to enable comparison of isotropic and anisotropic expanders of the same initial and final volumes. Figure 2.6 shows the cases for isotropic and anisotropic expansion of a cube. The initial volumes are the same, and thus the final volumes must also be the same (assuming an equal absorption of tissue fluid). Equation 2.2 and Equation 2.3 give the volume and area of the initial cubic volume, where the area does not include the base of the expander as no skin overlies this surface and thus it does not contribute to tissue expansion. Equation 2.4 and Equation 2.5 show the increase in volume and area for the isotropic case, and Equation 2.6 and Equation 2.7 show the volume and area for the anisotropic case. The volumes of the isotropic and anisotropic cases are the same (Equation 2.4 and Equation 2.6). However, the surface area of the isotropic case is given by Equation 2.5 and is shown to yield a smaller value than the anisotropic case (Equation 2.7). This shows that, in the case of a cube, for every unit volume of hydrogel, a greater area of new tissue is generated by the anisotropic expander. V_{cube} is the volume of the initial cube, A_{cube} is the area of the initial cube, $V_{cube,\,iso}$ and $A_{cube,iso}$ are the volume and area of the

isotropically expanded cube, $V_{cube,\,ani}$ and $A_{cube,ani}$ are the volume and area of the anisotropically expanded cube, n is the expansion factor (and $n > 1$) and x is the length of the initial sides of the cube.

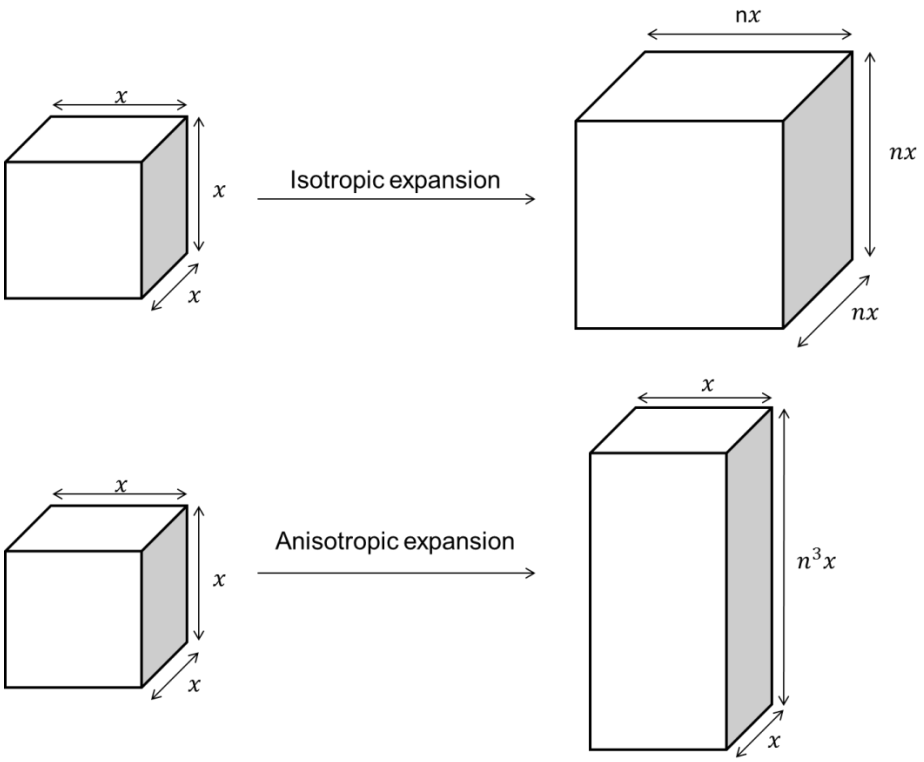

Figure 2.6 A schematic showing the change in dimensions for a cubic expander expanding isotropically (above) and anisotropically (below)

$$V_{cube,} = x^3$$

Equation 2.2

$$A_{cube} = 5x^2$$

Equation 2.3

$$V_{cube,\,iso} = n^3x^3$$

Equation 2.4

$$A_{cube,iso} = 5n^2x^2$$

Equation 2.5

$$V_{cube,\,ani} = n^3x^3$$

Equation 2.6

$$A_{cube,ani} = 4n^3x^2 + x^2$$

Equation 2.7

The same result can be shown for cylinders, as seen in Figure 2.7. In this case V_{cyl} is the volume of the initial cylinder, A_{cyl} is the area of the initial cylinder, $V_{cyl,\,iso}$ and $A_{cyl,iso}$ are the volume and area of the isotropically expanded cylinder, $V_{cyl,\,ani}$ and $A_{cyl,ani}$ are the volume and area of the anisotropically expanded cylinder, n is the expansion factor (and $n > 1$) and r is the initial radius of the cylinder and h is the initial height of the cylinder. Equation 2.8 and Equation 2.9 show the volume and area of the original cylinder, Equation 2.10 and Equation 2.11 show the volume and area of the isotropically expanded cylinder, and Equation 2.12 and Equation 2.13 show the volume and area of the anisotropically expanded cylinder. Again, for the same unit volume, the area of tissue generated by the anisotropic expander is greater than for that of the isotropically expanded device. The production of anisotropic devices will be discussed in section 2.2.5.

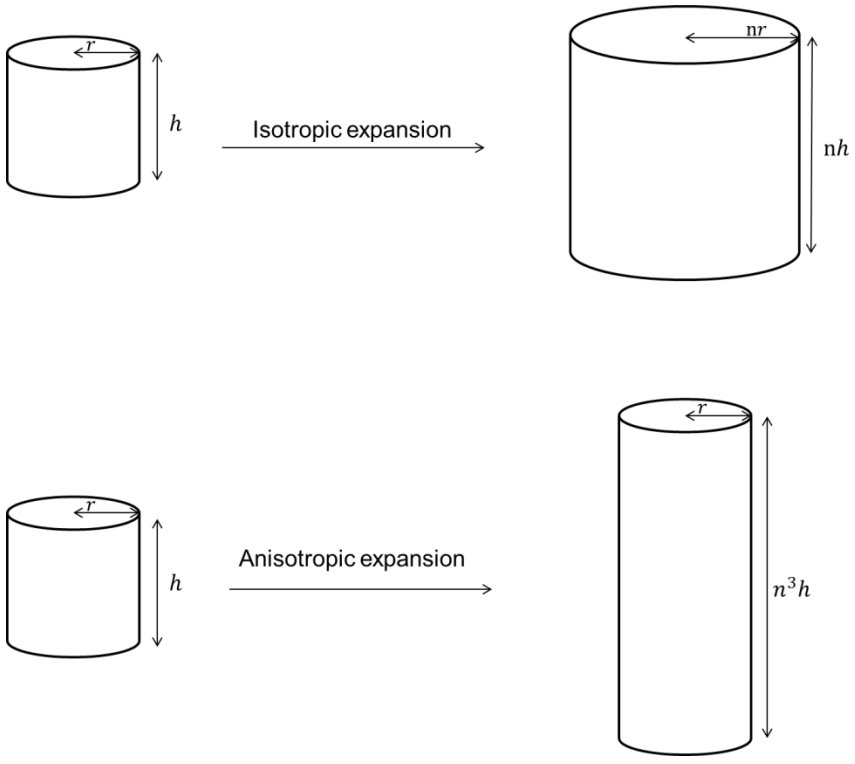

Figure 2.7 A schematic showing the change in dimensions for a cylindrical expander expanding isotropically (above) and anisotropically (below)

$$V_{cyl} = \pi h r^2$$

Equation 2.8

$$A_{cyl} = \pi r(r + 2h)$$

Equation 2.9

$$V_{cyl,\,iso} = n^3 \pi h r^2$$

Equation 2.10

$$A_{cyl,iso} = n^2 \pi r(2h + r)$$

Equation 2.11

$$V_{cyl,\,ani} = n^3 \pi h r^2$$

Equation 2.12

$$A_{cyl,ani} = \pi r(r + 2hn^3)$$

Equation 2.13

It is also possible that the final shape of the anisotropic devices may have an impact on the area and health of newly-generated skin tissue. For example, it may be of interest to develop a sample which can expand anisotropically from a flat, uniform disc into a predetermined non-prismatic shape (e.g. a dome). There are a number of clinical motivations for doing so. Firstly, as the skin grows, it would mean that the resting tension of the new tissue may match the shape of the expander. It is feasible, therefore, that an anisotropic expander could be developed which mimics the shape of the prosthetic which would replace it, therefore improving the aesthetic outcome of the surgery. This can be seen schematically in Figure 2.8. Furthermore, as shown in Figure 2.9, in cylindrical devices the sides are strained (therefore producing new tissue), whereas the top surface is not, but in domed samples there is a gradual distribution of strain. The 90° angle, present in the cylindrical samples, creates regions of high local stress at the interface between the top and side surfaces, potentially leading to damage to the tissue in this area. By gradually reducing the strain in the tissue overlying the expander, as in the case for the domed sample, the quality of the tissue produced may be improved. For these reasons, anisotropic samples which expand from a uniform disc to a shape with a non-prismatic cross-section (e.g. a dome) mark the next step

in the development of hydrogel tissue expanders. However, it should be considered that this may result in a lower area of new tissue being produced. Figure 2.10 shows a disc (A) expanding into a cylinder (B), or a hemi-sphere (C). The area of new skin generated by the cylinder is shown in Equation 2.14, where A_c is the area of new skin generated by the tissue expander, and r is the radius, and height of the device. The initial thickness of the disc is not taken into account (as it is constant for both shapes), and it is assumed that the top surface of the cylinder does not contribute to the generation of new tissue. The area of new skin generated by the hemi-sphere sample is given by Equation 2.15, A_d is the area of new skin generated by the tissue expander, and r is the radius of the hemi-sphere. It is shown that the area of skin generated by the hemi-sphere is half of that generated by the cylinder. This means that the most advantageous shape would be a cylindrical sample, with a domed top.

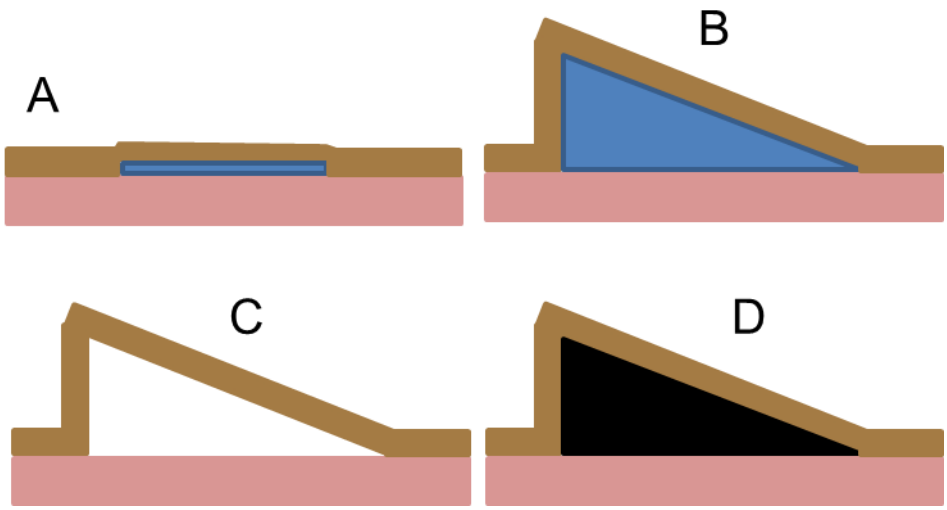

Figure 2.8 A schematic showing how non-prismatic expanders may be of use when new tissue is required to cover a permanent prosthetic. A) The flat hydrogel placed under the skin. B) The hydrogel expands into a triangular shape. C) The hydrogel is removed, and the newly grown skin tissue retains the triangular shape. D) The permanent prosthetic is inserted into the triangularly shaped cavity

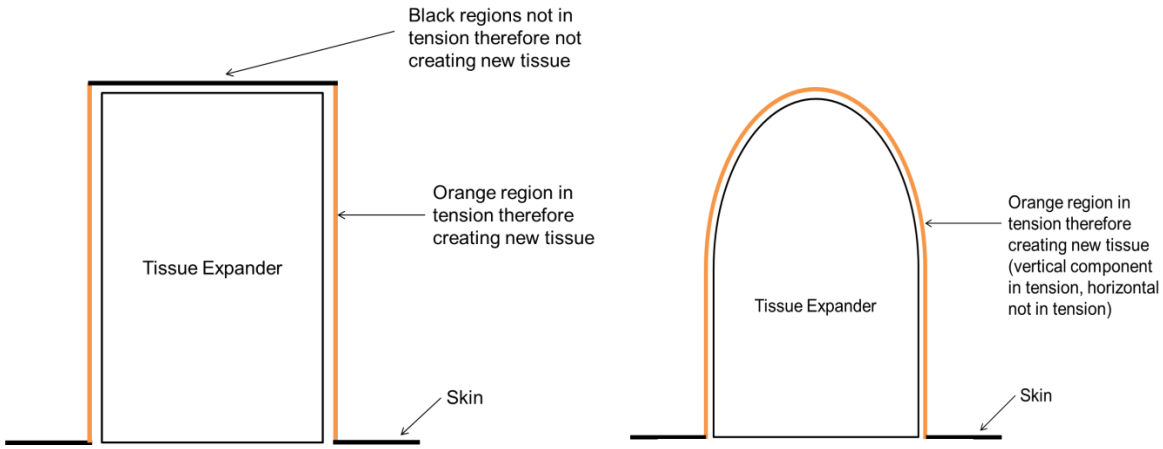

Figure 2.9 A comparison of the strained regions of skin overlying a cylindrical device (left) and a domed device (right)

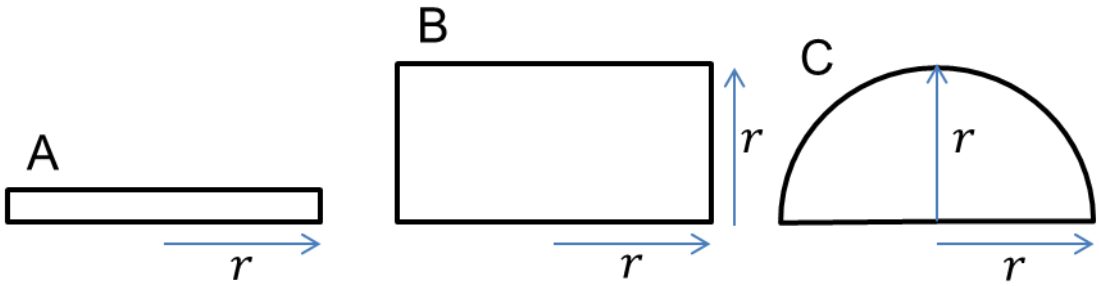

Figure 2.10 A comparison of the changes in surface area from a disc (A), into a cylinder (B) or dome (C)

$$A_c = 2\pi r^2$$

Equation 2.14

$$A_d = \pi r^2$$

Equation 2.15

2.1.3 Controlling the rate of expansion

A widely reported challenge for hydrogel expanders is controlling the rate of expansion. If the rate of expansion is too fast, then extrusion (device extrudes from surgical site), ulceration, fistulation (soft tissue rupture) and necrosis (device pressure limits blood flow to overlying tissue causing death of the tissue) may occur (2,14,15). Pain without serious complication is also reported in many cases. However, if the expansion is not sufficient, then the skin will not be under strain and no additional tissue will be generated. Another important consideration is that as the skin is held at a constant strain, stress-relaxation (also called biological creep) will

occur within the tissue (due to the restructuring of collagen fibres, growth of new collagen fibres and cell mitosis) (8,35–38). This stress relaxation begins to occur within minutes of expansion, and continues until the skin is at resting tension. The mechanical properties of the skin differ depending on the location (and orientation) of the skin and the age and lifestyle of the patient (39–43). Furthermore, as the skin is visco-elastic, the mechanical properties will be strain rate dependent (36,39,44). Table 2.1 gives examples of different observed mechanical properties (Young's modulus, ultimate tensile strength and failure strain) for different types of skin (40). Table 2.1 shows that, in general, higher failure strains are recorded at lower strain rates. Thus, it is preferable for a tissue expander to have a low expansion rate.

Table 2.1 Table reproduced from (40), comparing the tensile mechanical properties of skin, for humans, pigs and rats of different ages, with different strain rates used

Strain Rate	UTS (MPa)	Failure Strain (%)	Elastic Modulus (MPa)	Skin Type	Age
Quasistatic: 50mm/min	13.2-30	37-71	48.4-118.2	Back (human)	81-79 years
Quasistatic: 10%/min	2-15		18.8	Abdomen and thorax (human)	47-86 years
Quasistatic: 50mm/min	7-30	31-53		Abdomen and back (porcine)	7-8 months
Quasistatic: 0.25-10%/s	0.25-1	123-126	0.9-4.2	Abdomen (porcine)	9 months
Dynamic: 40-4000/s	25-57	40-60		Rump (porcine)	
Dynamic: 6000%/s	1.2-3.2	51.9-124.8		Dorsal skin (rat)	1-6 months
Dynamic	5.7-12.6	27-59	19.5-87.1	Forehead and arm (human)	62-98 years
Quasistatic		16-52	0.26-0.83	(human)	15-30 years
Dynamic: 1, 1.5, 2m/s	17.9-36.5	20.38-29.52	56.8-141.11	Back (human)	77-85 years

The expansion rate of the tissue expander will determine the strain rate of the overlying tissue. For balloon expanders, where expansion is controlled by injecting liquids, a balance must be made between the number of hospital visits required and the volume of expansion (and therefore rate of expansion) at each visit. However, one advantage of balloon expanders is that the surgeon is able to increase or reduce the expansion at each visit to adapt the surgery to each patient.

Initially, hydrogel devices did not have any rate control component, and the devices expanded within 24 hours of insertion. This caused numerous complications and device failures in both dermal and mucosal applications, e.g. fistulation and necrosis (45–51). Table 2.2 gives the changes in dimensions with time, for four different sizes of commercially available tissue expander. By considering this data it is possible to account for the observed clinical failures. The expanders are semi-spherical in shape. The strain of the overlying skin and the strain rate of expansion have been calculated. Whilst there is no direct overlap in the data presented in Table 2.1 and Table 2.2, the percentage strain imposed by the hydrogel on the overlying skin (Table 2.2), exceeds that of the failure strains of skin in each given case (Table 2.1). It also must be noted that the pressure generated by this device has not been considered, and it is possible that in some cases the pressure generated by the hydrogel may be insufficient to deform the overlying skin to the *in vitro* values seen in Table 2.1. However, in these cases a lower surface area of new tissue will be generated, potentially not yielding enough new tissue for the reconstructive surgery.

Table 2.2 Changes in dimension for Osmed semi-spherical devices (0.4ml-2ml), with corresponding strain and strain rate calculated

Initial Radius (mm)	Final Radius (mm)	Strain (%)	Time (min)	Strain Rate (%/min)
3	5.6	272.3	1440	0.2
4	7	235.6	1440	0.2
4.5	9	314.2	1440	0.2
5	10	314.2	2880	0.1

In response to this serious limitation of hydrogel expanders, Anwander *et al* (18) placed Osmed hydrogel devices in perforated (hole diameter and spacing not reported) silicone bags, as seen in Figure 2.11. The silicone bags are intended to slow the rate of expansion by limiting the rate at which fluid enters the hydrogel. However, as seen in Figure 2.11 the final swelling volume for the device inside the bag is lower than for the nude device (reported as 75ml and 60ml respectively). Though it is not discussed by Anwander *et al* (18), the final dimensions of the sample in the bag appear to be approximately the same as the initial dimensions of the bag, which means that the bag is limiting the final volume of the device. In clinical trials of silicone encapsulated, and not silicone encapsulated hydrogel expanders, it is consistently found that the encapsulated devices result in fewer complications (e.g. extrusions) compared to the hydrogels with no expansion rate control (18,51,52). However, it has been reported that most of the expansion still occurred within the first 24 hours of swelling, causing pain and discomfort to patients. Therefore, it may be possible that reducing the rate of water in the system using this method is not sufficiently limiting the expansion rate of the hydrogel, but that the early termination of expansion (caused by the mechanical constraint of the silicone bag) is reducing the complication rate. This means that the strain rate of the skin expansion is unchanged, but that the maximum strain induced in the skin by the underlying tissue expander is reduced.

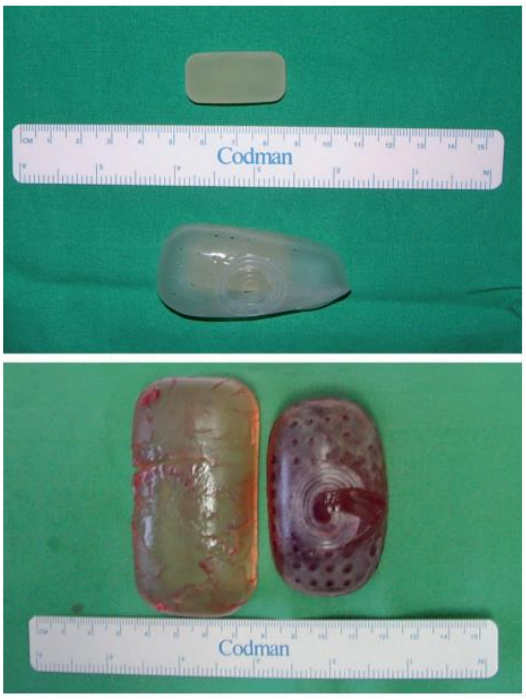

Figure 2.11 "Expander before (*above*) and after (*below*) expansion". Image reproduced from (18)

Another approach to controlling the rate of expansion of hydrogel expanders was investigated by Swan *et* al, for anisotropic hydrogel devices (6). In this case a perforated silicone coating was also used, but the volume encapsulating the hydrogel was equal to the volume of the initial hydrogel. Multiple devices were then placed on the same sheet as seen in Figure 2.12. This study also reported a reduced maximum swelling volume compared to the nude hydrogel. For samples of P(MMA-co-NVP) with a silicone coating with 75µm holes in a 2.0mm spaced array, implanted in the scalp of a pig, the time taken to reach 50% of expansion was 62.6 (±14.6) hours and the time to 100% expansion was 424.7 (±56) hours. Whilst the expansion is not linear, it is a significant improvement on previous samples (where majority swelling is reported within the first 24 hours). The change in height during swelling was not reported, so strain rates and strains cannot be calculated. The perforated silicone capsule effectively controlled the expansion from time, $t = 0$, and reduced the final swelling volume of the sample. The rate at which water diffused into the sample was shown to reduce the expansion rate, because as the pitch of the holes was decreased, and the diameter of the holes increased, the rate of swelling was increased. As with samples enclosed within

perforated silicone bags, the restrictive forces of the silicone sheets are likely to cause the reduction in final swelling volume.

Figure 2.12 "Fabricated tissue expander devices: coated, subunit 8 x 4 x 1mm". Image reproduced from (6)

Therefore, as silicone coatings in direct contact with the xerogel have been shown to control the expansion rate from time, $t = 0$, this rate control method appears to show the most potential. Furthermore, smaller devices, such as these, will have clinical advantages, for example it is easier to position the hydrogel in the surgical site more accurately if it is not enclosed within a bag. This is very important for anisotropic devices, where incorrect orientation on insertion could result in expansion into vulnerable regions, e.g. the throat. It is therefore most beneficial to investigate silicone coatings where the silicone is in direct contact with the xerogel. Applying a silicone dispersion directly to the hydrogel surface will result in a semi-permeable silicone membrane (47), and it may be possible that controlling the thickness of this coating would also control the rate of expansion effectively, thus reducing the number of steps required in manufacturing.

2.2 Hydrogels

This section of the literature review will begin by giving a background to the basic properties of hydrogels and their role in a variety of medical applications. After this, the review will focus primarily on literature directly related to the production of self-inflating anisotropic tissue

expanders. In some areas the literature is limited, and comparisons will be drawn from other areas of materials science.

2.2.1 Hydrogels in medicine

Hydrogels are cross-linked (either chemical or physical) hydrophilic polymer networks, which are able to absorb large volumes of water whilst maintaining their 3D structure (53–55). They are a commonly used material for medical devices. A brief overview of their use in tissue engineering, drug deliver and wound dressings will be given, before expanding on their use as tissue expanders. The hydrogel network can either be permanent or degradable with both categories of great interest for medical devices. Table 2.3 shows examples of the base polymers for different hydrogels and their common medical uses.

Table 2.3 Examples of different hydrogels

Name of hydrogel forming polymer	Chemical structure	Common hydrogel form	Common use
Poly(ethylene oxide) (PEO)	$(C_2H_6O_2)_n$	Cross-linked via Poly(urethane)	Scaffolds
Poly(vinyl alcohol) (PVA)	$(C_2H_4O)_n$	Cross-linked via repeated freeze drying	Scaffolds and Drug delivery
Polyacrylamide (PAM)	$(C_3H_5NO)_n$	Cross-linked via N.N-methylenebisacrylamide	Wound dressings
Polyvinylpyrrolidone (PVP)	$(C_6H_9NO)_n$	Cross-linked via Poly(methylmethacrylate)	Contact lenses and tissue expansion

The role of a tissue scaffold is to create a 3D environment where cell proliferation can be controlled and directed in order to generate new tissue or cell cultures (56). Hydrogels are often used for this purpose due to the similarity of the compression modulus of hydrogels and biological tissue (a factor known to effect cell proliferation), the porosity (allowing growth factor diffusion and cell attachment) and the opportunity to make the devices degradable (to return to normal biological function) (54,55,57–60). Hydrogels are also used to control the rate and location of drug release in drug delivery systems (53,61–65). The gels are loaded

into the system by hydration in a solution of the drug followed by evaporation of the solvent. On entry into the body, the hydrogel is rehydrated and the drug released. By controlling the hydrogel composition and structure, the rate of diffusion of the drug into the system can be regulated, as well as changes to this rate depending on chemical surroundings (e.g. pH), thereby reducing the systematic dose and risk of side effects (66–70). The controllable partial permeability of hydrogels also allows them to be used in wound dressings. Thin and flexible dressings can be developed which are permeable to gases, salts, metabolites and proteins but impermeable to bacteria (71). In addition hydrogels can be used in pastes or creams for wound healing. Hydrogel wound dressings have been shown to reduce adverse effects for patients compared to traditional dressings, such as discomfort, tissue trauma and pain on removal (72–74).

Finally, as discussed in section 2.1.1, hydrogels, in particular P(MMA-co-NVP), are of great interest for the development of tissue expanders. The hydrogel is a cross-linked block co-polymer, usually with a greater proportion of NVP (the hydrophilic component) than PMMA; a typically reported ratio is 10:90 MMA:NVP (16,5). The expansion of a hydrogel is a balance between expanding forces (hydrophilic side chains causing water absorption) and compressive forces (cross-linking, entanglement and hydrophobic regions). However, when being used in tissue expansion, the additional compressive force of the skin must be considered and thus the maximum swelling capacity of the gel may be reduced (4,35). As most studies use a commercially-produced device, it is not always possible to find information for the exact synthesis or mechanical properties of the gels used in reported clinical trials. However, there is literature on the synthesis of P(MMA-co-NVP) as well as the production of anisotropic tissue expanders (5,75).

It is clear that hydrogels are very important in a wide variety of biomedical applications. Furthermore, progress and research in gels designed for a particular medical application are likely to further the field as a whole. The next section of the review will focus on P(MMA-co-NVP) and its role in tissue expansion.

2.2.2 P(MMA-co-NVP)

Synthesis of P(MMA-co-NVP) will not be undertaken within this thesis, and therefore detailed comparison of different synthesis routes will not be discussed. Instead a brief account of the general processing route will be given.

P(MMA-co-NVP) is formed through free radical, addition polymerisation of the monomer units (methyl methacrylate and vinylpyrrolidone) in the presence of an initiator and a cross-linking agent (76–79). The chemical structures of the monomers are shown in Figure 2.13. The synthesis of the polymer used in this thesis is given in section 3.2.1. P(MMA-co-NVP) has a block copolymer structure. The vinylpyrrolidone units provide the hydrophilic properties, and the methyl methacrylate provides the mechanical stability. As the proportion of methyl methacrylate increases, the swelling capacity of the gel decreases. This can be seen in Table 2.4 (80).

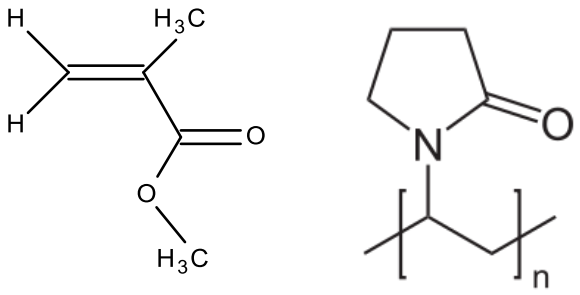

Figure 2.13 Monomer structure of methyl methacrylate (left) and vinylpyrrolidone (right)

Table 2.4 "Sample compositions, sol fractions and EWCs of poly(MMA-co-VP) hydrogels" reproduced from (80). EWC refers to the equilibrium water content which is defined in Equation 2.16

Sample	True copolymer composition	Sol fraction (wt%)	EWC (wt%)
MMA75/VP25	MMA 75·5/VP 24·5	0·7	15·2
MMA60/VP40	MMA 62·2/VP 37·8	3·5	30·4
MMA45/VP55	MMA 47·4/VP 52·6	5·1	47·6
MMA30/VP70	MMA 33·1/VP 66·9	9·5	63·8
MMA15/VP85	MMA 16·9/VP 83·1	11·5	75·9

2.2.3 Diffusion and swelling of hydrogels

When dry, the polymer network of a hydrogel (also called a xerogel in the dry state) is collapsed, as seen in Figure 2.14. When the gel is hydrated, the polar side groups attract the water molecules causing the water molecules to be absorbed. Hydrogen bonding occurs between the side groups (which can be δ^+ or δ^-) and either the δ^+ hydrogen atoms or the δ^+ oxygen atom. . The presence of these water molecules in the polymer network increases the internal pressure of the hydrogel and causes the polymer chains in the network to extend, thus expanding the whole network. As the network expands, there is further diffusion of water into the system due to an osmotic gradient. The volume fraction of solution to polymer varies between 20% and 99.99%, with systems above 95% being classed as superabsorbent (81). The equilibrium swelling point will be reached when the forces for expansion are equal to the restrictive forces (e.g. cross-links, any hydrophobic regions and resistance to chain extension) (16).

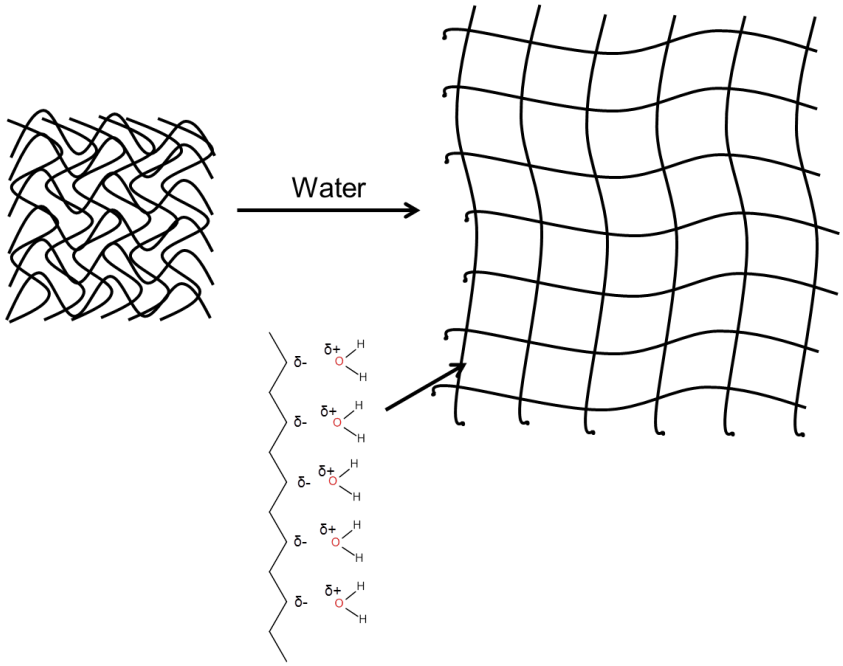

Figure 2.14 A schematic showing the change in hydrogel network structure between the dry (left) and hydrated (right) state. The chain back bone, with hydrophilic (δ-) side groups, and the water (δ+) are also shown

Water can exist in three different states within a hydrogel, identified by their different thermal transition temperatures (77,80,82). Firstly, there is the bulk, or free water, and this has a freezing temperature of 273K. Secondly, there is freezable-bound water, which has a freezing point of below 273K. Finally, there is bound, non-freezing water, which has no discernible freezing temperature within the range of 200K-273K. These are the first water molecules to enter the hydrogel network, and their shape is thought to be altered by the polymer network, thus reducing the strength of the hydrogen bonding (83). The greater the degree of polarisation, the greater the number of bound water molecules per unit polymer. Each VP unit in P(MMA-co-NVP) is reported to have approximately 7.5 molecules of bound water (77).

There are a number of methods for comparing the water uptake of hydrogels. A common method when hydrogels of different composition are being compared is to measure the equilibrium water content (EWC), which is defined by Equation 2.16, where M_0 is the mass of the hydrogel before swelling (the xerogel), and M_∞ is the mass of the hydrogel at equilibrium swelling.

$$EWC = \frac{M_\infty - M_0}{M_\infty}$$

Equation 2.16

In other situations it may be useful to present the mass uptake as a percentage increase, as described in Equation 2.17 (84), where M_t is the mass of the hydrogel at time, t. It can also be easily adapted to compare changes in diameter and height, as seen in Equation 2.18 and Equation 2.19 respectively, where d_t and d_0 represent the diameter at time t and before swelling respectively, and h_t and h_0 represent the height at time t and before swelling respectively.

$$Percentage\ change\ in\ mass = \frac{M_t - M_0}{M_0} \times 100$$

Equation 2.17

$$Percentage\ change\ in\ diameter = \frac{d_t - d_0}{d_0} \times 100$$

Equation 2.18

$$Percentage\ change\ in\ height = \frac{h_t - h_0}{h_0} \times 100$$

Equation 2.19

The rate of diffusion of water into the hydrogel network is governed by the hydrogel composition and structure, and can be characterised by the Diffusion Coefficient, D. The solute uptake of the polymer can be considered in two parts; the initial sorption of the solute into the hydrogel network, and the relaxation of the polymer chains which allows for diffusion through the polymer network (85,86). In the case of hydrogels, as the water diffuses into the network, it acts as a plasticizer, greatly increasing the relaxation of the polymer chains. However, this creates a system with a boundary between the rubbery region (where water is present) and the glassy region (which has not yet been hydrated) (87). This can cause

stresses to build up at the interface which are reported to be compressive in the direction of diffusion and tensile perpendicular to the diffusion direction (88). Depending on the relationship between the rate at which diffusion occurs and the rate at which chains relax, these stresses can lead to cracking, crazing and buckling of the gel at the interface (87,89,90).

The diffusion of solute into isotropic hydrogel networks has been modelled by considering the expansion of partially constrained sheets, cubes and discs, in order to predict the geometry of expansion (91,92). The initial swelling geometries are shown in Figure 2.15. In the cube, the increased surface area for diffusion (at the edges and corners) results in each side having a bowl-like geometry. In both the sheet and the disc a wrinkled pattern occurs as the volume of the expanded annulus increases.

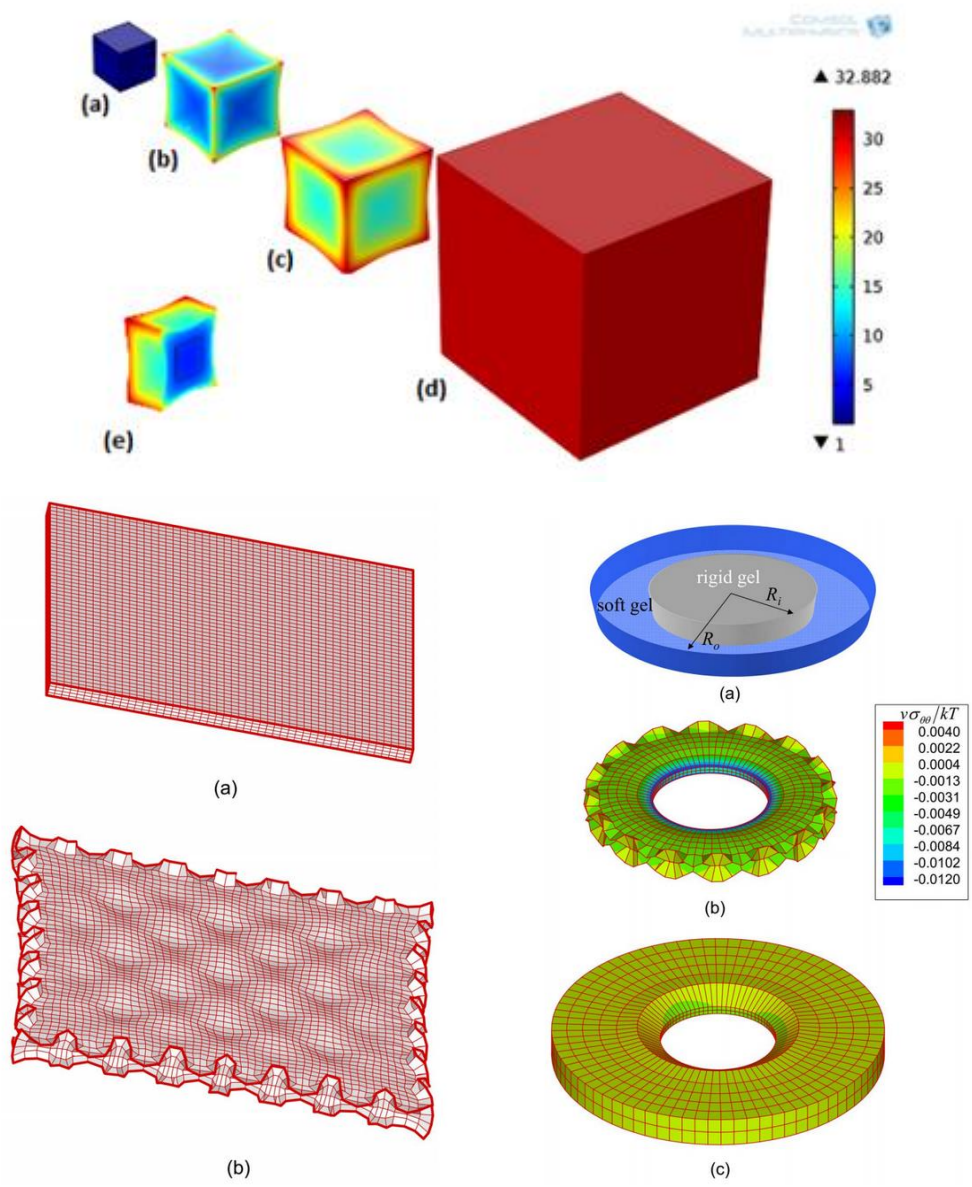

Figure 2.15 Examples of the geometries produced during the initial stages of swelling, reproduced from (91,92)

Diffusion of solvent into hydrogel networks is often characterised by considering the first 60% of the sorption curve (the short time approximation method) (93,94) and using the empirical power law model shown in Equation 2.20 (86), where: S_t is the mass of solvent at time t and S_∞ is the mass of the solvent at equilibrium, k is the equilibrium rate constant and n is the diffusion exponent (which also shows whether the swelling is Fickian or not- to be discussed in more detail below). By plotting the natural logarithms of the sorption curve (the natural log of swelling ratio vs the natural log of time) values for k and n can be determined. This can be seen in Equation 2.22, where it is clear that $\ln(k)$ is the curves intercept and n is the gradient

of the curve. For hydrogels Equation 2.21, (95) can then be used to find the diffusion coefficient, D. For a sheet or disc, l is taken as the thickness of the original (dry) hydrogel, and for a cylinder it is the radius.

$$\frac{S_t}{S_\infty} = kt^n$$

Equation 2.20

$$kt^n = 4\left(\frac{Dt}{\pi l^2}\right)^n$$

Equation 2.21

$$\ln\left(\frac{S_t}{S_\infty}\right) = \ln(k) + n\ln t$$

Equation 2.22

The diffusion exponent offers an insight into whether the diffusion is Fickian or not. Fickian diffusion is said to be occurring if the exponent is 0.5 (or less than 0.5 for pseudo Fickian) (95). For a Diffusion exponent of between 0.5 and 1 the diffusion is classified as Case III, and for equal to 1 (and occasionally above 1) the diffusion is Case II. Hydrogels predominantly fall into either Fickian (or pseudo Fickian) or Case II (93,94,96), and which occurs seems to be governed by the relationship between the rate of diffusion in and the ability for chain relaxation (85). In cases where Fickian diffusion is seen, the diffusion is much less than the chain relaxation and for Case II the opposite is true.

2.2.4 Anisotropy in hydrogels

A range of studies have been published on introducing anisotropy to hydrogel systems. The key areas are stress induced anisotropy (5), lyotropic liquid single crystal hydrogels (LSCH) (97), hydrogel composites (98) and directional freezing (99). Each of these techniques results in hydrogels with different structures, mechanical properties and swelling properties, and each of these properties can be useful depending on the desired application. Anisotropic swelling and mechanical stability *in vivo* are needed to produce a viable tissue expander, and

these are properties which may also be of significant use in other biological fields. In this section, each method of creating hydrogels with anisotropic properties will be reviewed in turn.

Due to the anisotropic properties of many biological tissues, the development of tissue scaffolds with an anisotropic pore structure has been widely researched (100–102). As mentioned in section 2.2.1, hydrogels are commonly used as the base material for developing tissue scaffolds. Anisotropy in hydrogel scaffolds has been widely achieved by directional freezing (99,103,104). During the preparation of PVA hydrogel, freeze thawing is regularly used to create physical cross-links (which provide the mechanical stability) (99). In order to produce elongated pores, a temperature gradient is established during freezing which creates long, parallel pores. A schematic of this process, as developed by Zhang *et al*, can be seen in Figure 2.16, with the resultant pore structure in Figure 2.17. Chen *et al* also used a similar process to develop samples which exhibit anisotropic mechanical properties, where the elastic modulus parallel to the direction of freezing was found to be in the range of 5-17kPa, and perpendicular to the direction of freezing was in the range of 1-10kPa (depending on the composition of the hydrogel) (99). The effect of this anisotropic pore structure and elastic modulus on the direction of swelling in the scaffolds is not discussed by the authors. However, as only the pores are anisotropic (rather than the molecule itself), it could be predicted that on hydration the hydrogel network will expand isotropically, but retain the internal structure (with pores holding free water) and mechanical properties.

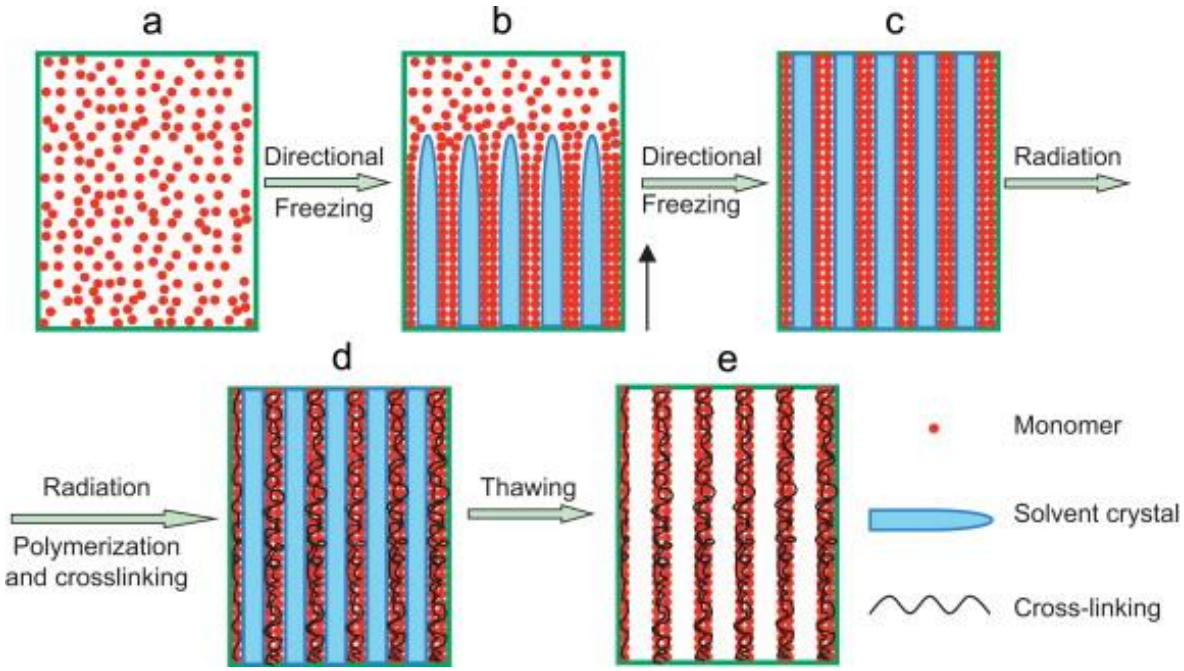

Figure 2.16 A shcematic of the process used to create anisotropic pores in PVA hydrogels for use as tissue scaffolds. Taken from (104)

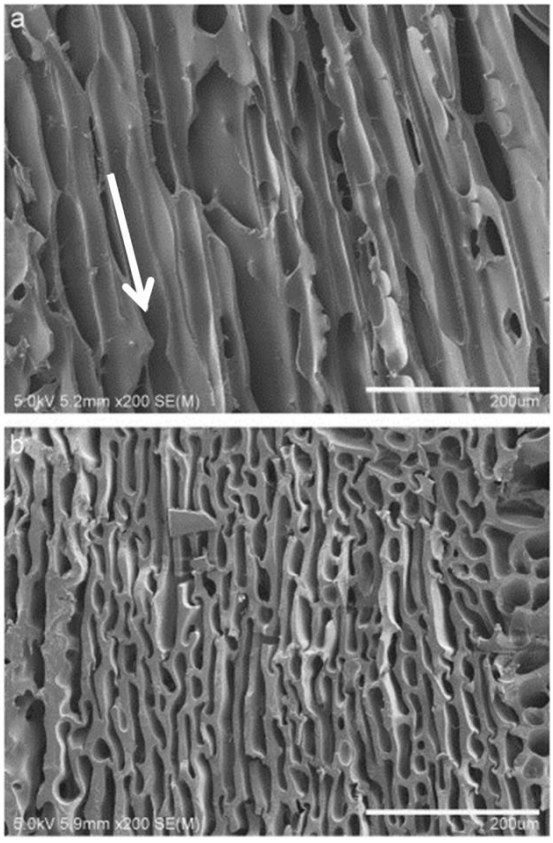

Figure 2.17 The resulting hydrogel microstructure taken from (99)**. "SEM photograms of the hydrogel surfaces parallel (a) and vertical (b) to the freezing direction. The hydrogel was made with 3 mol L−1 HEMA aqueous solution. The white arrow indicates the freezing direction"**

Another area of interest in anisotropic hydrogels is the development of lyotropic liquid single crystalline hydrogels (LSCH). These are water swollen cross-linked amphilic polymers which

form a macroscopically aligned lyotropic liquid crystal phase (97,105–107). These devices show the anisotropy and self-organisation associated with the liquid crystal phase, and the stability and rubber elasticity of the hydrogel (106). Potential applications for LSCH's are in bi-focal contact lenses (108), where the double refractive index allows for two focal points, as well as in biological sensor applications (109). Loffler forced uniaxial swelling of these polymers by expanding a LSCH in a glass tube, so causing the lyotropic hexagonal phase to form (97). However Fischer was the first to produce permanent uniform orientation of the liquid crystal phase (105). This was achieved by using a two-step reaction; in the first stage, polymerisation and a small amount of cross-linking was introduced to an isotropic, non-ionic surfactant, and in the second stage, cross-linking was carried out whilst the sample was held in tension. In addition to creating a LSCH with an anisotropic structure, Fischer observed macroscopic anisotropic swelling (110). This has been repeated using a different synthesis technique where the molecules used are based on rod-like amphilphiles (which produce a lamellar structure), which surround an aromatic core (providing the diamagnetic anisotropy) (106,108). Again, marginal anisotropic swelling (relative change of 1:1.09 for the z and x direction respectively) of the gel is observed. Whilst this technique produces synthetic hydrogels which could be of great use for mimicking cell membranes, it is inappropriate for use in tissue expanders as the synthesis route is complicated and the ratio of 1:1.09 is too small.

Composite hydrogel systems have also been used to generate anisotropic properties. Liu *et al* based their hydrogel design on mimicking the properties of cartilage, where the tissue is very strong in compression (111). This was achieved by using electrostatic repulsion between negatively charged uni-lamellar titanate nano-sheets which were embedded in the hydrogel (the hydrogel was formed around the sheets). This produced charged inorganic structures in the hydrogel which align cofacially in an applied magnetic field, which their stacking axis perpendicular to the field (112). This use of composite structures to control the properties of hydrogels has also been widely used (103,113). Dicker *et al* have investigated the use of flexible matrix composites, which partially constrain the gel (giving anisotropic

swelling) in order to increase the useful amount of work done when being utilized as a biological actuator (114,115). In other studies, aligned carbon nanotubes have been embedded in hydrogels in order to produce anisotropic electrical conductivity, which could be used to mimic some biological electrical conductivity, and therefore promote cell growth (116). Finally, it is possible to argue that the silicone bags used to control the rate of swelling can be considered as a composite device where the final expansion volume is controlled by constrained swelling (52). It is clear, therefore, that composite hydrogels have a vast range of potentials and applications, although their use is primarily in manipulating properties other than the bulk swelling direction.

Finally, we consider stress-induced anisotropy in hydrogels; the process used by Swan *et al* to develop anisotropic tissue expanders (5) in which dry pellets of P(MMA-co-NVP) were hot pressed (above the glass transition temperature) into discs. This resulted in the discs swelling anisotropically (increased swelling in the direction of initial compression) on hydration, with the level of anisotropy increasing with compression ratio (5). A maximum compression ratio of 7 was achieved, and beyond this the structural integrity of samples was compromised. However, these devices were produced empirically with a surgical goal in mind, and the work leaves some unanswered questions about the changes to the hydrogel structure which led to the anisotropic swelling. Further work in this area is required, focussing on the relationship between changes to the polymer structure caused by hot pressing, and the diffusion of water into the hydrogel (the important parameters of which are discussed in section 2.2.3). For this reason, improving the understanding of hot pressing the P(MMA-co-NVP) will be the focus of the first four research questions (to be posed in section 2.3).

2.2.5 Compression moulding

Understanding what happens to the P(MMA-co-NVP) network during compression moulding may offer a key insight into how anisotropic swelling occurs. There appear to be no comparable studies in the literature, so in this section the possible effects of compression moulding are considered through comparison with other, similar, systems.

When a polymer network is deformed above the glass transition temperature, and held in the deformed position until it is cooled below the glass transition temperature, residual stresses are frozen into the device (117,118). The greater the deformation, the greater the residual stresses. Residual stresses often change the mechanical and optical properties of components, and it is possible that they are a contributing factor to anisotropic swelling on expansion. Residual stresses are often seen in hot moulded components.

Injection moulding is one of the most common polymer manufacturing techniques (119). Parts are made by rapidly injecting the polymer melt into a mould. As the melt is injected, the polymer chains become aligned. When the flow makes contact with the mould wall it is rapidly cooled, resulting in this directionality becoming frozen in (a source of residual stress in the final product). As the rest of the melt flows into the mould, it cools less quickly, allowing some chain relaxation to occur. The variation in cooling rates within the sample results in thermally induced residual stresses (120). In addition, the flow rate, preferred orientation of the polymer chains and the feed conditions all contribute to flow induced residual stresses (117,121–123). A number of simulations and models have been developed to predict and explain the relationship between the different types of residual stress and their effect on the final properties (120,124,125). Changes to the polymer network will be considered in the first four research questions (posed in section 2.3). For the purpose of this research, it will be useful to consider the material flow of P(MMA-co-NVP) during hot pressing, to determine whether residual stresses could be creating regions of high strain and radial chain alignment. Radial chain alignment may produce anisotropic swelling, because when water diffuses into the collapsed isotropic structure, the chains are extended. If chains have already been extended in one direction, then it is possible that on hydration extension will only occur in a perpendicular direction.

In injection moulding, the interactions between the polymer melt and the mould wall are of great importance in the development of residual stresses. Similarly, in the development of aspherical glass lenses (and in other viscous systems), compression moulding has been shown to cause residual stresses, and the interfacial friction has been highlighted as an

important factor (126–128). In particular Jain *et al* (126) modelled a von Mises stress distribution, with a stick-slip boundary, using FEM (finite element model) inside a glass cylinder during compression (at 645°C). Samples were described as 'sticking' when there was not enough lateral force to overcome the friction at the interface, and slipping when this critical force was overcome. This model predicts that the stress build up will increase along the radius of the sample, and also that a zone of high stress will be observed in the center of the sample due to the constrained material flow. The predicted stress distribution can be seen in Figure 2.18. It is likely that the interface between the gel and the hot plates will affect the polymer flow during compression, and therefore the properties of the tissue expanders.

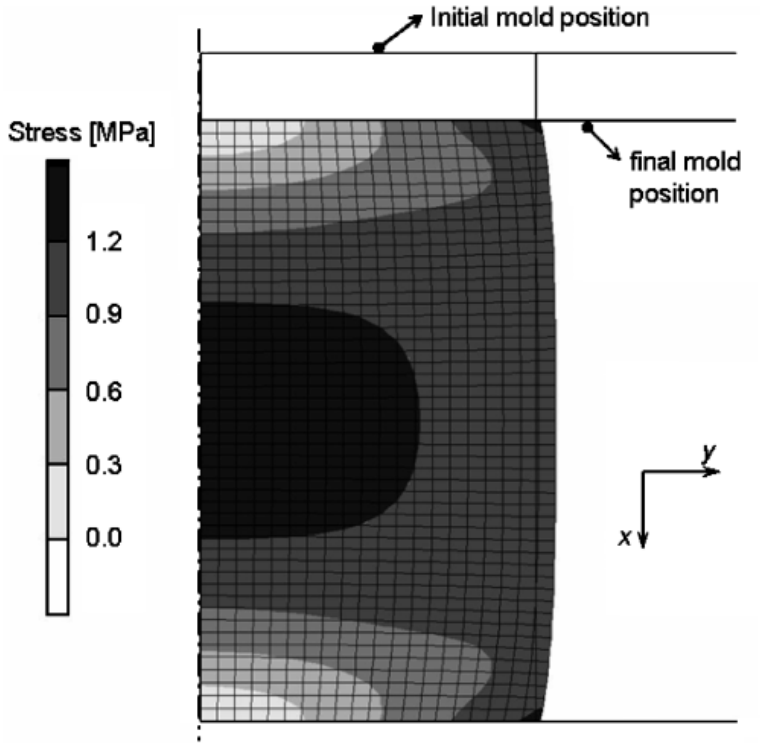

Figure 2.18 "Predicted equivalent von Mises stress distribution in a BK7 glass cylinder under compression at 645°C" reproduced from (126)

There are two key ways to experimentally measure residual stresses in hot moulded samples. The first technique is called the layer removal technique (118,129,130). This is where individual layers of the component are removed and the resulting deformation is monitored, allowing for both monitoring of small deformation and variation in deformation across the thickness of the sample. The second is to use stress optics to observe the residual stresses in a sample (131–133). This technique shows the most promise for

investigation in the residual stresses caused by compression moulding P(MMA-co-NVP) as it is non-destructive.

Stress optics measures the residual stress in a sample by observing changes in the birefringence. Birefringence occurs in a sample where there are two different refractive indexes – a property which can be intrinsic to a material, e.g. an anisotropic crystal, or can arise due to applied or residual stresses (134), for example chain orientation due to injection moulding (135). Birefringence can be measured using cross polarizers, as seen in Figure 2.19. An example of the birefringence caused by chain alignment during injection moulding is seen in Figure 2.20. White light is passed through a linear polarizing filter. This filter allows only one orientation of light to pass through. This plane-polarised light then splits as it passes through the sample. The light is then passed through the second polarizing filter (which can be set at different angles depending on the desired information) and the components of each wave in this direction recombine. If the sample has anisotropic properties, when the waves recombine there will be a lag (or retardation) between each wave. Optically, in the described set up, this will appear as coloured fringes. There are two types of fringes; isochromatic and isoclinic. The former relates the lines of constant principal stress difference and the latter to when the stress direction coincides with the axis of polarisation of the analysing filter (thus changing when the angle is changed). The Michel-Levy birefringence can be used to establish the value of birefringence.

Figure 2.19 Residual stresses in an injection moulded plastic disc (open source image-Zephyris)

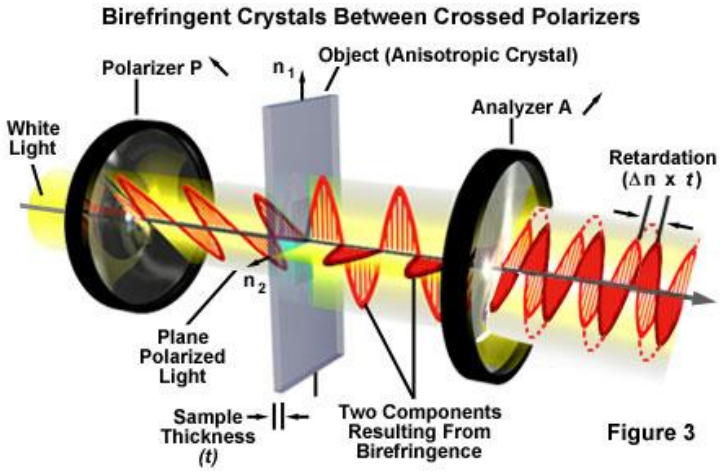

Figure 2.20 A schematic showing the path of light during analysis of a birefringent crystal between crossed polarizers. Image reproduced from "Molecular Expressions: Science, Optics and You. Optical Birefringence"

2.2.6 Sterilisation of hydrogels

All medical devices and pharmaceuticals must be sterilized before use to prevent infection and toxic shock. The SAL (sterility assurance level) must be 10^{-6} or better, which means that there has to be a maximum chance of one in one million particles of finding a contaminating molecule (136). There are a number of ways to sterilize medical devices (136–140); however the effect of the technique on the structure and properties of the device must also be understood. For example, heat can be used as a sterilization technique, as the high temperatures denature pathogens, but this comes at the cost of structural changes to the device (141). Additionally, ethyl oxide has also been used; however the difficulty in removing it after sterilization presents significant problems as it is a known carcinogen (139). The focus in this review will be sterilization by γ-irradiation.

Irradiation using γ waves is a commonly used technique for sterilizing medical devices and pharmaceuticals. The principal industrial source is Cobalt 60 (created by neutron bombardment of Cobalt 59) (137). A key advantage of γ-irradiation is that it is capable of low dosage but high penetration – a particularly important factor for tissue expanders as on hydration any contamination from the centre of the sample would then be able to diffuse into the surrounding tissue. It has been proposed that the radiation kills micro-organisms in one of two ways- directly or indirectly (142). For direct action, the γ-irradiation causes ionisation

of the DNA structure, preventing replication from occurring. In indirect action, the DNA is altered through secondary reactions which are caused by the free radicals created during irradiation (142). Whilst γ-irradiation is effective at sterilizing medical devices, it can initiate further reactions and therefore cause changes to the expected chemical structure and material behaviour. The radiation reacts with the material either by reaction with, or displacement of, the nuclei, or through interaction with the orbital electrons (143).

The effect of γ-irradiation on both natural and synthetic polymers is well researched. There are two key mechanisms that occur; chain scission and cross-linking, usually both at the same time (136,137,144–146). Chain scission is random rupture of the bonds, and so reduces the molecular weight and viscosity, whereas cross-linking creates new bonds between chains and thus results (or increases the bonding) in a 3D polymer network with improved tensile strength (147–150). If R represents the polymer chain, then during exposure to γ-irradiation Equation 2.23 and Equation 2.24 may apply, creating a free radical polymer chain and a free radical hydrogen atom, and a free radical polymer chain and hydrogen gas respectively (151). Alternatively Equation 2.25 could occur (chain scission) producing two (shorter) free radical polymer chains. The free radical polymer chains can then react further, either through Equation 2.26 or Equation 2.27 (crosslinking).

$$RH \rightarrow R^{\cdot} + H^{\cdot}$$

Equation 2.23

$$H^{\cdot} + RH \rightarrow R^{\cdot} + H_2$$

Equation 2.24

$$R - R \rightarrow \ R^{\cdot} + R^{\cdot}(scission)$$

Equation 2.25

$$H^{\cdot} + R^{\cdot} \rightarrow H_2 + unsaturation$$

Equation 2.26

$$R^{\cdot} + R^{\cdot} \rightarrow R - R\ (crosslinking)$$

Equation 2.27

$$R^{\cdot} + O_2 \rightarrow\ ROO^{\cdot}$$

Equation 2.28

There are a number of factors which can affect the rate of both chain scission and cross-linking, including the chemical structure, impurities in the system and whether there are any strains acting on the polymer. If the polymer chain follows the form $[-CH_2 - CHR-]_n$ then cross-linking is shown to dominate, whereas if the structure follows $[-CH_2 - CRR-]_n$ then chain scission will dominate (145). Therefore in P(MMA), chain scission is expected to dominate, whereas in P(VP) cross-linking is expected to dominate (144,152). The presence of oxygen increases the rate of chain scission and decreases the rate of crosslinking. For example, this has been shown in PVP hydrogels, where the cross-linking yield in an argon environment was 2.6×10^{-7} mol J^{-1}, but in an aerated environment this fell to 1.8×10^{-7} mol J^{-1} (153). This change occurs because the free radicals created during chain scission react preferentially with the oxygen, thus replacing the reaction seen in Equation 2.27 with the reaction in Equation 2.28. Other impurities could cause an increase in crosslinking (143). Finally, during radiation polymer networks which are strained may experience an increased rate of chain scission and cross-linking, for the same dose of γ-irradiation (154–156). Furthermore, the location of the new cross-links will cause the polymer set, i.e. the relaxed network structure, to restructure. This is because the new crosslinks will occur when the chains are aligned in one direction and can be observed schematically in Figure 2.21.

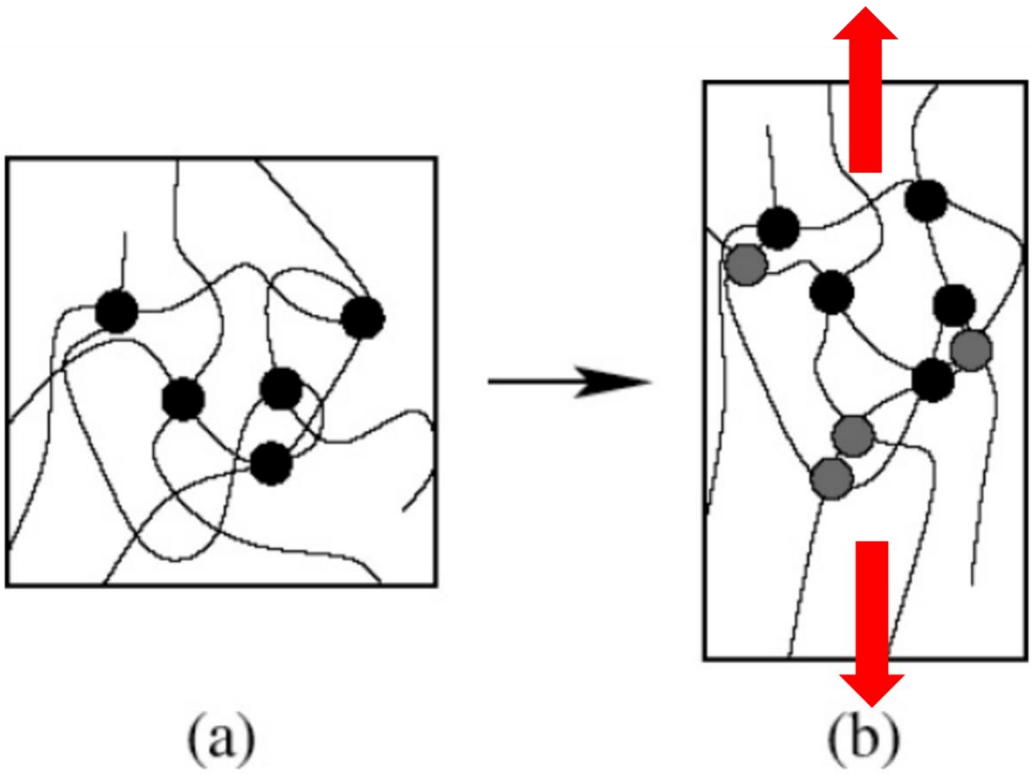

Figure 2.21 "Schematic depiction of the cross-linking/strain history of simulated networks (two-stage networks). Left panel: A network is formed from a melt of linear polymer chains in the unstrained state by the addition of cross-links (represented here by black circles). Right panel: The network is uniaxially deformed at constant volume, and new cross-links (grey circles) are added" Image reproduced from (154). Red arrows have been added on part (b) to indicate the direction of strain

γ-irradiation can alter the colour of polymers, and this has been observed in both PVP and MMA (148,157,158). They predominantly transition from colourless to yellow/orange/red colours on γ-irradiation. The yellow/orange/red colours have an absorption maxima between 270 and 615nm (138). It has been established that there are two types of colour induced in polymers via radiation; annealing and non-annealing; and both are caused by free radicals. Annealing colour is a direct result of the free radicals, and can be reversed by annealing at temperature (whether in air or not) due to radical recombination. Non-annealing colour results from radical-radical interactions and is likely to be caused by the coloured oxidation products, which contain conjugated bonds (138,157).

It will be important, in research, to assess the changes to the P(MMA-co-NVP) structure in order to be able to predict the swelling properties of the tissue expander. In particular, if the anisotropic samples have residual strains, it will be important to determine whether this changes the permanent set of the polymer network, and if so, how this affects the swelling of the device. Furthermore, if any by-products from reactions occurring during radiation (e.g.

free radical reaction products which may be yellow-red in colour) are present in the sterilised device, it will be important to establish whether there is potential for these to diffuse out of the sample and into the body.

2.3 Summary

In summary, there is a clear clinical need for anisotropic, self-inflating, rate controlled tissue expanders. The most suitable materials used thus far are a P(MMA-co-NVP) hydrogel, surrounded by a perforated silicone sheet or bag. However, there are a number of significant issues to be resolved, as well as potential advancements that should be investigated. These areas of interest can be summarised in the following research questions, which are presented in the order in which they will be addressed:

RQ1) What are the manufacturing limits to developing reliable, anisotropically expanding P(MMA-co-NVP) for use as tissue expanders?

There are currently very few studies available on anisotropically expanding hydrogels, therefore the starting point for the investigation must be to determine whether previous results are reproducible, and to ascertain the limits of manufacturing such devices.

RQ2) Why do compressed cylinders of P(MMA-co-NVP) show anisotropic swelling?

Once a suitable range of anisotropically expanding devices can be produced consistently, it is essential to establish why devices are showing anisotropic swelling; in particular the relationship between any changes to the polymer network and the gel expansion.

RQ3) What is the effect of the hot pressing process on the P(MMA-co-NVP) polymer network?

The effect of various polymer processing techniques has been discussed, including the effect of the process on the properties of the resulting product (in particular

residual stresses). This has not previously been investigated for P(MMA-co-NVP) and it is important to understand how changing parameters in the hot press may affect the resulting hydrogel. Understanding more about this processing technique may allow a wider range of devices to be developed.

RQ4) How can devices be designed so that they expand from a disc into a non-prismatic shape?

It is proposed that devices can be developed which expand from a flat disc, into a non-prismatic shape, and that these devices may improve the quality of the new skin grown, allowing for improved clinical outcomes (particularly in the cases where a prosthetic is to be implanted).

RQ 5) What is the effect of gamma radiation on P(MMA-co-NVP)?

As these devices are being developed for medical use, they must be adequately sterilized before use. Therefore it is of great importance to establish how exposure to radiation affects the swelling behaviour of the hydrogels.

RQ 6) What is the effect of residual molecules in the P(MMA-co-NVP), and how does removing these residual molecules affect the results of RQ5?

As discussed in section 2.2.6, residual molecules can increase the rate of polymer degradation when exposed to gamma radiation. It is important to establish whether there are any residual molecules in the P(MMA-co-NVP) used for these studies, and to determine if these molecules are playing any role in the effect of gamma irradiation on P(MMA-co-NVP)

RQ 7) How does the application of a semi-permeable silicone coating affect the swelling rate of devices?

As discussed in section 2.1.3, controlling the rate of expansion for hydrogel devices is important to prevent failures (such as extrusion). Whilst some success has been

achieved by using perforated silicone membranes, it is hypothesised that using a semipermeable membrane will allow for greater control of the expansion in the crucial first 24hours.

RQ 8) What is the effect of gamma radiation on the performance of the silicone coatings?

As mentioned in RQ5, the devices must be sterilized before medical use, and therefore any changes to the silicone coating due to radiation must be investigated.

RQ 9) What is the *in vivo* behaviour of a non-prismatic tissue expander

Investigating the swelling of non-prismatic tissue expanders *in vivo,* as well as the properties of the tissue produced, will help to ascertain whether they will be of clinical use (the theoretical benefits of such devices were discussed in section 2.1.2).

Chapter 3:

Anisotropic Swelling of P(MMA-co-NVP)

3 Anisotropic Swelling of P(MMA-co-NVP)

3.1 Introduction

This chapter aims to answer the first four research questions posed in section 2.3:

RQ1) What are the manufacturing limits to developing reliable, anisotropically expanding P(MMA-co-NVP) for use as tissue expanders?

RQ2) Why do compressed cylinders of P(MMA-co-NVP) show anisotropic swelling?

RQ3) What is the effect of the hot pressing process on the P(MMA-co-NVP) polymer network?

RQ4) How can devices be designed so that they expand from a disc into a non-prismatic shape?

RQ1 will be addressed by comparing a range of initial heights and compression ratios, and determining which combinations are reliably successful during both hot pressing and swelling expansion. Once an appropriate range has been established, samples within this range will be studied in order to answer RQ2 and RQ3. This will be achieved by investigating the samples in both the dry and swollen states. During swelling, particular focus will be given to the changes in dimension, the diffusion coefficients in the first 60% of swelling, and the geometry of expansion. Cross-polarized imaging, micro-hardness indentation and optical microscopy will be used on samples in the dry state in order to establish the causes for observed swelling behaviour. Furthermore, comparisons in the measured properties when the friction at the interface is changed will also be made in order to support the explanations developed whilst answering RQ2 and RQ3.

Finally, as mentioned in section 2.1.2, there may be significant clinical advantage to using non-prismatic geometries in tissue expansion. Using the findings of RQ1-3, the chapter will

conclude by describing the development of novel devices which expand from a flat disc into either a dome or wedge geometry.

3.2 Experimental Methods

3.2.1 Polymer synthesis

Polymeric Sciences Ltd (Longfield, Kent, UK) synthesised P(MMA-NVP) for this study. Pharmaceutical grade methyl-methacrylate (MMA) and N-vinylpyrrolidone (NVP) monomers were polymerised, through addition polymerisation, in the ratio 10:90 respectively to form a co-polymer with a cross-link density of 0.2%. The cross-linking agent used was allyl methacrylate (0.2 wt%), and the free radical initiator was azobisisobutyronitrile (AIBN) (0.2 wt%). The synthesis process and conditions are shown in Figure 3.1. Small angle neutron scattering has previously been used on P(MMA-co-NVP) provided by Polymeric Sciences Ltd, and has shown that the polymer is block co-polymer in nature (172). However, the regions are not distinctive, but exhibit a gradual change, leading to pure NVP regions, and regions which are rich in MMA.

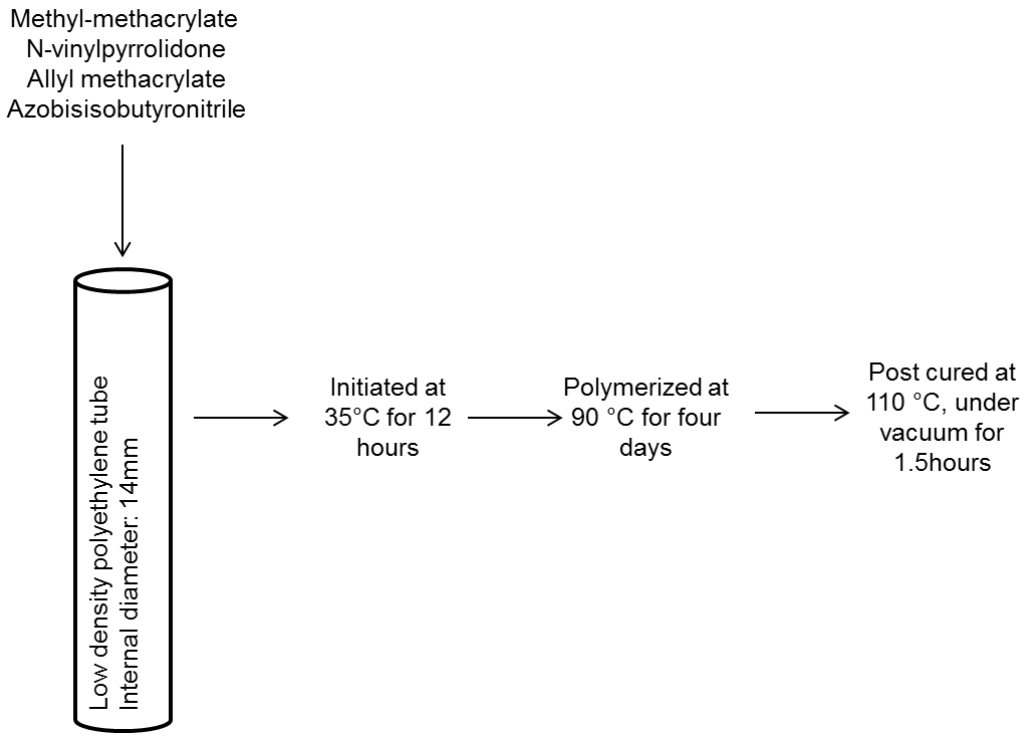

Figure 3.1 The process used by Polymeric Sciences Ltd to synthesise P(MMA-NVP)

Figure 3.2 shows the breakdown of the azobisisobutyronitrile into two free radicals and a nitrogen molecule. This occurs at 35°C for 12 hours and the nitrogen gas diffuses out of the solution. As the free radicals are produced, they react with the NVP and MMA monomers to form further free radicals; an example of this for NVP is shown in Figure 3.3 (the initiation reaction). When this free radical molecule is produced, it reacts further with MMA and NVP molecules to form polymer chains, as seen in Figure 3.4 (propagation). The reaction is terminated either by two of the molecules in Figure 3.4 combining, or through reaction of one molecule from Figure 3.4 reacting with a free radical produced in Figure 3.2. Crosslinking between the polymer chain occurs via the allyl methacrylate molecule, as seen in Figure 3.5.

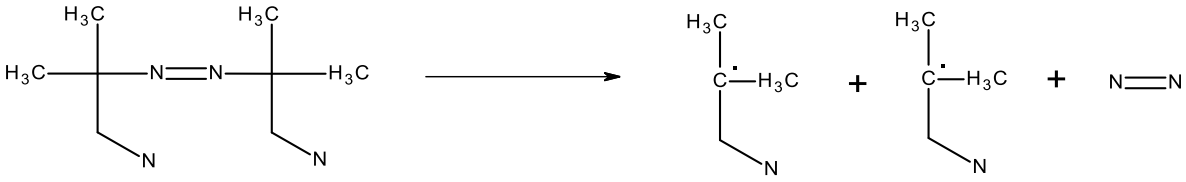

Figure 3.2 An azobisisobutyronitrile molecule breaking into two free radical molecules and a nitrogen molecule

Figure 3.3 Initiation reaction, where an NVP molecule reacts with a free radical (produced by the initiator) to form another free radical

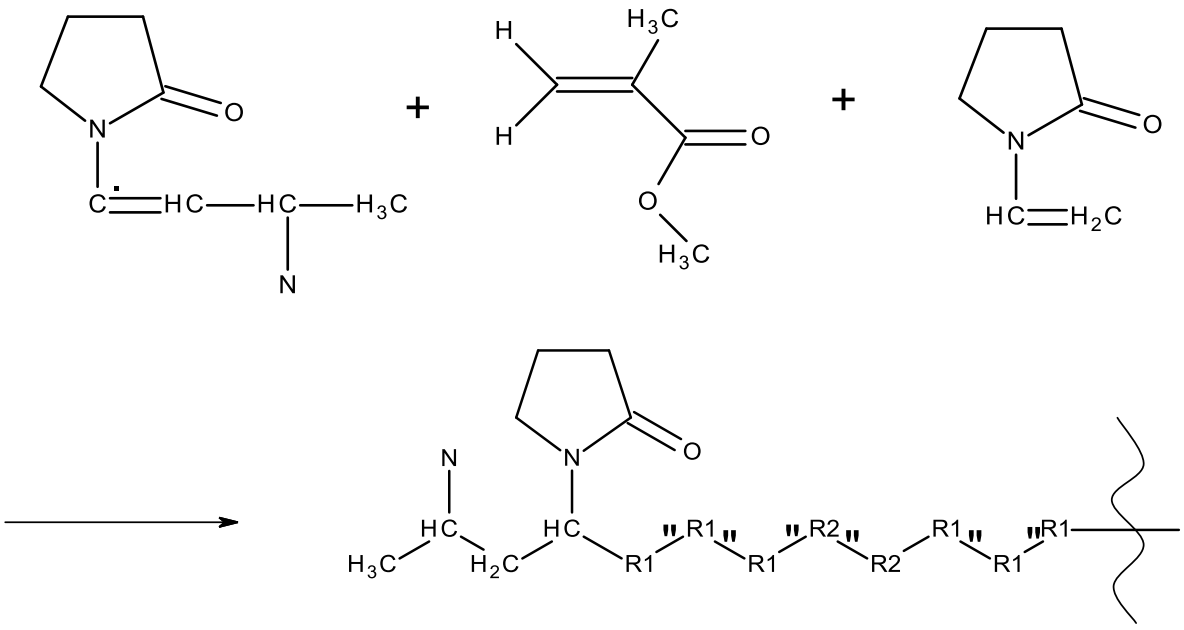

Figure 3.4 Propagation reaction, where the free radical produced in Figure 3.3 continues to react with monomers of NVP and MMA to form a polymer chain. R1 represents the NVP component and R2 represents the MMA component

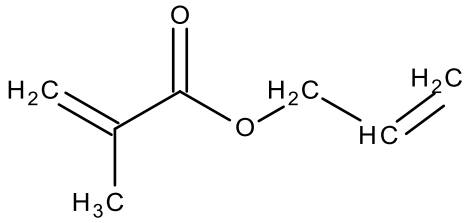

Figure 3.5 Allyl methacrylate molecule (crosslinking agent)

Samples were received as glassy polymer rods of diameter 14mm and an average length of 11cm, as seen in Figure 3.6. The rods were subsequently machined as required.

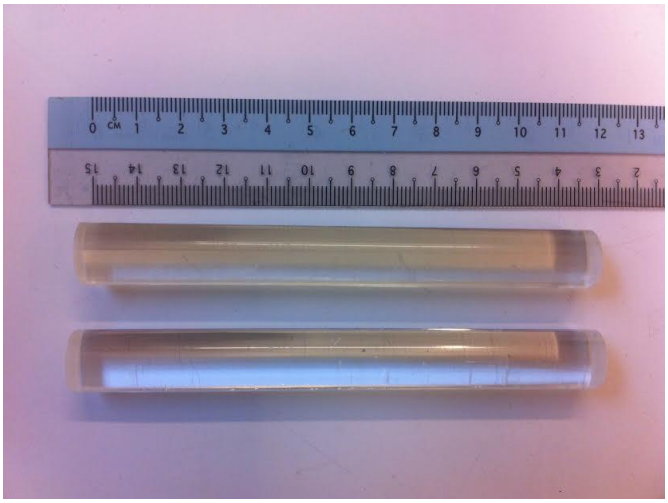

Figure 3.6 Rods of P(MMA-NVP) as-received from Polymeric Sciences Ltd

3.2.2 Hot pressing

The as-received rods were lathe cut to cylindrical pellets of heights 3mm, 6mm and 12mm, with diameters of 12mm using a carbide tipped turning blade (Korloy H01) on an 1440 (XYZ Machine Tools Ltd), at a spindle rate of 220RMP and a cutting rate of approximately 5mm/min or less.

The compression ratio, C, of a sample is defined by the initial height of the pellet, h_i, divided by the final height, h_f, of the pellet (the height of the sample mould) as shown in Equation 3.1. So a pellet which had not been pressed would have a compression ratio of $C = 1$, a disc of height 2mm, which was formed from a pellet of 6mm would have a compression ratio of $C = 3$. Discs of 1mm thickness were also lathed, but it was not possible to hot press these samples.

$$C = \frac{h_i}{h_f}$$

Equation 3.1

The hot pressing technique used in this thesis is based on that used by Swan in the initial device design (5,6). However, a number of changes were made in order to increase the number of devices which could be produced. Firstly, the time at temperature, before compression, was reduced from one hour to 15 minutes. Secondly, the compression of the devices was altered; previously devices were compressed by approximately 1mm and then left for a further 15minutes before the second compression, with this process repeated until the device reached its final height. Devices in this thesis were compressed at a constant (slower) rate until the final height. Finally, devices were not left overnight, but were removed after approximately four hours (once they had cooled below the glass transition temperature). The new processing route (as described below) was designed by considering the purpose of each stage. For example, it was found that by 15 minutes at temperature, the samples were already at the glass transition temperature, and thus holding this temperature for a further 45 minutes produced no gain. The gradual compression of devices allowed an increase in the

control over compression, and finally, once devices were cooled below the glass transition temperature they would not be able to recover their previous shape, thus there was no benefit in leaving them to cool (under pressure) overnight, compared to removing them after four hours. Devices were made using Swan's technique, as well as the technique described below, and there were no changes in swelling behaviour over the range of compression ratios tested (one to six).

Pellets were compressed using a Specac 15.041 thermal press and custom made moulds, as shown in Figure 3.7. Pellets were placed into the circular moulds, between the hot plates in the press. The plates were then heated to the glass transition temperature of P(MMA-NVP), 161°C (5), the samples were compressed to the appropriate height at an approximate rate of 0.5mms^{-1} , and subsequently a pressure of 300MPa was applied. The initial height of the pellet was therefore reduced to the height of the mould. The hotplates were then switched off, and the sample was left to cool under load.

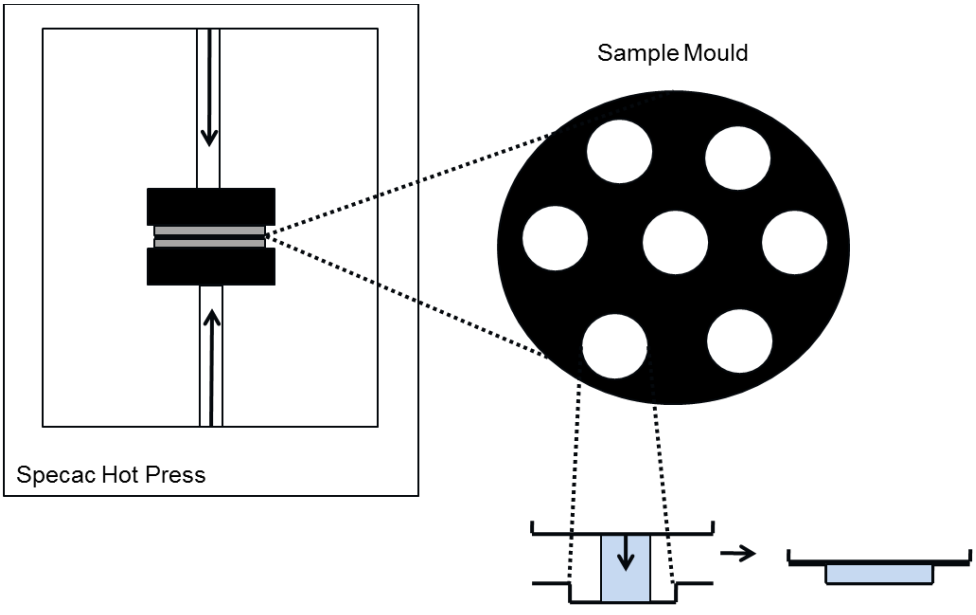

Figure 3.7 A schematic of Specac hot press and mould, illustrating the compression process

In order to investigate the effect of friction at the interface of the hot plate, some cylindrical pellets were moulded with Poly(tetrafluoroethylene) (PTFE) at the interface between the hot press and the sample, whilst the remainder used aluminium.

Non-prismatic samples were also produced, with a maximum height of 12mm and the curve or angle starting at 5.67mm. Domes were produced by using a custom made curved steel cutting tool with a radius of 6mm. Wedges were produced by grinding and polishing a 12mm sample a cylindrical sample on a Kent 3 (Kemet International Ltd), using carbide grit paper. Both wedges and domes were compressed in the same manner as the cylindrical samples, to a height of 4mm, as shown in Figure 3.8. For these samples, the compression ratio reflects the compression ratio of the highest point, thus samples have a compression ratio of $C = 3$.

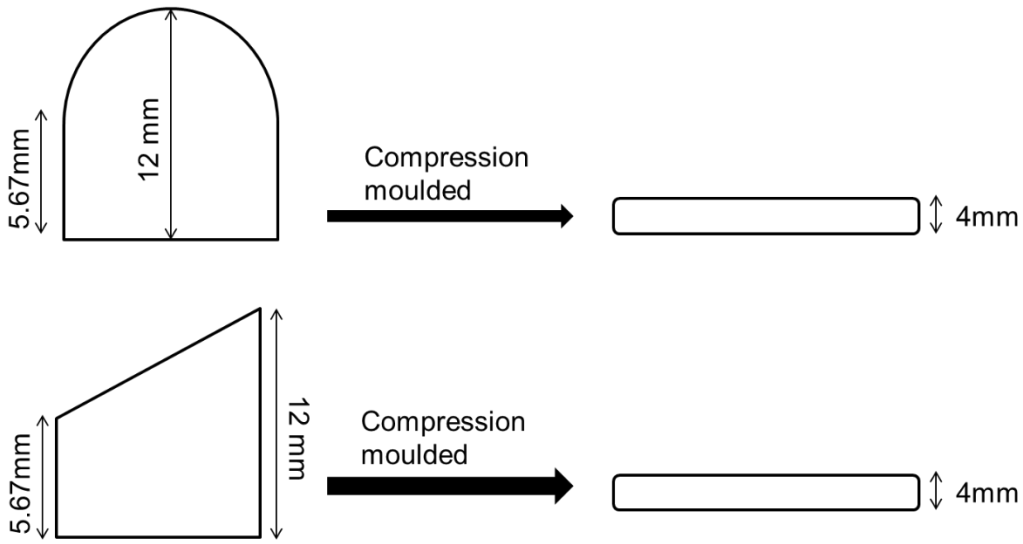

Figure 3.8 A schematic showing the cross section (parallel to rod length) of pellets which have been machined to either wedge (below) or dome (above) shapes and compressed to 4mm.

All samples were stored in a desiccator prior to experiments, and appeared transparent. Unless otherwise stated, in each experiment a minimum of three samples was used.

3.2.3 Swelling experiments

The swelling uptake of samples was determined by placing samples in excess distilled water in a water bath, at 37°C. The temperature was chosen to reflect normal human body temperature. Changes to the mass, diameter and height were recorded by removing the samples, drying them with filter paper and using a scale (BDH AA200DS -accurate to 0.0001g) and a Mitutoyo Absoulte Digimatic digital calliper (three measurements were taken at each location and an average was used for each dimension). The location of

measurements for height and diameter of the three different geometries (cylinder, wedge and dome) are shown in Figure 3.9. Readings were taken every 20 minutes for one hour, every hour for the subsequent six hours, and then approximately every 12 hours until equilibrium was obtained. The percentage change with time in each dimension (mass, diameter and height) was also calculated using Equation 2.17, Equation 2.18 and Equation 2.19 respectively. For wedge-shaped samples, the angle of the wedge slope at equilibrium was also recorded using a protractor.

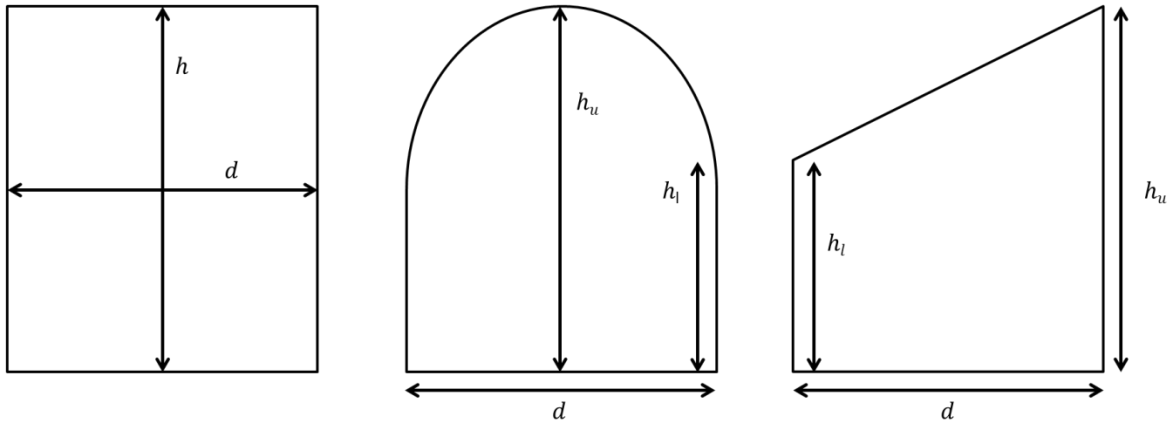

Figure 3.9 A schematic showing where measurements were taken from for cylinders (left), domes (middle) and wedges (right), where h represents height, d represents diameter, h_u represents the upper height, which is the maximum height of the expander and h_l represents the lower height- which is the height at which the curvature or the wedge or dome begins

Samples were imaged using a digital camera (Nikon D-610). For samples used to investigate the geometry of expansion, markings were made on the surface of the samples using permanent markers (Stabilo) prior to swelling. For each photograph, samples were removed from the water, dried as described above, and placed on 1cm x 1cm grid paper to be photographed.

In order to calculate the diffusion coefficient of samples, Equation 2.20 and Equation 2.21, were used as described in section 2.2.3. The first 60% of swelling data was used. The value used for l depended on the geometry of the device- samples where the diameter was 10 times the height were treated as hydrogel sheets, and so the sample height was used, and for samples which did not fit this criteria were treated as cylinders and therefore the radius was used for the l value (159).

3.2.4 Cross-polarized light images

Cylindrical samples of initial height 6mm and compression ratio $C = 3$ were imaged using an Olympus BX51 optical microscope. Two plane polarizing filters were used, set at 90° to each other as shown in the layout in Figure 3.10. The light source produced unpolarized light; this then passed through the first polarizing filter which only allowed parallel light waves through, and the plane-polarized light then passed through the sample. The theory is that if the sample shows birefringent properties, then some of the plane polarized light is re-orientated. If it does not, then only plane-polarized light will leave the sample. The light then entered the final filter (perpendicular to the first) and the analyzer. Images were captured using automatic capture at the 2x magnification level. Samples were then viewed using the DotSlide software.

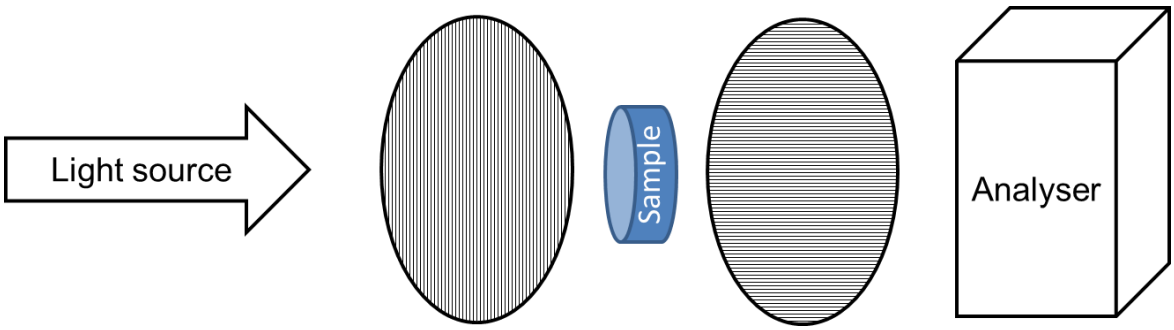

Figure 3.10 A schematic showing layout used to obtain cross polarized light images

Compressed samples with non-prismatic cross sections (i.e. wedge and domes with initial heights of 12mm and final heights of 4mm) were imaged using two Dynasun 77mm PL plane polarizing lenses and a Nikon D610 FX camera with a AF-S NIKKOR 16-35mm lens in the same configuration as shown in Figure 3.10.

3.2.5 Hardness indentation tests

Variation in hardness across the diameter of samples of initial height 6mm, and compression ratios $C = 1$ and $C = 3$, was tested using a Knoop indenter on a MHT-1, Matsuzawa Seiki. For the compression ratio $C = 3$, samples pressed with both Aluminum, and PTFE interface were measured. Measurements were recorded at regular intervals (250µm) along the radius of each sample. The time at load was 10 seconds and the load was 100g. The indentations

were then examined with a Zeiss Axiophot optical microscope, with a Nikon DS-FiI camera using NIS-Elements D3.0.

3.2.6 Statistical analysis

Statistical significance was tested using a Tukey's Test, which tests whether the group means are significantly different from each other using the formula for which is shown in Equation 3.2. Y_A is the larger mean value, Y_B is the smaller mean value SE is the standard error of the data and q_s is the value to be compared to the critical value (e.g. if $q_s > q_{critical}$ the means of the groups are significantly different). The analysis was carried out on Origin Pro 8 software to a significance level of 0.05 (unless otherwise stated). The error bars shown are the standard deviation of the data.

$$q_s = \frac{Y_A - Y_B}{SE}$$

Equation 3.2

3.3 Results

The results of each experimental method will be presented in turn, with the results for cylindrical samples preceding the non-prismatic samples.

3.3.1 Hot pressing

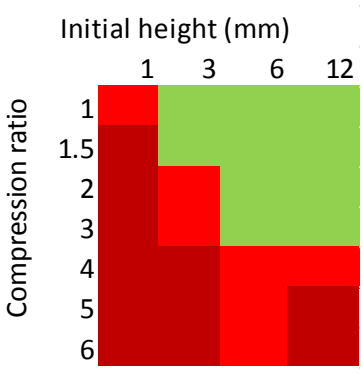

Figure 3.11 A chart showing the limits of manufacturing during compression

Figure 3.11 maps the limits of both initial height and compression ratio for the range of sizes tested. Dark red indicates that the samples could not be compressed with the hot press. For

samples of $\mathrm{h_i} = 1\mathrm{mm}$ this was because it was not possible for the hot press to accurately compress samples below this thickness. The remaining dark red regions, which could not be successfully hot pressed, failed during compression, with cracks appearing on the outer annulus (as shown in the photograph in Figure 3.12). The bright red regions show samples which it was possible to manufacture, but on submersion in distilled water the majority of them failed before equilibrium expansion was reached. For samples in this region with a pre-swelling height of $h_{t=0} \leq 1.5mm$ samples were not mechanically stable and disintegrated within the first 30 minutes of swelling. The remaining samples in the bright red region failed beyond this point, and a photograph of the crack propagation can be seen in Figure 3.13. The remaining green region indicates samples which could be manufactured and swollen successfully and consistently (no samples failed). These samples will be the focus of this thesis.

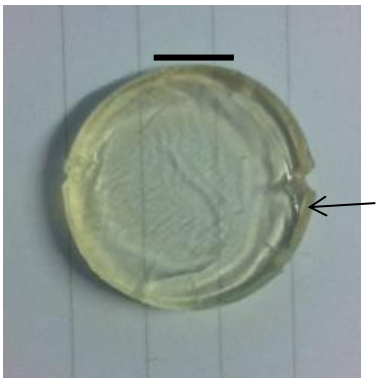

Figure 3.12 A photograph of a sample which has failed during hot pressing, with an arrow pointing to a failed region. The scale bar represents 2mm

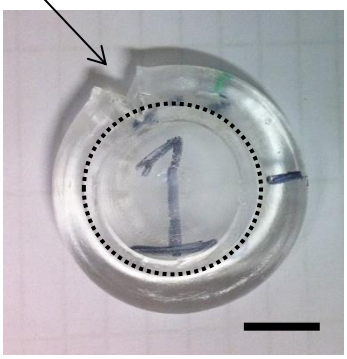

Figure 3.13 A photograph of a sample (hi=12mm, C=4) which failed during the first hour of swelling. The crack initiated at the arrow, and propagated around the dotted line. The scale bar represents 10mm

The non-prismatic samples (domes and wedges) were successfully manufactured to the specifications given in section 3.2.2.

3.3.2 Swelling experiments

In this section, the results of swelling experiments are presented. Cylindrical sample results will be given before non-prismatic sample results, and in both cases swelling data curves will be presented before photographs of swelling.

Swelling of cylindrical samples

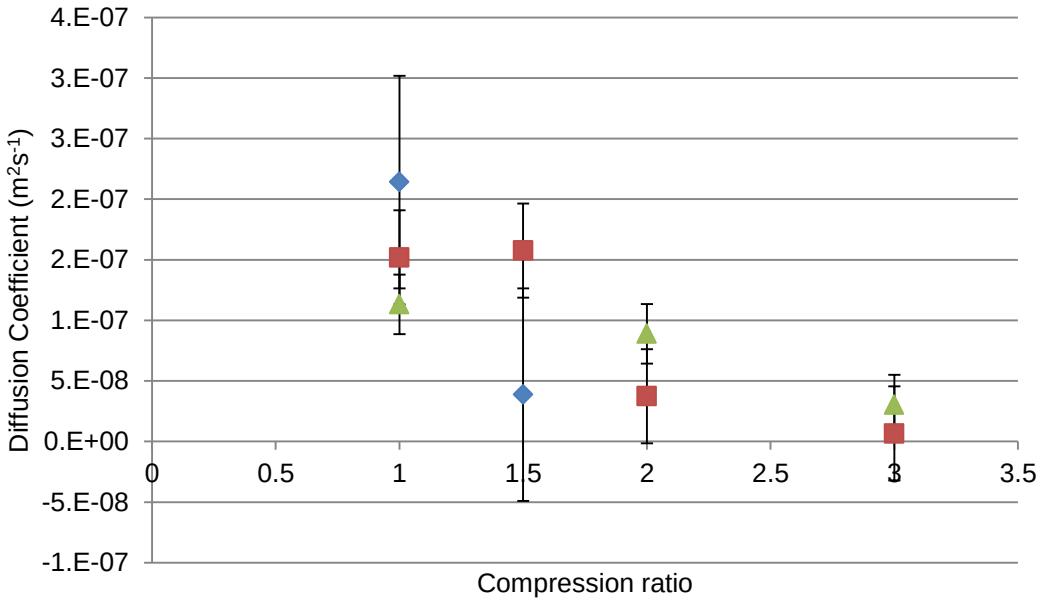

Figure 3.14 A comparison of the diffusion coefficients for samples with different heights and compression ratios. Blue diamond: $h = 3mm$. Red square: $h = 6mm$. Green triangle: $h = 12mm$

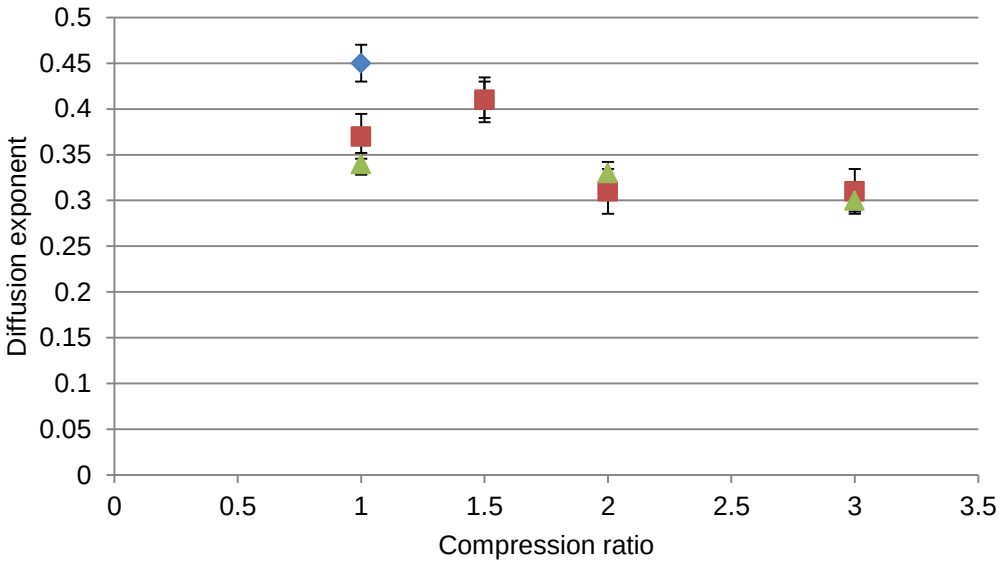

Figure 3.15 A comparison of the diffusion exponent for samples with different heights and compression ratios. Blue diamond: $h = 3mm$. Red square: $h = 6mm$. Green triangle: $h = 12mm$

Figure 3.14 shows the diffusion coefficients, calculated using Equation 2.20 and Equation 2.21, as described in section 2.2.3 and section 3.2.3, for samples with different initial heights and compression ratio. Figure 3.15 shows the diffusion exponents for the same samples. No statistically significant difference is observed between different initial heights for either the exponent or the coefficient, but a decrease tending to zero is observed as the compression ratio is increased.

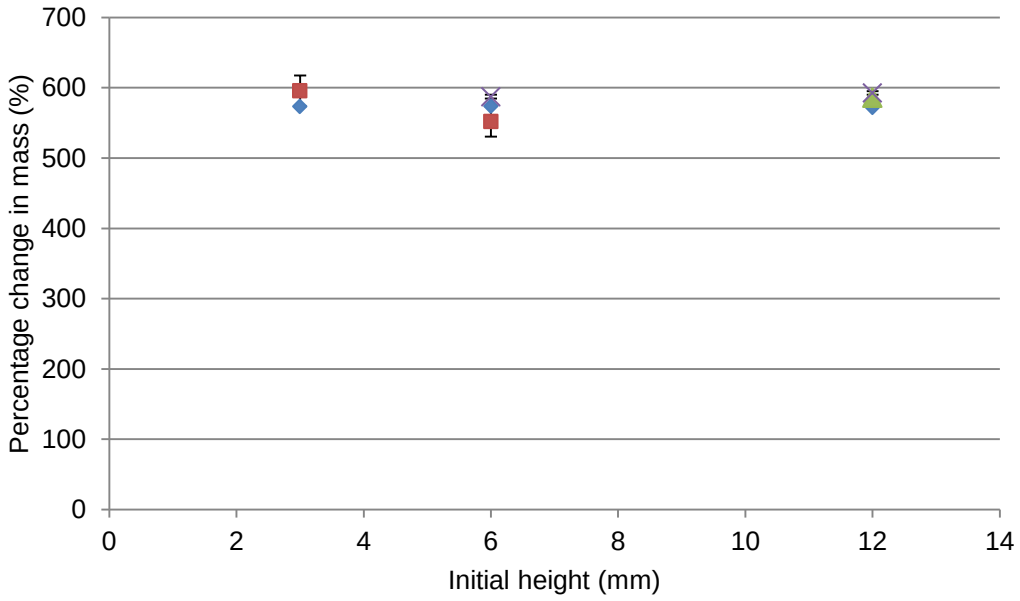

Figure 3.16 A comparison of the percentage change (between t=0 and equilibrium swelling) in the mass for compression ratios: 1 (blue), 1.5 (red), 2 (green) and 3 (purple)

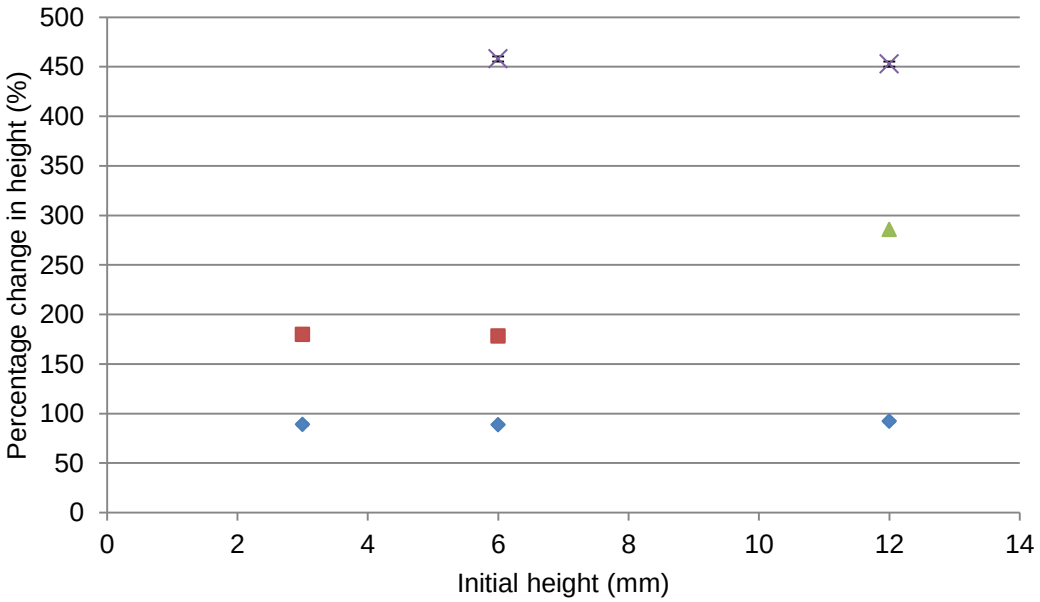

Figure 3.17 A comparison of the percentage change (between t=0 and equilibrium swelling) in height for compression ratios: 1 (blue), 1.5 (red), 2 (green) and 3 (purple)

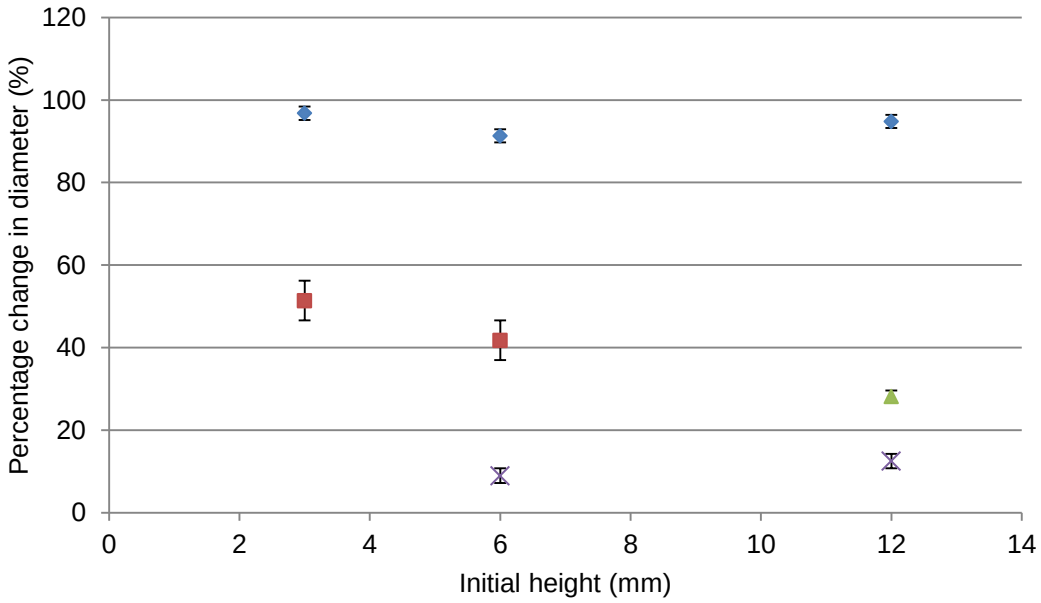

Figure 3.18 A comparison of the percentage change (between t=0 and equilibrium swelling) in the diameter for compression ratios: 1 (blue), 1.5 (red), 2 (green) and 3 (purple)

Figure 3.16 shows the percentage change in mass at equilibrium swelling for samples with various compression ratios and initial heights. There is no statistically significant difference in the percentage change in mass for samples with different initial heights and compression ratios. Figure 3.17 shows the percentage change in height at equilibrium swelling for the same range of samples. A significant difference is seen for samples with different compression ratios, but not for different initial heights. As the compression ratio increases, the percentage increase in height increases. Finally, Figure 3.18 shows the percentage change in the diameter. In this case as the compression ratio increases, the percentage change in diameter decreases. These results show that the final swelling capacity per volume of a gel is not affected by the initial height or compression ratio (within the range tested), and that the increase in height comes at the expense of the diameter. The percentage change in mass, diameter and height are not dependent on this initial height of the samples. This means that an average of the values of percentage change in height and diameter at each initial height can be used to compare percentage change in parameter to compression ratio.

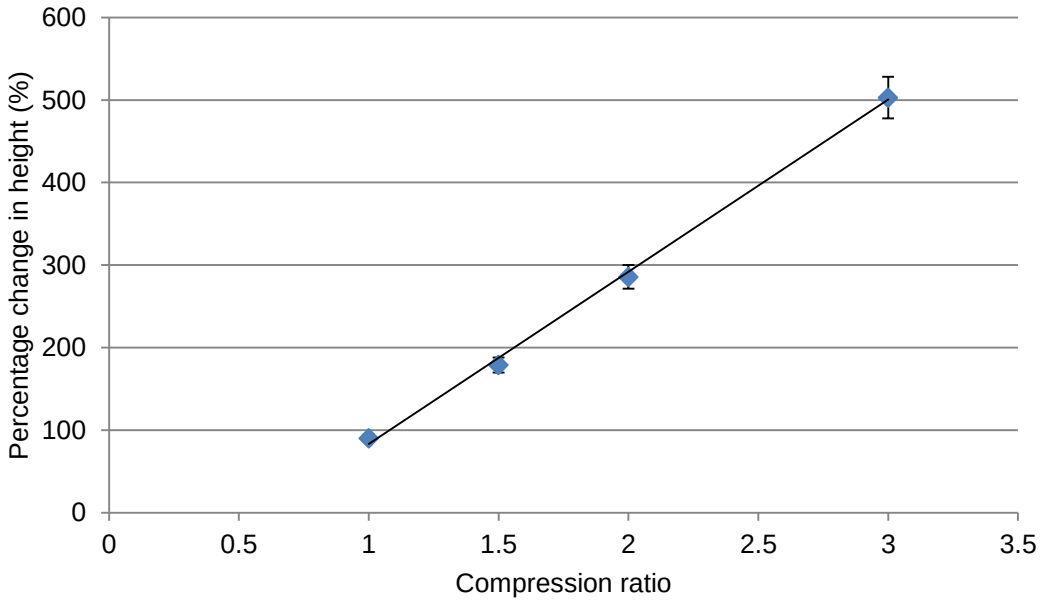

Figure 3.19 The percentage change in height vs compression ratio (average of all initial heights)

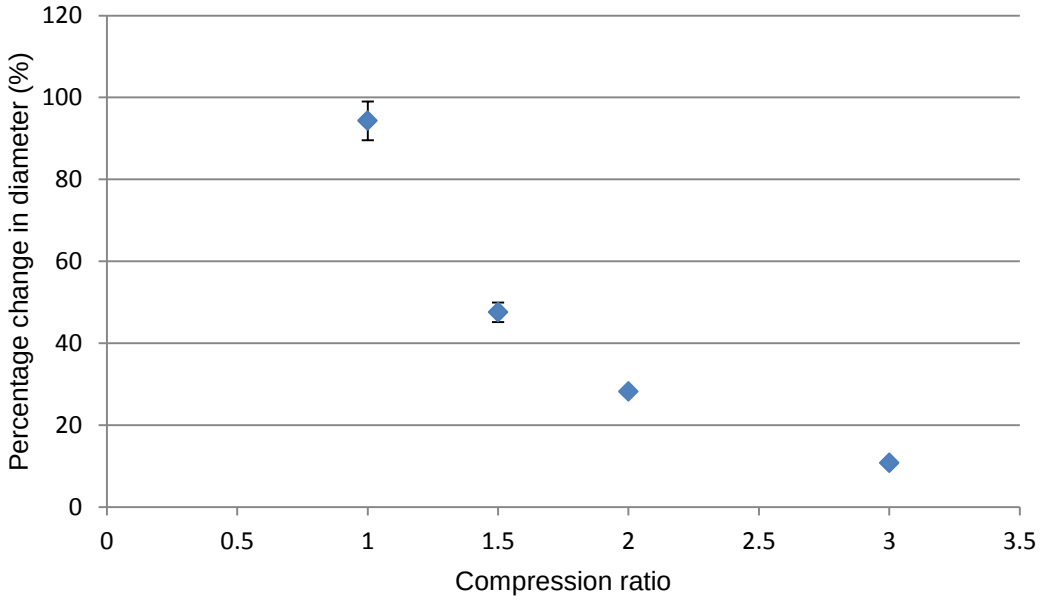

Figure 3.20 The percentage change in diameter vs compression ratio (average for all initial heights)

Figure 3.19 shows the trend between compression ratio and percentage change in height, where an average of each initial height has been used for each compression ratio. A linear fit is observed, following Equation 3.3, where C is the compression ratio, and $h_{\%}$ is the percentage change in height at equilibrium. The corresponding R^2 value is 0.9987. This curve can be used to predict the percentage change in height for different compression ratios for samples with initial heights between 3mm and 12mm.

Figure 3.20 compares the percentage change in diameter for the same range of samples. There is a negative, non-linear relationship.

$$h_{\%} = 209C - 125$$

Equation 3.3

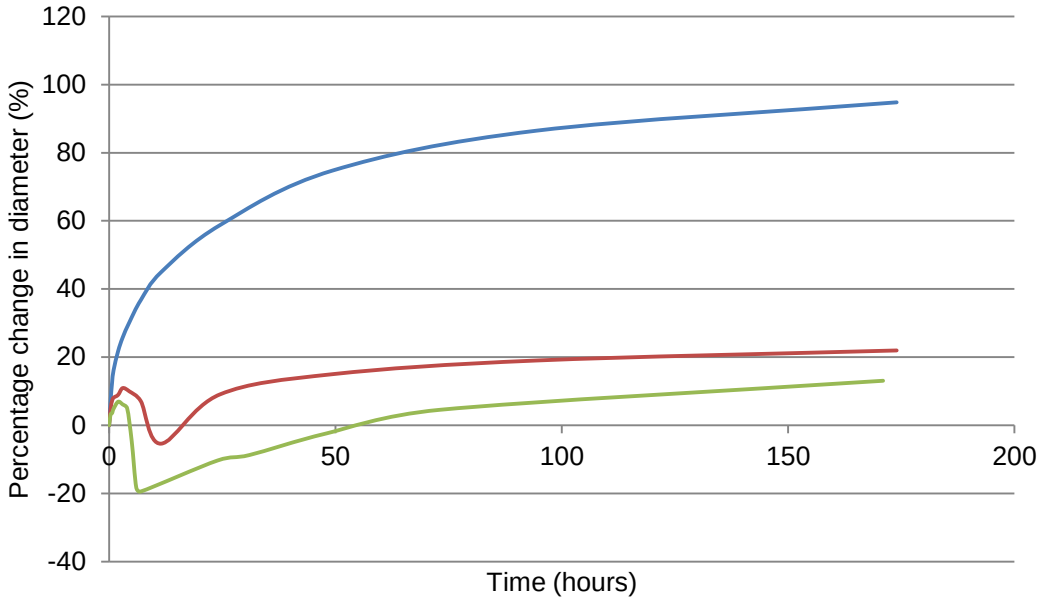

Figure 3.21 A comparison of the percentage change in diameter for samples of initial height 12mm, and compression ratios 1 (blue), 2 (red) and 3 (green)

Figure 3.21 compares the percentage change in diameter for samples of initial heights 12mm, with compression ratios 1, 2 and 3. For samples with compression ratio $C = 1$, the percentage change in diameter increases. The change is initially rapidly, before tending to an increase of approximately 94%. The curves show that as compressed samples expand, the percentage change in diameter initially increases, then decreases (to a negative percentage change), before finally increasing again. For samples with compression ratio $C = 3$, a lower percentage change is observed at each point.

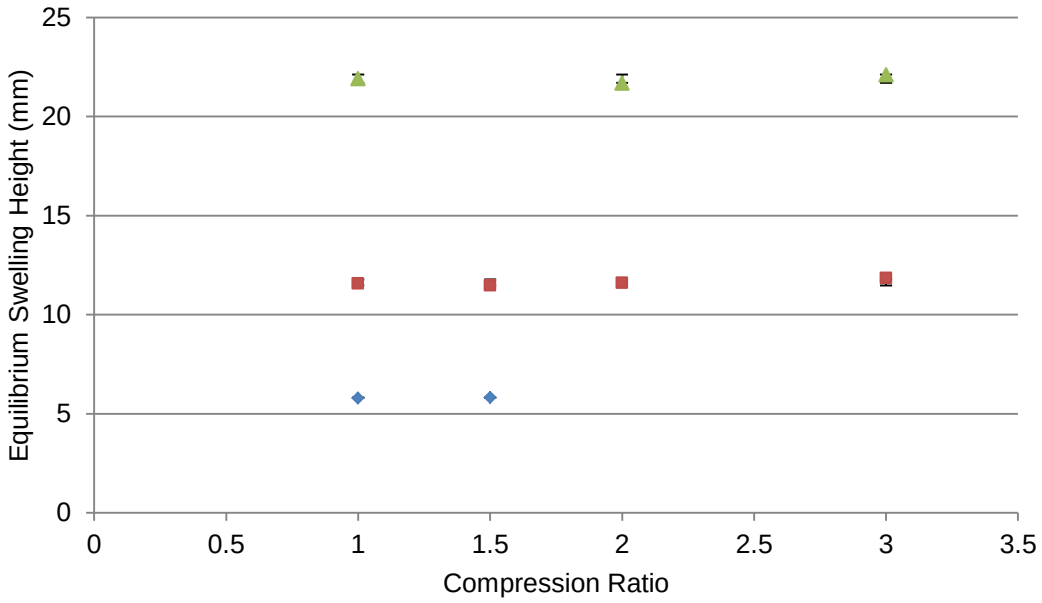

Figure 3.22 A comparison of the final swelling heights, for different compression ratios, and different initial heights. Blue diamond: $h = 3mm$. Red square: $h = 6mm$. Green triangle: $h = 12mm$

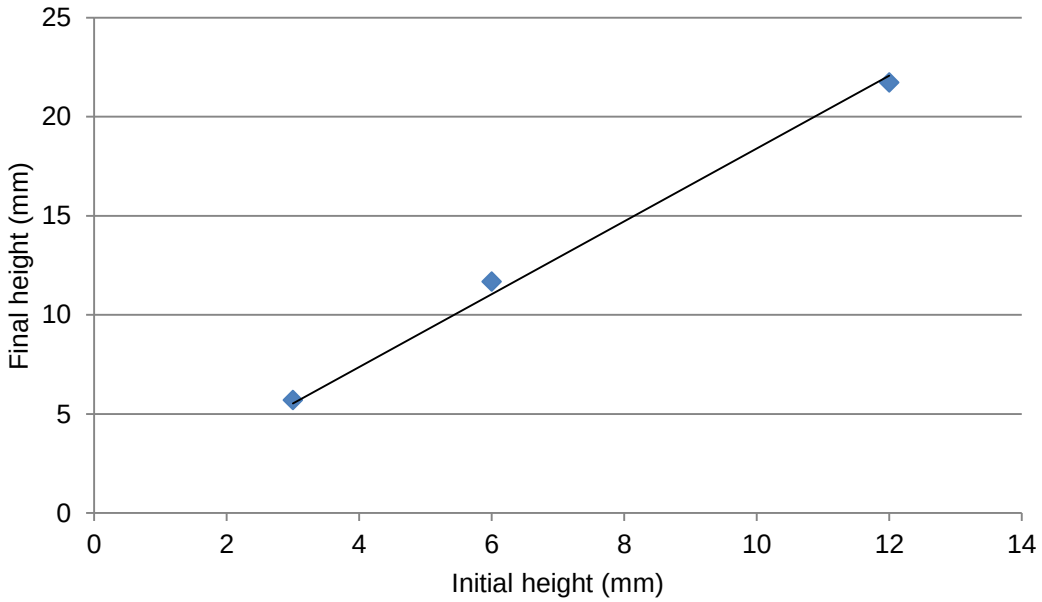

Figure 3.23 A comparison of the final height of samples which had a different initial height (3mm, 6mm and 12mm). The final heights are an average value of each compression ratio that was swollen to equilibrium for each initial height

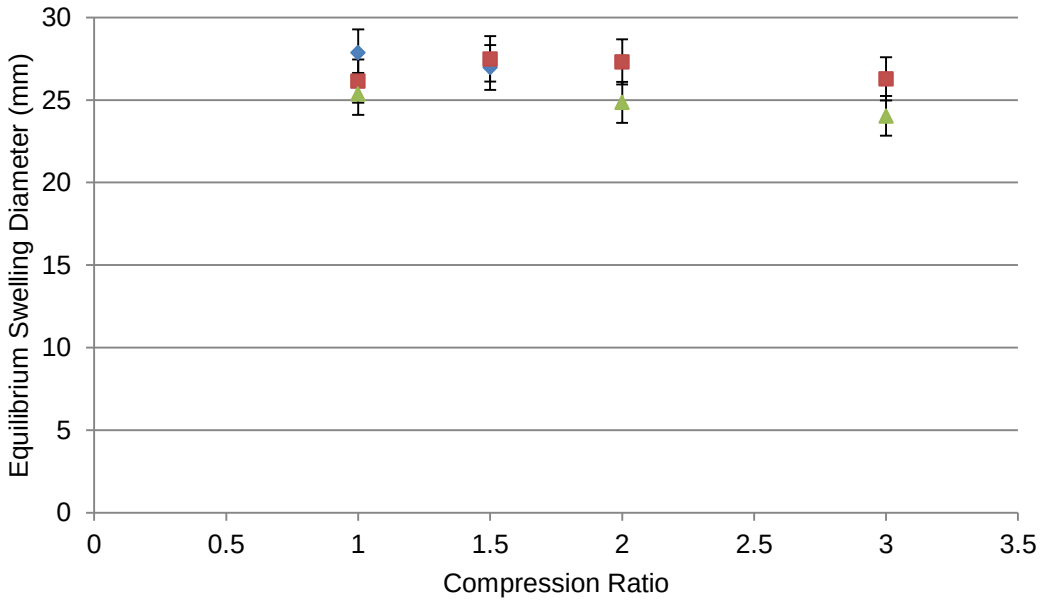

Figure 3.24 A comparison of the absolute final swelling diameters of samples with initial heights compared with the compression ratio. Blue diamond: $h = 3mm$. Red square: $h = 6mm$. Green triangle: $h = 12mm$

Figure 3.22 compares the final height of samples with different compression ratios (1, 1.5, 2, 3) and different initial heights (3mm, 6mm, 12mm). It shows that the final height of a sample with a fixed initial height is independent of the compression ratio. In Figure 3.23 the average final height (for each compression ratio) is plotted against the initial height, giving a linear relationship following Equation 3.4, with an R^2 value of 0.9958, where h_i and h_s are the initial and final (swollen) heights respectively.

Figure 3.24 compares the same parameters for final (absolute) diameter, and shows that the final diameter is independent of initial height and compression ratio. All of the samples had the same initial diameter. This is a key finding, as it shows that the swollen dimensions of the $C = 1$ sample can be considered the reference dimensions, and that at equilibrium swelling samples with $C > 1$ will have the same dimensions.

$$h_s = 1.8h_i$$

Equation 3.4

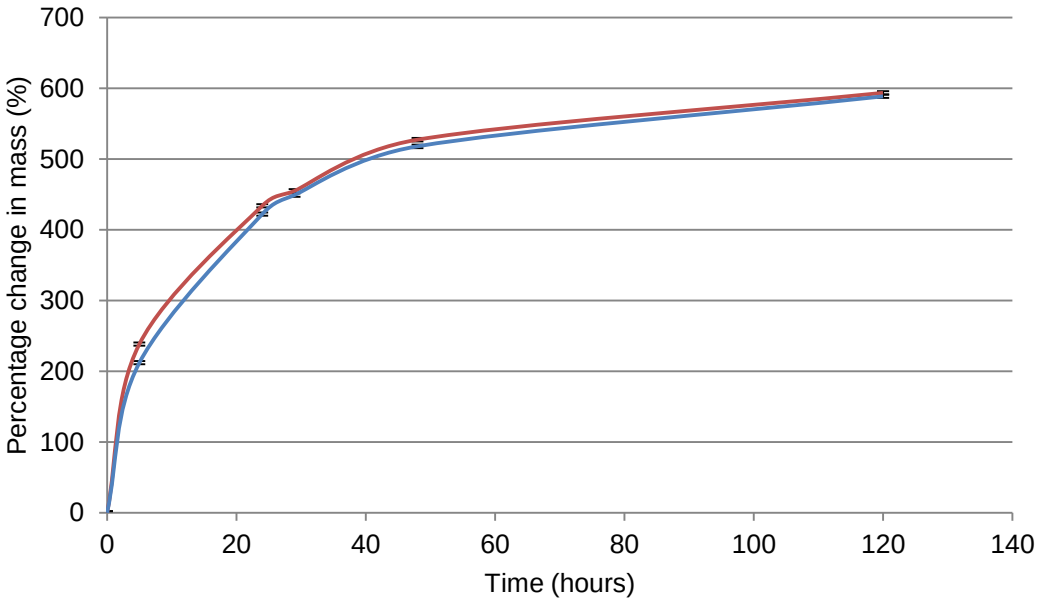

Figure 3.25 A comparison of percentage change in mass for samples pressed with an aluminium (blue) and PTFE (red) interfaces

Figure 3.25 compares the percentage change in mass with time for samples pressed with an aluminium or PTFE interface. No statistically significant difference was recorded between the two groups.

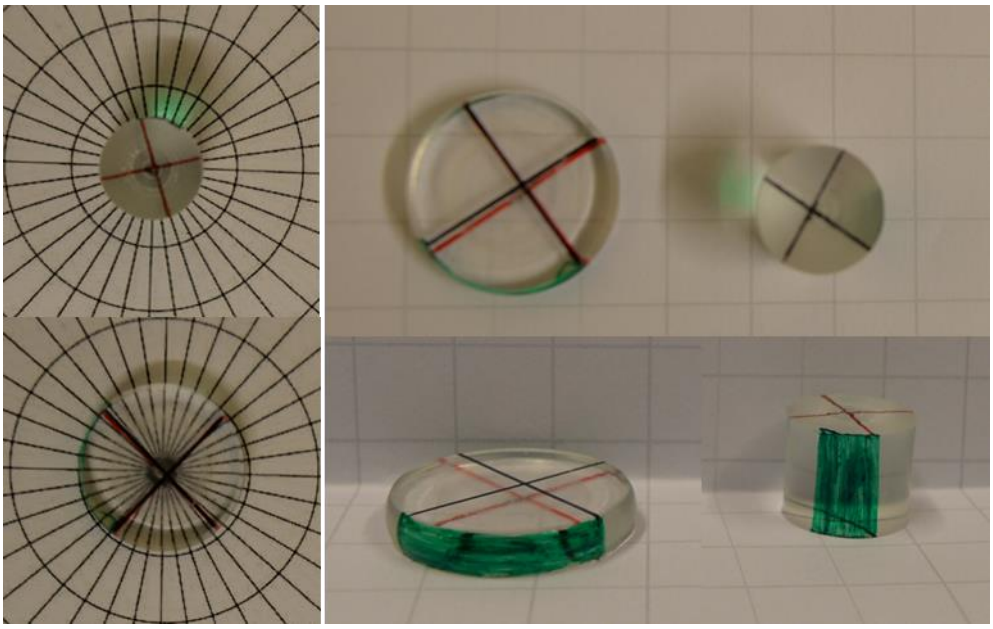

Figure 3.26 A comparison of samples at t=0 for compression ratios of 1 (top left) and 3 (bottom left). The initial height of both samples was 12mm. In both cases, a region of the edge of the cylinder is coloured green, and a black and red grid is drawn on the end surfaces of the cylinder. These have been drawn to help follow surface movement during expansion

Figure 3.26 shows the samples which were used for comparison of swelling geometry during expansion. Samples with initial heights 12mm, and compression ratios $C = 1$ and $C = 3$ were

used. A cross has been drawn on the top and bottom of each sample and a side edge is coloured green. The movement of these features can be tracked during swelling.

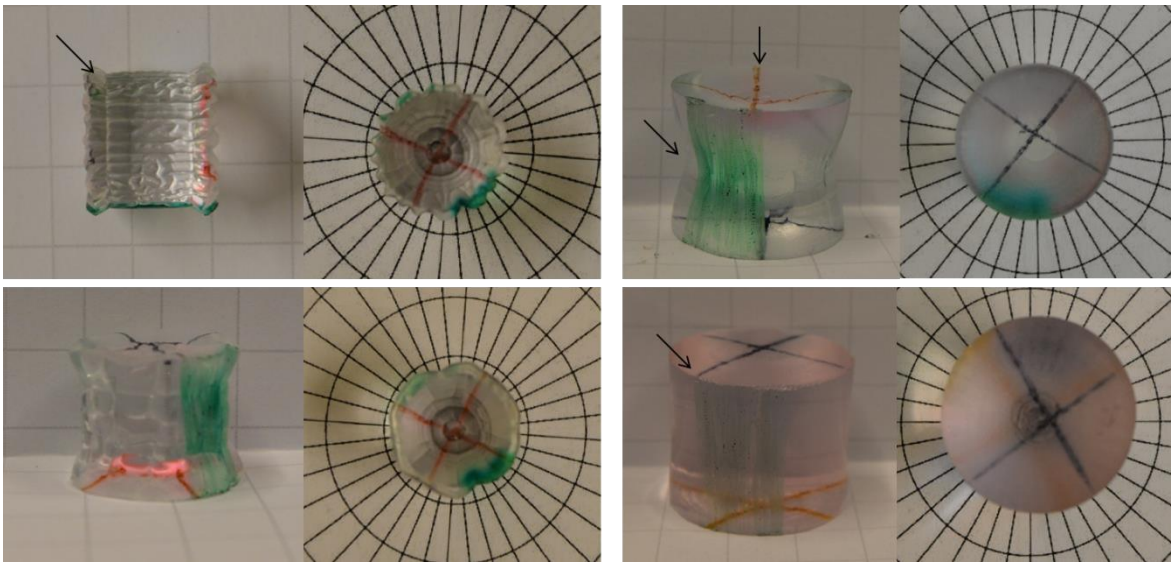

Figure 3.27 Photographs of a sample with initial height 12mm and a compression ratio of 1, during expansion. Expansion order is top left (t=1 hour) and continues to bottom left (t=5 hours), top right (t=12 hours) and bottom right (equilibrium swelling)

Figure 3.27 shows the expansion with time of a sample with an initial height of 12mm and compression ratio $C = 1$. As swelling occurs, the top and bottom outer circumferences of the pellet expand in volume and become wrinkled in appearance (top left). These regions continues to expand until the sample appears to have a waist, with the top surfaces forming a bowl like geometry (bottom left and top right). Finally, the sample expands into a cylinder (bottom right) with the crosses remaining on the top and bottom surfaces, and the green stripe remaining on the side of the cylinder.

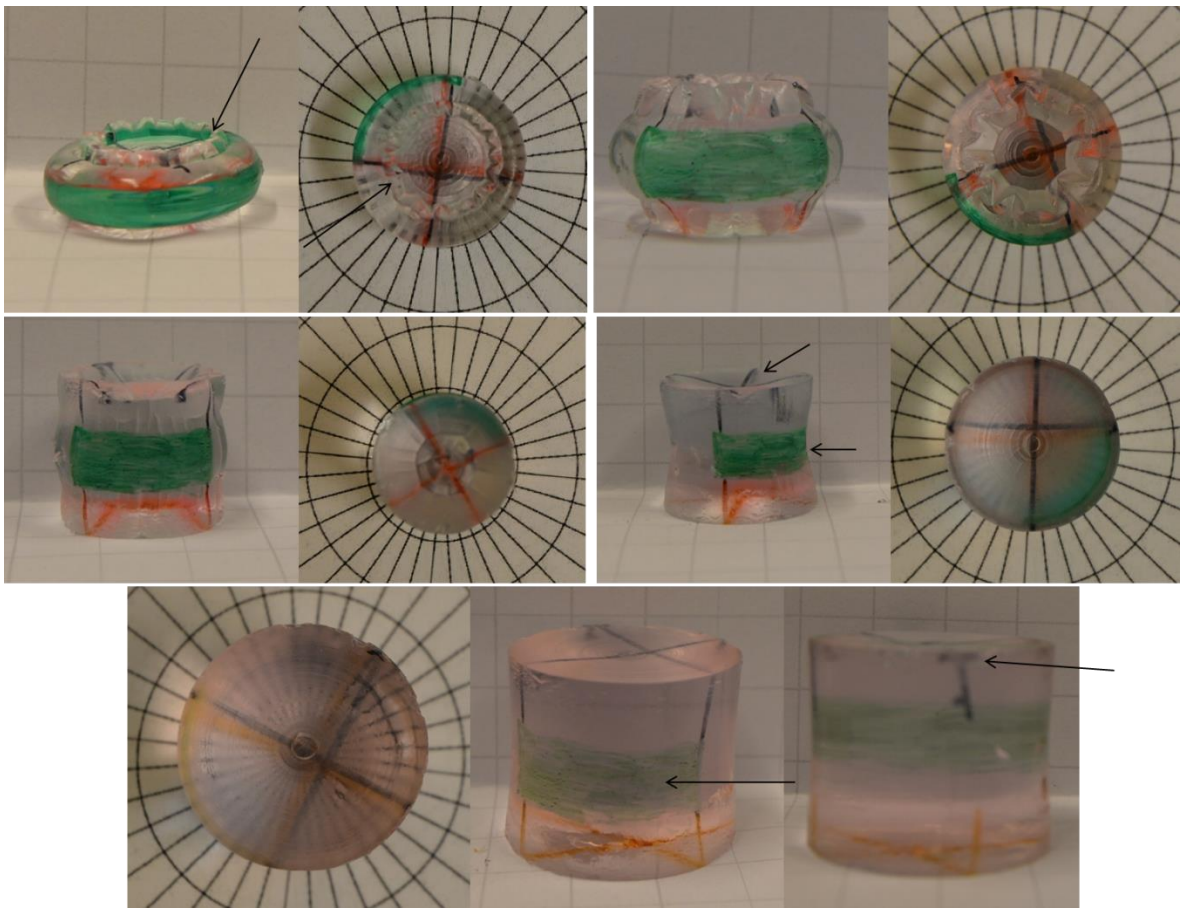

Figure 3.28 Photographs of samples with an initial height of 12mm and a compression ratio of 3 during expansion. The top left image is taken at 1 hour of swelling and expansion progresses from left to right in the image pairs, ending with equilibrium expansion on bottom row

Figure 3.28 shows the expansion with time of a sample with an initial height of 12mm and compression ratio $C = 3$. The swelling geometry of this sample is different to that of ratio $C = 1$. Firstly, a bulging annulus appears on the top and bottom of the sample (top left). As the sample continues to swell this annulus is the maximum height of the sample (top right). After approximately five hours, the gel diameter decreases significantly and the height increases (middle left). This is also observed in the change in diameter during swelling, as seen in Figure 3.21. At this point the boundary between the side and the top of the cylinder changes and now forms the bulging annulus. The previous boundary (described by the point where the green side strip and top cross meet) has moved to the edge of the cylinder. From this point the samples swell in the same manner as the samples with compression ratio $C = 1$, until they reach equilibrium (middle right and bottom). The marker shown in the final swelling photograph shows a mark on the new boundary that was drawn on approximately 4mm from the edge before swelling occurred.

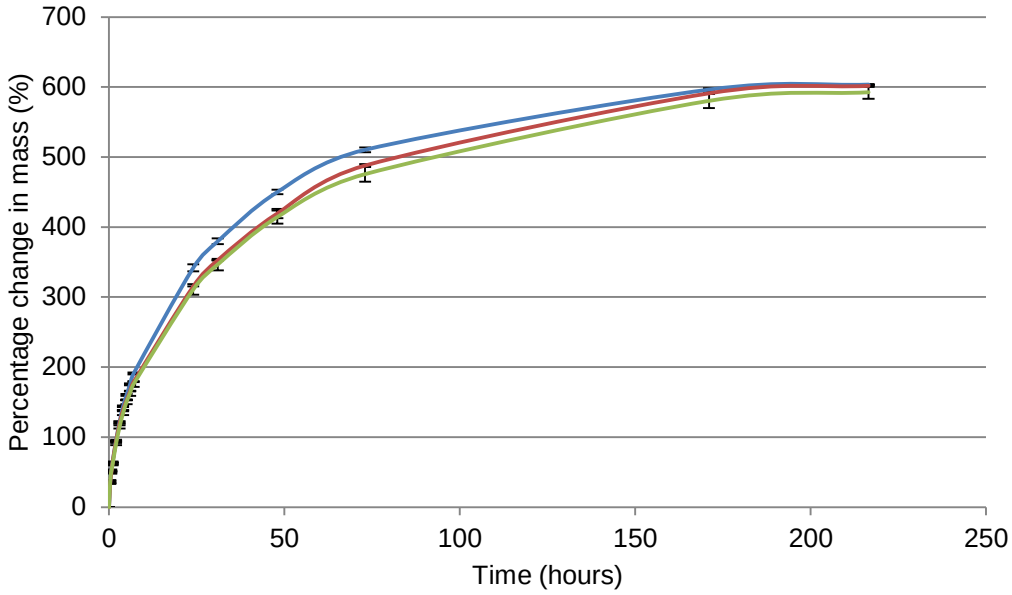

Figure 3.29 A comparison showing the percentage change in mass with time for domes (red), wedges (blue) and cylinders (green)

Dome and wedge samples were produced as described in section 3.2.2 and were successfully swollen to equilibrium. Figure 3.29 shows that the percentage change at equilibrium swelling does not differ between domes, wedges and cylinders. This result indicates that the geometry of samples does not affect the overall fluid uptake (per unit volume) of the samples.

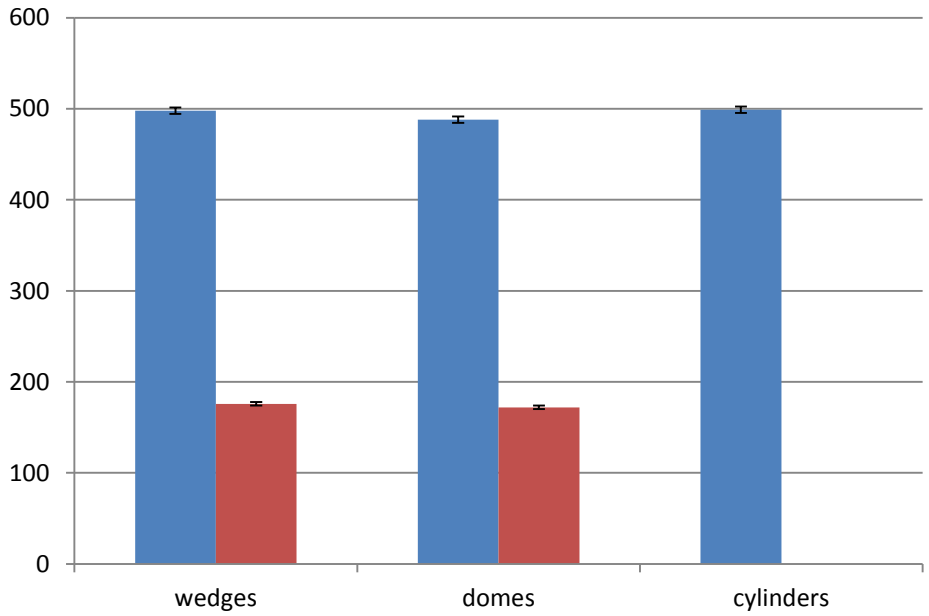

Figure 3.30 A comparison of the equilibrium percentage changes in lower heights (red) and upper heights (blue) for wedges, domes and cylinders

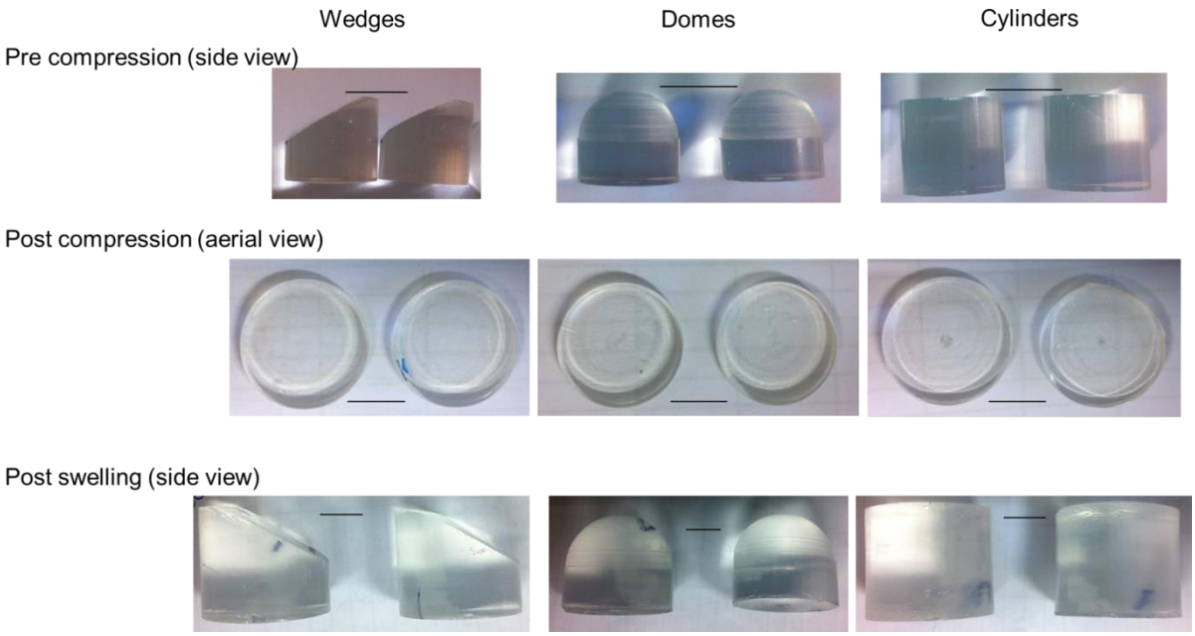

Figure 3.31 Photographs showing each shape before compression (side view), post compression (aerial view), and post swelling (side view). The black bar represents 10mm in each image

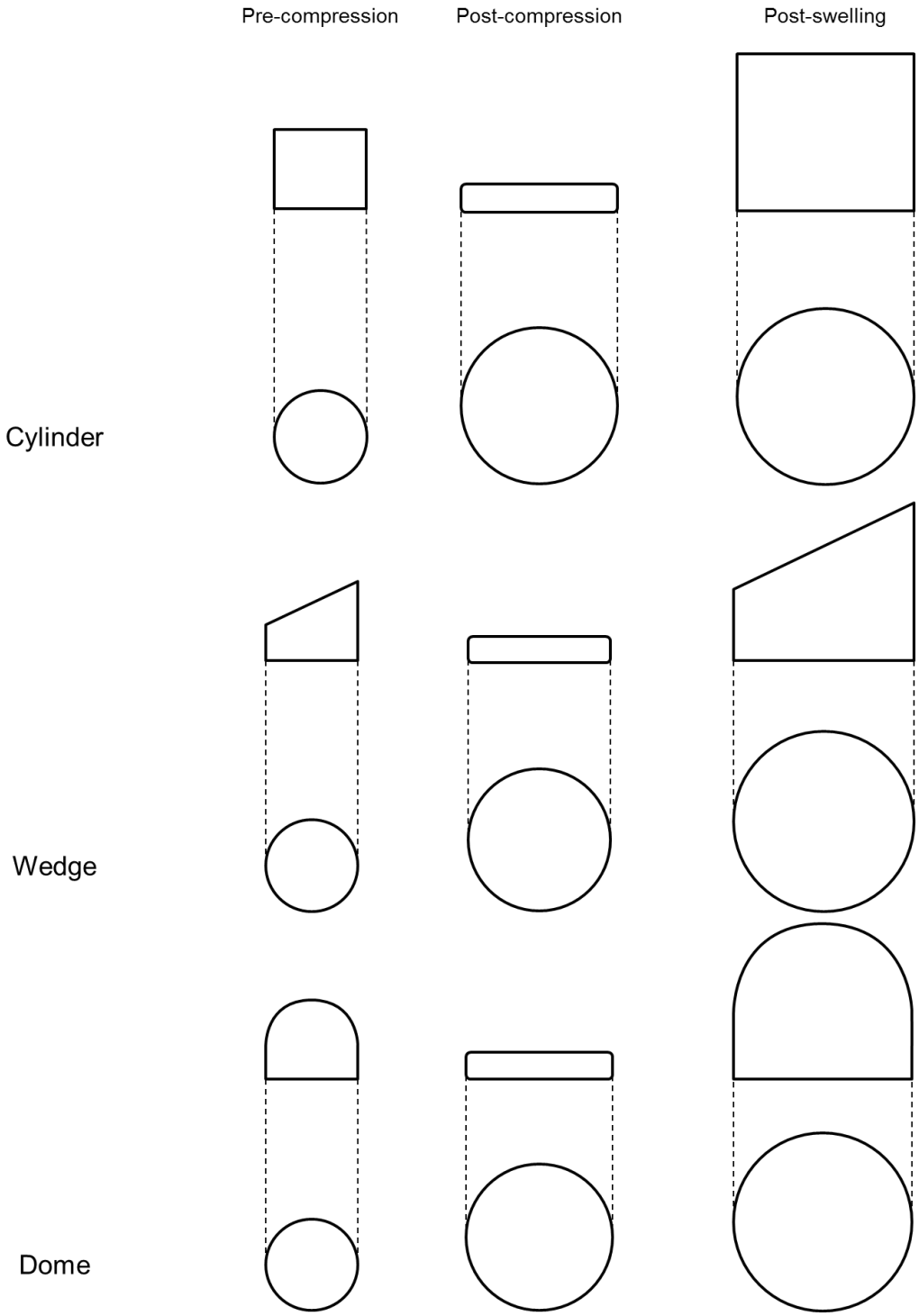

Figure 3.32 Scaled representations of the three different shapes before compression, after compression and after the swelling equilibrium has been reached. The cross section (above) and the aerial view (below) of the disc are shown in each case

Table 3.1 A comparison of the changes of ratio and angle for samples before compression and after swelling

	Ratio of upper height: lower height (mm)	Angle (DEG)
Pre compression (dome)	1.13:1	N/A
Post swelling (dome)	1.13:1	N/A
Pre compression (wedge)	1.13:1	24°
Post compression (wedge)	1.08:1	24°

Figure 3.30 compares the relative height changes (upper and lower) for the domes and wedges, and the height of the cylinders. There is no statistical difference between the upper heights (and height of cylinder) for any sample groups. There is also no statistical difference between the lower height for the dome and wedge shape (this dimension is not applicable for the cylinder shape). There is a statistically significant difference between the upper and lower heights for both domes and wedges. The lower height measurement (taken at the start of the wedge or dome shape) is 5.67mm and is compressed to 4mm, thus giving a compression ratio of $C = 1.42$. If this compression ratio is used in Equation 3.3, an expected percentage change in the lower height would be 171%. The average observed (for both wedges and domes) was 172% as shown in Figure 3.30. The maximum compression ratio in the domes and wedges is $C = 3$, which, using Equation 3.3, gives a predicted maximum percentage change of 502%, and the observed average value was 496%. This indicates that changes in the geometry of the initial samples are retained on swelling after compression moulding into a disc. This finding is also confirmed in Figure 3.31, which shows photographs of the different shapes before compression, after compression, and after swelling.

Table 3.1 shows the changes in the ratio of the upper and lower heights. It shows that proportions of the sample remain constant to two significant figures. Finally Figure 3.32 shows a scaled representation of the changes in dimension and geometry for samples at

different stages of the process. It has therefore been shown that it is possible to create devices which expand from a flat disc into a pre-determined shape with a non-prismatic cross-section.

3.3.3 Cross-polarized light microscopy

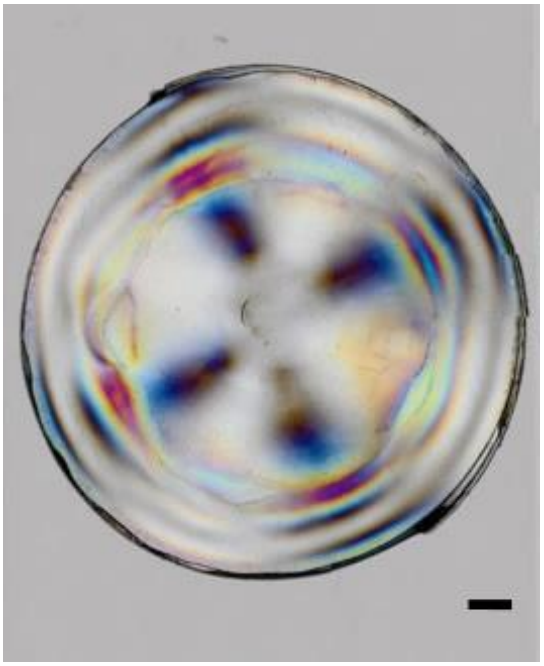

Figure 3.33 A cross-polarized light image of a sample with C=3, pressed with an aluminium interface. The scale bar represents 2mm

Figure 3.33 shows cross-polarized light microscopy image for a sample pressed with an aluminium interface with compression ratio $C = 3$ and initial height 6mm. The sample shows a Maltese Cross surrounded by concentric rings. This pattern is reflective of an outer annulus with increasing radial strain (160). This boundary occurs approximately 4mm from the edge of the sample, where a faint ring can be observed on the sample (total radius of sample 12.2mm). For a sample of initial height 12mm and compression ratio $C = 3$, the boundary occurs 6.3mm from the edge of the sample (total radius 12.5mm).

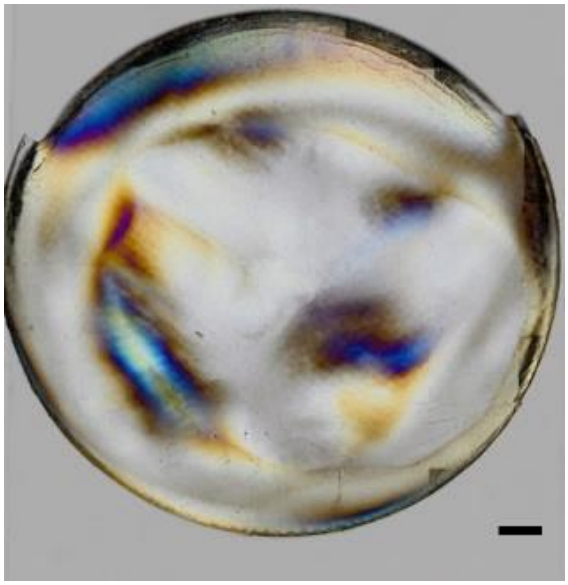

Figure 3.34 A cross-polarized light image of a sample pressed with a PTFE interface in the hot press. The scale bar represents 2mm

Figure 3.34 shows the cross-polarized image of a PTFE sample with compression ratio $C = 3$ and initial height 6mm, in which no distinct patterns can be identified. Instead there are random regions of strained material and an irregular pale yellow boundary. This implies that the material flow during pressing was not consistent.

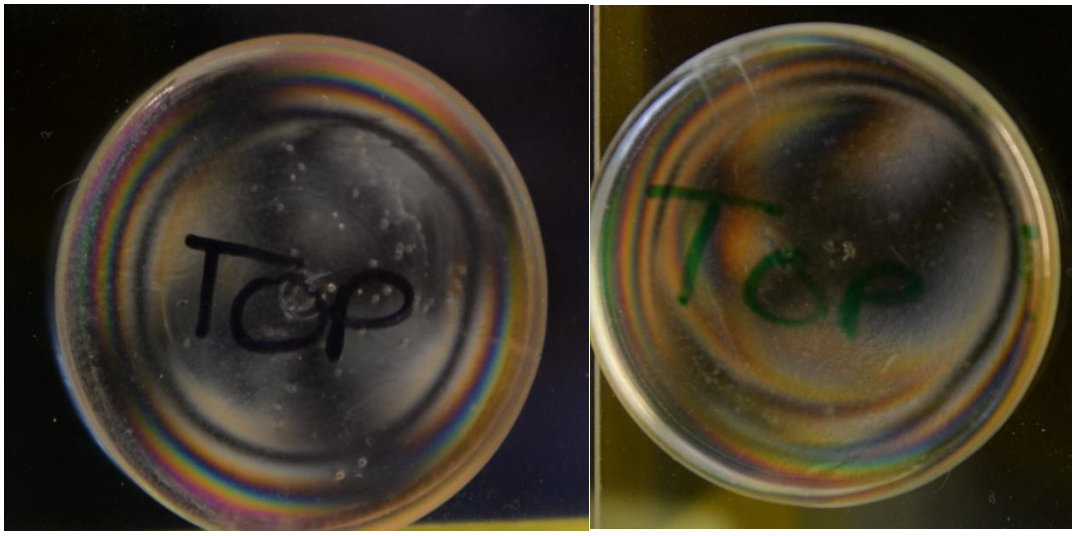

Figure 3.35 Cross-polarized light images for dome (left) and wedge (right). The diameter of both samples is 22mm

Figure 3.35 shows the cross-polarized light images for a dome and for a wedge. In the dome image, concentric rings can be seen starting at 4.6mm from the sample edge. However, in the wedge sample, the rings form a semi-circle, 5.7mm from the edge at the widest point- which corresponds with the highest point of the initial wedge-shaped pellet.

3.3.4 Hardness indentation

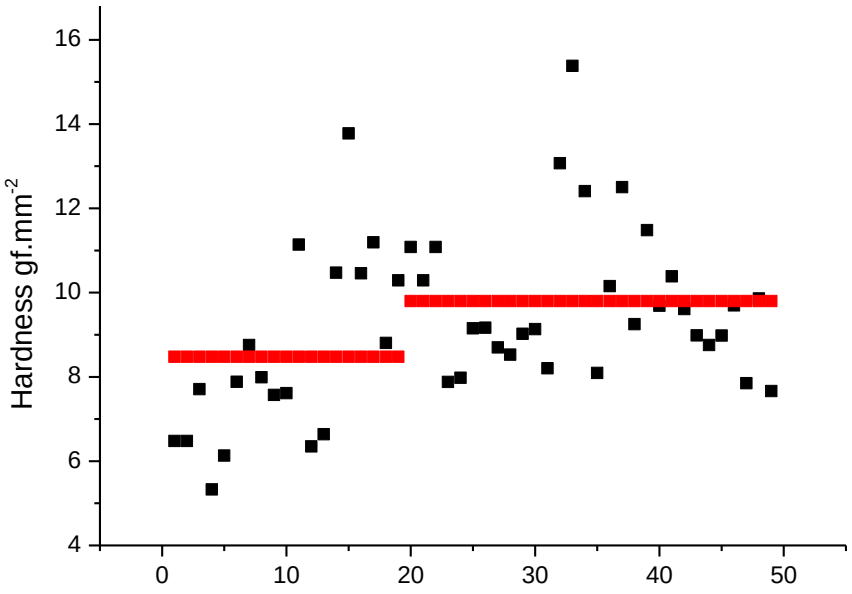

Figure 3.36 The microhardness results across the diameter of the sample (starting at the edge) each item reflects approximately 200μm. The red line shows the sample mean values for each region, with the boundary being determined by the maximum distance from the edge (item = 0) that statistical difference was observed.

Figure 3.36 shows the variation in hardness across a compressed disc (initial height of 6mm, compression ratio of $C = 3$). Two regions with statistically significant different mean hardness values are observed. The outer 4.2mm of the diameter had an average hardness value of 82HK (± 22HK), compared to 98HK (±18HK) for the central 13.5mm of the sample. The central region is slightly larger in diameter than the original P(MMA-co-NVP) rod.

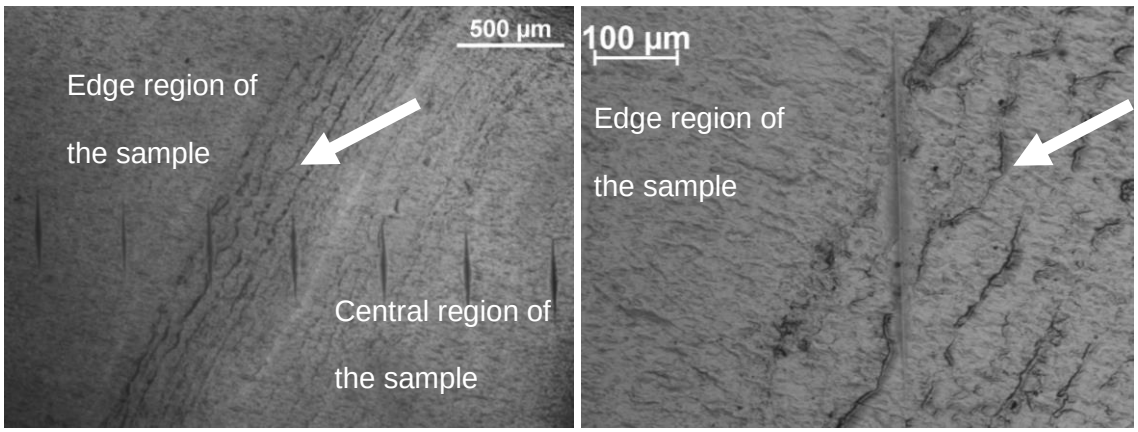

Figure 3.37 Micrographs of a sample pressed with an aluminium interface, at the boundary between the two regions found in Figure 3.36, approximately 4mm from the sample circumference. The white arrows indicate the damaged annulus.

Figure 3.37 shows a micrograph taken approximately 4mm from the sample circumference, where an annulus of damaged material can be observed.

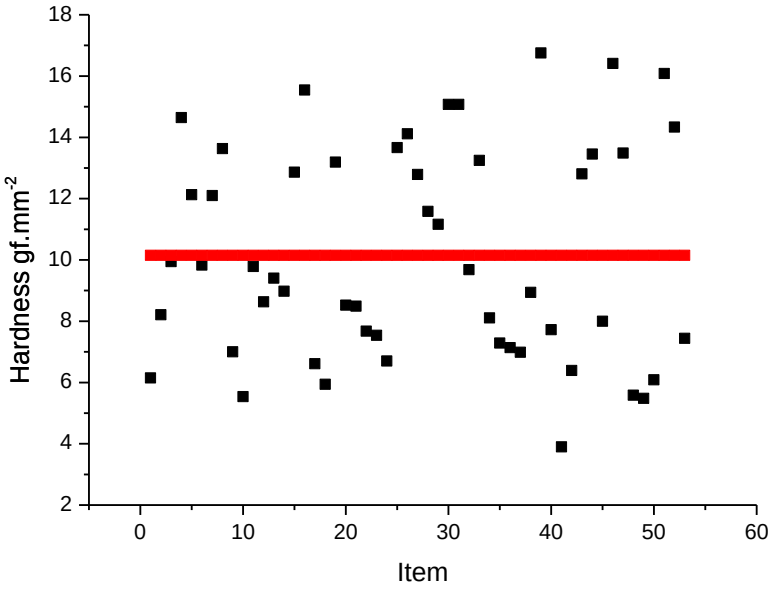

Figure 3.38 Microhardness results for samples pressed with a PTFE interface at the hot press. The red line shows the group mean

Figure 3.38 shows the variation in hardness across the sample pressed with a PTFE interface (initial height of 6mm, compression ratio of $C = 3$). A random distribution of hardness values along the diameter, with an average of 101.5HK (±34.7HK), is observed.

3.4 Discussion

This section will discuss the results presented in section 3.3. Results for cylindrical samples will be discussed first, before moving on to those with non-prismatic cross-sections.

3.4.1 Cylinders

Figure 3.23 indicates that for an increase in dry height of 1 mm, the swollen increase in height will be 1.8 times greater. Equation 3.3 shows the (empirically found) relationship between percentage change in height and compression ratio. However it is possible to determine a theoretical equation to define how the percentage change in height would vary with compression ratio, if the final swollen height of the sample is constant (as it has been shown to be within this chapter). The percentage change at equilibrium is found by using Equation 2.19, where h_t becomes $h_{t=\infty}$. The compression ratio is given by Equation 3.1. It is important to note that h_0 and h_f are the same value (the height after compression, which is also the dry height pre-swelling), and that for this purpose h_f will be used. By making h_f the subject of Equation 3.1, and substituting this into Equation 2.19, Equation 3.5 can be found. If the final swelling height is assumed to be constant (i.e. there is a constant reference swelling shape), then $h_{t=\infty}$ is constant with compression ratio. The initial height, h_i, is also constant. Therefore, the value of $\frac{h_{t=\infty}}{h_i}$ can be assumed to be constant with compression ratio, and is found to be approximately equal to two (Equation 3.4). This value can be substituted into Equation 3.5, to give Equation 3.6. This theoretical equation is in excellent agreement with the empirically found Equation 3.3, thus further supporting the key finding that samples return to a reference swollen state.

$$h_{\%} = 100\left(C\frac{h_{t=\infty}}{h_i} - 1\right)$$

Equation 3.5

$$h_{\%} = 200C - 100$$

Equation 3.6

The decrease in diffusion coefficient with compression ratio, as seen in Figure 3.14, and the decrease in the diffusion exponent with compression ratio, as seen in Figure 3.15, may be due to the changes in the arrangement of the polymer network due to compression. These changes will be discussed in more detail presently, but there is local densification of the chains parallel to the direction of the hot press, and extension of chains perpendicular to these. It is this densification parallel to the direction of the press that may cause the reduction in the diffusion coefficients and exponents with compression ratio; as a greater degree of chain alignment is required. The values for the diffusion coefficients and exponents were calculated from the first 60% of the swelling graph, and did not vary within this region. The exponents indicate that the diffusion is Fickian, thus agreeing with previous studies of the diffusion of water through P(MMA-co-NVP) (172). This is perhaps a surprising result as significant chain relaxation must occur for the bulk of the water molecules to penetrate the polymer network. However, as shown in Figure 3.20, the diameter of compressed samples is initially reduced (within the first five hours) and therefore some water must be diffusing into the sample to allow this chain rearrangement. It is possible that there is a difference in the diffusion behaviour of water molecules in different states within the hydrogel (for example, bound or free water). This could be investigated further using high resolution magnetic resonance imaging.

As stated in section 3.3.2, it is a key finding that for each initial height there is a ‘reference’ swollen dimension to which devices will always expand (as seen in Figure 3.22). Figure 3.39 shows this schematically. The observation of increasing anisotropy (tending towards uniaxial expansion) with increasing compression ratio is a factor of the geometry of the compressed samples; as the diameter of the compressed gel approaches that of the reference swollen diameter, the expansion will tend towards uniaxial. Figure 3.11 shows that it was not possible to reliably produce samples with compression ratios $C > 3$. As samples with a compression ratio greater than three also have a compressed diameter of greater than 25mm, this may indicate that when the diameter of the compressed disc is greater than the diameter of the

reference swollen state, the polymer network will incur significant damage, leading to sample failure (this will be discussed in more detail presently). Swan (5) reported a maximum compression ratio of $C = 7$. However, it should be considered that Swan (5) did not define how a successful device was recorded. For example, it is possible that out of six swollen devices with a compression ratio of $C = 7$, only one was swollen to equilibrium and this was taken. It is also possible that devices which had incurred damage (i.e. cracking) during swelling were also included in the results. Within the results presented here, the recorded devices were all required to swell, undamaged, to equilibrium. Additionally, for a group of devices to be considered a success, the majority had to swell successfully. However, for the devices which were successfully produced within this study, the swelling behaviors were in line with those presented by Swan (5). It is also of interest to consider what would happen at compression ratio $C < 1$ (which would indicate extension of the pellet). If it is assumed that the sample would still return to the reference swollen state, a compression ratio of $C < 1$ would lead to an increase in the percentage change of diameter, at the expense of the increase in height. This would therefore produce a biaxial expander. In this case, the x intercept of Figure 3.20 would predict the point at which pure biaxial expansion is predicted ($C = 0.6$). It is predicted that there will be some value of (extended) final height at which the extended height is greater than the reference swollen height, and the polymer network would incur significant damage, leading to sample failure. Further work in this area would be of great interest to generate bi-axially expanding hydrogels.

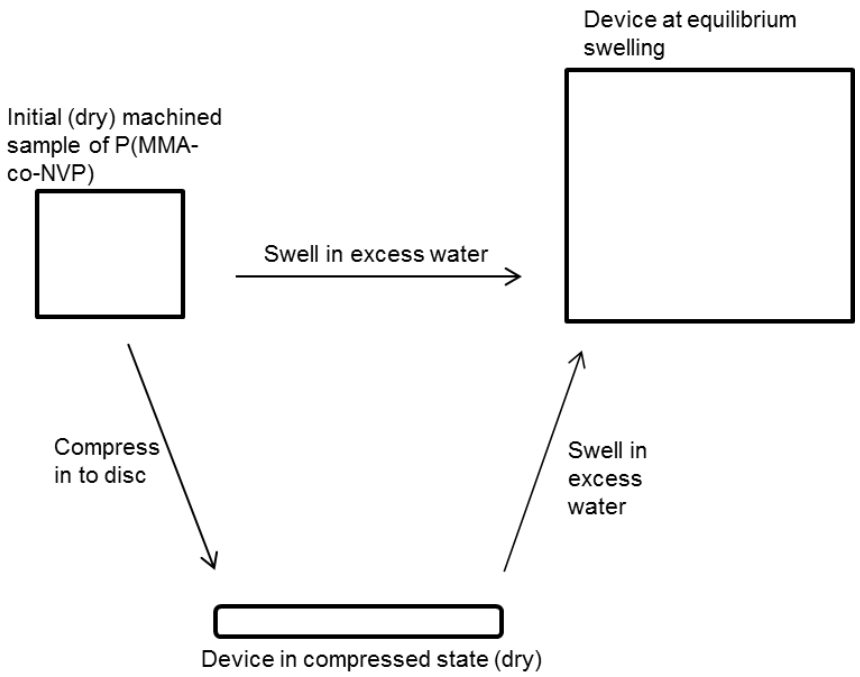

Figure 3.39 A schematic of the proposed shape memory process in P(MMA-co-NVP) polymers

In order for samples which have been compressed to swell to this reference state, any damage to the polymer network (e.g. breaking cross-links) during hot pressing must be below some critical point. The changes to the polymer set network can be seen in Figure 3.40. Network 'A' in the diagram shows the simplified polymer network in the hydrated state- the polymer chains are extended between the regular cross-linked regions. Network 'B' in the diagram represents the 'as-received', dehydrated polymer, where chains are densely packed. Network 'B' expands isotropically into the form of network 'A' on hydration. If the network is compressed within the manufacturing limit, it will take the form of network 'C', where chains parallel to the force are densely packed and chains perpendicular to the force are extended. On hydration network 'C' will expand anisotropically (as some chains are already extended) into network 'A'. For network 'C' to expand to network 'A', the number of broken chains and cross-links must be below some critical value. If after compression the critical value is exceeded, then network 'D' will be formed (with red crosses indicating cross-link or chain fracture) and fracture of the network will be observed either during compression or expansion.

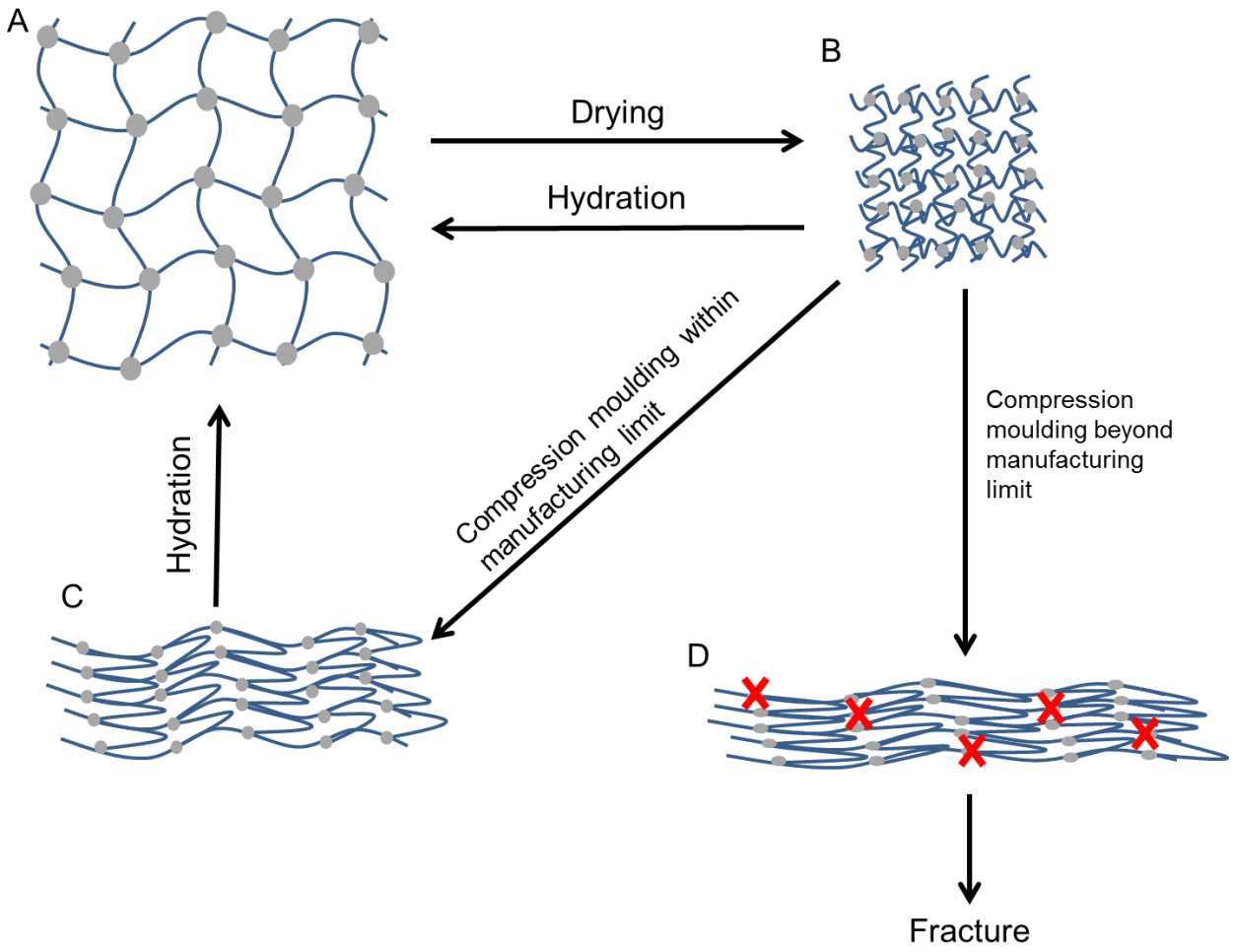

Figure 3.40 A schematic showing changes to the polymer set in different circumstances. A: hydrated polymer network, B: dehydrated isotropic polymer network (as-received samples), C: Compressed polymer network where cross-links have not been broken above the critical limit, D: Compressed polymer network where cross-links have been broken above the critical limit

As shown in Figure 3.27 and Figure 3.28, even though the final dimensions of the sample may be the same, the geometry of the sample during swelling is different. For samples with a compression ratio of $C = 1$, the geometries can be described mathematically by considering the swelling of a partially constrained gel (91,92). As the diffusion occurs, the swollen gel is constrained by the gel which is not yet swollen. The hydrated region will expand, but the region beyond the diffusion front will not. This causes a volume difference and thus wrinkles form on the surface of the gel to accommodate this change. The effect is more pronounced at the top and bottom of the cylinder as water diffuses into the region from both the top and side surfaces- creating a 'frill' on the top and bottom of the sample. As expansion progresses, the wrinkles disappear and an hourglass shape is observed. This shape may also be explained by considering the free swelling of a cubic gel (91,92), where during

expansion each side of the cube is predicted to have a ‘bowled effect’. However, to explain the geometry during the first five hours of expansion for samples with compression ratio, $C = 3$, the flow of material during hot pressing must be considered.

The movement of the surfaces during swelling of samples with compression ratio $C = 3$ (as seen in Figure 3.28) indicates that there is also movement of the surfaces during compression of the samples. This can be seen schematically in Figure 3.41. As the sample is compressed, the sides of the cylinder (bounded by *ad* and *bc*) slide out, whilst the top and bottom surfaces (*ab* and *dc*) stick to the hot press interface. The new boundaries between the sides and top surfaces are marked by *1, 2, 3* and *4.* On expansion of these compressed samples, the top and bottom surfaces *1a, 2b, 3c* and *4d* expand by following the marked arrows to become part of the side surfaces. If the boundaries from the pellet before compression are compared to the boundaries after swelling is completed, it can be seen that points *a, b, c,* and *d* remain the boundaries between the top and side surfaces.

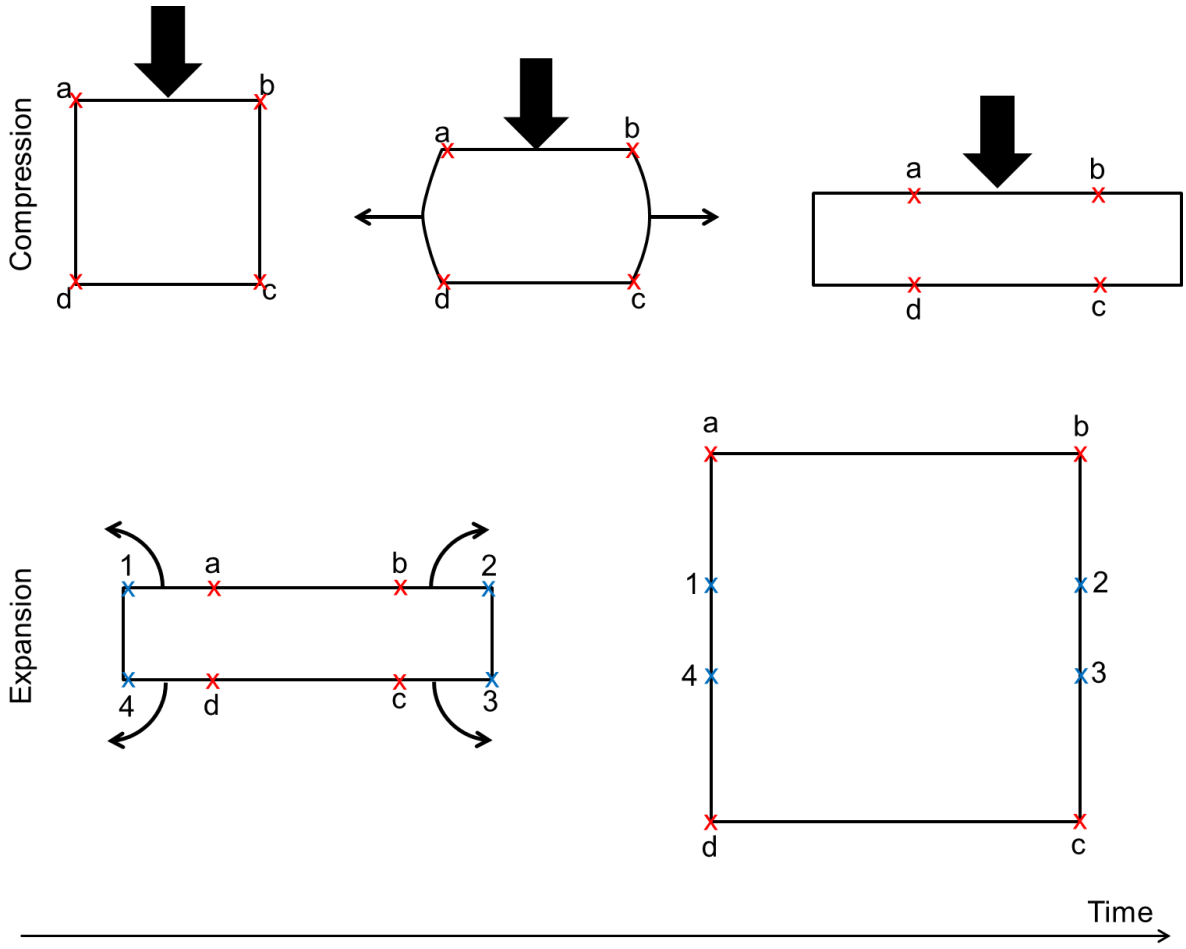

Figure 3.41 A schematic showing the surface movement of a cylindrical pellet which has been compressed and then expanded

The movement of these surfaces will have an impact on the P(MMA-co-NVP) network and this is considered in the schematics shown in Figure 3.42 and Figure 3.43. Each element contains a certain number of polymer chains and a certain number of cross-links. In the cylinder (before compression) the distribution and direction of these chains and cross-links is random and isotropic. The colours indicate which element boundaries are initially at which surface; for top and bottom surfaces it is red; for the side of the cylinder it is blue; and internal boundaries are black. Figure 3.43 shows that after pressing, some of the surface which was initially on the sides moves to the top and bottom surfaces, creating variation in the internal strains.

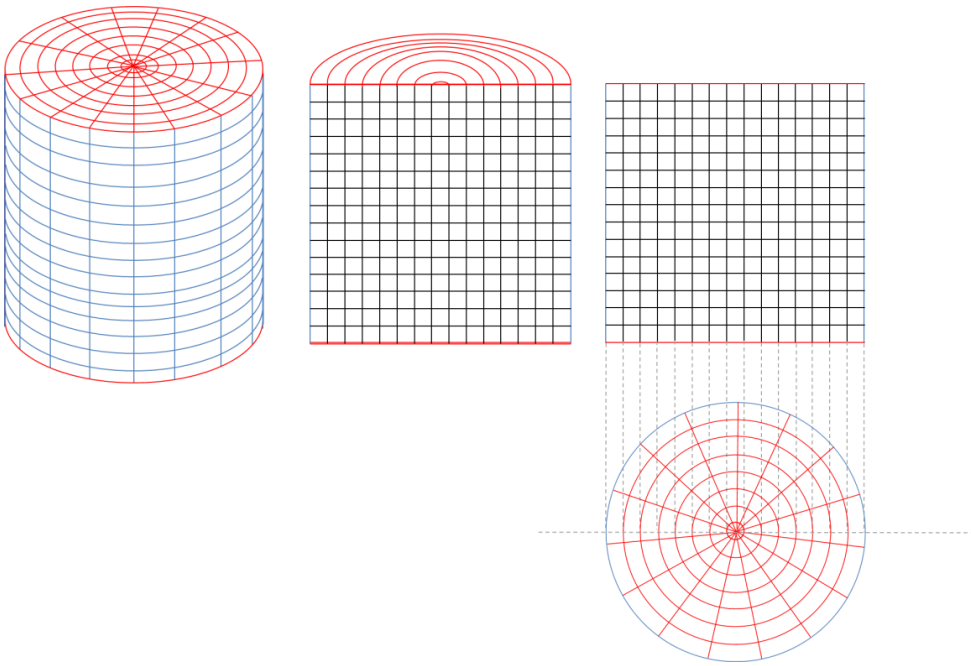

Figure 3.42: A schematic of a cylinder broken down into elements representing a cylindrical pellet of P(MMA-co-NVP)

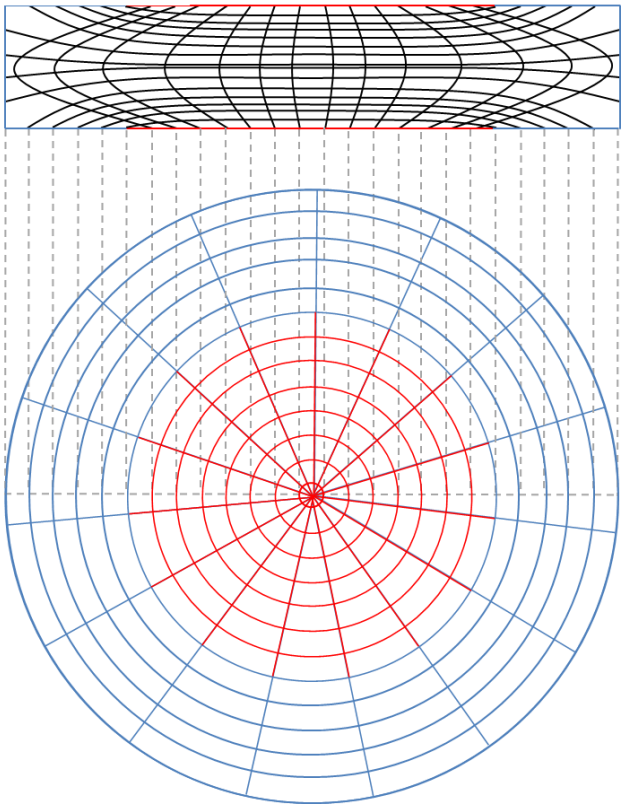

Figure 3.43 The sample shown in Figure 3.42 post hot compression moulding, based on the observed movement of the sample surfaces. The red region (initially the top of the pellet) now forms a central circle on top and bottom of the sample. The blue region (initially the side of the pellet) now forms an outer annulus on the top and bottom of the surface, as well as the side. The internal strains caused by this restructuring can be seen by comparing the elements to those shown in Figure 3.42

In Figure 3.43, at the boundary between the red and blue regions (which will become the boundary between the sides and top of the cylinder after expansion) there is localised compression. This means that there is a greater density of the hydrophilic polymer network, and hence on exposure to water this region will have a greater driving force for expansion. It is for this reason that swelling is faster here than in the rest of the sample, creating the bulging annulus seen during swelling (Figure 3.28). The compression in this region is also shown to be causing an annulus of damage to the structure (as seen in the optical microscopy image in Figure 3.37); this increase in surface area may also contribute to the rapid swelling seen in this region.

Figure 3.43 predicts that the highest strain will be at the circumference of the samples, which is supported by the cross polarization images in Figure 3.33, the photographs showing failure in the outer annulus and circumference (Figure 3.12 and Figure 3.13), and the reduction in microhardness at the outer annulus (Figure 3.36). Figure 3.44 shows a schematic that can be used to help explain why there is a reduction in hardness for samples which are within the manufacturing limits, and why failure occurs in this region for samples outside the manufacturing limits. In the polymer structure there is a range of chain lengths between cross-links, which can be assumed to follow a normal distribution. It can also be assumed that this distribution will not vary between the elements (which are defined in Figure 3.43), and nor will the number of cross-links in each element. As the strain is increased, the chains between cross-links will begin to extend, and then become straight, and then stretch elastically, and then the bond will fail. This critical strain will occur at different points along the distribution of chain lengths, with those at the lower extremity requiring very little strain to break the cross link. However, as the strain increases, so will the proportion of chains which fail. The fewer cross-links in the polymer, the lower the hardness (76), and at some point a critical proportion of the cross-links will fail, causing failure of the bulk (and therefore the network ‘D’ scenario as shown in Figure 3.40).

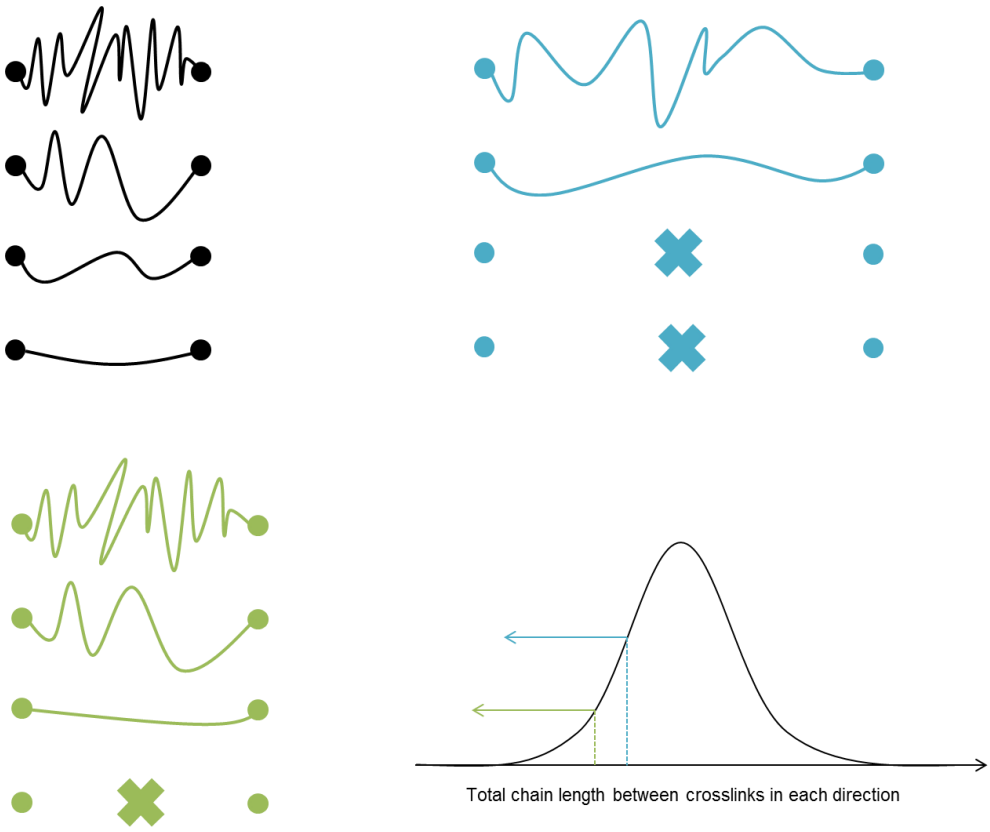

Figure 3.44 Chain length (lines) distributions between cross-links (dots) for initially isotropic samples (black) and samples under increasing strain (green and blue). The bottom right image indicates that as the strain increases, the proportion of failed cross-links in the distribution also increases

As shown in Figure 3.41, the boundary is caused by slipping and sticking of the pellet during hot pressing. By using a PTFE interface the friction between the press and the pellet was reduced. The cross-polarized light image (Figure 3.34) showed that by lowering the friction (using a PTFE interface), the boundary was no longer observed. Instead regions of strain were random across the sample surface. It is possible that these regions were caused, either by an instability in the direction of the hot press (which would result in non-unixial pressing), or by inhomogeneity on the sample surface (which could cause localised regions of slip and stick). The microhardness tests (Figure 3.38) also showed a random distribution, with an average of 101.5HK (±34.7HK), indicating that there is no slip-stick boundary present in this case.

The above discussion therefore supports the presence of a boundary created which defines one region which is slipping and one region which is sticking. It is possible to predict the observed boundary position by using von Mises criteria for yield in plain strain, in uniaxial compression.

Figure 3.45 and Figure 3.46 show the free body diagram of sticking and slipping respectively. The derivation for the following equations can be found in the appendix. R is the total disc radius, r is the distance from the centre to the boundary edge, h is the height of the sample, P is the stress applied during hot pressing, K is the yield stress in pure shear and Y is the yield strength of the disc.

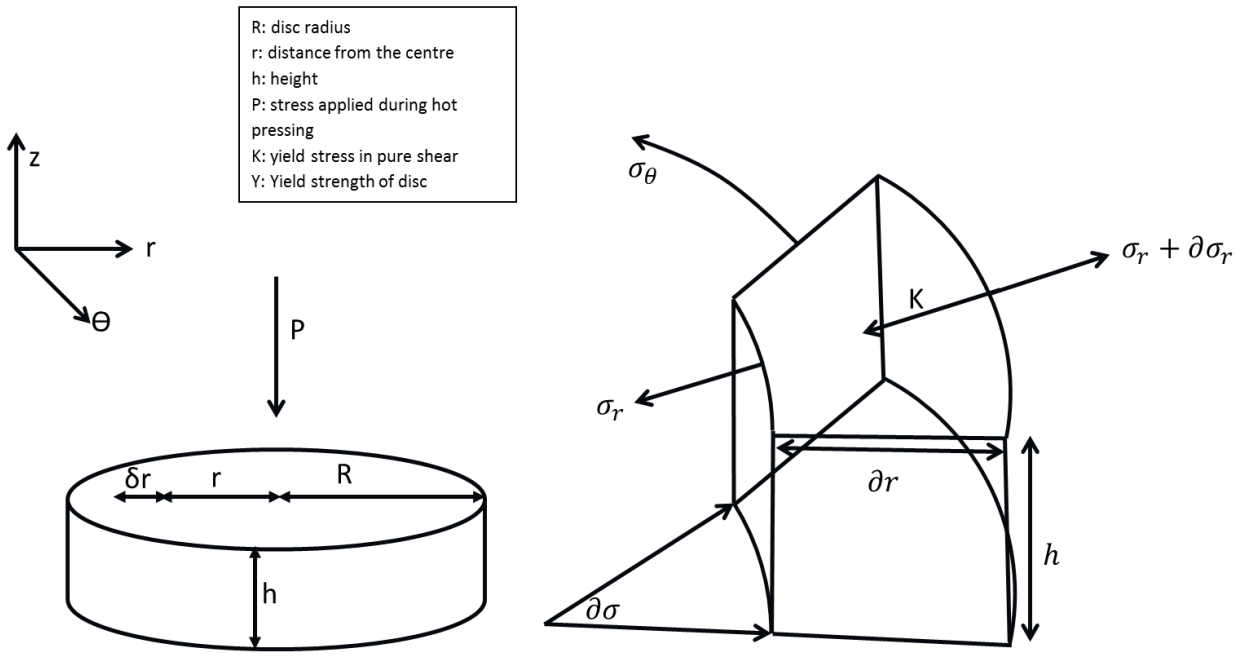

Figure 3.45 A schematic showing disc during hot pressing under sticking conditions with a free body diagram

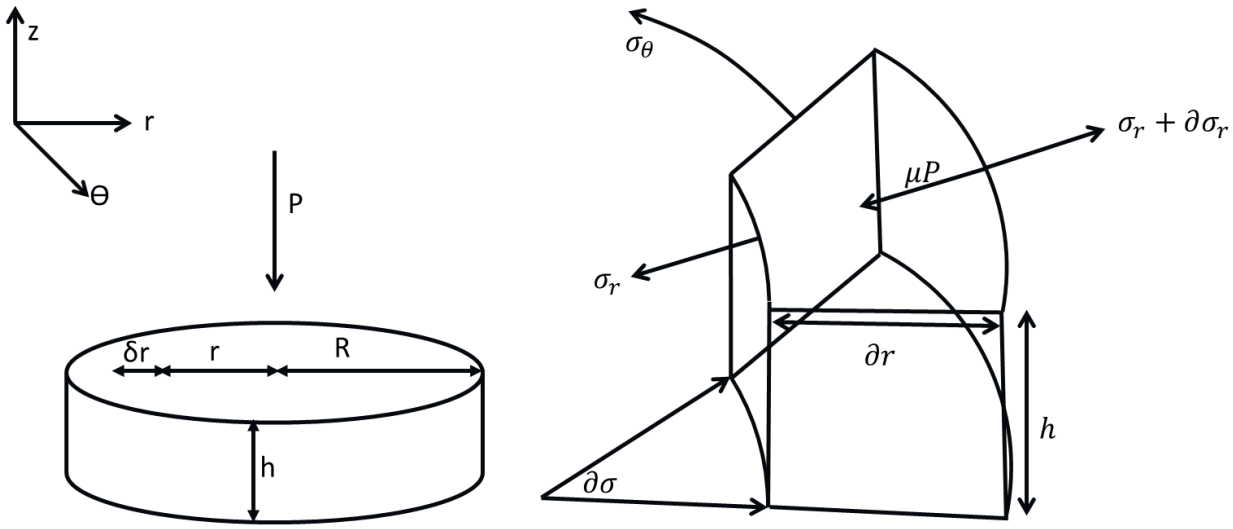

Figure 3.46 A schematic showing disc during hot pressing under slipping conditions with a free body diagram

Equation 3.7 outlines the conditions under which sticking occurs, where axi-symmetric pressing is assumed. (As shown in the appendix the boundary conditions of P and Y, and R and r are used to reach this equation).

$$P = Y + \frac{2Y}{\sqrt{3}h}(R - r)$$

Equation 3.7

Equation 3.8 outlines the conditions under which slipping occurs, where where axi-symmetric pressing is assumed. (As shown in the appendix) the boundary conditions $r = R, \quad \sigma_r = 0$ and $P = Y$ are used to reach this equation).

$$P = Yexp[\frac{2\mu}{h}(R - r)]$$

Equation 3.8

Combining Equation 3.7 and Equation 3.8 gives Equation 3.9, which defines the intersection between slipping and sticking. Rearranging Equation 3.9 for constant friction (μ) gives Equation 3.10. Equation 3.9 and Equation 3.10 can be used to predict the boundary size of a

sample pressed with different interfacial frictions, or to predict the friction between the sample and the interface in cases where a clear boundary is observed.

$$Y + \frac{2Y}{h\sqrt{3}}(R - r) = Yexp\left[\frac{2\mu}{h}(R - r)\right]$$

Equation 3.9

$$\mu = \frac{h}{2(R - r)} log\left[\frac{2}{h\sqrt{3}}(R - r)\right]$$

Equation 3.10

Equation 3.10 gives the values of μ of 0.083 (using values of R=13 and r=5) for aluminium, and μ of 0.067 for PTFE (using values of R=13 and r=0). As expected the coefficient of friction between P(MMA-co-NVP) and PTFE is lower than that of P(MMA-co-NVP) and aluminium. The coefficient of friction between aluminium and PTFE is 0.42, and between PTFE and PTFE is 0.04 (161), the values for the coefficient of friction between hydrogels are reported to be between 0.02-0.1 (162,163). The values found are therefore reasonable compared to the literature.

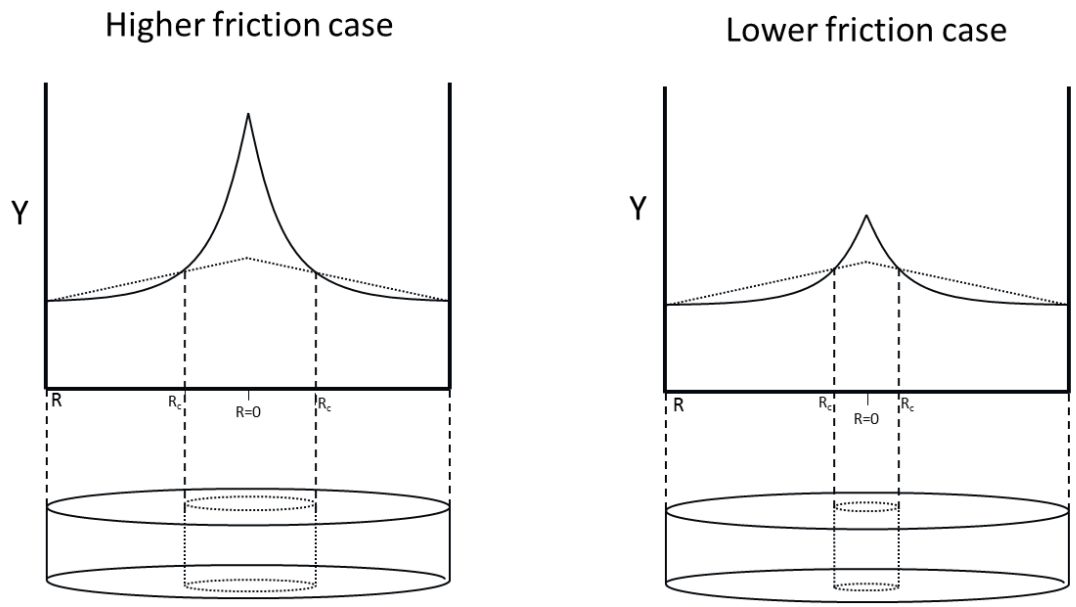

Figure 3.47 A schematic illustrating the effect of a change in the co-efficient of friction on the disc

Figure 3.47 shows a schematic of this combined effect. Between the edge and R_c deformation has occurred through slipping. Between R_c and the center deformation has occurred through sticking. By comparison of the two cases, it can be seen that as the coefficient of friction between the disc and the surface reduces, so does R_c.

3.4.2 Non-prismatic shapes

The finding that compressed samples expand to a reference state (Figure 3.39) means that (so long as critical damage does not occur during pressing) samples with a non-prismatic structure can be compressed into a disc which will expand anisotropically into the non-prismatic structure again. This is shown in Figure 3.30 and Figure 3.31. It has been shown that the final swelling geometry of a wedge and dome, which has been compressed, retains the same ratio dimensions as the initial pellet; as seen in Figure 3.31 and Figure 3.32.

Figure 3.35 showed the birefringence for domes and wedges, which can be compared to those of cylinders. The general form of the pattern produced by a compressed dome is comparable to that produced by a compressed cylinder; an outer annulus of concentric fringes, reflective of the slip/stick behaviour discussed above. However the ratio of the central radius to the total radius (r/R) for a dome (max height 12mm) is 0.57, compared to

0.5 for a cylinder (max height 12mm, compression ratio $C = 3$)- indicating that a greater proportion of the top surface has deformed through slip during compression in domes compared to cylinders. This can be understood by considering Figure 3.48. The semi-circle in part A represents the domed surface. In part B a slice of this is shown broken down into discs of uniform height ∂h. The ratio of slip to stick in each of these discs is assumed be constant, and it is assumed that each thickness can be considered independent of those above and below. Red indicates a region in stick, and blue indicates a region in slip. The final disc would have the same diameter as the cylindrical sample. The sum of these is considered schematically in part C. Figure 3.49 shows the original birefringence image for the dome with the regions of slip and stick (at the surface) marked.

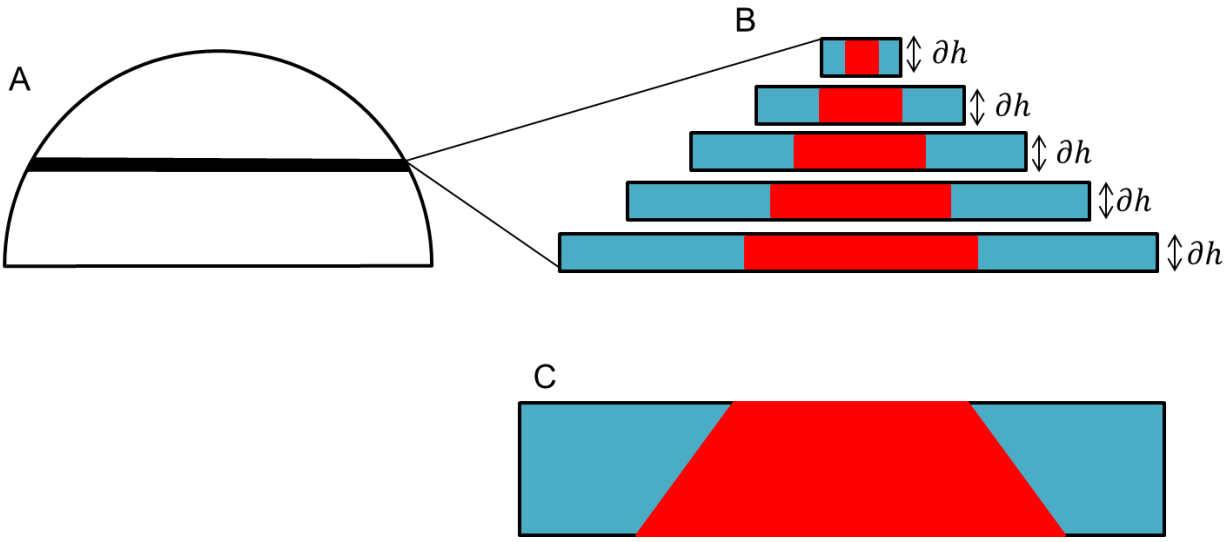

Figure 3.48 A schematic of how the slip stick interface changes for domed samples

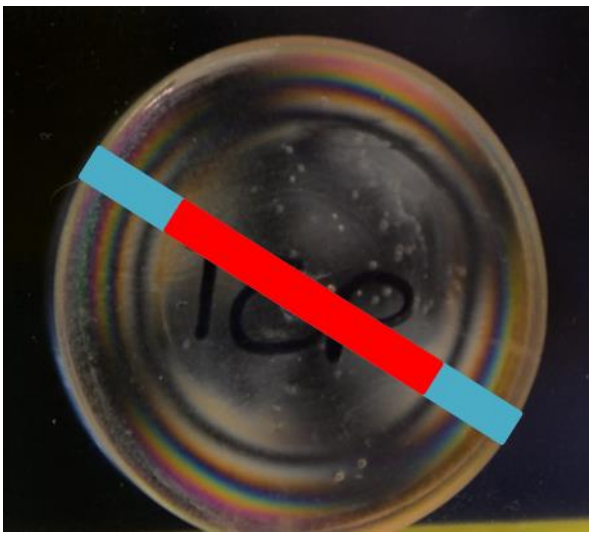

Figure 3.49 Cross-polarization photograph of domed sample, with regions of slip and stick marked

A similar process can be used to explain the horseshoe fringe lines observed for the wedge samples. For the thickest region of fringes, the ratio of slip to stick is 0.4 and the narrowest end is 0.8. Figure 3.50, part A shows the wedge simplified to a right angled triangle. In part B a slice of this triangle is broken into discs of uniform height ∂h. Again, the ratio of slipped to stuck for each cylinder is assumed to be constant, with minimal interaction between layers, part C showing the schematic summation of this. This finding is supported by the fact that the lower side of the device expands with the bulging annulus in a circle, as observed for cylindrical samples. This form is reflected in the cross-polarization images, where the slip-stick surface has been marked on in Figure 3.51.

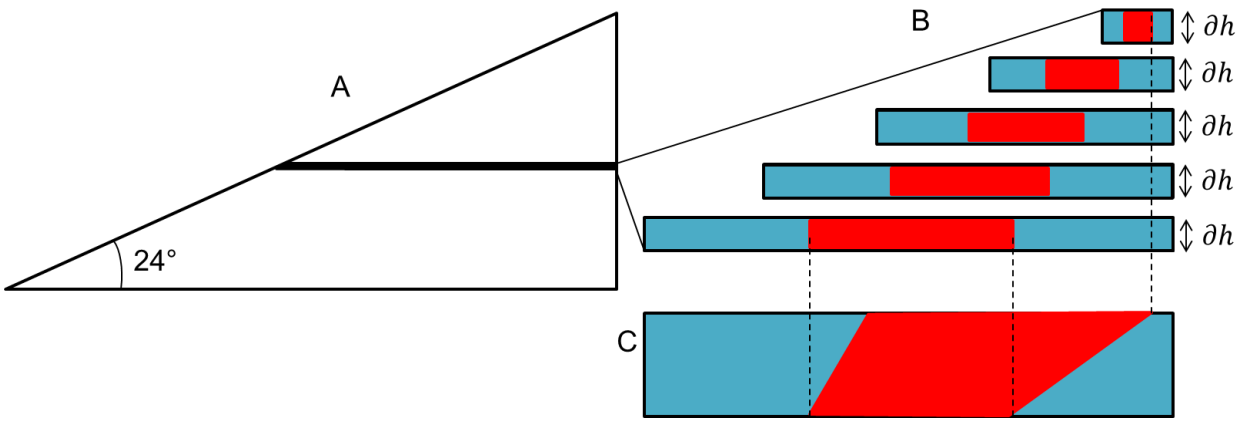

Figure 3.50 A schematic of how the slip stick interface changes for wedged samples

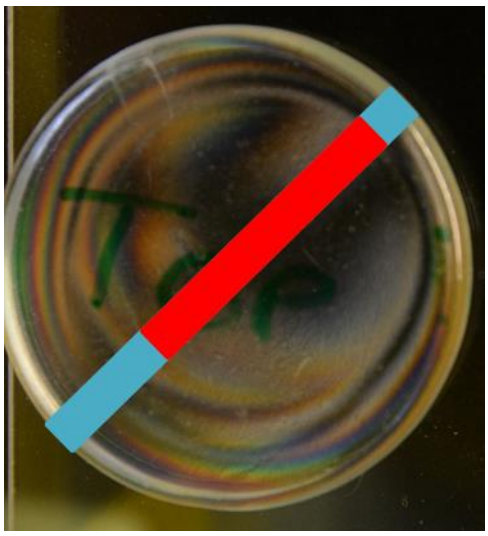

Figure 3.51 Cross-polarization photograph of wedged sample, with regions of slip and stick marked

3.5 Summary

This chapter has investigated the first four research questions posed in the introduction. A summary of the results and implications will be outlined within this section:

RQ1) What are the manufacturing limits to developing reliable, anisotropically expanding P(MMA-co-NVP) for use as tissue expanders?

It was found that for samples with initial heights 1mm, 3mm, 6mm and 12mm, compression ratios of 1, 1-3, 1-6 and 1-4 respectively could be successfully manufactured (with no visible damage to the sample). However, this was reduced to 1-1.5, 1-3 and 1-3 when considering samples which could be both reliably manufactured and reliably swollen to equilibrium. When samples failed, both in the press and during swelling, cracks originated from the circumference of the sample and propagated towards the sample center.

RQ2) Why do compressed cylinders of P(MMA-co-NVP) show anisotropic swelling?

The swelling behaviour of samples with different initial heights and compression ratios was compared. It was found that when the compression ratio is held constant, and the initial heights are varied (e.g. $C = 1$ for initial heights 3mm, 6mm and 12mm), the equilibrium percentage change in height, diameter and mass is constant. If the average of these values

is plotted against compression ratio, there is a strong linear ($R^2 = 0.9987$) relationship between the compression ratio and the equilibrium percentage change in height. There is also a linear relationship between the compression ratio and the equilibrium percentage change in diameter ($R^2 = 0.8826$). The equilibrium percentage change in mass was constant across both compression ratio and initial height. However, when the absolute changes in dimensions were considered, it was then found that if the initial height of the sample is fixed, the absolute final height and diameter will be the same regardless of compression ratio. This means that the samples which have been compressed are returning to the same expanded geometry as the sample which had not been compressed. The anisotropy that has been observed is the result of the diameter of the compressed gel, approaching that of the diameter of the swollen (uncompressed) gel. The compressed gel will expand to the swollen (uncompressed) gel dimensions, and therefore very little change in diameter will be observed. It follows that if significant damage occurs during the hot pressing process, expansion to equilibrium will not occur. It is likely that this is the constraint on the maximum possible compression ratio, and possible resolutions will be discussed in Chapter 8.

RQ3) What is the effect of the hot pressing process on the P(MMA-co-NVP) polymer network?

It has been shown that by considering the geometry of the swollen device, and combining it with the finding that samples will return to a ‘reference swollen state’, there is movement of the surfaces during compression. It is proposed that an explanation of this is as follows: during compression, the top and bottom surfaces remain static, and large portions of the side surfaces slip to become the top surface of the compressed gel. On expansion of compressed gels, this top surface (which was initially a side surface) moves back to its original position as a side surface. In doing so, a number of distinctive swelling geometries occur (such as a bulging annulus at the final side-edge boundary).

A hypothesis about how the polymer was moving in the melt was proposed. This was then tested by modelling the technique using a slip-stick boundary, and comparing samples hot

pressed with lower (PTFE) and higher (aluminium) friction interfaces. The compression was then modelled using von Mises criteria for yield in plain strain in uniaxial compression. It was shown that samples pressed with aluminium exhibited residual strain which increased radially from an region approximately 4-5mm from the sample edge (cross-polarized light microscopy) and a reduction in hardness within this 4-5mm outer annulus. It is proposed that the increased strain in this region caused failure of the cross-links, which in turn resulted in lower hardness. On the other hand, samples which were pressed with a PTFE interface showed random residual strain, and a large range of hardness values. It could be that when the top surface does not stick during the compression processing, there are a number of competing mechanisms for compression (e.g. the stability of the hot press) creating unpredictable sample properties. Within all other work presented in this thesis, samples were pressed with an aluminium interface in order to maximise predictability.

RQ4) How can devices be designed so that they expand from a disc into a non-prismatic shape?

The finding that compressed samples will return to the same dimensions of the swollen $C = 1$ sample created an opportunity to answer the fourth research question posed in the introduction. Samples were machined into domes and wedges, and their expansion was compared to that of a cylinder. These samples were all successfully swollen to equilibrium. The effect of hot pressing on these samples was considered, and supported by cross-polarized light images. These samples may offer considerable surgical scope and will be discussed further in Chapter 6 and Chapter 8.

These findings give us a greatly improved understanding of how the compression moulding process affects the swelling behaviour of samples. As devices are to be used for medical applications, it is essential that the effects of γ-irradiation (required to sterilise devices) on the swelling behaviour are properly understood.

CHAPTER 4:

Processing a Viable Tissue Expander

4 Processing a Viable Tissue Expander Using P(MMA-co-NVP)

4.1 Introduction

This chapter aims to answer the following research questions posed in section 2.3:

RQ 5) What is the effect of γ-irradiation on P(MMA-co-NVP)?

RQ 6) What is the effect of residual molecules in the P(MMA-co-NVP), and how does removing these residual molecules affect the results of RQ5?

In order to answer these questions, samples with different processing routes were compared, including; not-washed samples, with and without γ-irradiation; different methods of washing samples (non-irradiated); and samples which have been washed and γ-irradiated. To determine the effect of γ-irradiation on not-washed samples, swelling measurements and photographs, ultra-violet–visible spectroscopy and thermogravimetric analysis were used. To establish whether it is possible to remove residual molecules swelling measurements and photographs, thermogravimetric analysis, cross-polarized light microscopy and differential scanning calorimetry were used. Finally, to determine whether removing residual molecules changes the effect of γ-irradiation on samples, swelling measurements and photographs, ultra-violet–visible spectroscopy and thermogravimetric analysis were used.

This chapter is focussed on cylindrical samples. Shaped samples will be discussed in Chapter 6.

4.2 Experimental Methods

Unless otherwise stated, pellets and compressed samples were made as described in section 3.2. Similarly, swelling measurements, cross-polarized microscopy, statistical

analysis and photography were conducted as described in sections 3.2.3, 3.2.4 and 3.2.6 respectively.

4.2.1 Exposure to γ-irradiation

In order to assess the effects of γ-irradiation on the swelling properties of samples, devices were sent to Swann Morton Ltd (contract product irradiation using γ-irradiation from a Cobalt 60 source) and subjected to γ-irradiation of dosage 25kGy. This is equivalent to that required to sterilize medical devices (137).

4.2.2 Washing

As-received samples were washed in excess distilled water at 21°C in an attempt to remove any possible residual monomers, cross-link agent, or initiator. Table 4.1 summarises the three methods used to wash samples, and the three methods used to dry samples, giving a total of nine methods.

In order to minimise the difference in uptake during swelling, samples were sectioned into pellets after swelling. This was achieved by marking on the desired length prior to expansion, and sectioning into pellets of this size with a razor. For example, to make a sample with an initial height of 6mm, a 6mm length was marked on to the sample prior to swelling and on expansion the swollen rod was cut on this marker.

Table 4.1 Summary of washing and drying methods used in sample preparation

Washing Acronym	Washing Method	Drying Method Name	Drying Method
m1	24 hours in distilled water at 21°C	d1	16 hours in oven at 80°C
m2	72 hours in distilled water at 21°C	d2	72 hours air dried, 16 hours in oven at 80°C
m3	One week in distilled water at 21°C	d3	Two weeks air dried, 16 hours in oven at 80°C

4.2.3 Thermogravimetric Analysis

Thermogravimetric Analysis (Discovery TGA, TA Instruments) was used to measure the percentage change in sample mass as a function of temperature. The instrument heats samples using a temperature-controlled thermo-balance which is isolated from the furnace. The change of mass during heating can be caused by loss of volatiles, polymer decomposition, or sample oxidation. Powdered samples (15mg) were loaded into pans, and heated from 50˚C to 600˚C at a rate of 10˚C per minute. A minimum of three samples per condition were used. Samples prepared with each different washing technique were compared to not-washed samples and to each other. Subsequently, samples washed with m2d2 technique, and not-washed samples, were compared with and without exposure to γ-irradiation, and with and without heat treatment. Results were analysed using TRIOS software (TA Instruments).

4.2.4 Differential Scanning Calorimetry

Differential Scanning Calorimetry (Discovery DSC, TA Instruments) was used to determine points of thermal transition in a sample. A reference pan, containing Indium, and a pan containing the sample were heated at the same rate, and by comparing the difference in power required to heat the two pans, the specific heat capacity of the sample, and any thermal transitions can be identified. Washed (using m2d2), and not-washed, with and without γ-irradiation exposure, were compared. Powdered samples of 15mg were prepared in a ball mill (Retsch PM100), and stored in a vacuum for 24 hours before analysis (to try to eliminate any remaining water content). Samples were heated from 10˚C to 500˚C at a rate of 10˚C per minute, in a platinum pan and in an inert Argon gas environment. Three samples were used for each condition. TRIOS (TA Instruments) software was used to analyse the results.

4.2.5 Ultra-Violet – Visible Spectroscopy

Ultra-Violet – Visible Spectroscopy, UV-VIS, is used to analyse the absorption behaviour of samples, and therefore better understand the electron arrangement and bonding in the

sample. Two beams are passed through a series of diffraction grids and mirrors. One beam is passed through the sample. The intensity of each beam is measured at the end I (sample beam) and I_o (reference beam). If these values are equal, then there is no absorption by the sample within the UV-VIS range.

UV-VIS (NIR 570) was used to compare not-washed samples with samples washed with method m2d2, and both exposed to γ-irradiation and not exposed. Samples were analysed in the solid state, between wavelengths 250nm and 900nm.

4.2.6 Dynamic mechanical analysis (DMA)

Samples were produced from fully hydrated samples, as shown in Figure 4.1, to approximately 5mm x 6mm x 2.5mm. The samples were then stored submerged in distilled water. A DMA machine (Perkin Elmer, DMA7) was used to produce stress-strain curves by applying a linear compressive load, with maximum force of 8N and a ramp rate of 500mN/sec. The gradient of the linear portion was used to establish the modulus.

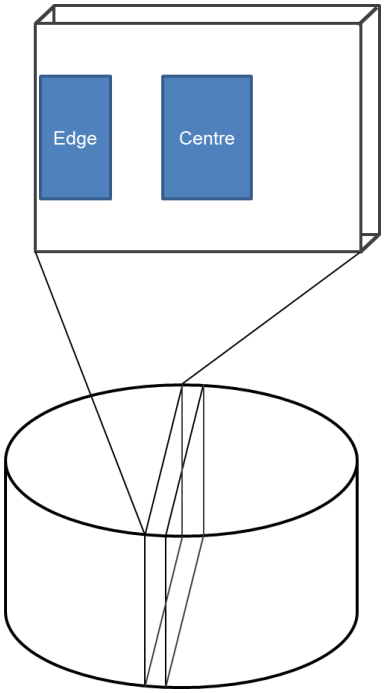

Figure 4.1 A schematic showing how the samples were sectioned for DMA. Each blue section was then further cut into different samples of size 5x6x2.5mm

4.3 Results

In this section the results are presented for each experimental procedure. For section 4.3.1 and section 4.3.2 the results have been further split into γ-irradiation, washed, and washed and γ-irradiated samples.

4.3.1 Sample production

γ-irradiated

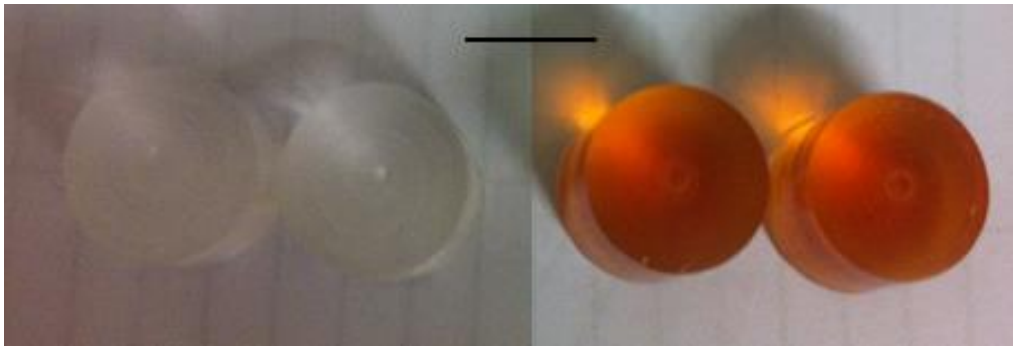

Figure 4.2 A comparison of P(MMA-co-NVP) before (left) and after (right) γ-irradiation. The scale bar represents 10mm

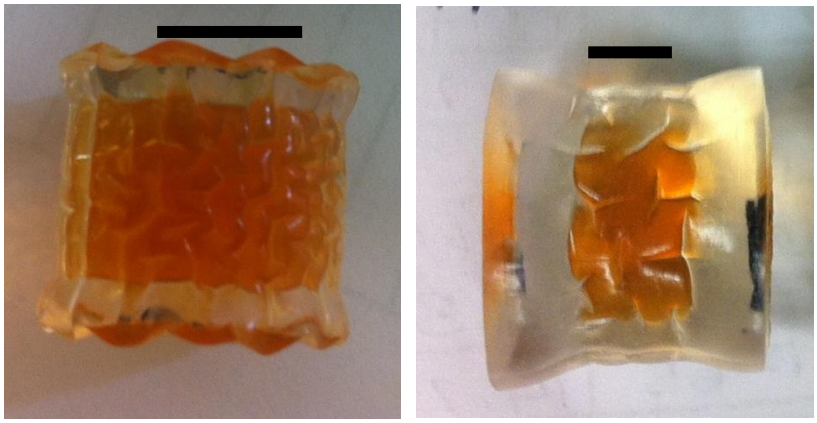

Figure 4.3 An image of the geometry and colour change during hydration for γ-irradiation samples with a compression ratio of 1. The black lines represent 10mm

Figure 4.2 compares pellets before and after γ-irradiation and clearly shows a significant colour change in the latter, which would not be tolerated clinically. The change in colour is not affected by heating the sample (up to 161℃), but as seen in Figure 4.3, during hydration the sample gradually returns to colourless. When the sample is subsequently dried, it also remains colourless, indicating that the loss of colour is genuine, rather than a reduction in intensity. The loss of colour follows the progression of the glassy front, indicating that the

coloured molecules are soluble in water. It is also important to note that the typical geometry of swelling for samples with a compression ratio of $C = 1$ is present; a wrinkled outer annulus which progresses into an hourglass shape (with concave ends) before returning to a cylindrical geometry at equilibrium expansion.

Washed samples

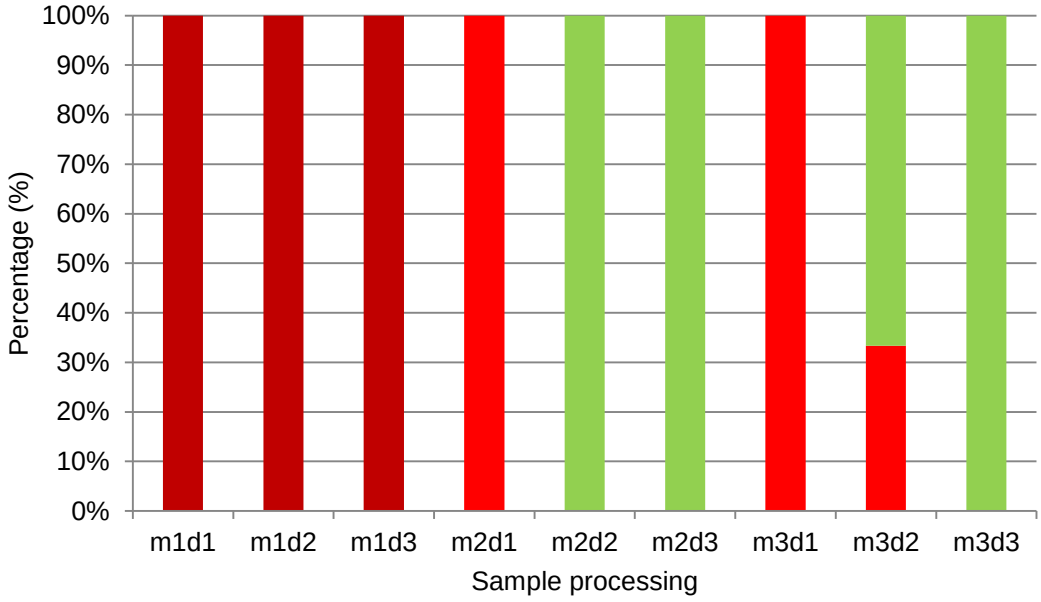

Figure 4.4 A summary of failure rates in samples washed and dried with different techniques. Dark red indicates failure during processing, bright red indicates failure during swelling, green indicates successfully swollen devices

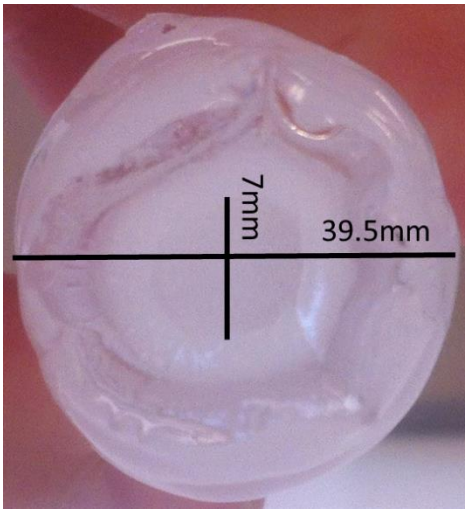

Figure 4.5 A sample swollen for 24hours with glassy polymer core and soft outer annulus

Figure 4.4 shows the failure rates for samples washed and dried for different lengths of time. Dark red indicates that samples failed during processes, bright red indicates that samples

failed during swelling, and green indicates that samples swelled to equilibrium. The samples washed for 24 hours (method M1) were unable to be processed into uniform pellets after washing, as the core was too hard to be sectioned with a razor (and the outer annulus was too soft to be cut by saw or lathe). This means that there was no way to effectively cut the sample into intact 6mm pellets. The failed hard core and soft outer annulus of samples washed over the 24hour period can be seen in Figure 4.5.

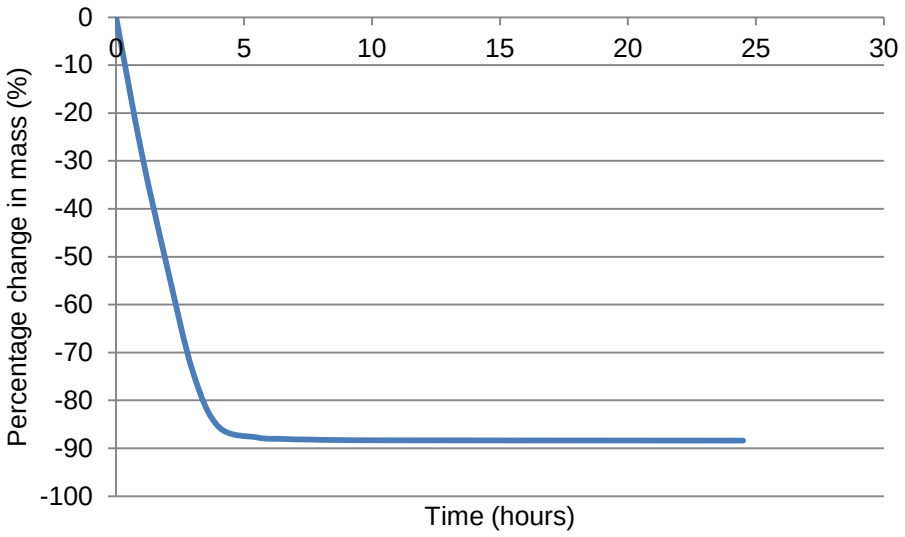

Figure 4.6 The percentage change in mass for initially hydrated samples, placed in an oven [80°C] for 24 hours

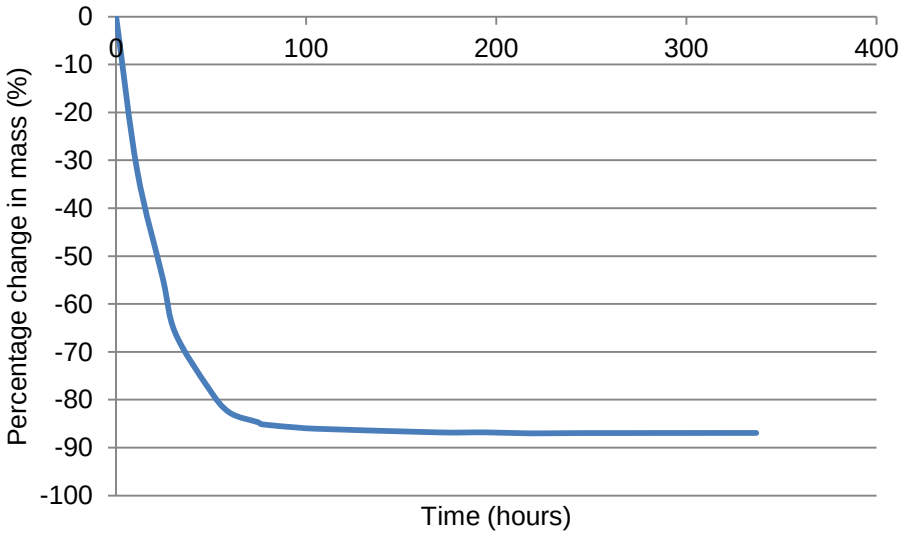

Figure 4.7 The percentage change in mass for initially hydrated samples, air dried over a two week period

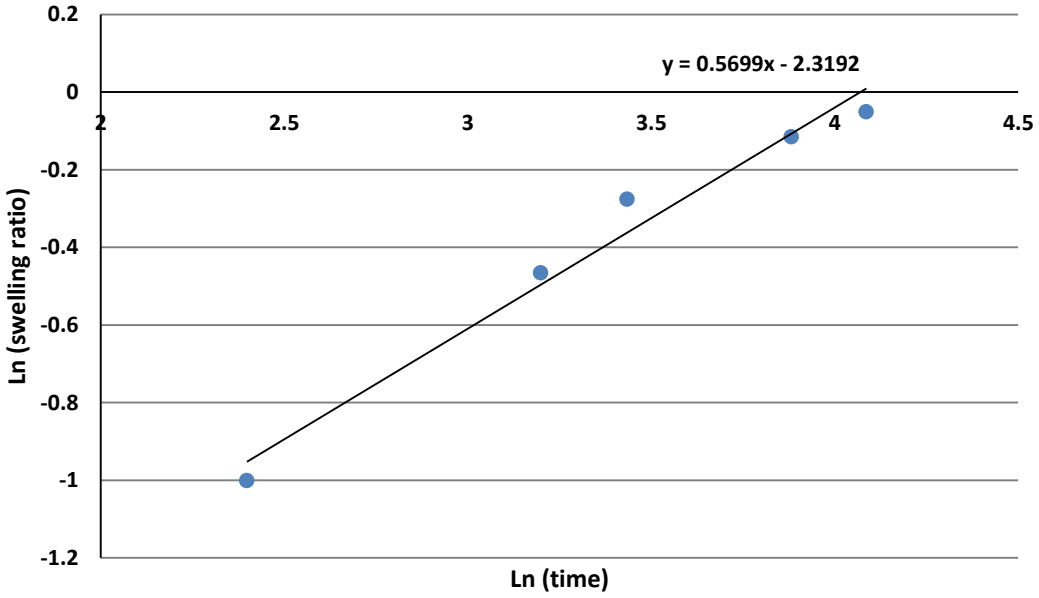

Figure 4.8 The plot used to determine the diffusion coefficient and the diffusion exponent of samples dried in the air

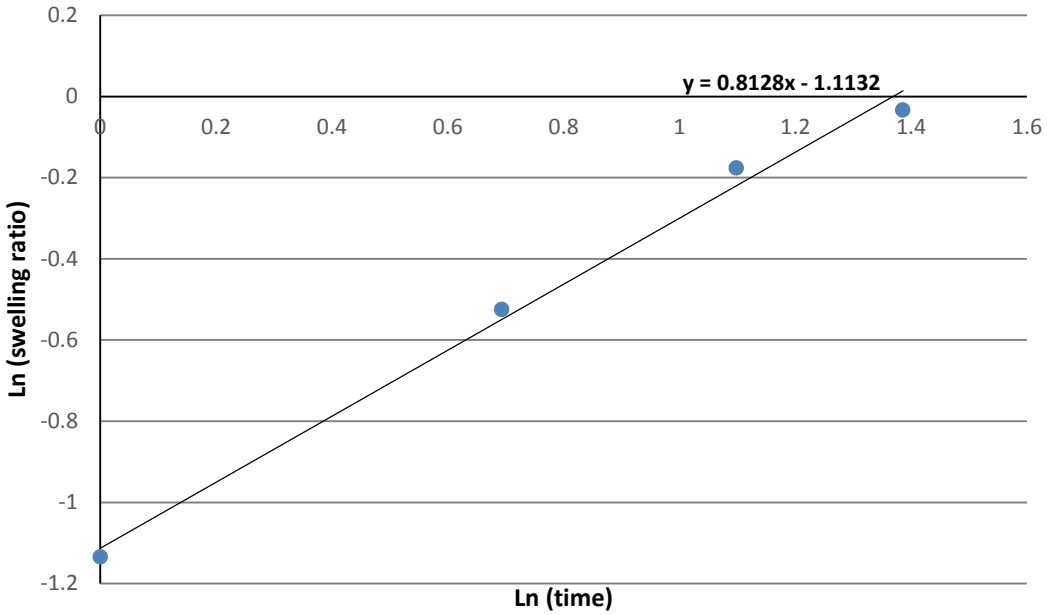

Figure 4.9 The plot used to determine the diffusion coefficient and the diffusion exponent of samples dried in the oven

Table 4.2 The Diffusion coefficients and exponents for air and oven dried samples

	Air-dried	**Oven-dried**
Diffusion exponent (n)	0.57 ± 0.05	0.81 ± 0.06
Diffusion coefficient ($m^2 s^{-1}$)	$9.1 \pm 0.3 \times 10^{-8}$	$9.1 \pm 0.4 \times 10^{-10}$

Figure 4.6 and Figure 4.7 show the percentage change in mass that occurred as samples were oven-dried and air-dried respectively. Figure 4.8 and Figure 4.9 show the log/log curves used to calculate the diffusion exponents and coefficients. The diffusion exponents and the diffusion coefficients are shown in Table 4.2. These values were calculated using equations Equation 2.20 and Equation 2.21, as described in section 2.2.3, from the first 60% of swelling time (pre-equilibrium swelling) shown in Figure 4.6 and Figure 4.7. The values appear to be constant within this range. It should be noted the swelling ratio was used in the fuller form, shown in Equation 4.1. to take into account the fact that the samples were drying, where $m_{t=0}$ is the mass of water at time $t = 0$, $m_{t=t}$ is the mass of the water at a defined time t, and m_∞ is the mass of water at equilibrium (which is 0).

$$Swelling\ ratio = \frac{m_{t=t} - m_{t=0}}{m_\infty - m_{t=0}}$$

Equation 4.1

Washed and γ-irradiated samples

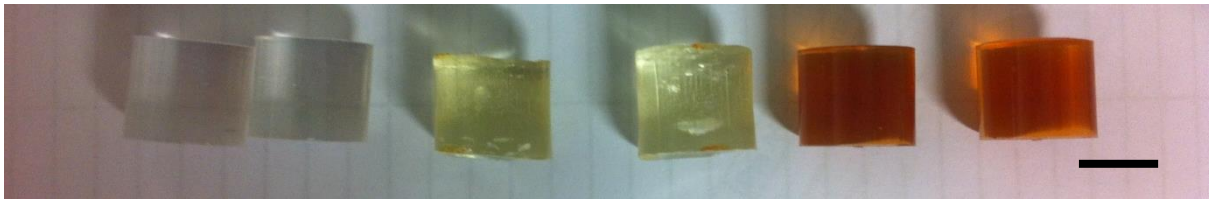

Figure 4.10 An image of pairs of samples (from left to right): 1) not-washed, and non-irradiated, 2) washed, and γ-irradiated and 3) not-washed, and γ-irradiated

Figure 4.10 compares the appearance of samples which are not-washed, not-washed and γ-irradiated, and washed and γ-irradiated. It is shown that when both washed and γ-irradiated, the red colour (seen in not-washed and γ-irradiated) does not occur. There is a very slight yellowing of the sample.

4.3.2 Swelling experiments

γ-irradiated

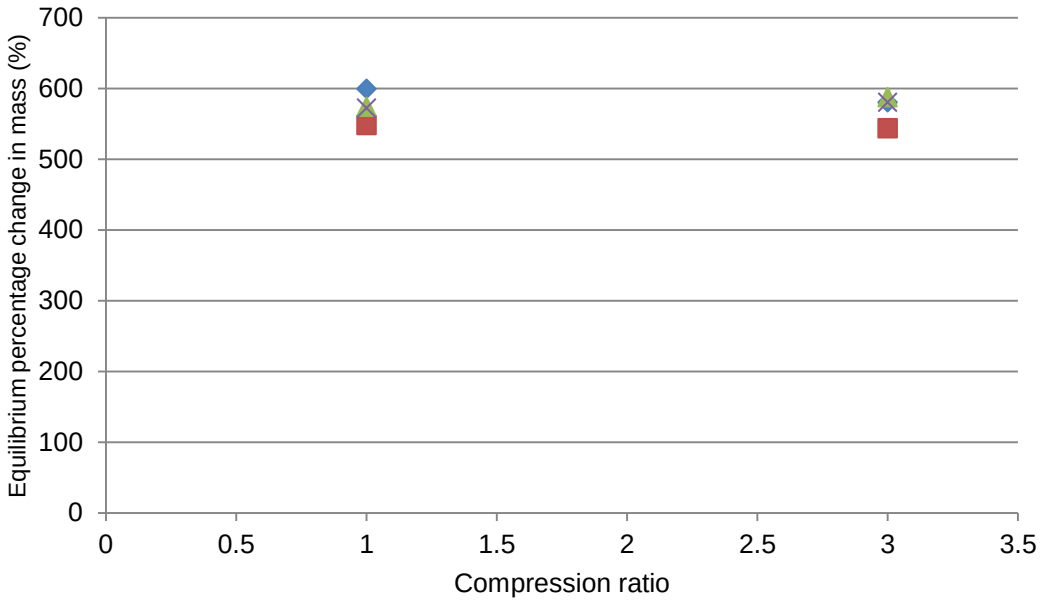

Figure 4.11 A comparison of equilibrium percentage change for samples with initial heights: Purple: $h = 12mm$, non-irradiated. Blue: $h = 12mm$, γ-irradiated. Green: $h = 6mm$, non-irradiated. Red: $h = 6mm$, γ-irradiated

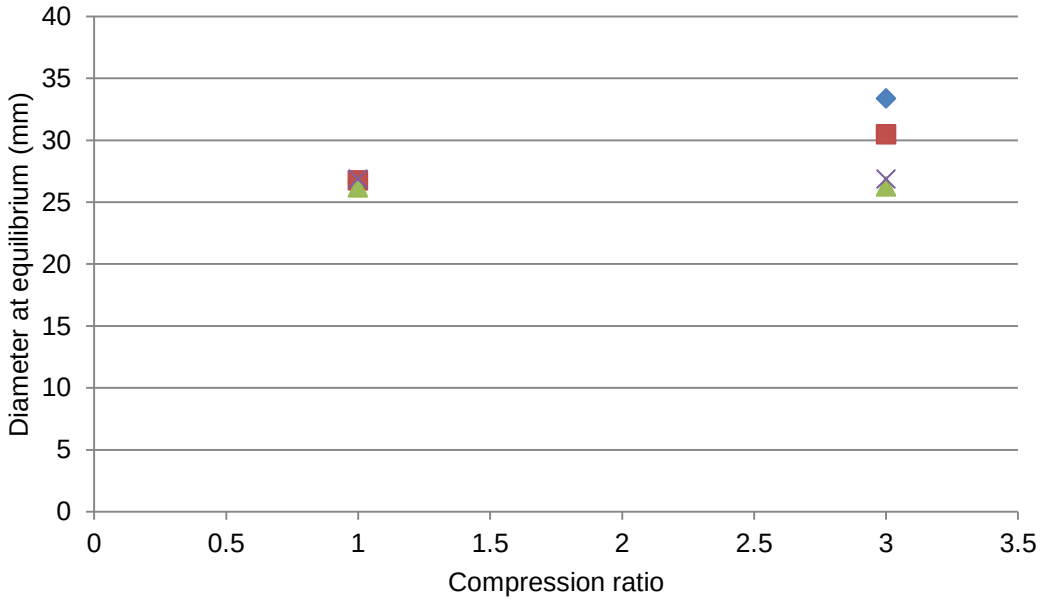

Figure 4.12 A comparison of equilibrium diameter for samples with initial heights: Purple: $h = 12mm$, non-irradiated. Blue: $h = 12mm$, γ-irradiated. Green: $h = 6mm$, non-irradiated. Red: $h = 6mm$, γ-irradiated

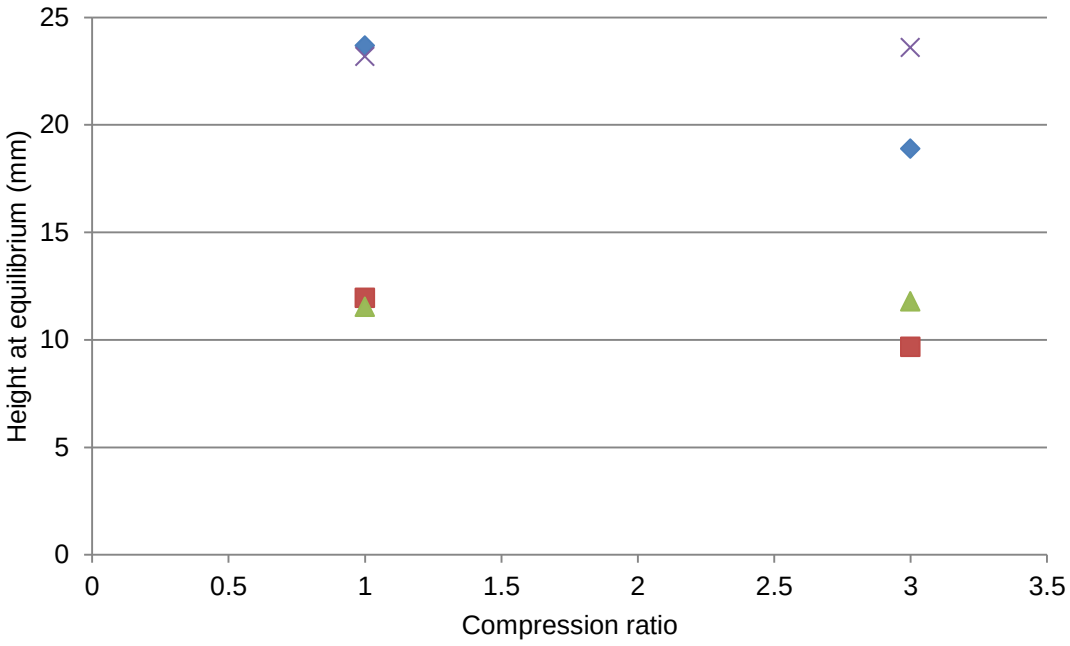

Figure 4.13 A comparison of equilibrium height for samples with initial heights: Purple: $h = 12mm$, non-irradiated. Blue: $h = 12mm$, γ-irradiated. Green: $h = 6mm$, non-irradiated. Red: $h = 6mm$, γ-irradiated

Figure 4.11 shows that there is a negligible change in the swelling mass uptake after exposure to γ-irradiation for samples with compression ratios $C = 1$ and $C = 3$. However, Figure 4.12 and Figure 4.13 show that anisotropic and isotropic samples do not exhibit the same dimensional changes after compression; γ-irradiated samples show a decrease in the equilibrium height, and an increase in the equilibrium diameter. For non-irradiated samples, anisotropic gels will return to the reference $C = 1$ dimensions after swelling, as seen in Figure 3.22.

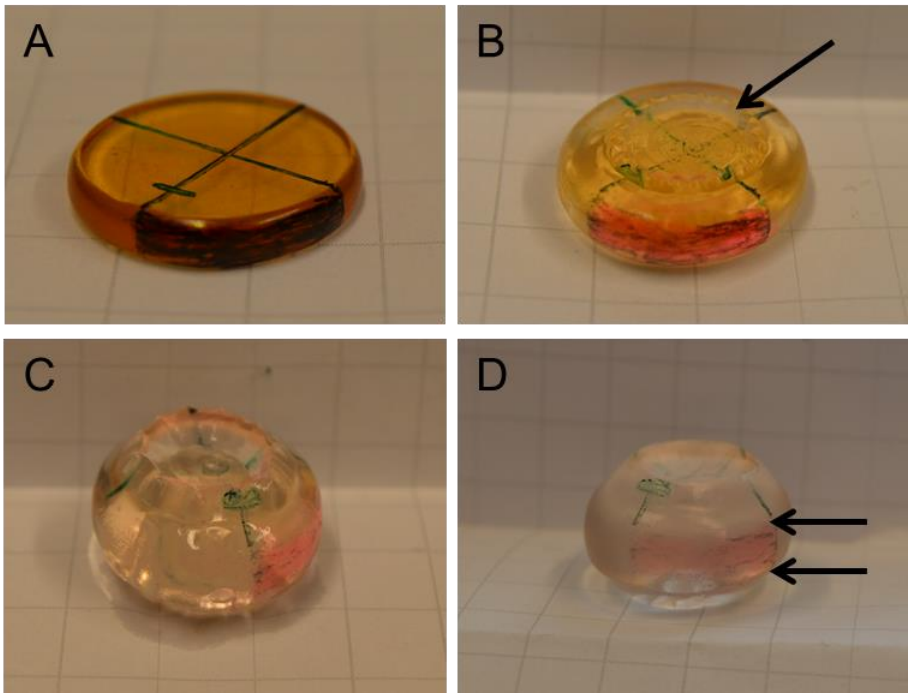

Figure 4.14 Swelling geometry of a γ-irradiated anisotropic sample, with swelling progressing from part A to part D. The sample has reached equilibrium swelling in part D. The samples are on printed graph paper of 10mm by 10mm. The arrow in part B indicates the bulging annulus, and in part D the arrows show the final position of the shaded edge section

Figure 4.14 shows the expansion geometry of an γ-irradiated sample with an initial height of 12mm and a compression ratio of 3. Part A shows the xerogel, where a grid has been marked on to the top surface, and a section of the side surface has been shaded. Additionally, a mark has been made 4mm from the sample edge to compare the slip-stick boundary with that seen in section 3.4. Part B shows that, as in non-irradiated samples, a bulging annulus appears during the initial stages of swelling. This annulus appears at the 4mm mark. As swelling progresses (part C), the geometry begins to diverge from that seen in non-irradiated samples; there is some increase in height, but the sample diameter does not reduce (as seen in non-irradiated samples in Figure 3.21). Finally, in part D of Figure 4.14, the equilibrium geometry is seen to be significantly different to that observed in non-irradiated samples (see Figure 3.28); the sample has not returned to a cylindrical shape. Instead it is barrelled with concave ends. However, one similarity is that the top surfaces have moved to the edge, as seen by the movement of the initial markings.

Washed samples

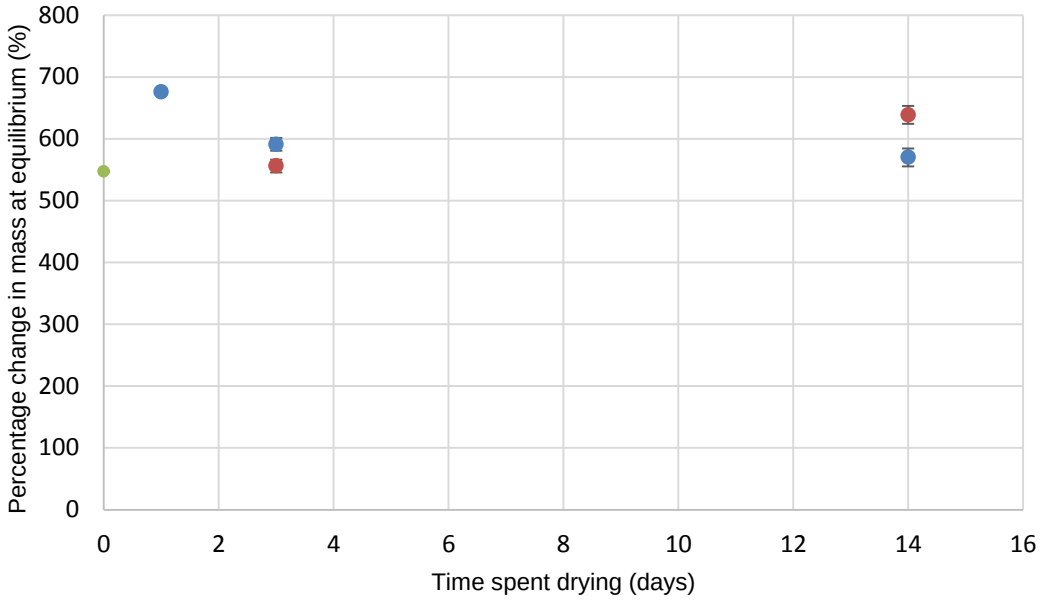

Figure 4.15 A comparison of the percentage changes in mass at equilibrium for samples processed with different washing and drying techniques. Blue: Washed for three days, Red: Washed for 14days, Green: Not-washed

Figure 4.15 compares the equilibrium percentage change in mass vs. time for samples which were washed for 0, 3 and 14 days. All samples which had been washed showed an increase in swelling uptake. It appears that when samples are washed for three days, the longer they spend drying, the lower the percentage change, whereas for samples washed for 14 days the opposite is true.

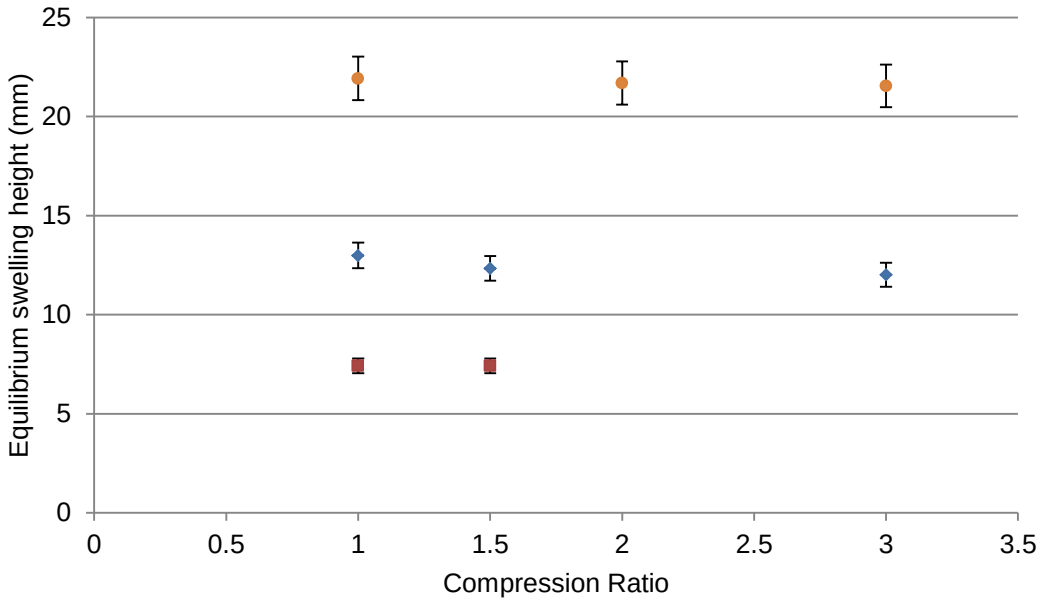

Figure 4.16 A comparison of the final heights of washed samples (m2d2) for different compression ratios, for samples with initial heights, 3 (red), 6 (blue) and 12mm (orange)

Figure 4.16 shows the final heights of washed samples with different compression ratios, for samples with a different initial height (3mm, 6mm and 12mm). For each initial height there is no statistically significant difference between the final geometries for different compression ratios, indicating that washed samples behave in the same manner as not-washed samples, as seen in section 3.3.2; after hot pressing they will return to the same geometry as a sample with $C = 1$.

When comparing these results to that of the not-washed samples, neither 6mm nor 12mm samples show a statistically significant difference in final height. However, the washed 3mm samples showed a slight increase in final swelling height compared to not-washed 3mm samples.

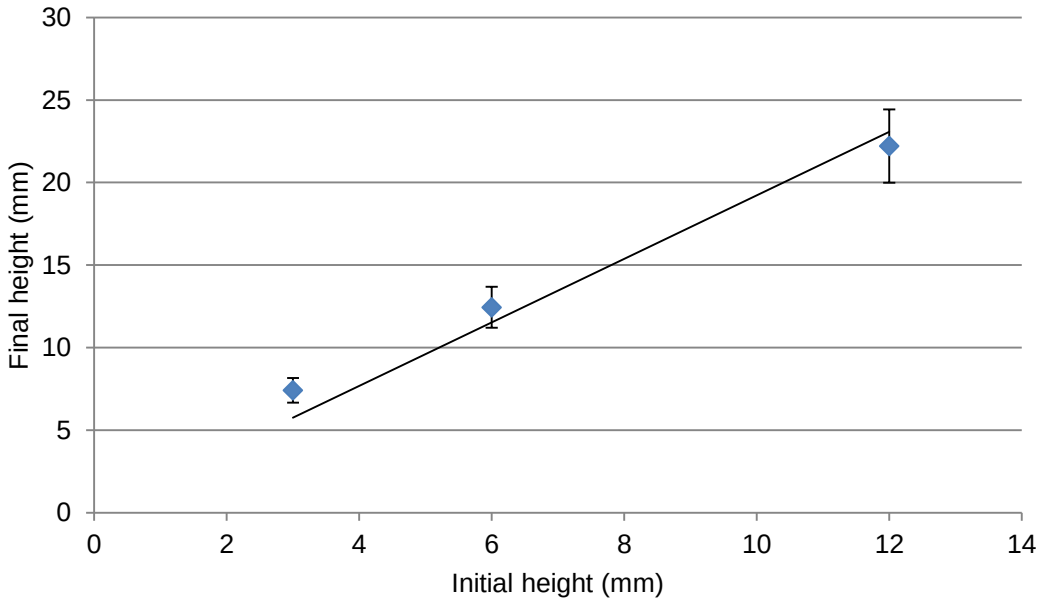

Figure 4.17 A comparison of final swelling heights of samples which have different initial heights. The values are an average of the different compression ratios. The line of best fit (plotted through (0,0) is used to calculate Equation 4.2

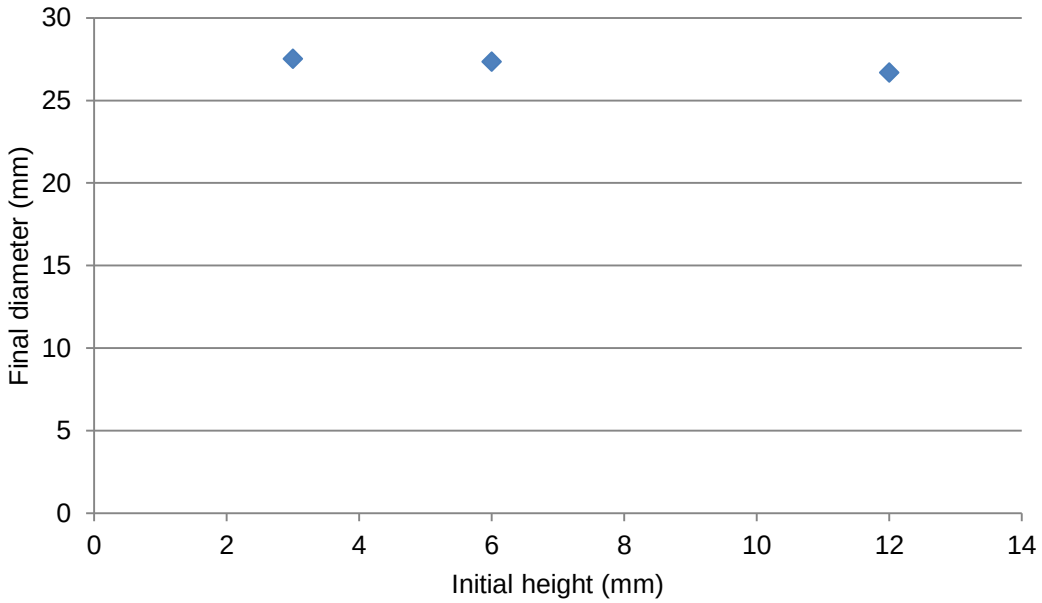

Figure 4.18 A comparison of final swelling diameters of samples with different initial heights. The values are an average of the different compression ratios

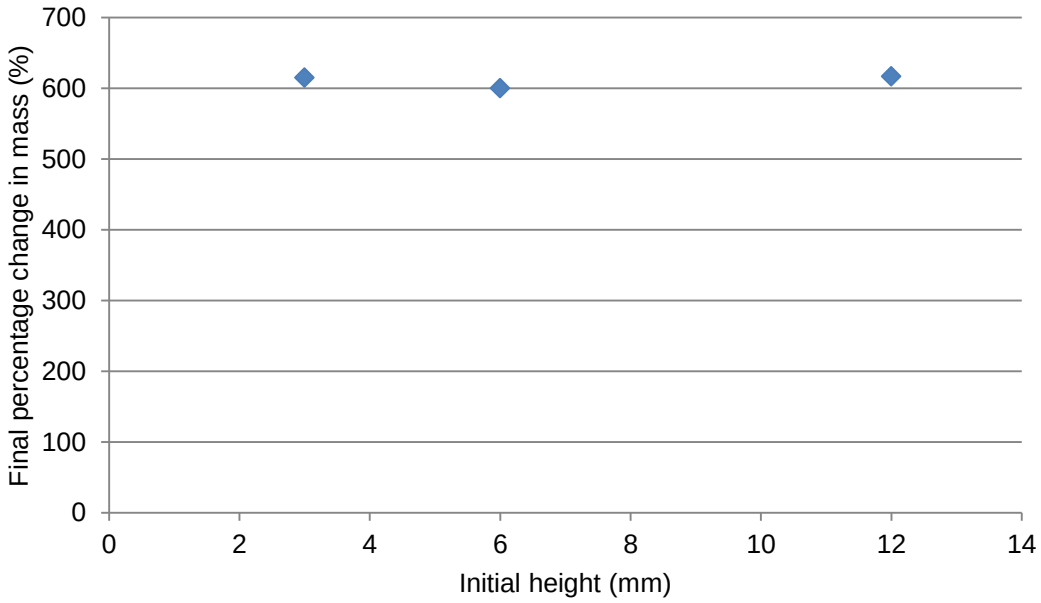

Figure 4.19 A comparison of final swelling masses of samples which have different initial heights. The values are an average of the different compression ratios

Figure 4.17 compares the final swelling heights for samples of different initial heights (using average values for each compression ratio tested. The curve follows the equation shown in Equation 4.2, with an R^2 value of 0.96, where h_i and h_s represent the initial and final heights respectively. These values are in line with those of the not-washed samples, as presented in section 3.3.2. Figure 4.18 shows that for each initial height the final diameter is constant. The values are also not statistically different (as defined in section 3.2.6) from the not-washed samples. Finally, Figure 4.19 shows that the final percentage change in mass of samples with different initial heights is the same.

$$h_s = 1.9h_i$$

Equation 4.2

Washed and γ-irradiated samples

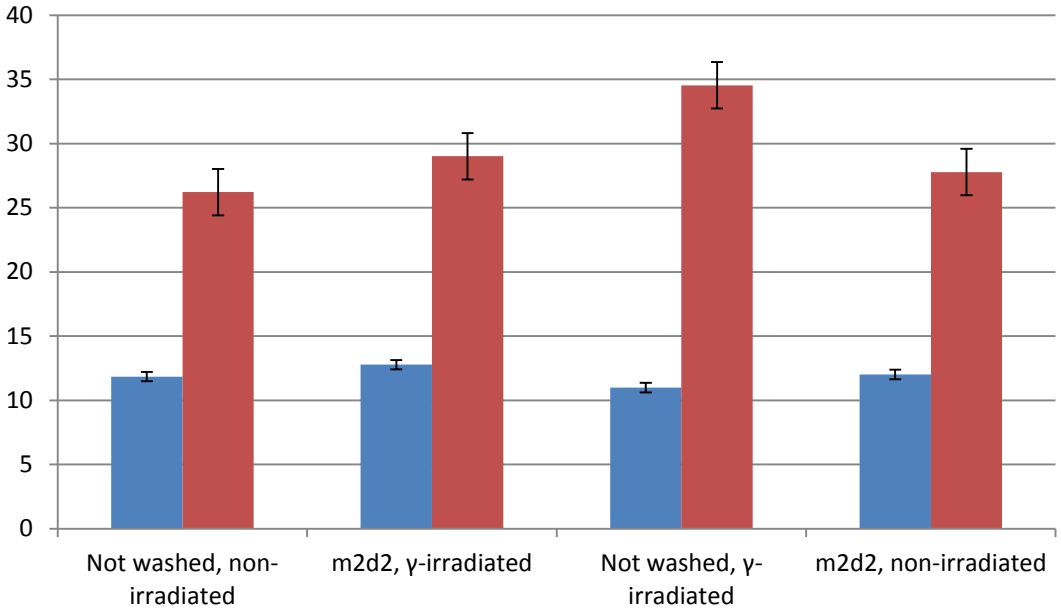

Figure 4.20 A comparison of the final heights (blue) and diameters (red) of anisotropic samples with each combination of washing and γ-irradiation. Initial sample height of 6mm and compression ratio of 3

Figure 4.20 compares the final heights and diameters for samples for each combination of washed and γ-irradiated. It shows that the loss of height and increase in diameter caused by γ-irradiation is prevented by removing the impurities before exposure to γ-irradiation.

4.3.3 Cross-polarized light microscopy

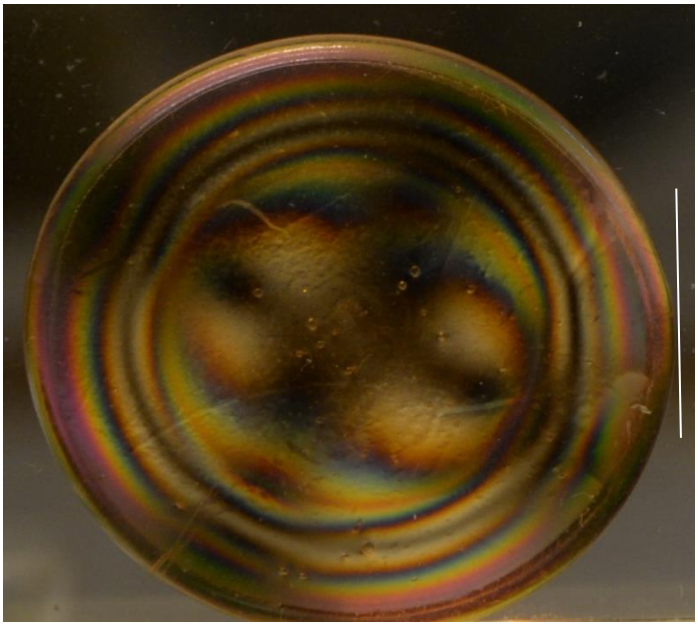

Figure 4.21 Birefringence of a γ-irradiated, anisotropic sample. The white line represents 10mm

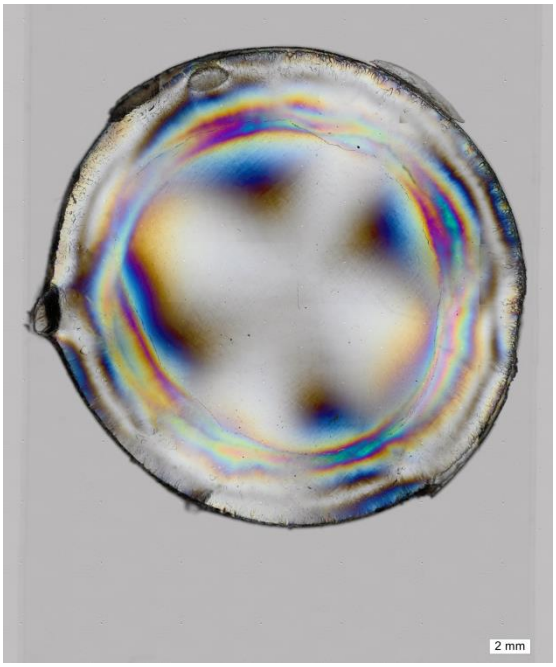

Figure 4.22 An image of a washed sample taken using cross-polarized microscopy

Figure 4.21 shows the birefringence of an γ-irradiated anisotropic sample. The sample still shows regions of radially increasing strain from a boundary approximately 5mm from the edge of the sample. Figure 4.22 shows a cross-polarised image of a washed sample which has been compressed. Again, concentric rings are observed beginning approximately 4-5mm from the sample edge.

4.3.4 Thermogravimetric Analysis

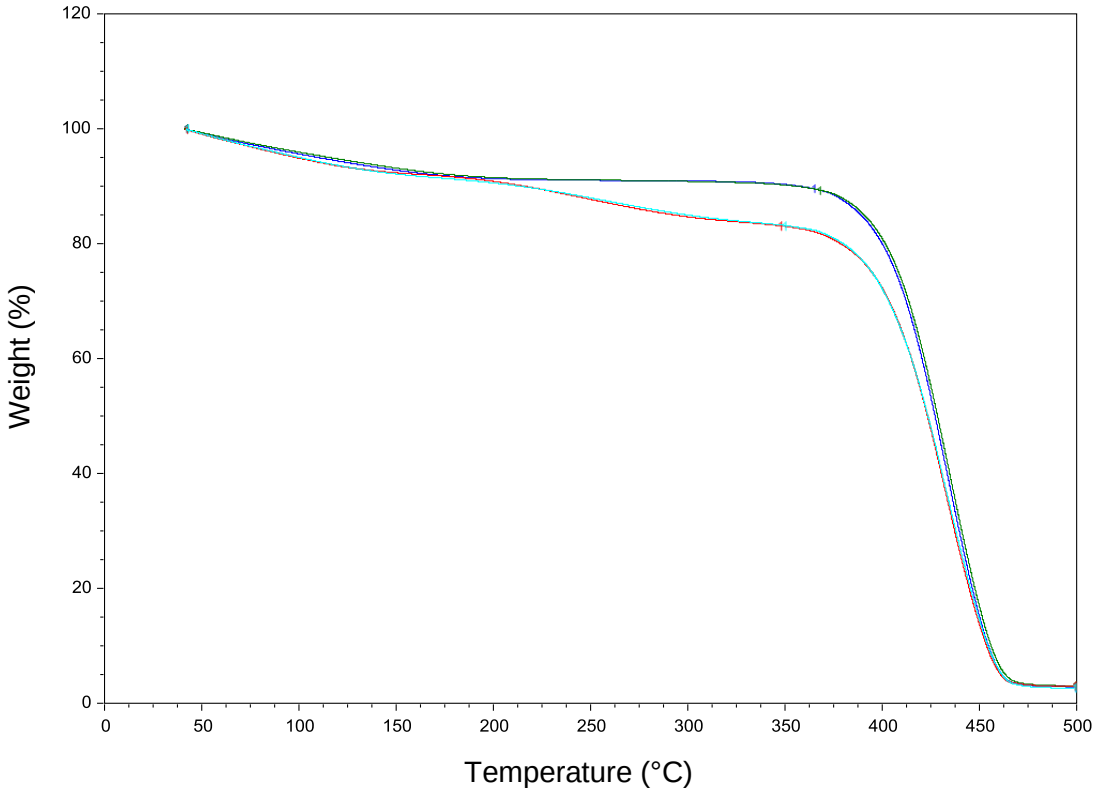

Figure 4.23 TGA spectra comparing samples before (red and turquoise) and after (blue and green) γ-irradiation

Figure 4.23 shows the TGA data for samples before and after γ-irradiation. The first 10% of mass lost can be attributed to surface water on the powdered samples (147). For samples exposed to γ-irradiation, no degradation of the polymer is observed until 400°C, the temperature at which P(MMA-co-NVP) degrades (147). Conversely, non-irradiated samples lose an additional 10% of mass between 200°C and 400°C.

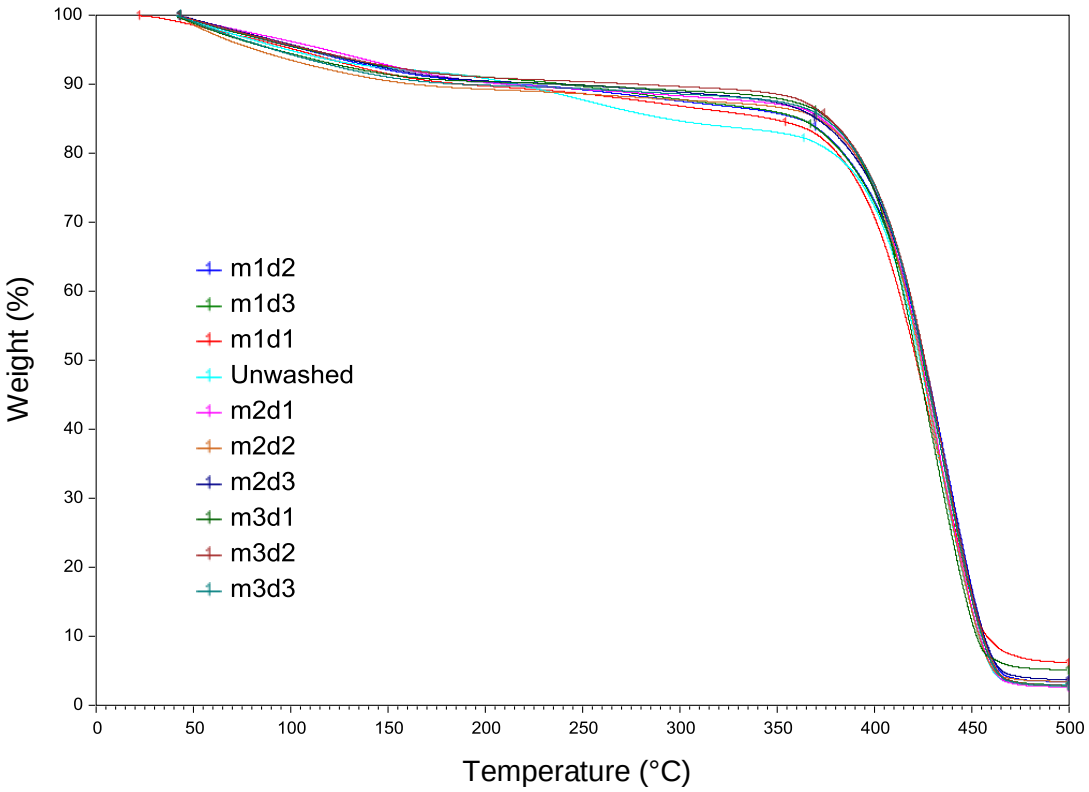

Figure 4.24 TGA analysis of samples washed with different methods with temperature between 0°C and 500°C

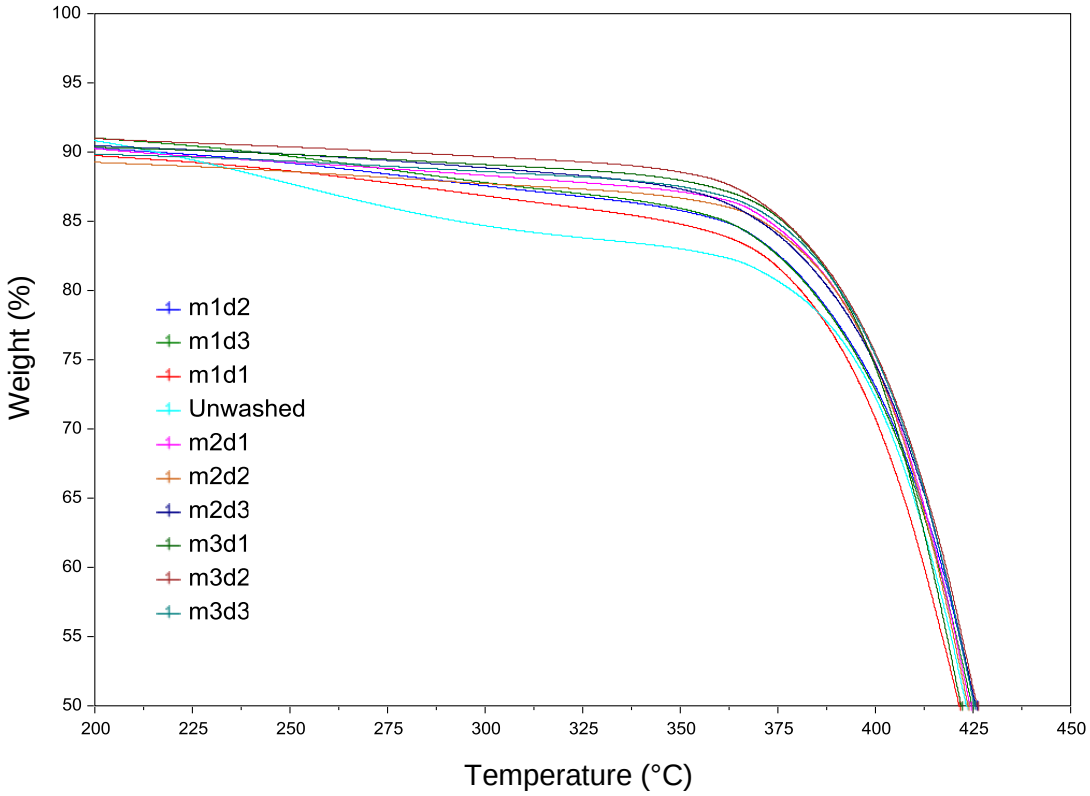

Figure 4.25 TGA analysis of samples washed with different methods, with temperature between 200°C and 450°C

Figure 4.24 and Figure 4.25 show the TGA data for samples washed and dried for different periods of time. The first 10% of mass loss is again attributed to surface water. The graphs show that the longer a sample is washed, the less degradation occurs between 200°C and

400°C. For all samples, the degradation of the bulk P(MMA-co-NVP) structure occurs at 400°C. Drying conditions are not expected to make a difference to thermal decomposition, due to the fact that samples were powdered and kept under vacuum prior to TGA analysis.

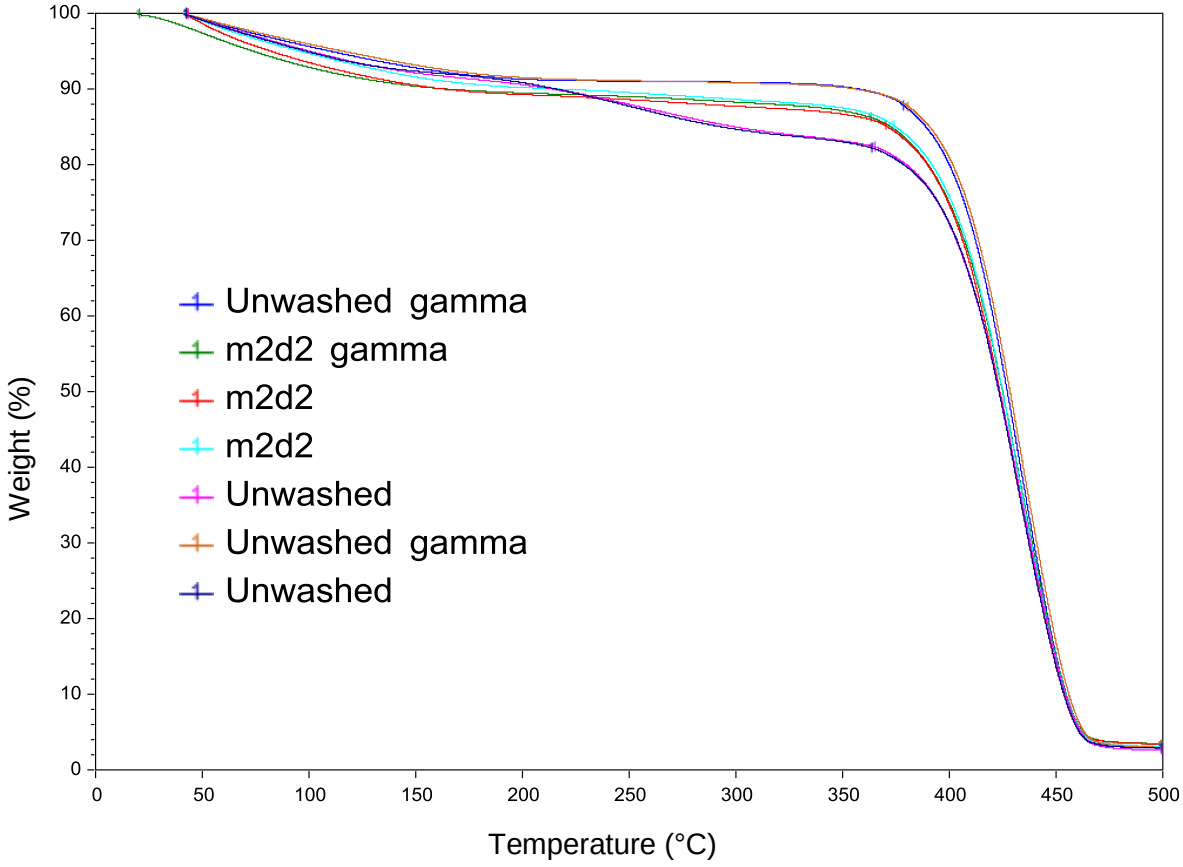

Figure 4.26 TGA curves for each combination of washed/ not-washed, and γ-irradiated / non-irradiated

Figure 4.26 shows the TGA data for all combinations of washing and γ-irradiation. This data shows that at temperatures below 200°C, washed samples (both γ-irradiated and not) lose a greater weight percentage than not-washed samples (both γ-irradiated and not). Degradation in this region is attributed to surface water, and as not-washed and washed samples were stored in identical conditions, which would remove all surface water, but were processed on separate days, differences in the humidity on the day of processing is the most likely cause of the discrepancy. However, in the region of interest (~225°C to 400°C), all washed samples are stable, confirming that the residual molecules are no longer present. Furthermore, the washed (m2d2) samples show the same degradation profile before and after γ-irradiation.

4.3.5 Differential Scanning Calorimetry

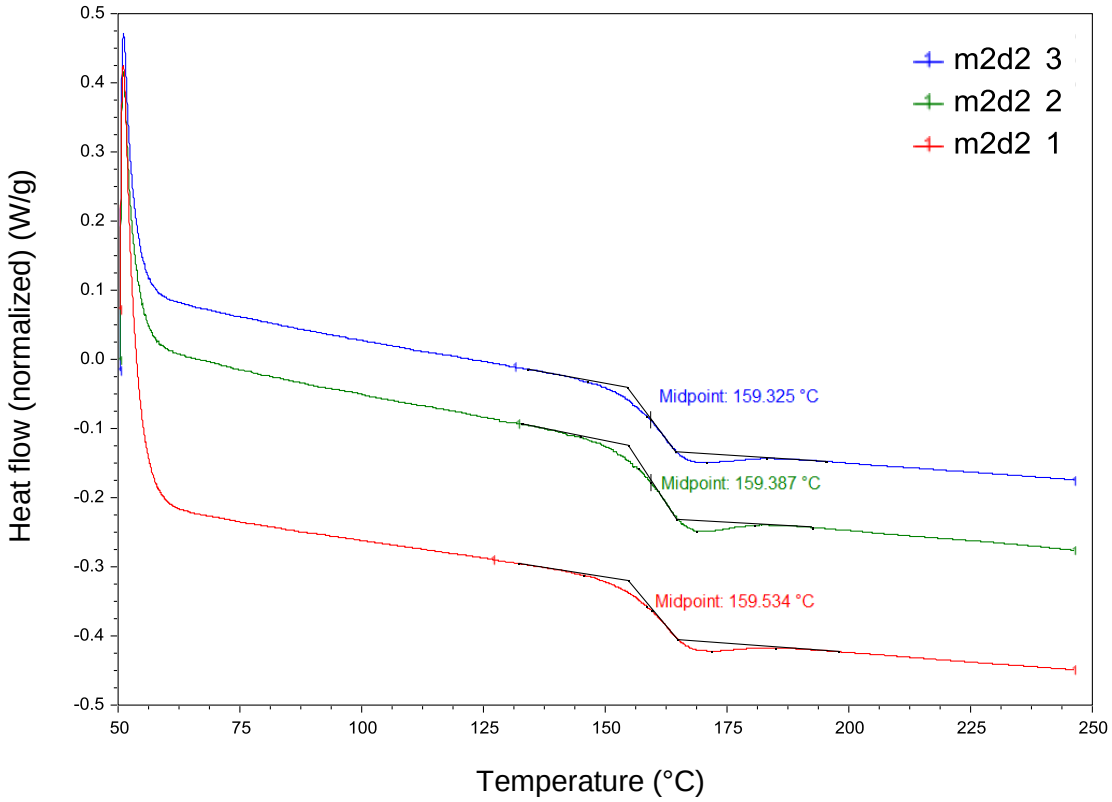

Figure 4.27 DSC results for P(MMA-co-NVP) which has been washed with method m2d2

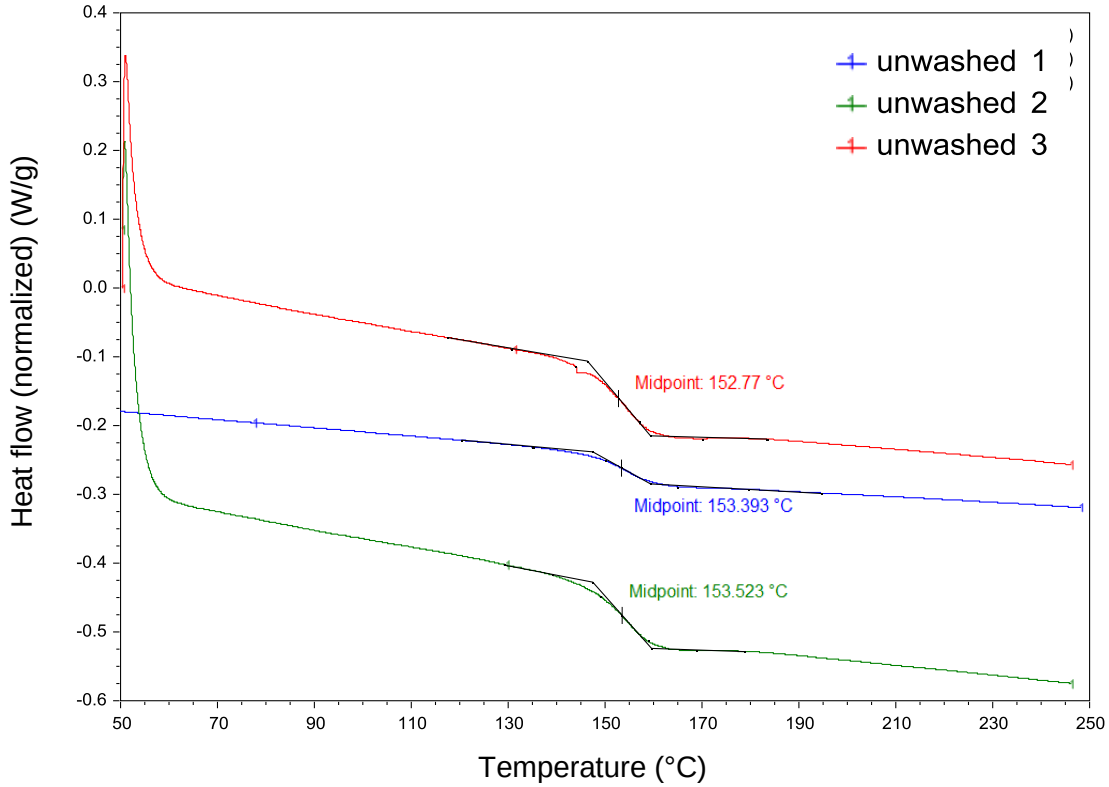

Figure 4.28 DSC results for P(MMA-co-NVP) which has not been washed

Figure 4.27 and Figure 4.28 compare the DSC results found for washed and not-washed samples. They show that the glass transition temperature increases by approximately 6°C after washing.

4.3.6 Ultra-Violet – Visible Spectroscopy

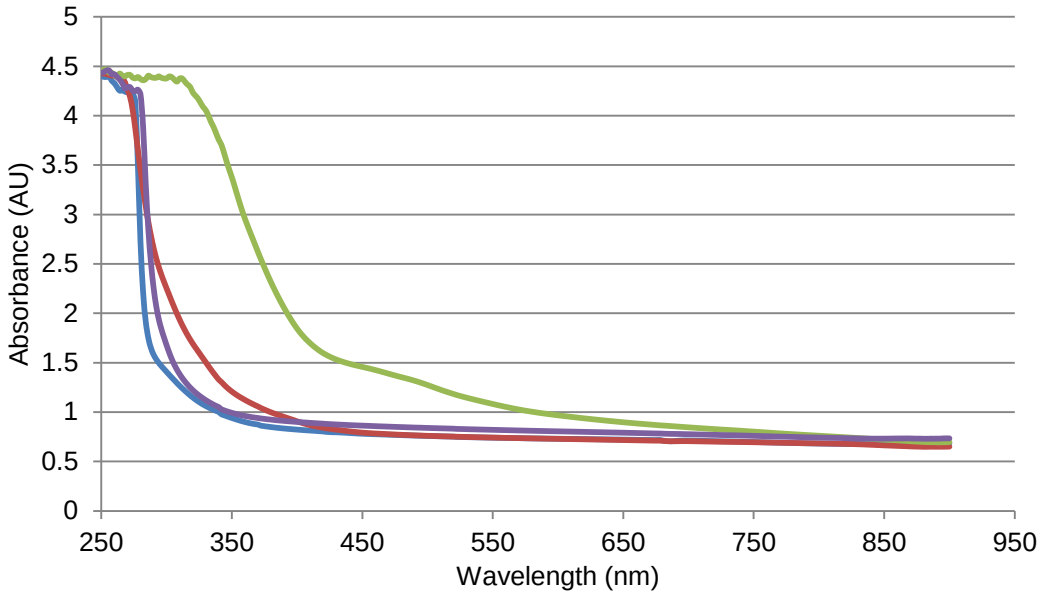

Figure 4.29 UV-VIS results comparing: Blue: washed, non-irradiated. Red: washed γ-irradiated, Purple: not-washed, non-irradiated, Green: not-washed, γ-irradiated

Figure 4.29 compares the UV-VIS spectrum before and after γ-irradiation, for both washed (m2d2) and not-washed samples. For the non-irradiated samples, washing did not have a noticeable effect on the absorbance profile of the sample. However, for samples which have been γ-irradiated, there is a significant difference depending on whether the sample has been washed before exposed to γ-irradiation. The not-washed, γ-irradiated show increased absorbance between 300nm and 650nm, compared to washed, γ-irradiated samples. The washed, γ-irradiated samples, show slightly increased absorbance between 300nm and 400nm, when compared to the not-washed, non -irradiated samples.

4.3.7 Dynamic mechanical analysis

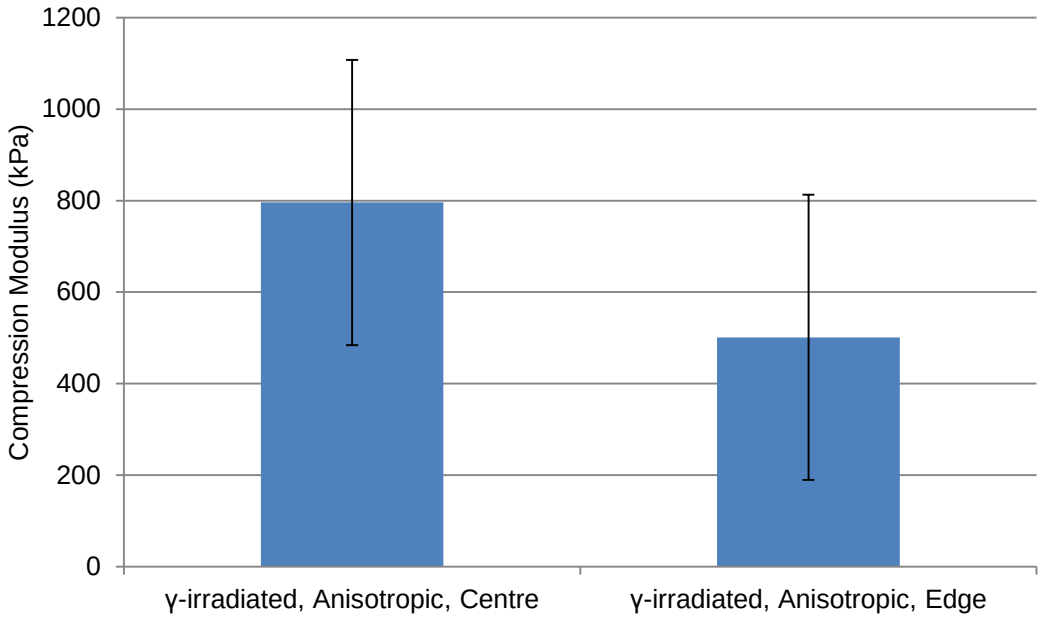

Figure 4.30 A comparison in the modulus for the centre and edge of fully hydrated anisotropic γ-irradiated samples

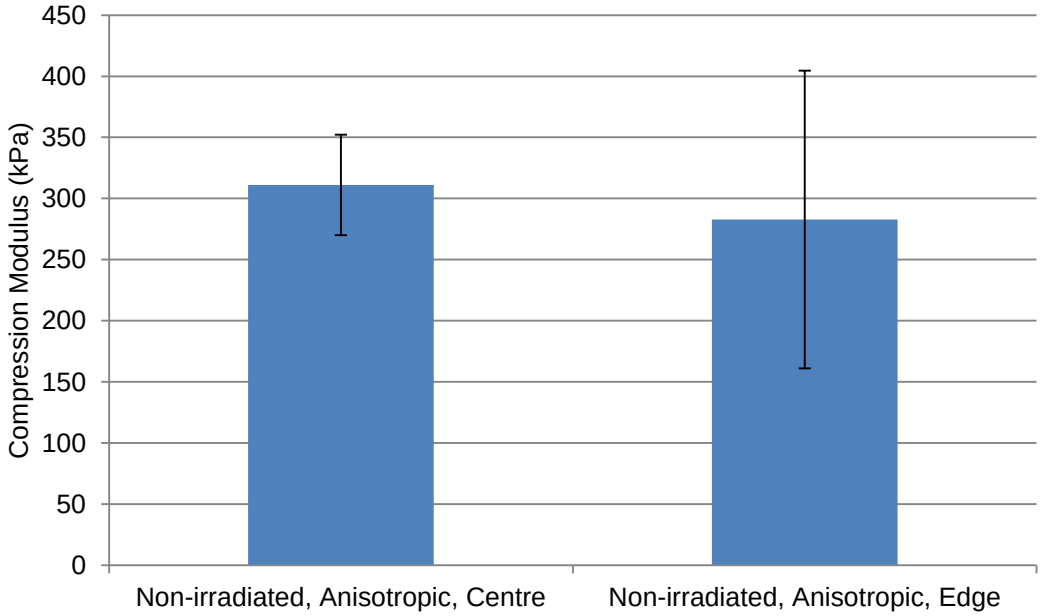

Figure 4.31 A comparison in the modulus for the centre and edge of fully hydrated anisotropic non-irradiated samples

Figure 4.30 compares the modulus of sections of hydrated γ-irradiated samples from the edge and centre. The samples taken from the centre showed an increase in stiffness, which is consistent with increased cross-linking and decreased swelling. Figure 4.31 compares the modulus of sections of hydrated non-irradiated samples from the edge and centre. There is no statistical difference between the two regions; however, both regions show a reduction in compression modulus compared to both regions in the γ-irradiated samples.

4.4 Discussion

The results presented in section 4.3 are discussed in this section. The effect of γ-irradiation on not-washed samples will be discussed first. Following this the effect of washing on both non-irradiated and γ-irradiated samples will be discussed.

4.4.1 The effect of γ-irradiation on not-washed samples

γ-irradiation of not-washed samples is shown to cause changes to the composition and the swelling behaviour. Figure 4.2 shows that after γ-irradiation, samples with $C = 1$ and $C = 3$ change from colourless to an orange/red colour. However, during swelling, there is a colour change from orange/red back to colourless, which follows the diffusion front as seen in Figure 4.3, indicating that the source of the orange/red colour is soluble. The UV-VIS spectrum shown in Figure 4.29 also shows that γ-irradiated, not-washed samples, show an increase in absorbance between wavelengths of 300nm and 650nm compared to non-irradiated, not-washed samples. This change in absorbance is in agreement with the orange/red colour change observed in Figure 4.2. The colour change during γ-irradiation could be a result of either by-products produced during further reaction of the P(MMA-co-NVP) network, or by reactions of smaller residual molecules present in the initial samples (148,157,158). Residual molecules would be most likely to include NVP, MMA, allyl methacrylate and azobisisobutyronitrile, as these are the molecules present during synthesis (the presence of these residual molecules will be discussed in more detail later within this section). However, the resulting (orange/red) molecules are stable until the bulk material degrades (as seen in Figure 4.23). Pure PVP has a UV-VIS absorbance peak of 440nm (148), and a shoulder is observed at this point (Figure 4.29) for the washed γ-irradiated sample. Low molecular weights of MMA have also been shown to be red in colour (158), and therefore could be contributing to the colour change. Chain scission of the network could result in low molecular weight MMA, and in the presence of pure PVP. However, if the residual molecules consisted primarily of NVP, it is also possible that γ-irradiation could cause polymerisation of these NVP molecules into PVP chains (thus giving an absorbance

peak for PVP (148)). It is most likely that multiple reactions are occurring (including cross-linking, chain scission and further reactions of any residual molecules). However, as impurities are known to increase the rates of both chain scission and cross-linking (discussed in section 2.2.6), removing the residual molecules may eliminate the orange/red colour, even if the residual molecules are not directly responsible for the colour change (143,153).

Figure 4.30 and Figure 4.31 compare the compression moduli for the centre and edge regions of γ-irradiated and non-irradiated samples. γ-irradiated samples exhibit an increased compression modulus, which is reflective of an increase in cross-linking. This is expected, as the network is predominantly PVP, and, as discussed in section 2.2.6, during γ-irradiation of PVP cross-linking normally dominates over chain scission (81). Davis *et al* (76) noted that there was an increase in cross-linking density after γ-irradiation for P(MMA-co-NVP).

Figure 4.11 shows the swelling mass uptake of samples (not-washed) before and after γ-irradiation. There is no statistical difference in mass uptake between samples with initial heights of 6mm and 12mm, and compression ratios $C = 1$ and $C = 3$, before or after γ-irradiation. As shown in Figure 4.12 and Figure 4.13, there is no statistically significant difference between the final swelling dimensions for samples with compression ratio $C = 1$ before and after γ-irradiation. Therefore the additional cross-linking (shown by the change in compression modulus) does not appear to affect the average mass uptake (independent of compression ratio) or the average dimension changes for height and diameter in samples with compression ratio $C = 1$. However, Figure 4.12 and Figure 4.13 also show that for samples with compression ratio $C = 3$, there is a significant difference in the final swelling dimensions for non-irradiated and γ-irradiated samples. After γ-irradiation, the final height is reduced and the diameter is increased, giving the barrelled shape shown in Figure 4.14. These findings are summarised in Figure 4.32. As discussed in section 3.4.1, samples with compression ratios $C > 1$ will have the same final swelling dimensions as a sample (of the same initial size) with $C = 1$, as the network structure has not been altered. This implies that γ-irradiation is causing changes to the network structure of compressed samples, which is

does not cause in the isotropic samples. Therefore the likely root of these changes is most likely to be the residual strain in the compressed samples (discussed in section 3.4.1).

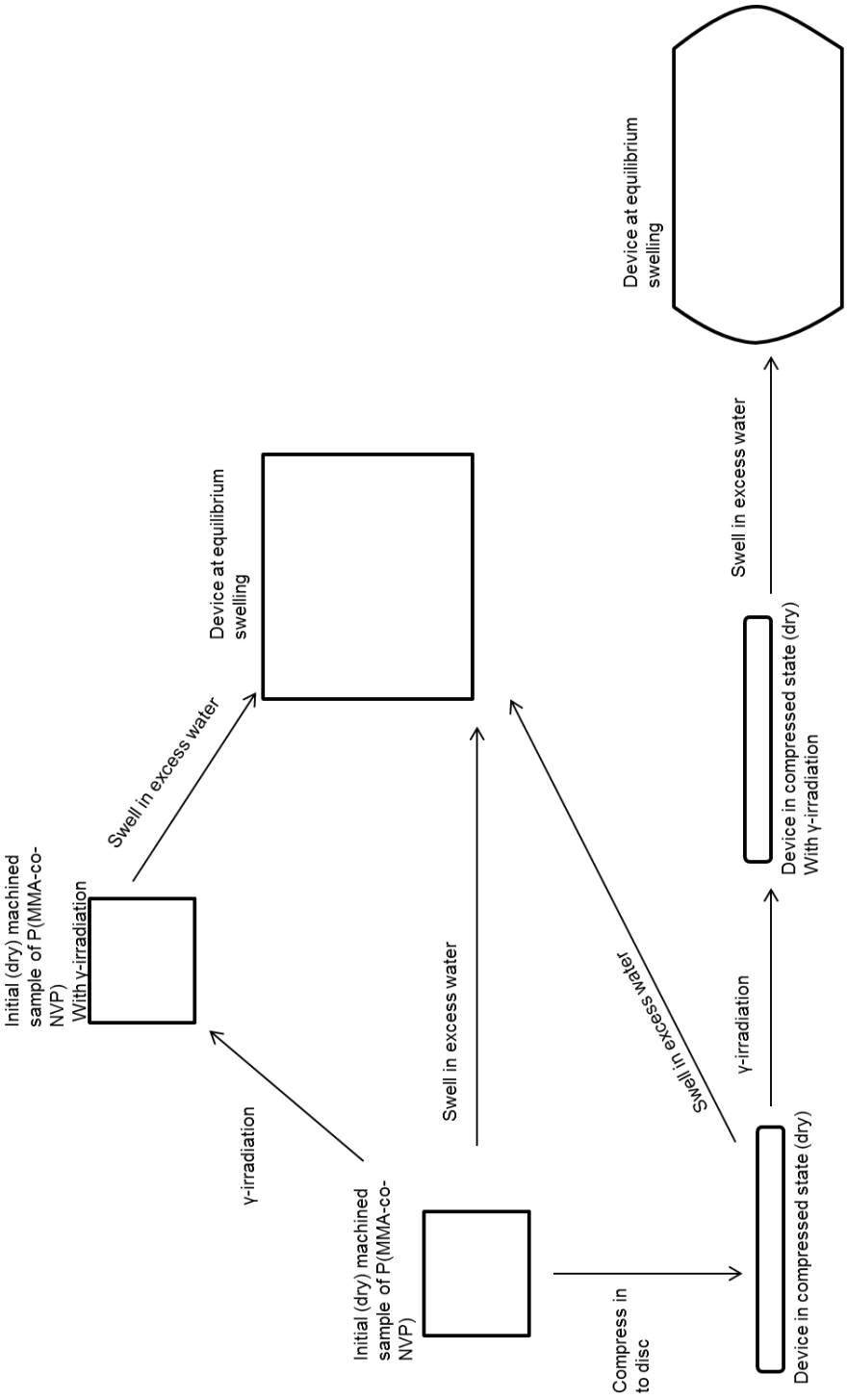

Figure 4.32 A schematic showing the changes in swelling dimensions depending on whether samples have been compressed, γ-irradiated, or both.

The barrel shape of these samples is likely to be caused by changes in the ratio of cross-linking to chain scission in different regions of the sample. For example, as shown in Figure 3.42, the central region of the device has a greater degree of compression than the outer

region. Therefore, when this region is γ-irradiated new cross-links may form very easily, altering the structure of the polymer network (and therefore the structure of the expanded device). This can be seen in Figure 4.33, and has been observed in other systems (154–156) as discussed in section 2.2.6. The same may be predicted in the outer region, with new cross-links altering the network structure. Furthermore, as the compression modulus is lower in this region, it is possible that a greater degree of chain scission is also occurring in the radially-strained polymer chains (Figure 4.33). It is due to the residual strains in the polymer network that the reference swelling state exists, and therefore if these are reduced by cross-linking and chain scission, the polymer will be unable to return to the reference shape. Chain scission in the radially-aligned polymer chains would account for the increased diameter of the barrelled shape.

It is possible that the previously discussed residual molecules are increasing the rate of cross-linking and chain scission during γ-irradiation. If this is the case, then by removing the residual molecules, the devices (washed, compressed and γ-irradiated) will expand to the same reference state as the not-washed, compressed, non-irradiated samples.

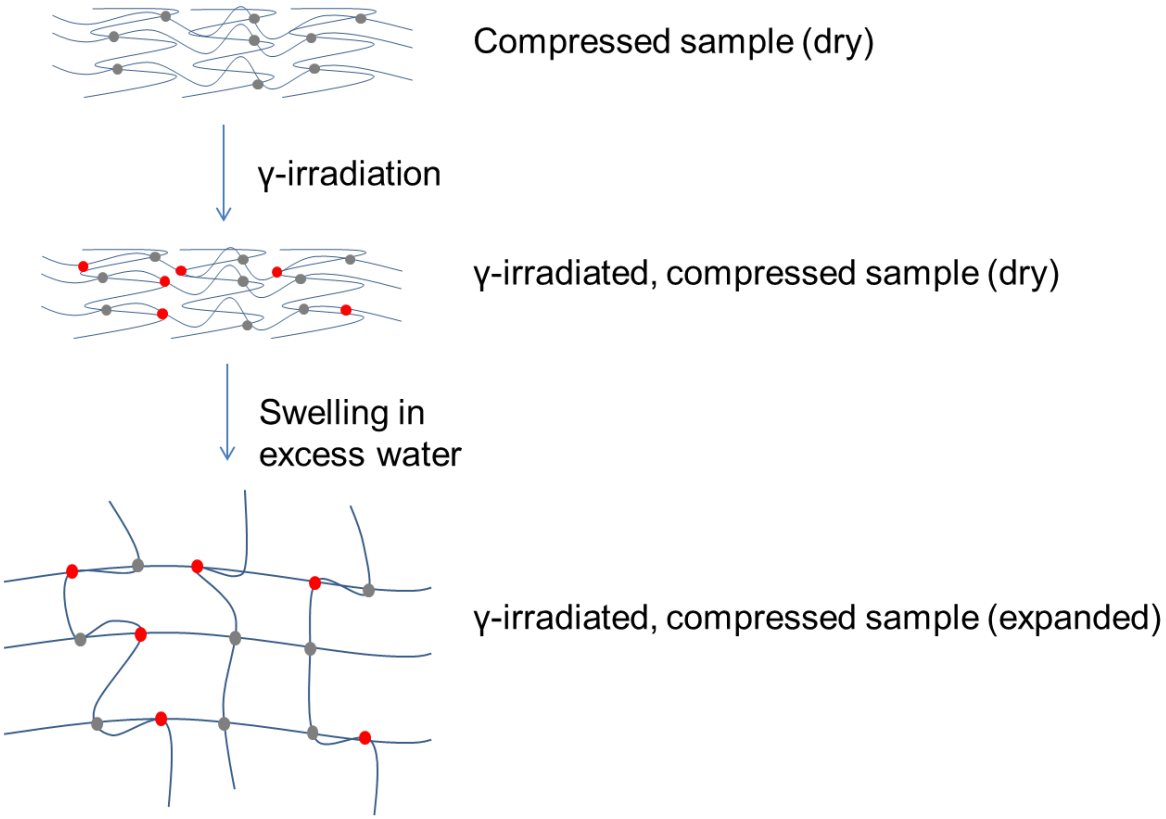

Figure 4.33 A schematic showing the changes in the polymer network due to γ-irradiation. Grey circles: existing cross-links. Red circles: New crosslinks caused by γ-irradiation

4.4.2 Samples with residual molecules removed

Figure 4.24 and Figure 4.25 show the TGA results for different washing and drying routes, as well as not-washed samples. As the length of time that a sample is washed for increases, the percentage weight loss between 220°C and 400°C decreases (by approximately 10% for the longest washing time). This indicates that residual molecules with degradation temperatures within this range are being removed by washing, and that the longer the sample is washed, the more residual molecules are removed. The degradation temperatures of the possible residual molecules (NVP, MMA, allyl methacrylate and azobisisobutyronitrile) are shown in Table 4.3. P(allyl methacrylate) and polymer units or oligomers of NVP and MMA fall within the range shown. It is likely that the residual molecules consist of a combination of these. DSC data, shown in Figure 4.28, also shows that as samples are washed, residual molecules are removed, as the glass transition temperature for washed samples is on average 6°C higher than for not-washed samples. In the not-washed samples residual

molecules would act as a plasticiser, thus decreasing the glass transition temperature of the sample.

Table 4.3 A comparison of the degradation temperatures of the molecules present in the synthesis of P(MMA-co-NVP)

Chemical	TGA degradation temperature	Reference
NVP	88°C	(164)
MMA	100.5°C	(165)
P(allyl methacrylate)	200°C	(166)
Azobisisobutyronitrile	85°C	(167)

Figure 4.4 shows the swelling success for samples with different washing and drying times. As mentioned in section 4.3.1, it was not possible to process the samples washed for 24hours (m1), because the glassy core was still present (seen in Figure 4.5). Samples dried in the oven for 24 hours immediately after swelling (d1) failed during swelling. These samples also showed evidence of cracking before swelling. The failure of these samples (d1) can be understood by considering the diffusion exponents of fully swollen samples dried in the air and oven (seen in Table 4.2). As discussed in section 2.2.3, diffusion in hydrogels is governed by the relationship between the chain relaxation and the diffusion within the polymer, and sample failure can occur during rapid diffusion. The diffusion exponent for the oven-dried samples is reflective of Case III diffusion (where the rate of diffusion is said to be comparable to that of chain relaxation), whereas the diffusion exponent for the air-dried samples is reflective of Fickian diffusion (where the diffusion rate is much slower than the rate of chain relaxation). It is possible that in the Case III diffusion, the rate of chain relaxation is not sufficiently faster than the rate of diffusion and therefore the samples are subject to increased stresses and thus are cracking. This effect is seen when fully hydrated samples are oven-dried; however, if the initial diffusion is slower (through air-drying) and rapid oven drying is used on a partially swollen hydrogel, then failure is not observed. This is most likely because less relaxation is required to change from partially dried dimensions to fully dry dimensions. The complicated effect of both the change in water content and the

change in temperature on the diffusion of the water molecules out of the sample, should also be considered. In order to investigate this more closely, environmental dynamic mechanical analysis may be required.

Figure 4.15 shows that for all washed samples, a slightly higher percentage mass was observed at equilibrium when compare to not-washed samples. However, this can be explained by the fact that the initial mass of not-washed samples includes the mass of the residual molecules. This is illustrated in Equation 4.3, which shows Equation 2.16 modified to take the residual molecules into account. M_W is the mass of water absorbed by the gel, M_x is the mass of the xerogel network and M_r is the mass of the residual molecules in the sample (which diffuse out). For this reason, considering the changes in the dimensions for washed samples will be of more use than the change in mass.

$$\frac{M_x + M_W - M_x}{M_x} > \frac{M_x + M_W - (M_x + M_r)}{M_x + M_r}$$

Equation 4.3

In order to compare the effect of washing samples on the behaviour of compressed samples, processing route m2d2 was chosen as a balance between amount of residual molecules removed, and time taken to produce samples. Figure 4.16 shows the final swelling dimensions of m2d2 samples for different initial heights and compression ratios. When compared to the same results for not-washed samples (Figure 3.22), there is no statistically significant difference for samples with initial heights 12mm and 6mm, between compression ratios 1 and 3. These samples return to the reference dimensions of a not-washed sample with a compression ratio of $C = 1$. Therefore the results for initial heights of 12mm and 6mm, indicate that for these samples, removing the residual molecules has not significantly affected the P(MMA-co-NVP) network, or the behaviour during hot pressing. As discussed in section 3.4.1, it is this network which allows the sample to return to the reference dimensions. Furthermore, this observation is supported by the cross-polarized light image (Figure 4.22) which shows the same distinctive patterns as that of a not-washed sample

(Figure 3.33). However, there is a significant difference for samples with initial height 3mm. It is possible that as the sample heights are marked on rods before expansion, and then cut with a razor on expansion, the smaller the sample the less accurate the initial height measurement.

Furthermore, we find that for compressed samples washed with m2d2 prior to γ-irradiation, the final samples do not exhibit a barrelled shape (as they do for not-washed, γ-irradiated- Figure 4.3), but instead return to the same reference dimensions as not-washed, non-irradiated (Figure 4.20). This indicates that while the combination of residual molecules and residual strain are responsible for the restructuring of the polymer network (discussed in section 4.4.1), neither one individually can cause sufficient disruption to the polymer structure to prevent expansion to the reference state. Figure 4.10 also shows that the orange/red colour is greatly reduced, but a very pale yellow colour is still visible. This is also reflective of the UV-VIS data (Figure 4.29), where the washed, γ-irradiated samples have a slightly increased absorbance (between 300nm-400nm) when compared to non-irradiated samples (both washed and not-washed), but a greatly reduced absorbance in this region compared to the not-washed, γ-irradiated samples. The absorbance beyond this region (400nm-700nm), whilst still increased for not-washed, γ-irradiated, is indistinguishable for the non-irradiated samples, and the washed (m2d2), γ-irradiated samples. The research has therefore shown that by removing residual molecules from the P(MMA-co-NVP) sample, some reactions during γ-irradiation are prevented. These further reactions result in poor swelling performance (barrelled samples) and a red/orange soluble molecule.

4.5 Summary

This chapter aimed to answer the following research questions, originally posed in section 2.3:

RQ 5) What is the effect of γ-irradiation on P(MMA-co-NVP)?

It has been shown that there is a difference in effect of γ-irradiation on the as-received P(MMA-co-NVP) depending on the compression ratio of the sample irradiated. Both samples with compression ratio $C = 1$ and $C = 3$ experience a colour change from colourless to red/orange which is thought to be due to the reaction of residual molecules with each other, by-products of reactions with the polymer network, or a combination of these two possibilities. The source of the colour is soluble in water, and thus could be leached out of the device into the surrounding tissue.

The swelling behaviour (change in mass, diameter and height) for γ-irradiated samples with compression ratio $C = 1$ is not significantly different to the equivalent non-irradiated samples. This indicates that any changes to the polymer set are not significant enough to change the swelling behaviour. Other studies have found an increase in cross-linking density, but the result presented here neither contradicts nor supports this argument, as cross-linking may be dominant but not sufficient to change the swelling properties.

However, the swelling behaviour (change in mass, diameter and height) for γ-irradiated samples with compression ratio $C = 3$ is significantly different to that of equivalent non-irradiated samples. Whilst the overall change in mass does not appear to be affected by the γ-irradiation, the final dimensions have been. The barrelled shape of samples is hypothesised to be the result of changes in the ratio between cross-linking and chain scission due to the effect of the strain distribution through the sample. In regions of compression (e.g. the center) the cross-linking density appears to dominate (identified by a higher compression modulus and reduced swelling capacity) and in regions of strain (e.g. the outer annulus) chain scission appears to dominate (identified by lower compression modulus and increased swelling capacity). This results in a barrelled outer region, constrained by the inner region.

RQ 6) What is the effect of residual molecules in the P(MMA-co-NVP), and how does removing these residual molecules affect the results of RQ5?

It has been shown that if the residual molecules in the samples are removed (by washing in distilled water), the orange/red colour does not appear after γ-irradiation. Furthermore, the swelling behaviour of compressed samples which have been washed and γ-irradiated is not significantly different to the swelling behaviour of non-irradiated samples. This means that by removing the residual molecules, there is not a significant change in the network set, thus indicating that the residual molecules play a significant role in the cross-linking and chain scission reactions during γ-irradiation.

These findings are allow design processes to be developed which minimise the effect of the sterilisation process on the swelling behaviour of the devices, thus improving the quality of the device produced. As discussed in section 2.1.3, controlling the rate of expansion is also essential in order to grow new, healthy tissue, and this will be the topic of the next chapter.

CHAPTER 5:

Controlling the Swelling Rate

5 Controlling the Swelling Rate

5.1 Introduction

This chapter aims to answer the research questions RQ7 and RQ8, posed in section 2.3:

RQ 7) How does the application of a semi-permeable silicone coating affect the swelling rate of devices?

RQ 8) What is the effect of γ-irradiation on the performance of the silicone coatings?

In order to address these questions, a polydimethylsiloxane (PDMS) coating was applied via dip coating. Different numbers of cycles of dip coating were applied to a range of samples and the resulting thickness measured. The swelling behaviour was monitored over a six-week period (to reflect a realistic clinical time frame (15)), with changes to the mass, height and diameter recorded. The strain rate of the coating during expansion was also calculated. These results were compared for non-irradiated and γ-irradiated samples. Only compressed cylindrical samples are investigated in this chapter, with Chapter 6 applying these findings to non-prismatic shapes.

The uniaxial mechanical properties (ultimate tensile strength, Young's modulus and failure strain) of cast sheets of PDMS were also investigated using a universal testing machine. Again, these results are compared for non-irradiated and γ-irradiated samples.

5.2 Experimental Methods

5.2.1 Casting silicone sheets

Polydimethylsiloxane (PDMS), MED 66-606 (Nusil, Silicone Technology) was cast into an array of polystyrene petri dishes (diameter 90mm) using a 20ml wide nozzle polypropylene syringe (BD Plastipak). In order to cure the PDMS sheets, the array was placed on a flat surface in a fume hood in atmospheric conditions for three days (as per the manufacturer's

instructions). Table 5.1 shows the different volumes cast and the corresponding post curing sheet thicknesses. The sheets were then sectioned (using a razor blade) into six samples of length 60mm and width 10mm. Three samples of each thickness were subsequently sent for γ-irradiation, as described in section 4.2.1.

Table 5.1 The volume of PDMS cast into 90mm petri dish, and the resulting thickness of the PDMS sheet

Volume Cast (ml)	Resulting Thickness (mm)
5	0.2
10	0.4
15	0.6
20	0.8

5.2.2 Mechanical testing

The Young's modulus, ultimate tensile strength and failure strain were measured on a Shimadzu, Autograph AGS-X universal tensile testing machine. The results were recorded and analysed using Trapezium-X software. Samples were prepared as described in section 5.2.1. 40mm of the sample was held in the clamps and thus there was a 20mm length between the clamps. The clamped sections of silicone were held between two cardboard sheets to prevent surface damage. The tensile strain was increased 100% per minute (20mm/min) to allow a run time of a few minutes.

5.2.3 Manufacturing devices with PDMS coatings

Samples were coated with PDMS, MED 66-606 (Nusil, Silicone Technology). This material was chosen as it can be cured at room temperature without the need for a solvent (both of which are processes which may alter the properties of the underlying hydrogel). Similar PDMS coatings have recently been used to coat the hydrogel samples (171), however these coatings have required the use of a solvent in order to be applied. A tab of cured silicone was glued to one edge of the sample using PDMS solution. This was left to dry overnight. The tab was then used to hold the sample during dip coating. The process of dip coating can be seen schematically in Figure 5.1. Coatings were applied in cycles, where one cycle was defined as

a three second submersion in the PDMS solution. There were 15minute intervals between the coating cycles. After all coating cycles were complete, the samples were left to cure in the fume hood for three days (as per manufacturer's recommendations).

Cylindrical P(MMA-co-NVP) samples were produced as described in section 3.2.2. Samples with initial heights 6mm and 12mm, and compression ratio $C = 3$ were coated with between one and 12 coating cycles. Initially a minimum of three samples were produced for each coating thickness and initial height to establish whether coatings would fail during expansion. Subsequently, a further six samples with coating cycles four, eight and 12 were made for initial height 12mm, compression ratio $C = 3$. Half of these samples were sent for γ-irradiation, as described in section 4.2.1.

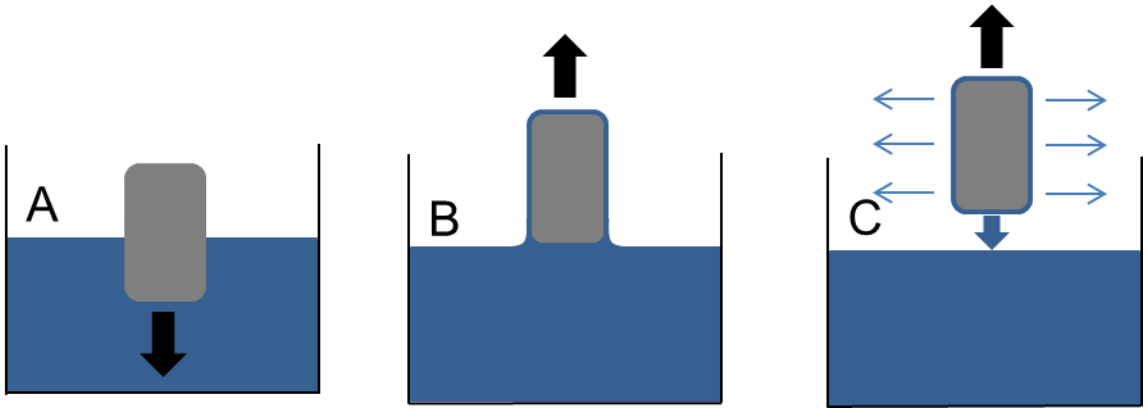

Figure 5.1 A schematic showing the process of dip coating. A: The sample is immersed in a solution containing the desired coating and a solvent. B: The sample is slowly extracted, creating the formation of a wet coating on the sample surface. C: Excess solution drips from the bottom of the sample into the tank, solvent evaporates from the sample surface leaving the desired coating

5.2.4 Swelling experiments

Samples were hydrated in distilled water at 37°C for six-weeks. The water was replaced every week. Measurements were taken three times a day for the first week, and once a week for the remaining five weeks. The mass, height and diameter were recorded as described in section 3.2.3. The percentage changes in these parameters were calculated using Equation 2.17, Equation 2.18 and Equation 2.19 respectively. Additionally, strain rate was calculated using Equation 5.1 at time t_2 (reflecting the strain rate between t_1 and t_2), where h_{t_1} and h_{t_2} are the heights are t_1 and t_2 respectively. Equation 5.1 refers to the strain rate which any overlying skin will experience as the height of the expander increases.

$$strain\ rate = \frac{h_{t_1} - h_{t_2}}{h_{t_1}(t_2 - t_1)}$$

Equation 5.1

5.3 Results

The results are presented in four sections. Firstly, the Young's modulus for non-irradiated and γ-irradiated samples is presented. Secondly, the manufacturing limits of coating is reported. The final two sections present the swelling behaviour of samples with initial height 12mm and compression ratio $C = 3$, for non-irradiated and γ-irradiated respectively.

5.3.1 Mechanical testing

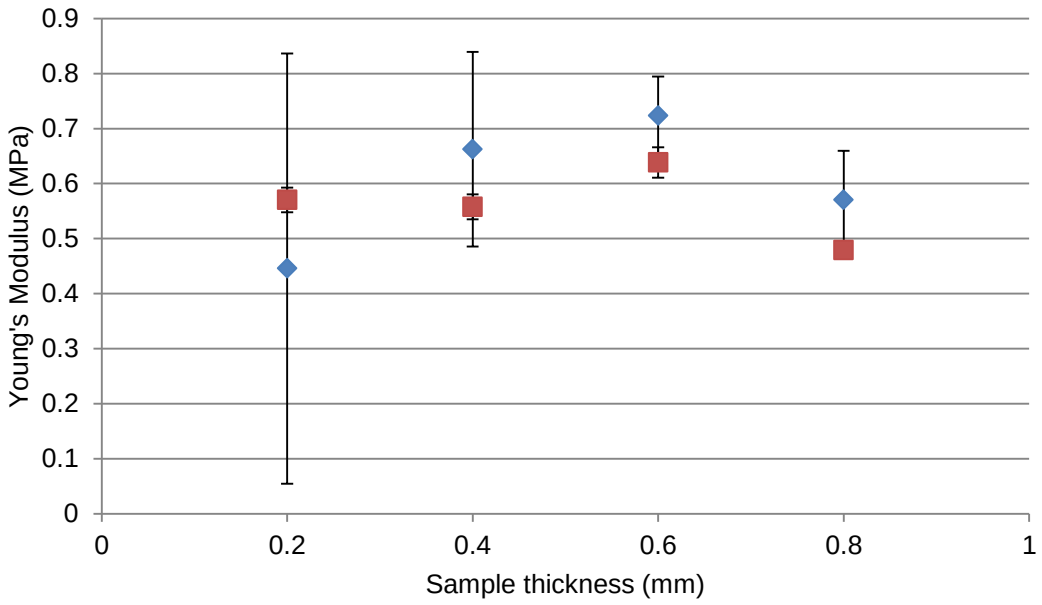

Figure 5.2 A comparison of the Young's Modulus for sheets with different thicknesses, for non-irradiated (red) and γ-irradiated (blue) samples.

Figure 5.2 compares the difference in Young's modulus for PDMS sheets of different thicknesses, both non-irradiated and γ-irradiated. For thicknesses 0.4mm, 0.6mm and 0.8mm, the non-irradiated samples have a lower Young's modulus than the γ-irradiated samples, but for 0.2mm the trend is reversed. However, these differences are not statistically significant (as described in section 3.2.6). Furthermore, there is no statistically significant

difference between samples of different thickness within the non-irradiated and γ-irradiated groups.

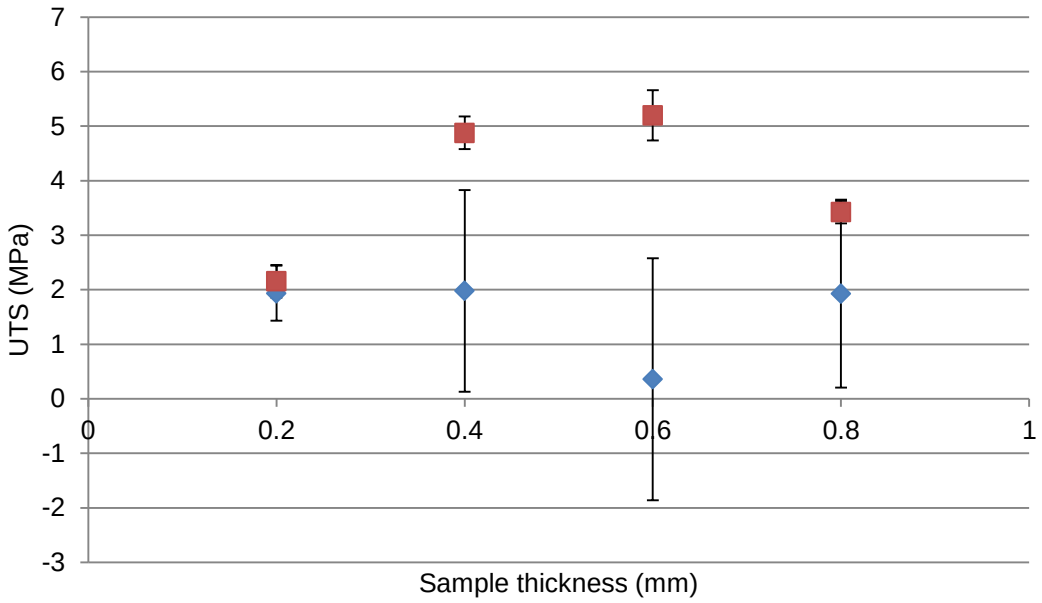

Figure 5.3 A comparison of the UTS values for sheets of different thicknesses, for non-irradiated (red) and γ-irradiated (blue) samples

Figure 5.3 compares the difference in ultimate tensile stress (UTS) for PDMS sheets of different thicknesses, both non-irradiated and γ-irradiated. The non-irradiated samples show higher UTS values than the γ-irradiated samples. However, no statistical difference is found between, or within the groups (despite no overlap in the error bars).

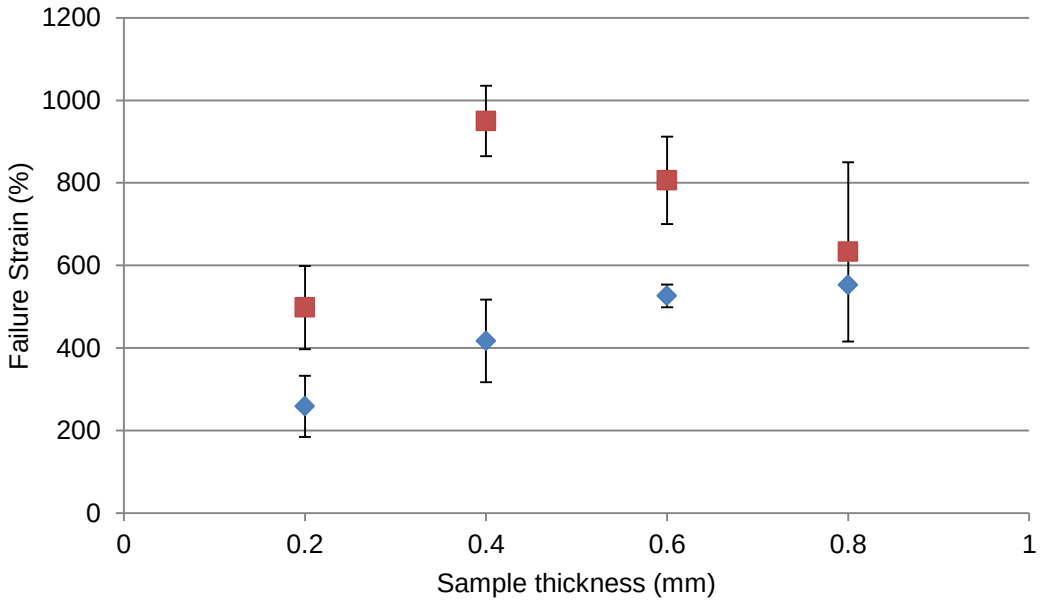

Figure 5.4 A comparison of the failure strains for sheets with different thicknesses, for non-irradiated (red) and γ-irradiated (blue) samples.

Figure 5.4 compares the difference in failure strain for PDMS sheets of different thicknesses, both non-irradiated and γ-irradiated. For every thickness the non-irradiated samples have a higher failure strain than the γ-irradiated samples. This difference is statistically significant for every thickness except 0.8mm. Within both non-irradiated and γ-irradiated samples there is no significant difference between the different thicknesses.

5.3.2 Manufacturing devices with PDMS coatings

Table 5.2 A comparison of number of dip coating cycles and average increase of sample thickness

Number of coating cycles	Average coating thickness (mm)
1	0.133 ± 0.029
2	0.190 ± 0.032
4	0.375 ± 0.038
8	0.573 + 0.052
12	0.600 ± 0.045

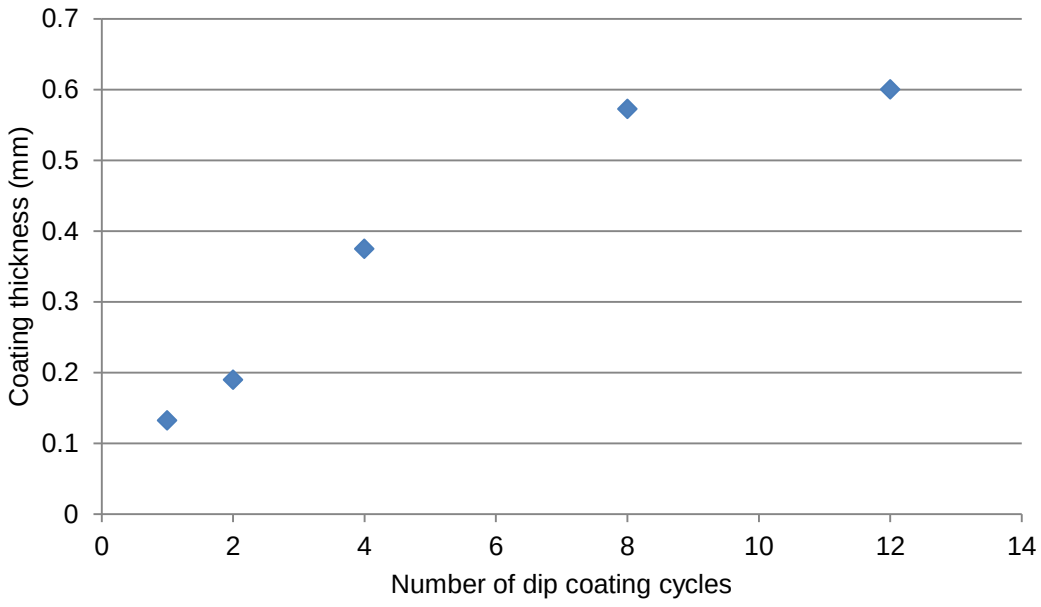

Figure 5.5 The resulting coating thickness for different numbers of dip coating cycles

Table 5.2 compares the average coating thickness for different numbers of coating cycles. This data is also shown in Figure 5.5. Initially the coating thickness increases in proportion to

the number of coating cycles, however, beyond eight cycles the coating thickness plateaus, tending towards a thickness of 0.6mm.

Table 5.3 A comparison of successful coating methods for cylindrical samples

Initial Height (mm)	Compression Ratio	1 coat	2 coats	4 coats	8 coats	12 coats
6	3	Failed (expansion)	Failed (expansion)			Failed (processing)
12	3	Failed (expansion)	Failed (expansion)			

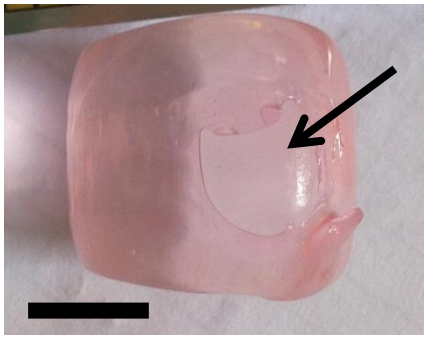

Figure 5.6 A side view of a hydrogel sample coated with two coating cycles of PDMS, which has failed during expansion. Non-irradiated. Initial height of 6mm, compression ratio of $C = 3$. The arrow indicates the failure site and the scale bar represents 10mm

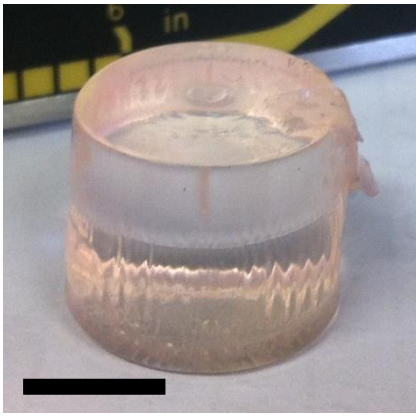

Figure 5.7 A hydrogel sample coated with four coating cycles of PDMS. Non-irradiated. Initial height of 6mm, compression ratio of $C = 3$. Photograph taken after six-weeks in distilled water. The scale bar represents 10mm

Table 5.3 shows which samples were successfully coated and expanded. Samples coloured bright red failed during expansion, samples coloured dark red failed during processing, and green samples were successfully swollen over a six-week period with no visible damage to the PDMS coating. Figure 5.6 shows an example of a hydrogel where the PDMS coating has

failed (two coating cycles). The hydrogel has expanded more rapidly at the failure site causing non-uniform expansion (marked by the arrow). After failure of the coating, the hydrogel will expand to the equilibrium size reported in section 3.3.2. By contrast, Figure 5.7 shows a sample which has successfully swollen. The cylindrical shape has been preserved. The samples with initial height 6mm and 12 coating cycles failed during manufacturing because the silicone tab repeatedly detached during the final four coating cycles (six samples attempted).

5.3.3 Swelling behaviour of PDMS coated, non-irradiated samples

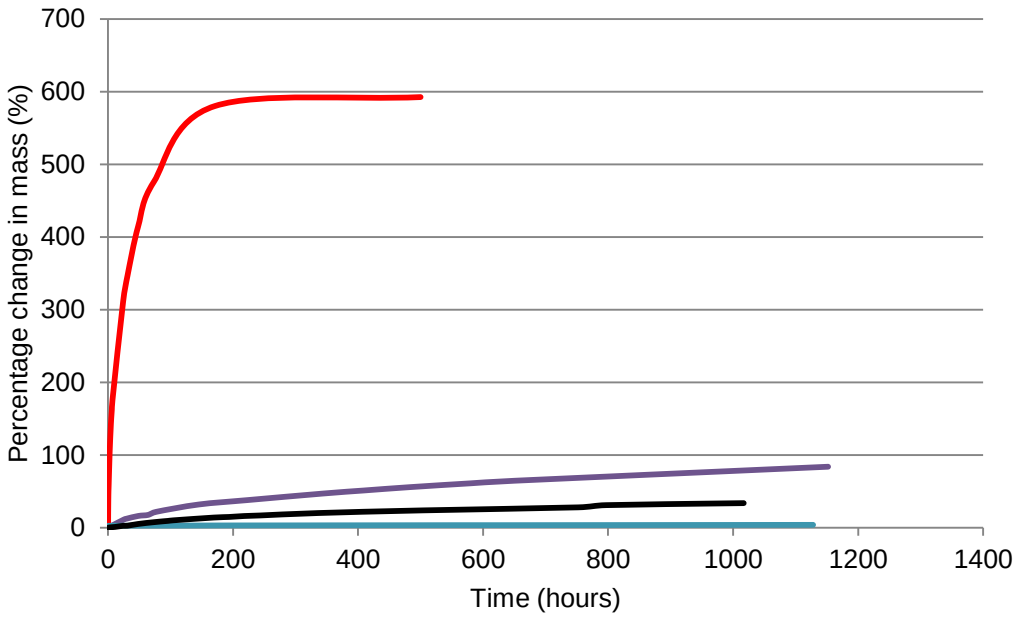

Figure 5.8 A comparison of the percentage change in mass with time for samples with different thicknesses of coatings (non-irradiated). Red: nude, purple: four coating cycles, black: 8 coating cycles, blue: 12 coating cycles

Figure 5.8 compares the percentage change in mass with time for samples with different coating thicknesses over a six-week period. The change in mass for coated samples was less than 100% for all thicknesses, compared to approximately 600% for the nude samples. This shows that the mass uptake is significantly reduced by coating samples. Of the coated samples, samples which were coated with four cycles showed the greatest increase in mass, eight coatings had the next greatest increase in mass, and 12 coatings had the lowest increase in mass.

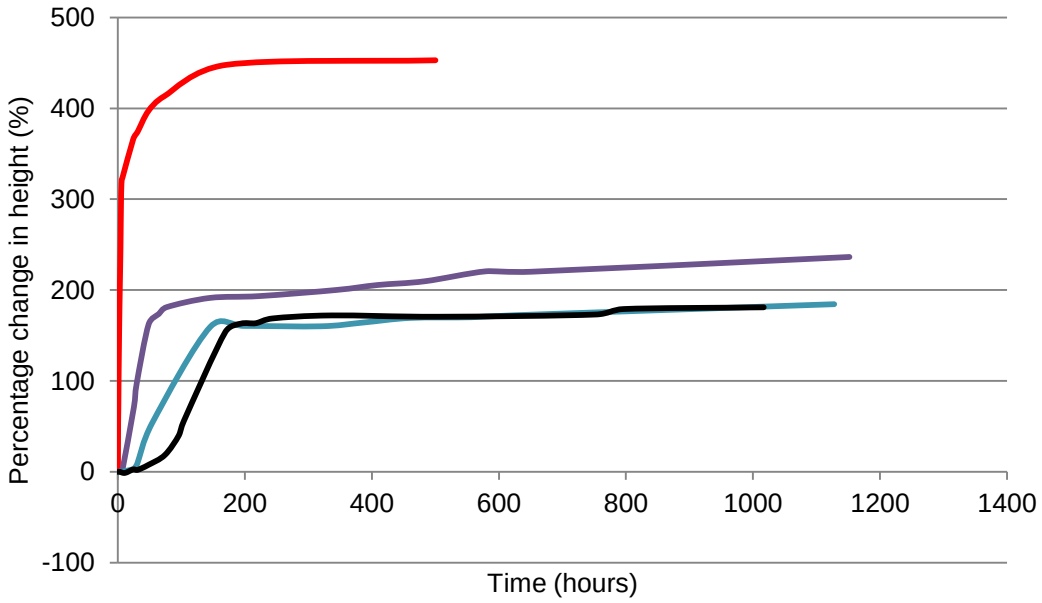

Figure 5.9 A comparison of the percentage change in height with time for samples with different thicknesses of coatings (non-irradiated). Red: nude, purple: four coating cycles, blue: 8 coating cycles, black: 12 coating cycles

Figure 5.9 compares the percentage change in height with time for samples with different coating thicknesses over a six-week period. The coated samples all showed a reduced percentage change in height over the six-week period, with eight and 12 coating cycles reaching 185% increase, and four coating cycles reaching an increase of 236%. For all coated samples, an increase of ~165% was reached within the first 200hours.

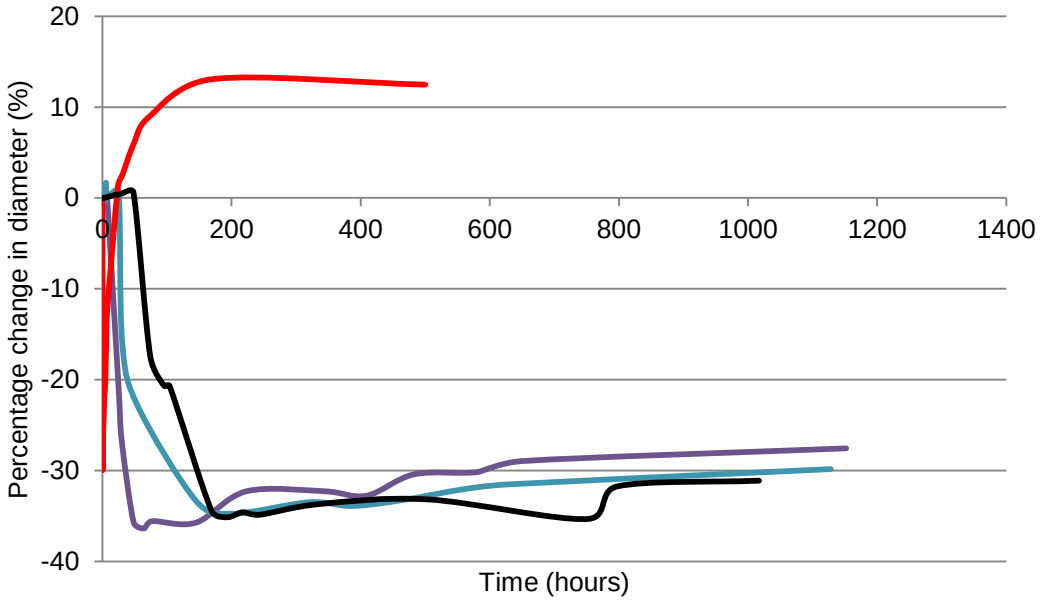

Figure 5.10 A comparison of the percentage change in diameter with time for samples with different thicknesses of coatings (non-irradiated) Red: nude, purple: four coating cycles, blue: 8 coating cycles, black: 12 coating cycles

Figure 5.10 compares the percentage change in diameter with time for samples with different coating thicknesses over a six-week period. Figure 5.10 shows that an initial reduction in diameter is observed in coated samples (approximately 30% for nude and 35% for coated), followed by a gradual increase in diameter over the remainder of the six weeks. This is also seen in nude samples, as shown in Figure 3.28.

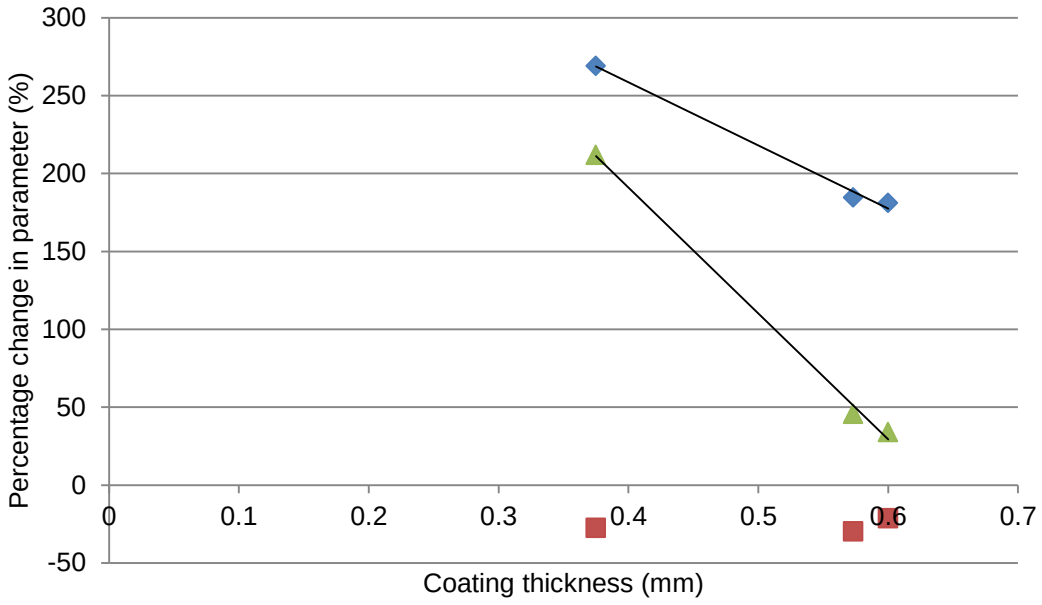

Figure 5.11 The percentage change in height, diameter and mass of samples with different numbers of coatings after six weeks hydration (non-irradiated). Blue: height, red: diameter, green: mass

Figure 5.11 compares the percentage changes in height, mass and diameter after six weeks, for coatings of different thicknesses. The number of coating cycles that each thickness corresponds to can be seen in Table 5.2. The change in height at six weeks fits a linear trend following Equation 5.2 with an R^2 value of 0.994. The change in mass at six weeks fits a linear trend following Equation 5.3 with an R^2 value of 0.997. It can be seen that the change in diameter at six weeks is not affected by the coating thickness. $h_{\%}$ and $m_{\%}$ represent the percentage change in height and mass (after six weeks) respectively and t represents the coating thickness (in mm).

$$h_{\%} = -405t + 420$$

Equation 5.2

$$m_{\%} = -809t + 515$$

Equation 5.3

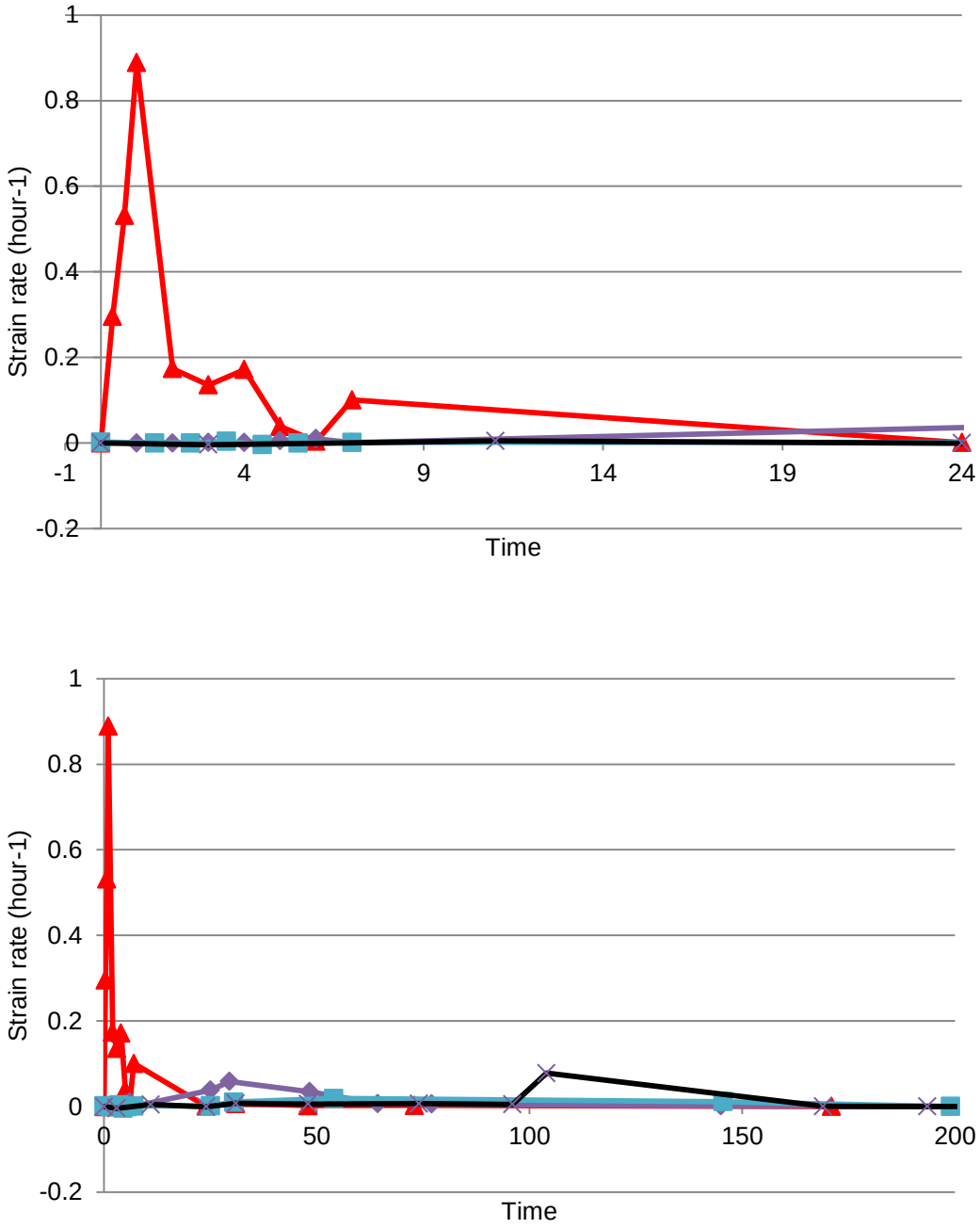

Figure 5.12 The strain rate experienced during the first 24 hours (top), and 200 hours (bottom) of expansion for samples with different coating thicknesses (non-irradiated). Red: nude, purple: four coating cycles, blue: 8 coating cycles, black: 12 coating cycles

Figure 5.12 shows the changes in the strain rate (as calculated by Equation 5.1) over the first 24 hours and 200 hours of expansion. For nude samples, there is an initial increase during the first five hours, with a maximum strain rate of 0.89h^{-1}, whereas for all coated samples

(four, eight and 12 cycles) this feature is not observed, and the maximum does not exceed $0.1h^{-1}$.

5.3.4 Swelling behaviour of PDMS coated γ-irradiated samples

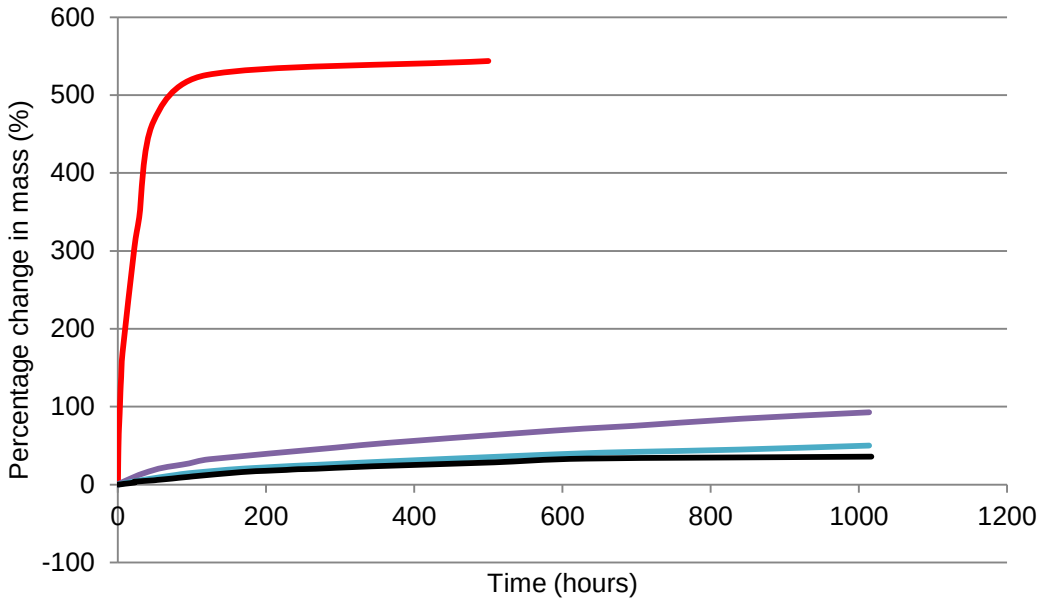

Figure 5.13 A comparison of the percentage change in mass with time for samples with different thicknesses of coatings (γ-irradiated). Red: nude, purple: four coating cycles, blue: 8 coating cycles, black: 12 coating cycles

Figure 5.13 compares the percentage change in mass with time for γ-irradiated samples with different coating thicknesses over a six-week period. The change in percentage mass for all coated cycles does not exceed 100%, compared to the 550% increase for nude samples. Samples with four coating cycles show an increase of 93%, whereas samples with eight and 12 cycles show increases of 50% and 36% respectively.

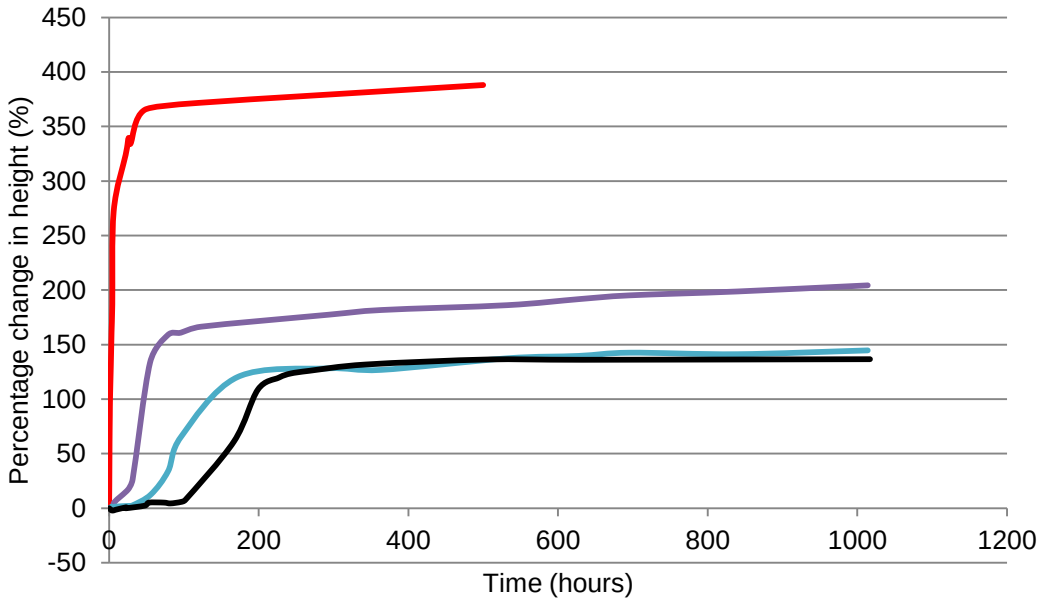

Figure 5.14 A comparison of the percentage change in height with time for samples with different thicknesses of coatings (γ-irradiated). Red: nude, purple: four coating cycles, blue: 8 coating cycles, black: 12 coating cycles

Figure 5.14 compares the percentage change in height with time for γ-irradiated samples with different coating thicknesses over a six-week period. All coated samples show a reduction in percentage change in height after six weeks when compared to the 388% increase observed in the nude samples. Samples coated with four cycles show an increase of 204%, those with eight cycles show an increase of 144%, and those with 12 cycles an increase of 137%.

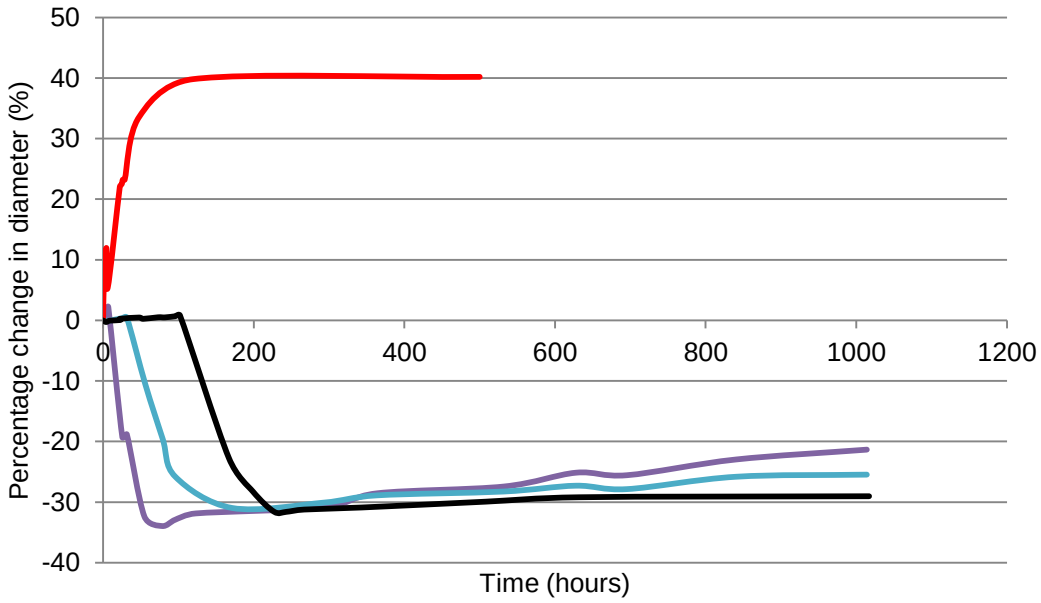

Figure 5.15 A comparison of the percentage change in diameter with time for samples with different thicknesses of coatings (γ-irradiated). Red: nude, purple: four coating cycles, blue: 8 coating cycles, black: 12 coating cycles

Figure 5.15 compares the percentage change in diameter with time for γ-irradiated samples with different coating thicknesses over a six-week period. Unlike non-irradiated samples, the γ-irradiated nude samples do not initially reduce in diameter, but increase to 40% within the first 200 hours. However, coated and γ-irradiated samples show a reduction in diameter of approximately 34%. This reduction occurs after 96, 171 and 243hours for samples coated with four, eight and 12 cycles respectively. After this initial reduction, the diameter gradually increases to give a final reduction in diameter of 21%, 25% and 29%, for samples coated with four, eight and 12 cycles respectively.

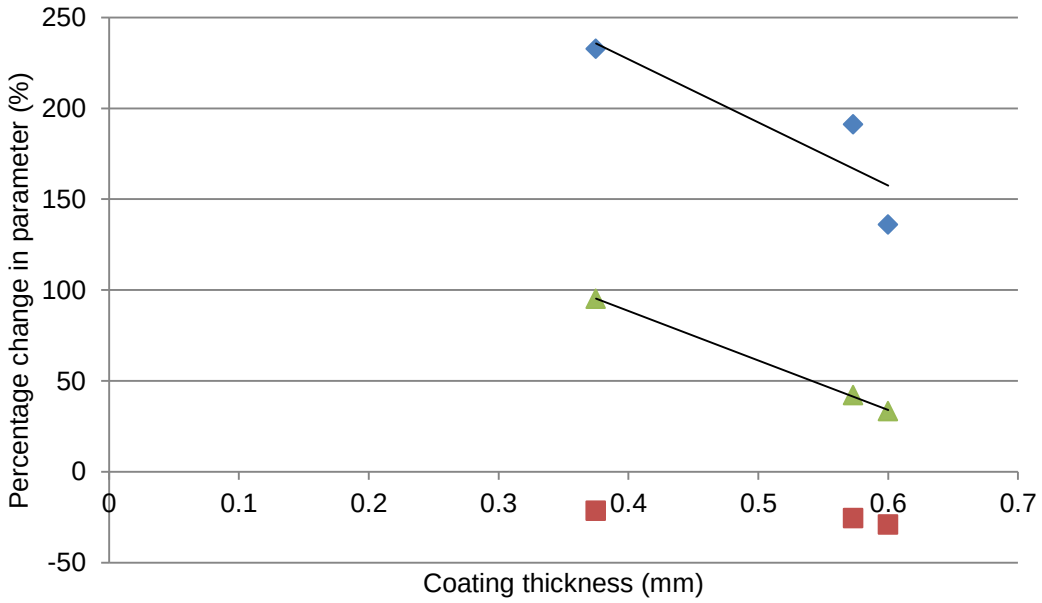

Figure 5.16 The percentage change in height, diameter and mass of samples with different numbers of coatings after six weeks hydration (γ-irradiated). Blue: height, red: diameter, green: mass

Figure 5.16 compares the percentage changes in height, mass and diameter after six weeks, for coatings of different thicknesses for γ-irradiated samples. The number of coating cycles that each thickness corresponds to can be seen in Table 5.2. The change in height at six weeks fits a weak linear trend following Equation 5.4 with an R^2 value of 0.776. The change in mass at six weeks fits a linear trend following Equation 5.5 with an R^2 value of 0.999. It is also shown that the change in diameter at six weeks is not affected by the coating thickness. $h_{\%}$ and $m_{\%}$ represent the percentage change in height and mass (after six weeks) respectively and t represents the coating thickness.

$$h_{\%} = -348t + 366$$

Equation 5.4

$$m_{\%} = -273t + 198$$

Equation 5.5

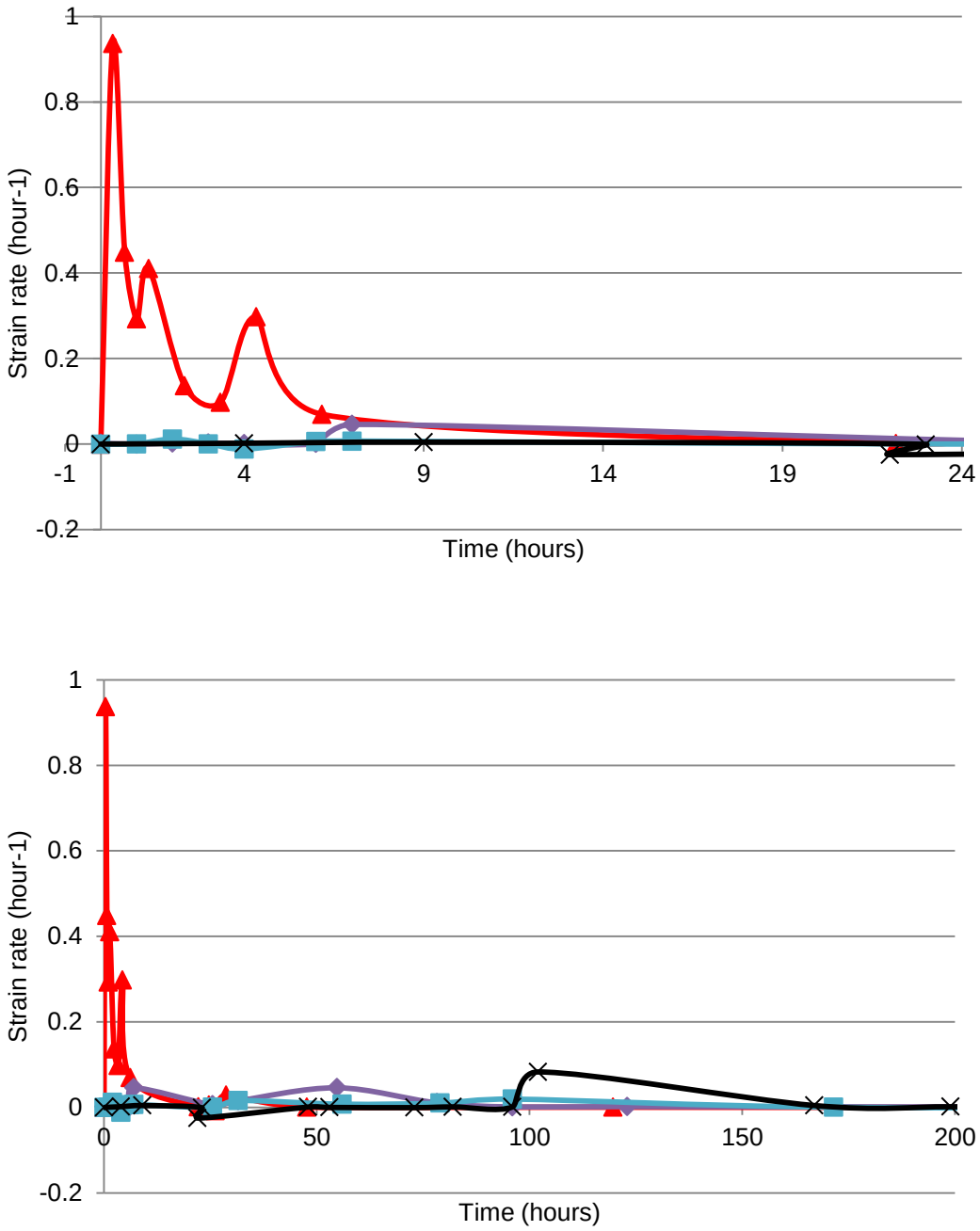

Figure 5.17 The strain rate experienced during the first 24 hours (top), and 200 hours (bottom) of expansion, for samples with different coating thicknesses (γ-irradiated). Red: nude, purple: four coating cycles, blue: 8 coating cycles, black: 12 coating cycles

Figure 5.17 shows the changes in the strain rate (as calculated by Equation 5.1) over the first 24 hours and 200 hours of expansion for γ-irradiated samples. For nude samples, there is an initial increase during the first five hours, with a maximum strain rate of $0.94h^{-1}$, whereas for all coated samples (four, eight and 12 cycles) this feature is not observed, and the maximum does not exceed $0.1h^{-1}$.

5.4 Discussion

The discussion for this chapter is broken into three sections; the mechanical properties of the cast sheets of PDMS; the manufacturing of devices coated with PDMS; and the swelling behaviour of samples coated with PDMS.

5.4.1 Cast sheets of PDMS

The Young's modulus, ultimate tensile stress and the failure strain of the samples are shown in Figure 5.2, Figure 5.3 and Figure 5.4 respectively. As no statistical difference was observed within the non-irradiated and γ-irradiated groups, an average of the values can be used to compare the non-irradiated and γ-irradiated groups. This result is shown in Table 5.4. Reported values for non-irradiated PDMS (MED6-6606) for Young's modulus, UTS and failure strain are 0.3±0.04MPa, 7.5±1.1MPa and 899±102% respectively (168). The results presented in Table 5.4 are in approximate agreement with these values. Samples which had been γ-irradiated show a reduced UTS and failure strain, and a slightly increased Young's modulus compared to the non-irradiated samples. The difference is not statistically significant for the Young's modulus, but is for the UTS and failure strain. This indicates that there has not been a significant increase in the cross-linking of the silicone sheets (as this would be expected to result in an increased Young's modulus (169)), but that the γ-irradiation has caused an increase in the defect size, or the generation of brittle regions, in the sample (therefore causing a reduction in the UTS and failure strain (170)).

Table 5.4 A comparison of the key mechanical properties for non-irradiated and γ-irradiated samples

	Young's modulus (MPa)	**UTS (MPa)**	**Failure strain (%)**
γ-irradiated	0.60 (±0.10)	2.7 (±0.69)	439 (±116)
non-irradiated	0.56 (±0.06)	3.9 (±1.2)	722 (±171)

5.4.2 Manufacturing devices with PDMS coatings

There are two important outcomes when considering the manufacturing limits of dip coated hydrogels; firstly, whether the coating fails during manufacturing; and secondly, whether the device fails during expansion. These are considered in turn.

In order for a device to be considered to have been a success during manufacturing, the device must have a known and predictable coating thickness which can be consistently reproduced. As shown in Figure 5.5 the coating thickness initially increases, but then tends towards 0.6mm. This may be explained by considering that as each coating cycle is carried out; the same volume of PDMS adheres to the device surface. However, as the number of cycles increases, so does the surface area being coated, therefore if the volume is conserved, the thickness of the coating is reduced. It may also be that at higher cycle numbers the total mass of applied (and not fully cured) PDMS is too great and therefore drainage of the underlying layers (as well as the most recently applied layer) occurs. The thickness of similar PDMS coatings after dip coating has previously been measured by partial removal of the resulting layer, followed by measurement with a scanning electron microscope (171). The results of this study are shown in Figure 5.18, where the relationship between coating cycles and thickness appears to be linear. However, a smaller range of coating cycles was tested, and the data for the first eight cycles (presented in Figure 5.5) shows strong agreement with the results shown in Figure 5.18.

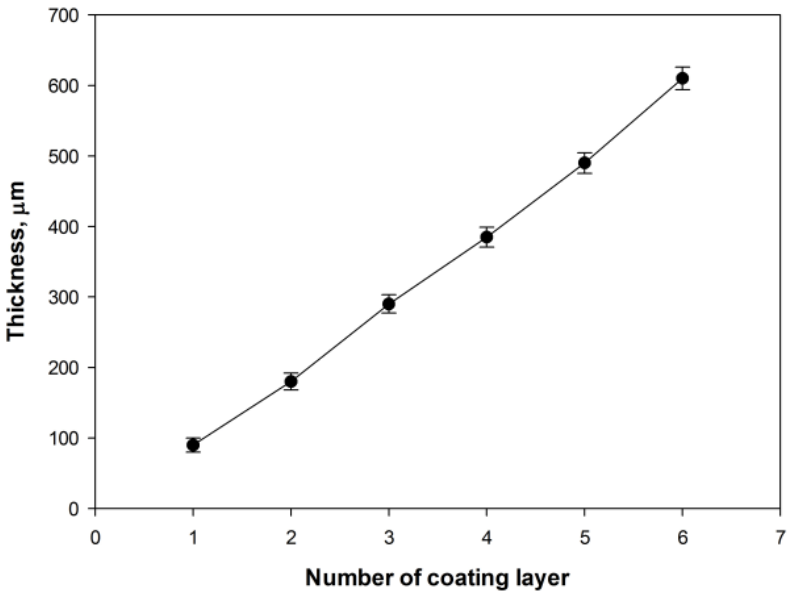

Figure 5.18 "Thickness as a function of coating layer" reproduced from (171)

As shown in Table 5.3, it was not possible to coat samples of initial height 6mm with 12 coating cycles due to failure of the tab. Samples of initial height 12mm with 12 coating cycles could be manufactured consistently. The diameters of the discs are approximately constant, but the thicknesses are 2mm and 4mm for initial heights 6mm and 12mm respectively. There are two possible explanations for tab failure. Firstly, the weight of the P(MMA-co-NVP) disc and the wet layer of PDMS could exceed the maximum load that the tab-disc interface can hold. Secondly, the solvent in the PDMS dipping solution could penetrate the tab-disc interface- leading to failure. However, in both of these cases it would be predicted that the thicker disc would fail first, thus making the result shown in Table 5.3 unexpected. It is therefore possible that some experimental factor is contributing to the manufacturing failure. For example, the lighter samples may be disproportionally affected by the air flow within the fume hood, causing increased motion of the joint during the three days of drying, leading to failure of the tab joint by fatigue. Further work in this area, including increasing the sample size and range, and considering different applications techniques will be discussed in Chapter 8.

The thickness of the PDMS sample has been shown, in section 5.3.1, to have no effect on the recorded mechanical properties (Young's modulus, UTS or failure strain). However, as observed in Figure 5.11 and Figure 5.16, the thickness of the PDMS affects the swelling

behaviour of non-irradiated and γ-irradiated samples. This has also been observed in other studies (171). Therefore, the rate of expansion of the underlying gel increases as the coating thickness decreases. It is possible that this increased expansion rate contributes to premature rupture of the PDMS coating. Furthermore, other factors may complicate the comparison of cast PDMS and dip coated PDMS. For example, the surface of the substrate on to which the PDMS is cast may affect the presence of defects in the PDMS. Surface debris or a rough polymer surface could cause a defect in the coating, and it is possible that the surface of the P(MMA-co-NVP) discs creates more defects than the surface of the PS petri dish. Similarly, controlling local variation in the thickness of the coating is more difficult in dip coating than casting a flat sheet. Therefore it is possible that regions of thinner PDMS exist within the coatings, but not within cast sheets. If a region of the coating is defected, or thinner than the surrounding coating, then the rate of diffusion of water into this region increases; thereby increasing the local rate of expansion, and so increasing the likelihood of failure. This behaviour was observed in the failed samples (Figure 5.6), and is shown schematically in Figure 5.19.

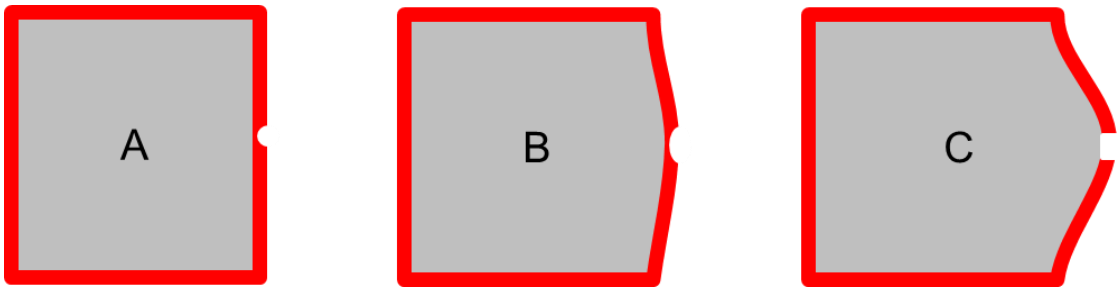

Figure 5.19 A schematic showing the result of increased diffusion into a hydrogel at a defect site. A: Defect present in coating. B: Hydrogel is immersed in water, increased diffusion at the defect site leads to increased swelling of the local hydrogel and therefore increased local stresses in the PDMS coting. C: Coating ruptures due to increased local stresses

As γ-irradiation of the cast PDMS sheets appears to cause an increase in defects (thus lowering the UTS and failure strain) it may be expected that the γ-irradiated coatings fail prematurely compared to the non-irradiated coatings. As a smaller range of coatings cycles were used on γ-irradiated samples it is not possible to make this comparison. However, all (initial height 12 mm, compression ratio $C = 3$) samples coated with four, eight and 12 coating cycles, which were γ-irradiated swelled successfully (no rupture in the coatings). This may be because whilst the new defects were large enough to cause failure at just under

3MPa, they were not sufficient to affect the rate of diffusion into the samples (therefore not increasing the risk of coating failure).

5.4.3 Swelling behaviour of coated samples

Figure 5.12 and Figure 5.17 show that for both non-irradiated and γ-irradiated samples there is a significant reduction in the strain rate of expansion (calculated by Equation 5.1). As discussed in section 2.1.3, the rapid expansion of a hydrogel device (both nude and contained within a silicone bag) causes pain and discomfort in patients, with the nude hydrogels causing necrosis and rupture of the tissue (18,45). The strain rates found for both non-irradiated and γ-irradiated samples are considerably lower than the expansion rates determined for the commercially available isotropic hydrogel devices (shown in Table 2.2). With the greatly reduced strain rate, it is hypothesised that expanders coated directly with PDMS will cause fewer of the aforementioned complications *in vivo.*

Figure 5.8 and Figure 5.13 show that the reduction in swelling rate is accompanied by a (well documented (18,6,171,172)) reduction in maximum swelling uptake for both non-irradiated and γ-irradiated samples. As seen in Figure 5.11, the reduction in the percentage change for mass and height increases with coating thickness, therefore it is recommended that the minimum reliable coating thickness is used for coating hydrogels. This will ensure that a safe expansion rate is achieved, with the maximum area of tissue generated. Equation 5.2 and Equation 5.3 describe how the percentage change in height and mass respectively vary with coating thickness. The constant values (height: 420 and mass: 515) should predict the percentage swelling in parameter with a coating thickness of zero. These values are underestimates; however it should be considered that the coated devices were swollen over a six-week period and not to equilibrium, and therefore an underestimate in nude final swelling would be expected. Equation 5.2 and Equation 5.3 can therefore only be used when considering samples within the range shown. It should be noted that other coating studies have recorded the devices swelling until swelling mass equilibrium (taking up to eight months), rather than over the course of normal clinical use (18,6,171,172). As seen in Figure 5.8 and Figure 5.13, the gels in this study were not at equilibrium mass after six weeks of

expansion. The time scale of expansion for other coated devices, as well as percentage changes compared to the nude sample, are not given, therefore direct comparison of the changes to swelling behaviour with different coating methods are not available. An important feature of the curves showing percentage change in diameter with time for both ɣ-irradiated non-irradiated, Figure 5.10 and Figure 5.15, is that there is a delay before expansion occurs. This delay is caused by the initial time required for water to diffuse across the silicone membrane, before an osmotic gradient is established and bulk diffusion occurs. The effect appears to be more pronounced in the ɣ-irradiated samples. Further investigation into this phenomenon is of interest, as a delay before swelling would allow time for wound healing to occur.

As discussed in 2.1.2, the increase in height of a tissue expander is the most important parameter for increasing the surface area of skin generated. It is therefore an important finding that whilst there is an average reduction of 94% of mass increase during expansion, the reduction in height is only 46%. This is the case for both non-irradiated and ɣ-irradiated samples. Nude samples also initially exhibit this behaviour, as described in section 3.3.2, where an initial increase in the height but a decrease in diameter is observed during the first five hours of expansion (due to the residual strains induced by compression moulding). For coated samples, this appears to occur during the first 200 hours (Figure 5.9 and Figure 5.14). Table 5.5 shows that this increase in height requires a smaller volume of water than subsequent increases in height, hence explaining the difference in reduction of parameters. The height is gained at the expense of the diameter.

Table 5.5 A comparison of the number of grams of water required to increase the height of the sample 1mm, for samples coated with four, eight and 12 coating cycles (non-irradiated samples)

	Number of coating cycles		
	4	**8**	**12**
Initial 200 hours of expansion	0.10 g/mm	0.06 g/mm	0.05 g/mm
Remaining 800 hours of expansion	0.60 g/mm	0.98 g/mm	0.62 g/mm

The γ-irradiated samples also showed a reduction in the strain rate with coating (Figure 5.17), a reduction in the overall swelling which increased with coating thickness (Figure 5.16, Equation 5.4 and Equation 5.5), and a greater reduction in diameter than height. However, the dependency of swelling on the coating thickness for γ-irradiated samples differ from that of non-irradiated samples. For coating cycles eight and 12 there is very little difference observed between the final percentage changes in mass, height and diameter for non-irradiated and γ-irradiated samples. However, for four coating cycles the percentage change in mass and height is lower for γ-irradiated samples than non-irradiated samples. This result is not expected as it indicates an increase in the stiffness (and therefore cross-linking) of the PDMS coating, which is not observed in the PDMS cast sheets (as discussed in 5.4.1). As the underlying hydrogels contain residual molecules (discussed in Chapter 4), it is possible that these residual molecules facilitated cross-linking of the PDMS at the interface between the hydrogel and the PDMS. This would disproportionally affect the thinner coating (four cycles), as the residual molecules would only be in contact with the PDMS at the interface. It is not possible to confirm that this is the case from the work presented; however suggestions for future work will be given in Chapter 8.

5.5 Summary

This chapter addressed questions research questions RQ7 and RQ8. A summary of the findings and implications will be given in this section:

RQ 7) How does the application of a semi-permeable silicone coating affect the swelling rate of devices?

Coatings below 0.375mm are ineffective at controlling the swelling, despite films of this thickness exhibiting theoretically sufficient tensile strength. A possible reason for this premature failure has been proposed; i.e. any defected reason will cause an increase in diffusion at that point, thus increasing the local stresses at the defected site and causing rupture. These failures have not been observed in thicker coatings.

It has been shown that coatings of thicknesses between 0.375mm and 0.600mm are effective at reducing the rate of expansion of hydrogel devices over a six-week period (as seen in Figure 5.12 and Figure 5.17). This reduction in the rate of increase in the height of the device (and therefore the strain rate of the overlying coating and skin during expansion) may be key in reducing the pain and discomfort experienced by patients, particularly during the early stages of expansion.

The swelling mass uptake and the increase in height are shown to be lower for the coated samples than the nude samples. This trend follows a linear decrease as the coating thickness is increased. However, the diameter of the device is initially reduced, resulting in a greater increase in height per gram of water absorbed during the initial 200 hours, and thus compensating for some of the lost expansion. As this loss can be predicted, it may be possible to adapt the hydrogel dimensions to suit different clinical situations (accounting for coating losses). The recommended coating thickness is four coating cycles (0.375mm), as this thickness is the minimum thickness (therefore minimising the loss in height) which can reliably reduce the swelling rate.

RQ 8) What is the effect of γ-irradiation on the performance of the silicone coatings?

The effect of γ-irradiation on the cast sheets of silicone is to reduce the failure strain and UTS values; however the Young's modulus is not affected. It is therefore proposed that the γ-irradiation is causing an increase in defects in the silicone sheet.

The key behaviours are not affected by γ-irradiation; the strain rate is lowered considerably, and there is a reduction in the swelling mass uptake of the samples. There are some minor discrepancies in the changes for different coating thickness. It is possible that these are caused by interactions with the residual molecules in the hydrogel. Suggestions for determining this more decisively are given in Chapter 8.

These findings mean that the rate of tissue expanders can be effectively, and reliably, controlled, without the need for additional components (e.g. a silicone bag, or injection port).

The reduction in expansion rate, particularly within the first 24 hours, is predicted to reduce the surgical complication rates experienced with hydrogel tissue expanders.

CHAPTER 6:

Animal Model

6 Animal Model

6.1 Introduction

RQ 9) What is the *in vivo* behaviour of a non-prismatic tissue expander?

As discussed in section 2.1.2, samples which expand anisotropically from a disc into a device with a non-prismatic cross-section may be of clinical use in reducing complication rates, by improving the quality of the tissue produced, and in growing excess skin with anisotropic resting tension. Such devices have been developed within this thesis, as discussed in section 3.4.

This chapter will aim to answer RQ9 by first establishing whether a viable, anisotropic non-prismatic device can be produced. It describes an experimental procedure in which the dome and wedge devices were washed, for reasons described in Chapter 4, and then coated in 0.375mm of PDMS coating in order to control the rate of expansion (Chapter 5). Once a viable device had been produced, it was implanted in the limb of a Dorper sheep. The most important aim of this procedure is to establish whether the non-prismatic shape would be retained during *in vivo* swelling, and this was achieved through daily measurements and photographs of the expander during inflation. Furthermore, tissue samples were taken in order to determine whether there had been any detrimental change to the expanded tissue.

6.2 Experimental Methods

Device preparation and *in vitro* swelling experiments were conducted by the author in the United Kingdom. The *in vivo* experiments (including surgery, swelling measurements, observations, photographs, histology and microscopy of histological sections), were conducted on behalf of the author by the University of Malaya and the University of Putra Malaysia.

6.2.1 Sample Preparation

Six dome-shaped samples and four wedge-shaped samples were lathed as described in section 3.3.1. In order to remove the residual molecules, the samples were hydrated for six hours. The time was calculated by determining the number of hours required to remove residual molecules from 1mm^3 of P(MMA-co-NVP), as seen in Equation 6.1. This value was then used to determine the number of hours of hydration required to remove the residual molecules from domes and wedges, shown in Equation 6.2 and Equation 6.3 respectively. $t_{v=1mm}$ represents the time (in hours) required to remove the residual molecules from 1mm^3 of P(MMA-co-NVP); t_c is the time to wash a single rod of P(MMA-co-NVP); v_c is the volume of a single rod of P(MMA-co-NVP); t_d is the time required to wash a dome pellet; v_d is the volume of a dome pellet; t_w is the time required to wash a wedge pellet; v_w is the volume of a wedge pellet. The samples were then left to air dry for six hours, before being dried in an oven overnight at 80°C. All samples were then compressed to a height of 4mm, as described in section 3.2.2. Following compression, all samples were coated in PDMS (as described in section 5.2.3) with four coating cycles (giving each expander a coating thickness of 0.375mm). Finally, coatings were exposed to 25kGy γ-irradiation, as described in 4.2.1.

$$t_{v=1mm} = \frac{t_c}{v_c} = 0.0040744h.mm^{-3}$$

Equation 6.1

$$t_d = t_{v=1mm} * v_d = 6.5h.mm^{-3}$$

Equation 6.2

$$t_w = t_{v=1mm} * v_w = 6.6h..mm^{-3}$$

Equation 6.3

Clinical results for a further two cylindrical expanders were provided by Oxtex Ltd. These devices were also manufactured using (residual free) P(MMA-co-NVP) rods (Polymeric

Sciences Ltd (Longfield, Kent, UK)). The compression ratio of the device was approximately $C = 3$. Samples were coated with perforated silicone- with two perforation points which are indicated on Figure 6.10.

6.2.2 *In vitro* swelling experiments

Four domed samples and four wedged samples were expanded in distilled water at 37°C, as described in 3.2.3. The mass, upper and lower heights, and diameters of the samples were recorded as described in section 3.2.3, with the percentage changes in each parameter being calculated using Equation 2.17, Equation 2.18 and Equation 2.19 respectively. These results were used to determine which expanders were most suitable for implantation.

6.2.3 Surgical procedures (implantation and device removal)

. The research was approved by Institutional Animal Care and Use Committee (IACUC) of the Faculty of Veterinary Medicine, University Putra Malaysia, UPM/IACUC/AUP-R031/2013. The results provided by Oxtex Ltd were also obtained by the aforementioned institutions, following the protocol described below.

Two male Dorper sheep, aged between six to 12 months were chosen for this study. One domed sample (as described in section 6.2.1) was implanted in the front left limb of each sheep[1]. The body weight of the sheep ranged between 35kg and 50kg. The sheep were fasted for 24 hours prior to surgery, and weighed one hour before sedation in order to calculate the appropriate sedation dosage. The sedation was achieved through a mixture of 3-5 ml ketamine, 100 mg/ml (Vetoquinol, UK) and 1-2 ml diazepam, 10 mg/2 ml (Diapine, Atlantic Labs, Thailand). The drugs were administered intravenously through the jugular vein. The left forelimb of the sheep was shaved and cleaned with alcohol. For induction, a needle was inserted into its cephalic vein and 2 ml ketamine, 100 mg/ml (Vetoquinol, UK) was introduced. Before intubation, soft rope was placed around each the upper and lower jaw to facilitate the mouth opening and for the head to be elevated and extended. The endotracheal

[1] Due to constraints of our collaborators this was the maximum number of devices which could be implanted. Therefore, the domed devices were prioritised and previous results of similar cylindrical devices will be used for comparison.

tube was inserted, secured and the cuff was inflated. The inhalation anaesthetic was maintained with isoflurane (Piramal, India).

Prior to incision, the thickness of the limb at the surgical site was measured with callipers in order to ascertain the degree or stretch and growth in the tissue after implantation. The surgical site was cleaned with Ethanol (R&M chemicals, UK), povidone iodine (Vetasept, UK) and distilled water. A 3 cm horizontal incision was made 3 cm from metacarpal dorsal. Subcutaneous dissection was made and the expander was inserted. The incision was sutured with vicryl 3-0 (Ethicon Ltd, US). After implantation, the thickness of the limb at the surgical site was measured again with callipers in order to ascertain the degree of stretching caused by the device in the dry state.

The device was removed after 14 days *in situ*, with the same surgical conditions as described above. In order to explant the device, a vertical elliptical shape incision was made on the side of the site of the expander. The fibrous capsule surrounding the device was undermined. A small incision was made on the outer wall of the capsule, followed by blunt dissection to expose the device. The expander was carefully removed from the fibrous capsule. The expanded skin tissue was harvested and stored in 10% formalin. The remaining skin tissue was sutured to recover the normal condition.

6.2.4 Monitoring *in vivo* expansion

During the 14 days in which the device was inserted in the sheep, the animals were allowed free access to food and water. The behaviour of the sheep was closely monitored during the 14 days, and any abnormal behaviour (including reduced appetite, limping and other signs of pain) was recorded. Daily measurements of the implant site were taken using digital callipers, at the maximum expansion point. To determine the percentage change in height Equation 2.19 was used, with the measurements taken as shown in Figure 6.1. Daily photographs (Canon EOS 60D, Japan) were also taken to monitor the shape of the expanded devices.

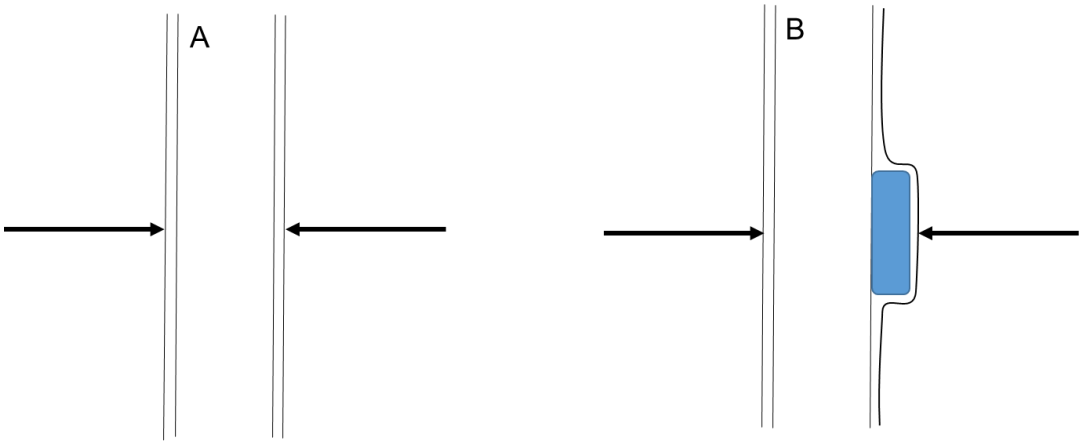

Figure 6.1 A schematic showing how the measurements of *in vivo* expansion were acquired. A: pre-surgery measurement of the leg thickness (showing leg with overlying skin). B: Measurements taken immediately after expansion, and every day during expansion

6.2.5 Histology

The harvested expanded tissue, as well non-expanded tissue from the same limb (to act as a control), was fixed using 4% paraformaldehyde in a buffered solution. The fixation of tissue took 48 hours and was carried out at room temperature. In order to dehydrate the tissue after fixation, the tissue was placed in a series of alcohol baths of increasing concentration (70% alcohol, 95% alcohol, and finally absolute alcohol and toluene) at 4°C. The dehydrated tissues were then immersed in liquid paraffin wax at 58°C for 15 minutes. The paraffin block (with embedded tissue) was then cooled. The tissue was sectioned using a microtome with 10 serial sections of thickness 4 µm.

Samples were stained with haematoxylin and eosin stain (H&E). The features which the H&E stain identifies are given in Table 6.1. Before staining with haematoxylin, the samples were rehydrated. This was achieved by immersion in xylene blue, followed by immersion in alcohol of decreasing concentrations (absolute alcohol, 95%, 70%) and finally water. The haematoxylin stain was then applied, and the sample washed in water. As eosin is more soluble in alcohol than water, the specimen was again dehydrated with alcohol (as described previously) before the eosin stain was applied. The sample was then passed through xylene, before being placed between glass cover slips for microscopy work.

The samples were analysed with Panoramic Viewer software (3D Histech Kft, Budapest, Hungary).

Table 6.1 The tissue components which are stained by haematoxylin and eosin

	Tissue type	Examples
Haematoxylin	Basophilic	cell nucleus, RNA, proteins in cytoplasm, mucus, mucoproteins
Eosin	Eosinophilic	cytoplasm, muscle fibre, connective tissue fibre, secretory granules, erythrocytes, fibrous tissue, protein precipitate

6.3 Results

6.3.1 Swelling Profile (*in vitro*)

All domed samples were swollen without coating rupture over the six-week period. However, two of the wedge samples failed; the first to fail failed at two weeks, the second at five weeks. The following results only include samples which had no coating damage at week six.

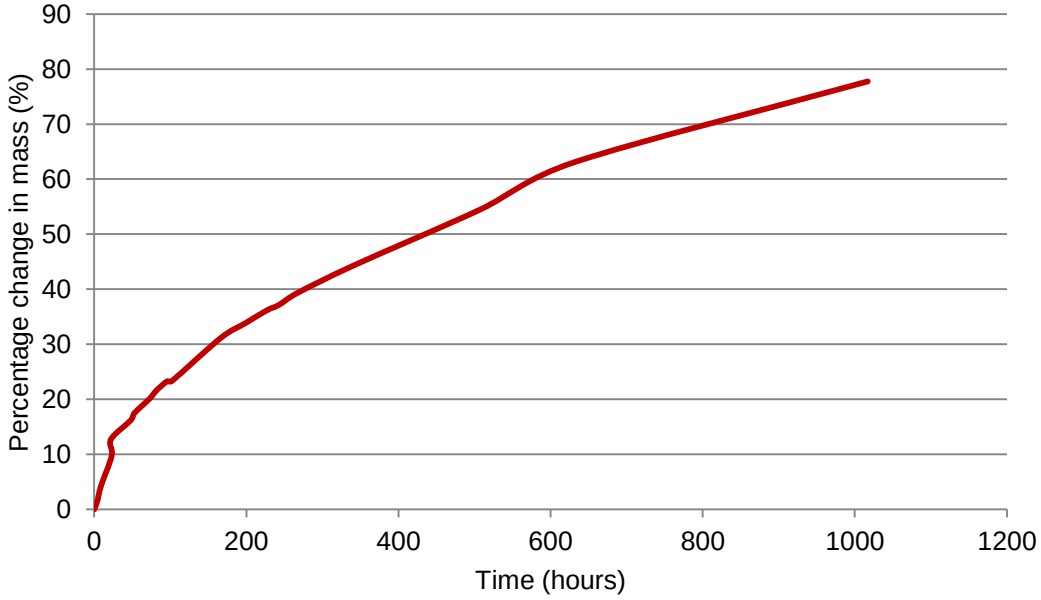

Figure 6.2 A comparison of the percentage change in mass for a dome-shaped, coated sample over a six-week period

Figure 6.2 shows the percentage change in mass for the coated, domed sample. The change in mass is decreased from an increase of almost 600% for the nude samples (Figure 3.29) to an increase of almost 80%.

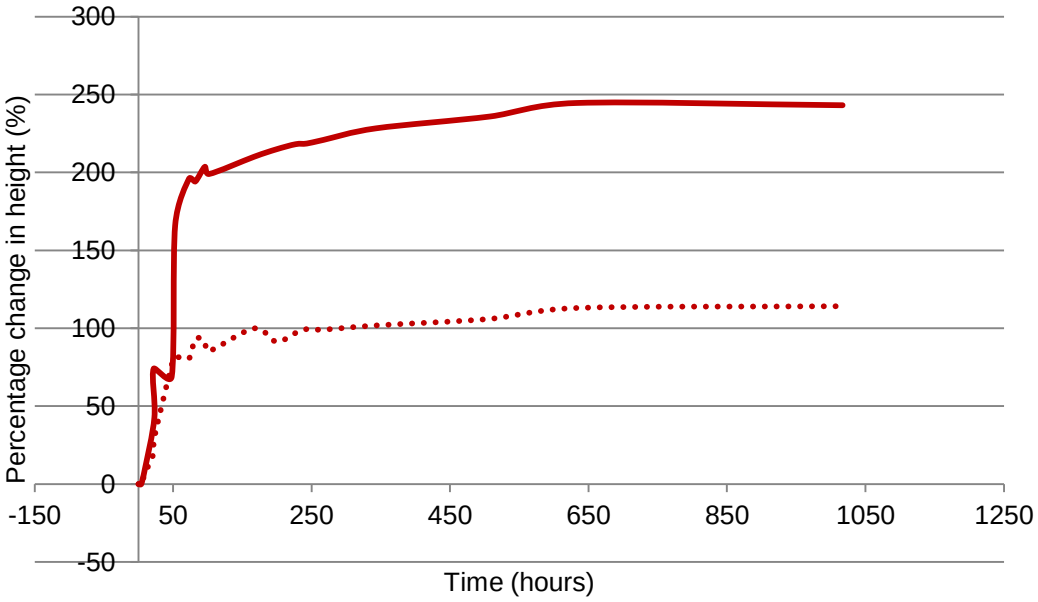

Figure 6.3 A comparison of the percentage change in the lower (dotted) and upper (solid) heights (as defined in 3.2.3) for a coated domed sample over a six-week period

Figure 6.3 compares the percentage change in the lower and upper heights (as described in 3.2.3) for domed samples. The percentage change for the upper height is approximately half of the percentage change of the nude samples at equilibrium. The lower height is approximately two thirds of the percentage change of the nude values at equilibrium. The first 70% of increase in height occurs over the first 100 hours. The corresponding strain rate in this time reaches a maximum of $0.023h^{-1}$.

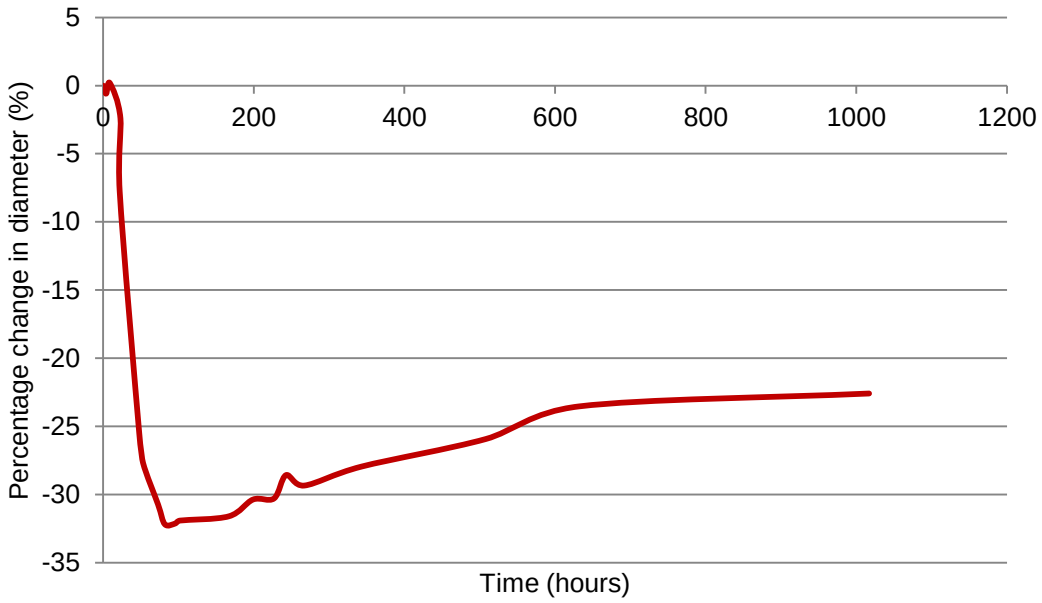

Figure 6.4 A comparison of the percentage change in diameter for a coated domed sample over a six-week period

Figure 6.4 compares the percentage change in diameter for coated domed samples. The diameter initially reduces by approximately 30% during the first 100 hours, and then increases gradually to -22% of the initial diameter over the remainder of the six weeks.

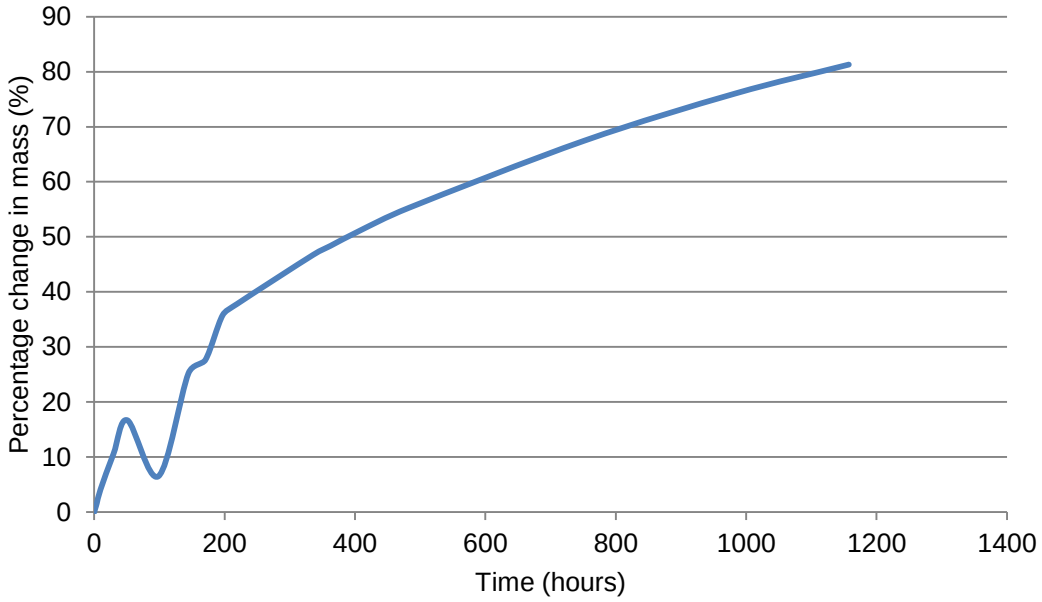

Figure 6.5 A comparison of the percentage change in mass for a coated wedged sample over a six-week period

Figure 6.5 shows the percentage change in mass for the coated, wedged sample. The change in mass is decreased from an increase of almost 600% for nude samples (Figure 3.29) to an increase of approximately 80%.

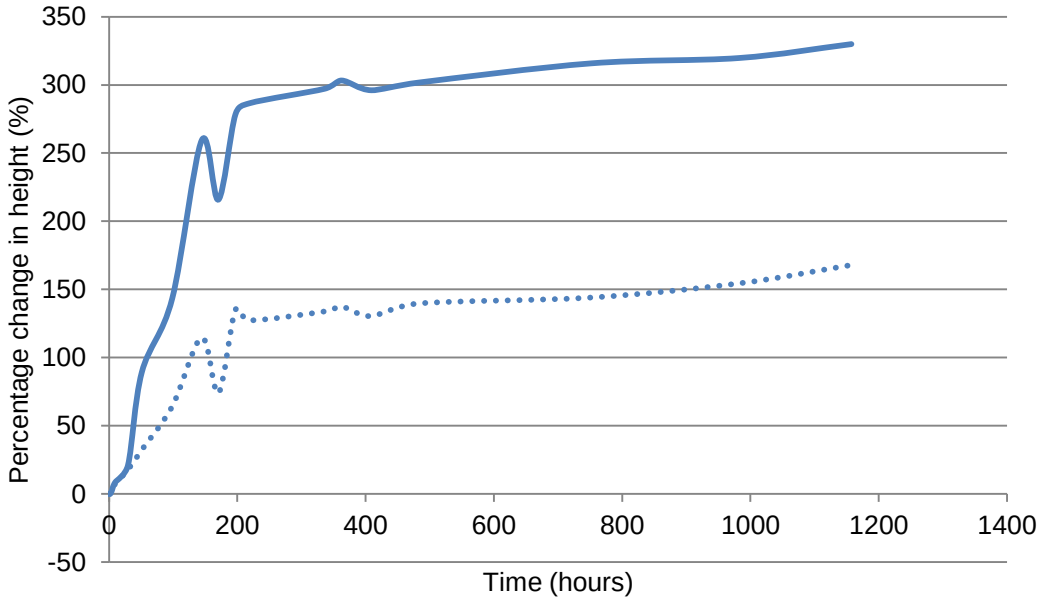

Figure 6.6 A comparison of the percentage change in the lower (dotted) and upper (solid) heights (as defined in section 3.2.3) for a coated wedge sample over a six-week period

Figure 6.6 compares the percentage change in the lower and upper heights (as described in section 3.2.3) for wedged samples. It can be seen that the device has expanded to a maximum increase of 330% (two thirds of the nude sample), and a lower height increase of 168% (0.96 of the nude sample). 70% of the expansion occurs within the first 200 hours.

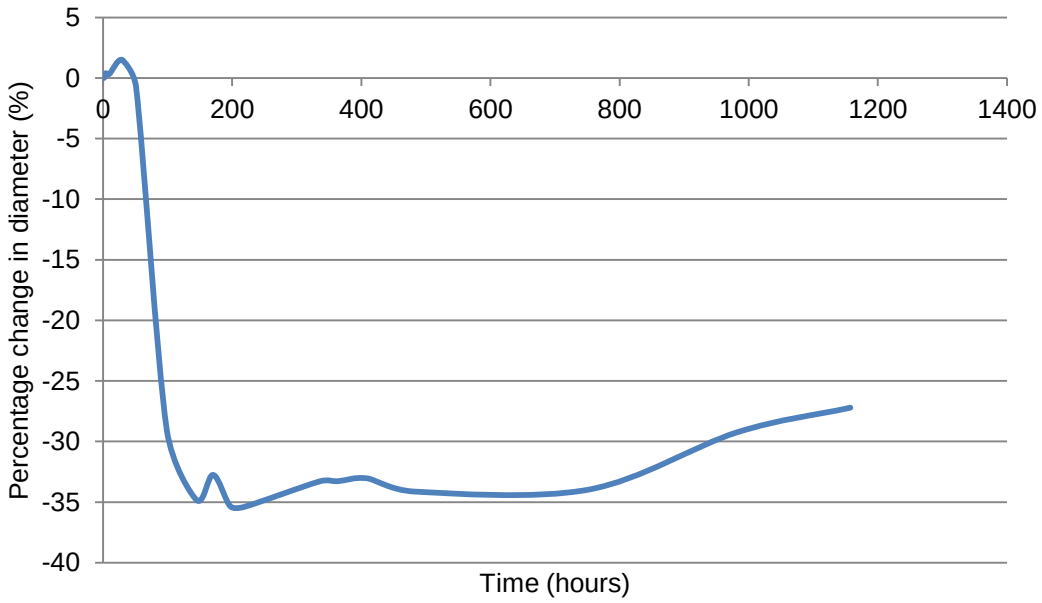

Figure 6.7 A comparison of the percentage change in diameter for a coated wedged sample over a six-week period

Figure 6.7 compares the percentage change in diameter for coated wedge samples. The diameter initially reduces by approximately 35% during the first 100 hours, and then increases gradually to -27% of the initial diameter over the remainder of the six weeks.

Figure 6.8 A photograph of a coated wedge sample (washed and γ-irradiated) after six weeks expansion. The scale bar represents 10mm

Figure 6.8 shows an image of a coated wedge sample (expanded over six weeks). It can be observed that the wedge shape is retained during expansion within the PDMS coating.

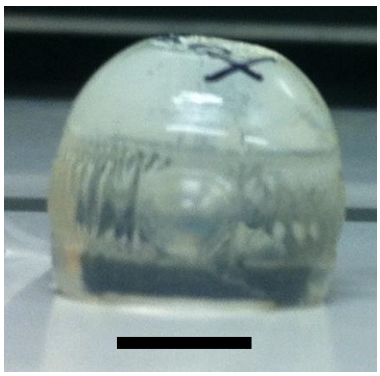

Figure 6.9 A photograph of a coated dome sample (washed and γ-irradiated) after six weeks expansion. The scale bar represents 10mm

Figure 6.9 shows an image of a coated dome sample (expanded over six weeks). It can be observed that the dome shape is retained during expansion within the PDMS coating.

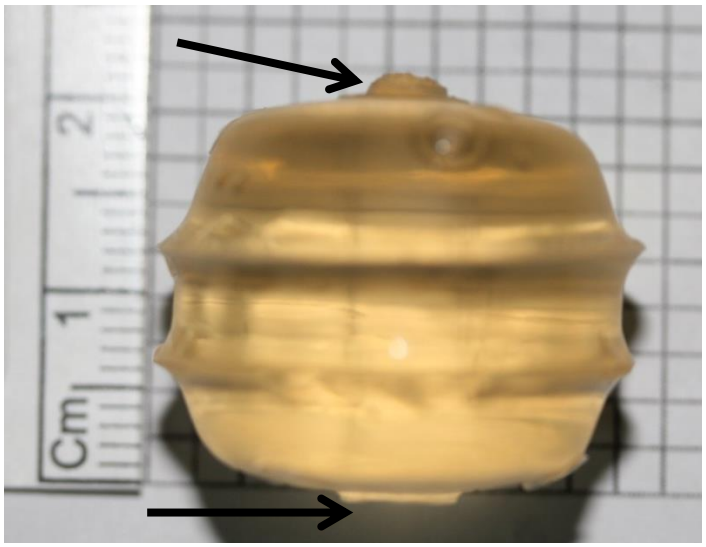

Figure 6.10 A photograph of an Oxtex Ltd expander (at equilibrium swelling). The arrows indicate the perforation points on the silicone

Figure 6.10 shows an image of an Oxtex Ltd expander at equilibrium swelling. The device has a slightly barrelled geometry, and a swelling height of approximately 2cm.

6.3.2 Swelling Profile (*in vivo*)

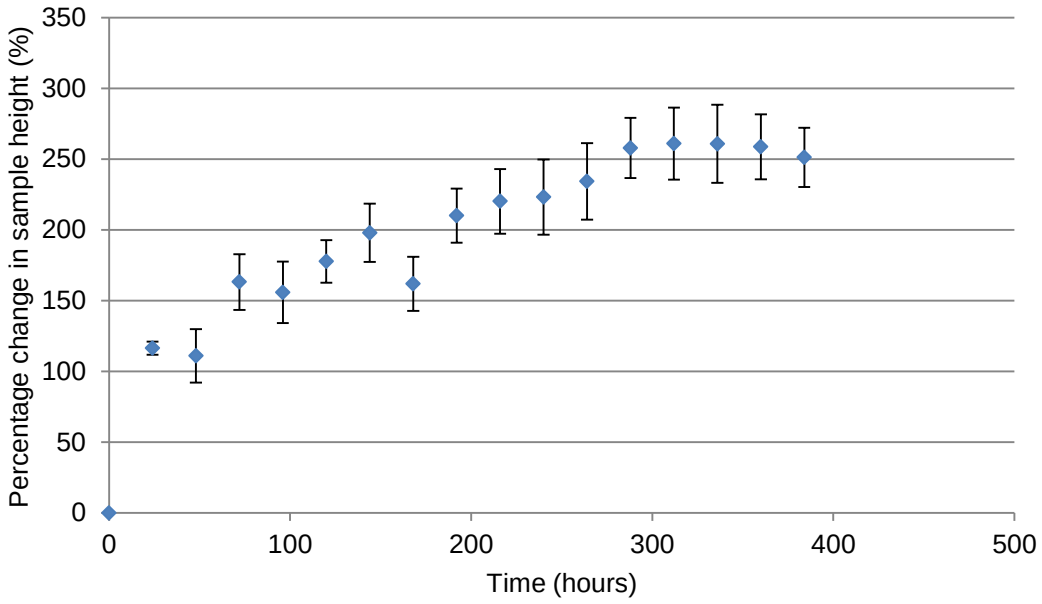

Figure 6.11 The percentage change of maximum height of domed devices inserted in the limb of a sheep over a two-week period

Figure 6.11 shows the percentage change in the maximum height for domed samples *in vivo*. In the first 24 hours the expander doubles in height; however the expansion between 24 hours and 300 hours is approximately linear. At 300 hours the height appears to have reached a maximum.

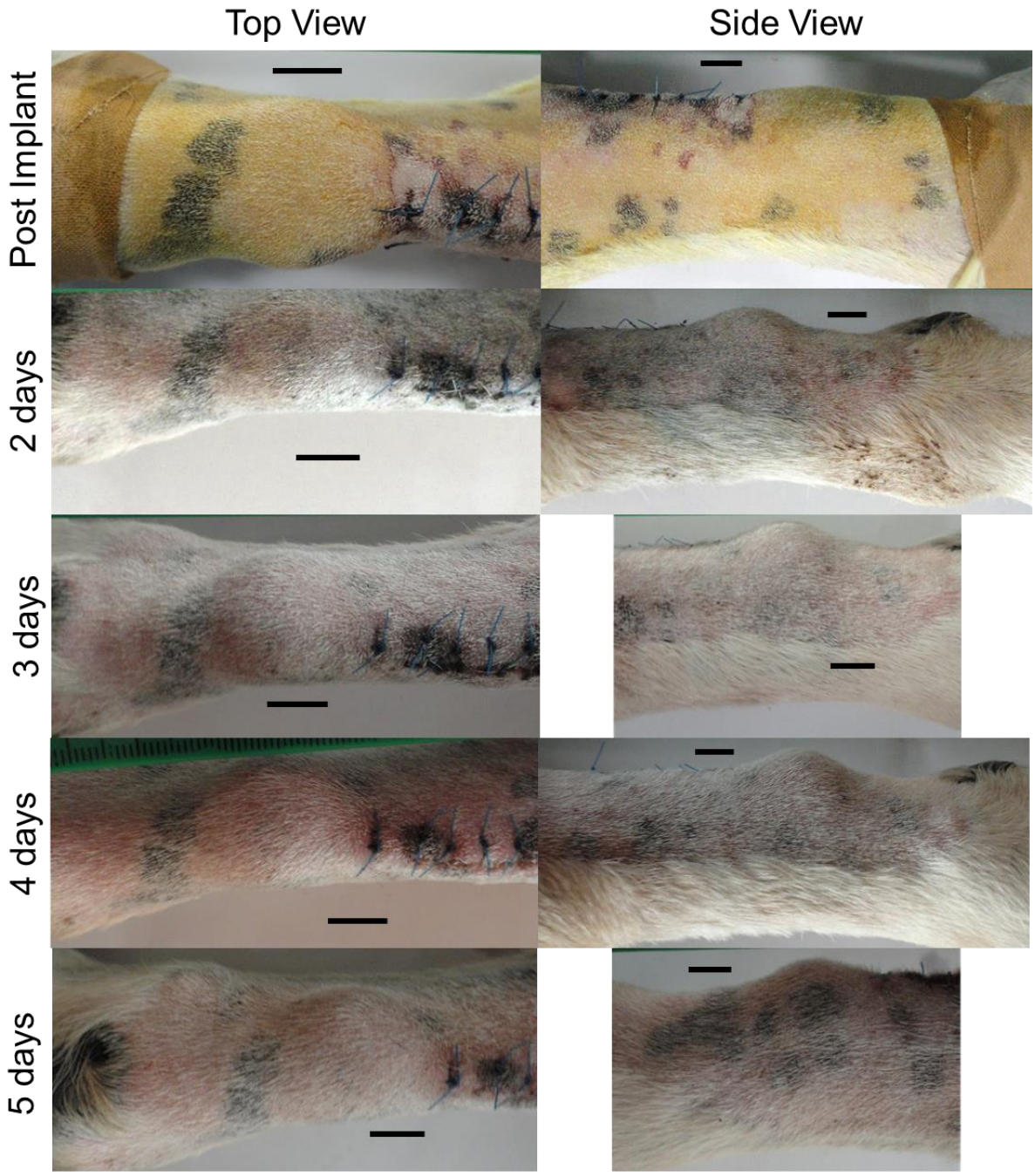

Figure 6.12 Photographs showing the shape of the expansion of a domed device during the first five days *in vivo*. Scale bars represent 10mm

Figure 6.12 shows the shape of the device during the first five days of expansion. The dome shape of the expanders is observed from day two.

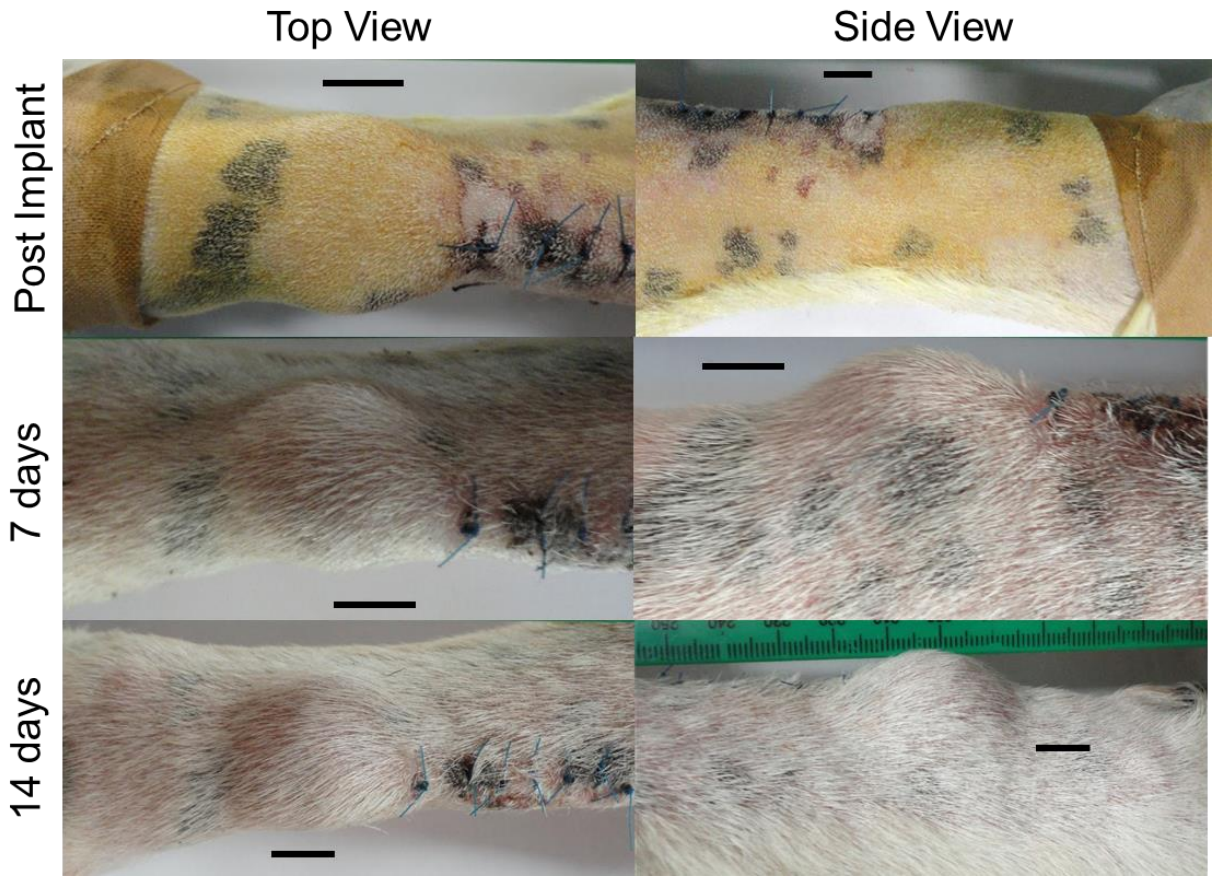

Figure 6.13 Photographs showing the shape of the expansion of a domed device during the first fourteen days in vivo. Scale bars represent 10mm

Figure 6.14 shows the expansion of the domed device over the 14-day period. The dome shape is still observed at the seven- and 14-days points. However, the vertical sides of the domed shape expander are not visible.

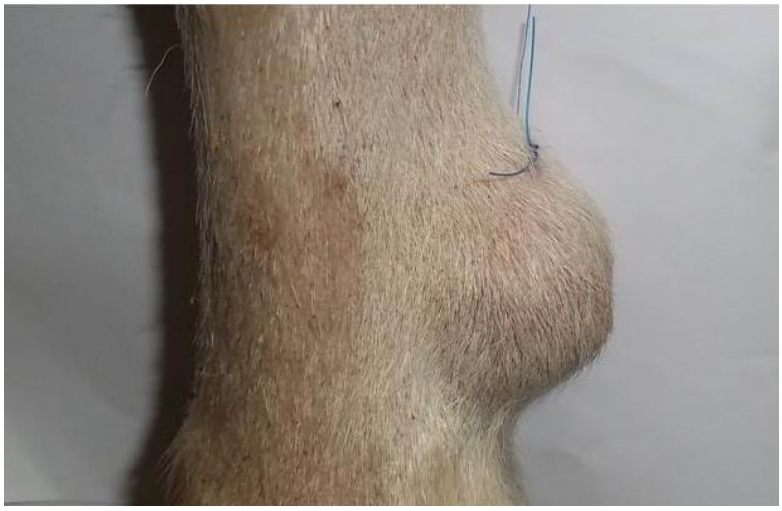

Figure 6.14 Photograph showing the shape of expansion of a cylindrical device (manufactured by Oxtex Ltd) during *in vivo* expansion (scale bar not available)

Figure 6.14 shows an Oxtex Ltd expander after two weeks of expansion. The shape of the expander is preserved (compared to the photographs of the expander swelling *in vitro*- shown in Figure 6.10).

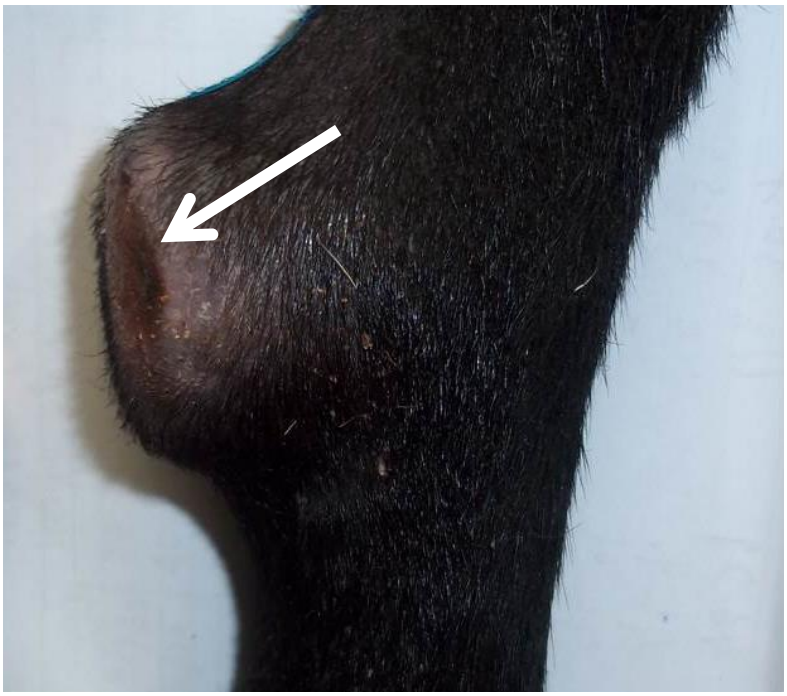

Figure 6.15 Photographs showing the shape of expansion of a cylindrical device (manufactured by Oxtex Ltd) during *in vivo* expansion (scale bar not available). The arrow marks a region of damage to the tissue at the edge of the cylinder

Figure 6.15 shows a different Oxtex Ltd expander, where damage to the soft tissue has occurred to the skin covering the top edge of the cylinder (marked by the white arrow).

6.3.3 Histology

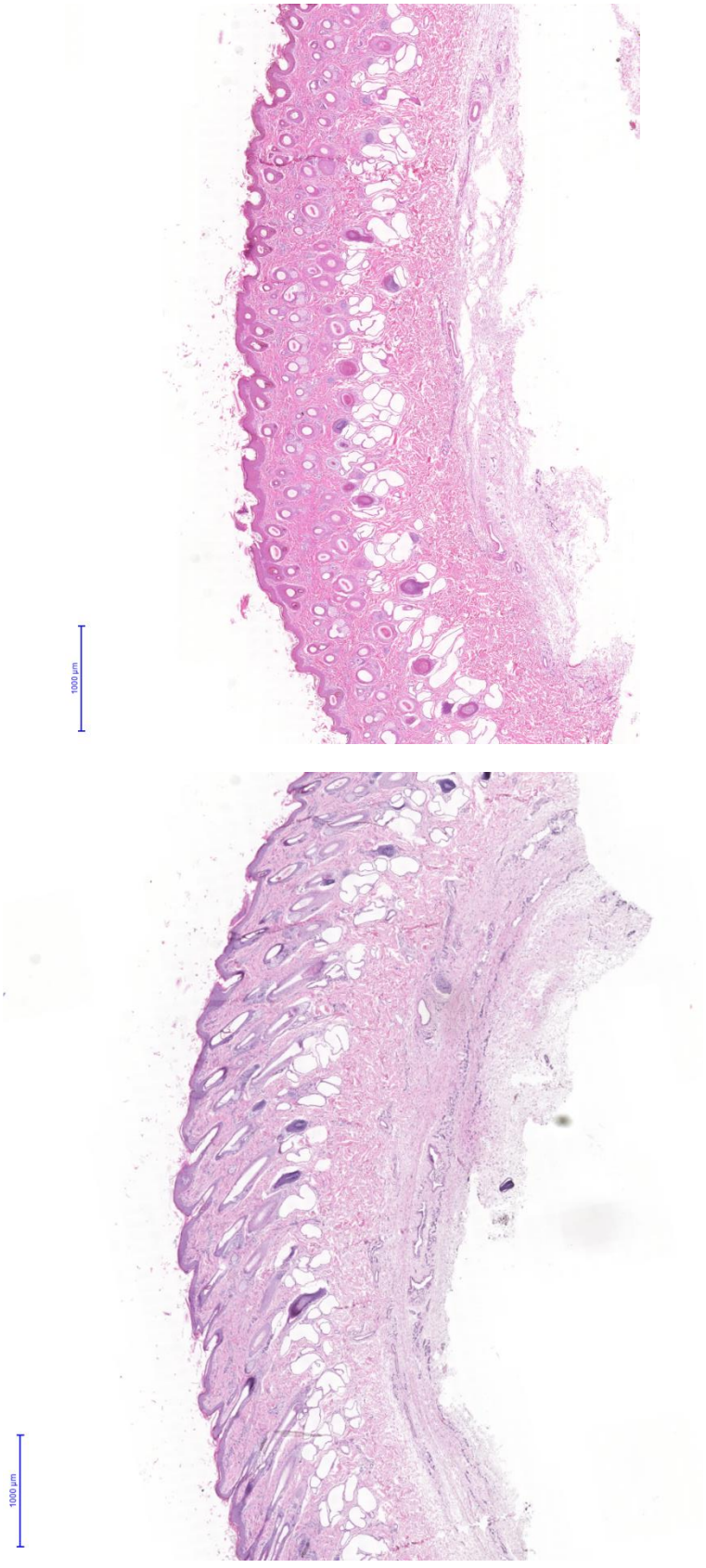

Figure 6.16 A comparison of the histology of control tissue (top) and expanded tissue (bottom). The scale bars represent 1mm

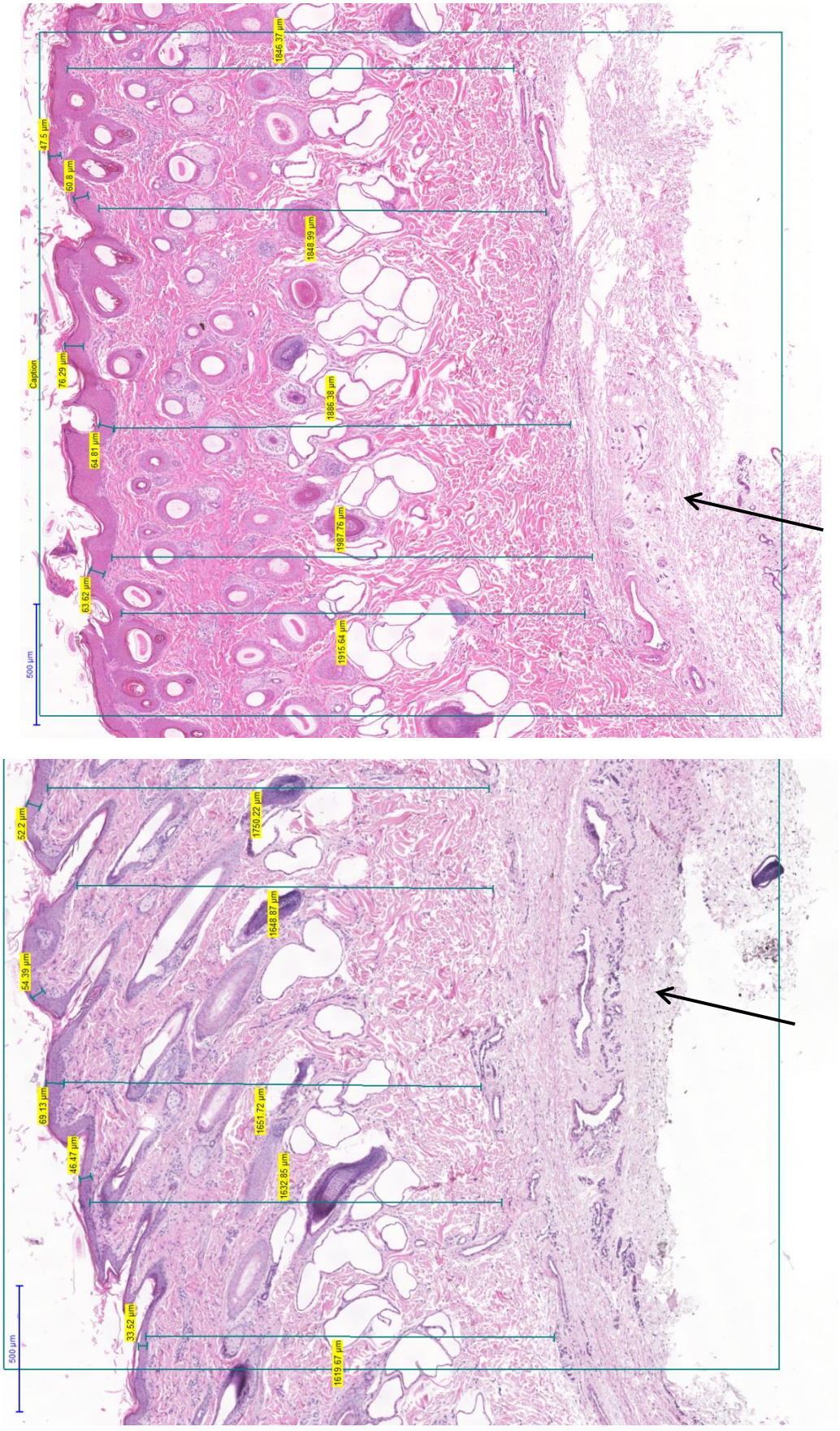

Figure 6.17 A comparison of the histology of control tissue (top) and expanded tissue (bottom). The arrows indicate fibroblasts, the scale bars represent 500µm, and the averages of the marked distances are reported in Figure 6.18 and Figure 6.19

Figure 6.16 and Figure 6.17 compare histology of the tissue for the control and expanded skin. The expanded tissue appears healthy and undamaged, with features such as hair follicles, sweat glands, and blood vessels appearing unchanged. In the expanded tissue there appears to be an increase in the numbers of fibroblasts present.

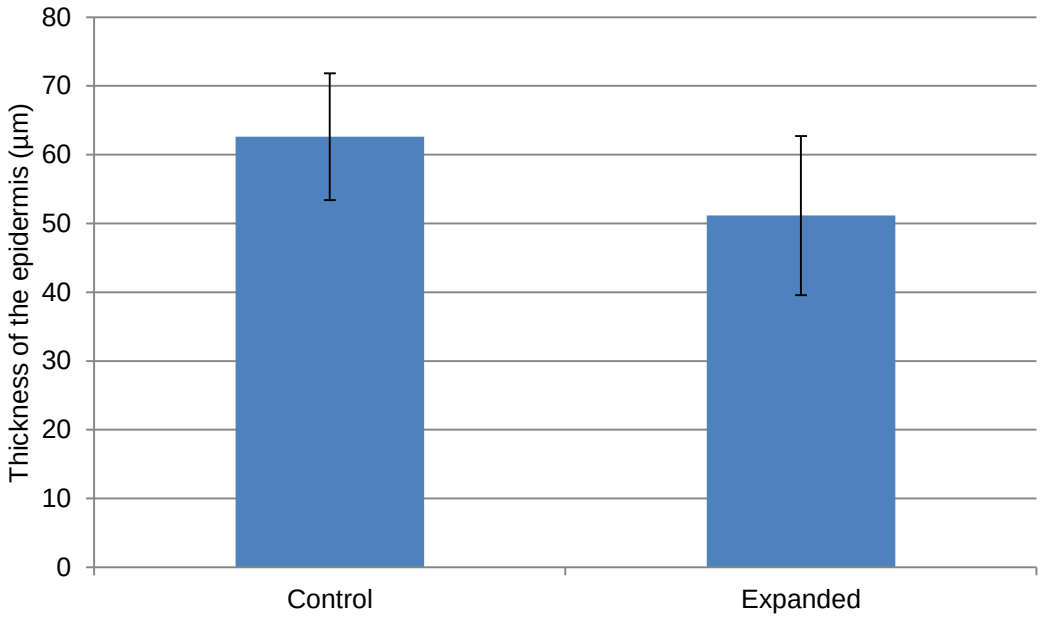

Figure 6.18 A comparison of the changes in thickness of the epidermis in expanded tissue compared to control tissue

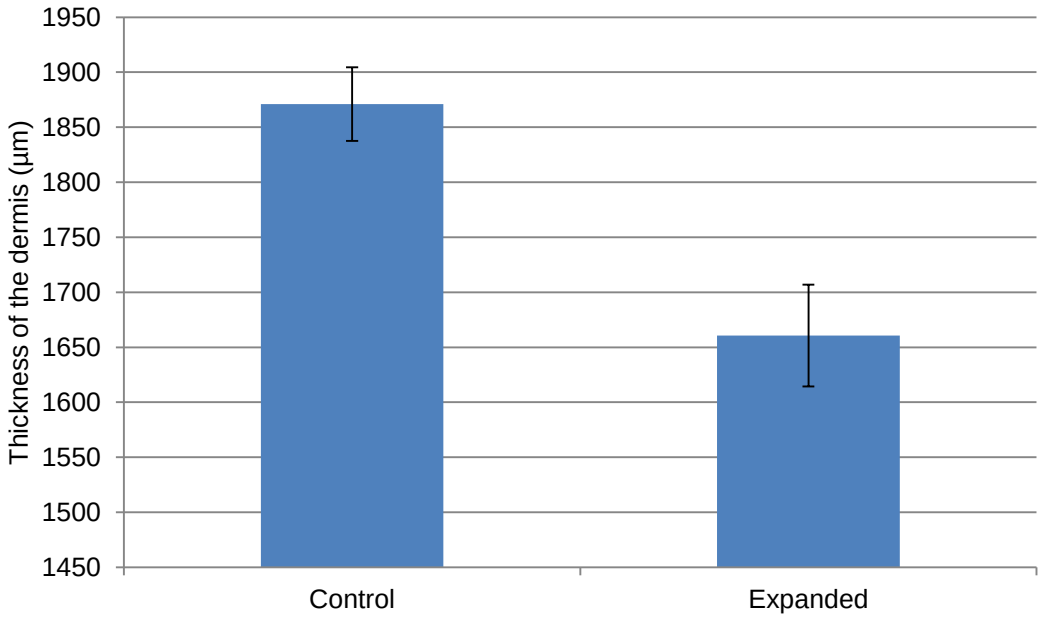

Figure 6.19 A comparison of the changes in thickness of the dermis in expanded tissue compared to control tissue

Figure 6.18 and Figure 6.19 compare the thicknesses of the epidermis and dermis respectively, for control and expanded skin. There is no statistical difference (as defined in section 3.2.6) in the thickness of the epidermis; however the dermis is statistically significantly thinner in the expanded tissue than in the control tissue.

6.4 Discussion

6.4.1 *In vitro* swelling

As mentioned in section 6.3.1, whilst all domed samples swelled successfully (without coating rupture), half of the wedge shape sample coatings ruptured during expansion. It is most likely that this rupture is the result of high stresses in the coating as the tip of the wedge shape protruded from the hydrogel disc. In both failed samples, the rupture in the coating appear to have initiated in this region.

Figure 6.3 and Figure 6.6 show that there was a reduction in the percentage change in height of coated (0.375mm of PDMS) dome and wedges respectively (when compared to the nude samples shown in Figure 3.30). Figure 6.2 and Figure 6.5 show that there was also a reduction in the mass uptake coated (0.375mm of PDMS) domes and wedges respectively (when compared to the nude samples shown in Figure 3.29). Finally, Figure 6.4 and Figure 6.7 show that there was a reduction in the percentage change in diameter of coated (0.375mm of PDMS) dome and wedges respectively. Furthermore, a reduction in the expansion rate, compared to the nude cylindrical samples, was also observed. These results indicate that the findings of Chapter 5 – that the PDMS coatings control the rate of expansion, but at the cost of total expansion volume – also apply to samples with non-prismatic cross-sections. A key finding is that, as seen in Figure 6.3 and Figure 6.6, the reduction in the upper and lower heights for both domes and wedges is not equal; the upper height is reduced more than the lower height. An explanation for this is that the ratio of surface area (covered in the PDMS coating) to volume of hydrogel varies in each geometry. This can be shown by considering the three geometries of the top of the samples, shown in Figure 6.20. The ratio of surface area to volumes for each geometry are given in Table 6.2,

and show that the wedge and dome samples both have a greater surface area to volume ratio. This means that for every unit volume of hydrogel (which is generating the force for expansion), there is an increased area of PDMS coating (which is opposing the force for expansion). The result of the changes in the ratio of surface area to volume would be for the restrictive force for the upper region to be greater than for that of the lower region- thereby resulting in the observed change in ratio of upper height to lower height.

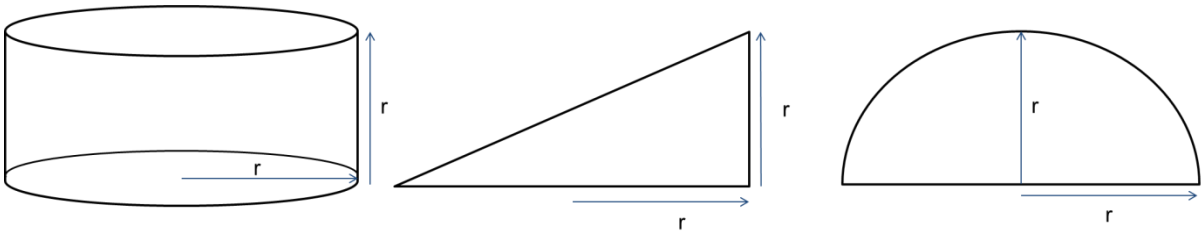

Figure 6.20 A schematic of the cylindrical (left), wedge (centre) and dome (right) geometries

Table 6.2 A comparison of the ratio of surface area to volume for cylinder, wedge and dome shapes

Shape	Surface area/ Volume (mm)
Cylinder	$0.25r$
Dome	$0.22r$
Wedge	$0.15r$

6.4.2 *In vivo* swelling

Figure 6.11 shows that the expansion for the domed samples *in vivo* was very similar to the expansion *in vitro* (upper height- Figure 6.3). The maximum swelling dimension was approximately the same, indicating that the *in vivo* pressure generation for devices with non-prismatic cross-sections is sufficient to deform skin. Furthermore, the expansion rate over the first three days was reduced; with 50% of swelling observed in the first 72 hours for *in vivo* samples. This compares very favourably with the clinical studies of hydrogels contained within perforated silicone bags, for which between 90-100% of final expansion was observed during the first three days (45,49,50,173).

The histology results indicate that the expanded tissue is healthy and has not been damaged by the expander. Fibroblasts are associated with the growth of collagen tissue, and therefore it is unsurprising that there is an increase of these cells in the expanded tissue (174). Furthermore, the decrease in thickness for the expanded dermis is consistent with other studies of expanded tissue (18,6,168). If further studies were conducted, it would be of interest to determine the degree of collagen alignment in the expanded tissue, at different positions on the surface of the expander. This will be discussed further in Chapter 8.

Figure 6.14 and Figure 6.15 show example images of *in* vivo expansion of the commercially produced cylindrical devices (Oxtex Ltd). Both images show a flat top surface, reflective of the cylindrical geometry. The slight barrelling of the cylinder sides, seen in Figure 6.14, is also observed in the *in vitro* swelling of the same device (Figure 6.14) and is caused by the thick ring of PDMS around the sample. As discussed in 2.1.2, one of the motivations for developing non-prismatic devices was to eliminate the 90° angle, which is thought to be the reason for failure in samples such as Figure 6.15). Figure 6.12 and Figure 6.13 show the profile of one of the domed devices during swelling. It is shown that during implantation the domed shape has been preserved (thus eliminating the 90° angle). This is a very encouraging result and is a strong motivation for further *in vivo* studies of non-prismatic devices (recommendations for which will be discussed in Chapter 8).

6.5 Summary

This chapter aimed to answer the final research question posed in section 2.3:

RQ 9) What is the *in vivo* behaviour of a non-prismatic tissue expander?

In this chapter it has been shown that non-prismatic devices do retain their shape when used *in vivo,* and that the percentage increase in height of the device *in vivo* is comparable to the percentage swelling of the device *in vitro*. The tissue produced by the expanders was shown to be healthy, with the typical markers of new tissue growth through tissue expansion

(reduced dermis thickness and increase in fibroblast count, as seen in Figure 6.16 and Figure 6.17 respectively).

These findings are key steps in the development of complex shape anisotropic tissue expanders, and the next steps required to validate these findings will be discussed in Chapter 8.

CHAPTER 7:

Summary

7 Summary

Each of the research questions, posed in section 2.3, has been answered in the summary at the end of each chapter. This section will highlight the key findings from each chapter.

- The first experimental chapter (Chapter 3) focused on the compression moulding of pellets of P(MMA-co-NVP), aiming to answer RQ1-RQ4. The key finding was that, after swelling, each device (that was made from the same size initial pellet) would return to the same reference dimensions. This finding allowed for the development of the devices which expanded anisotropically from discs into devices with non-prismatic cross-sections (wedges and domes).These devices are thought to have great clinical potential, improving the quality of tissue produced, and allowing for skin with anisotropic resting tension to be produced.

- The attention of the second experimental chapter (Chapter 4) was directed towards the effect of γ-irradiation on the P(MMA-co-NVP) samples of various compression ratios, aiming to answer RQ5 and RQ6. γ-irradiation was found to have a detrimental impact on the colour and swelling properties of the devices. However, it was found that these changes were reduced significantly when residual molecules were removed from the devices prior to compression.

- The third experimental chapter (Chapter 5) addressed the issue of rate control in samples by investigating a semi permeable PDMS coating, applied directly to the surface of the P(MMA-co-NVP) disc, aiming to answer RQ7 and RQ8. It was found that the rate of swelling could be successfully controlled in this way, requiring a minimum coating thickness of 0.375mm. A linear decrease in swelling capacity was observed as the coating thickness increased. However it was found that the height was the least affected parameter (reducing the potential loss of new tissue).

- Finally, the last experimental chapter (Chapter 6) showed a proof of concept animal trial for anisotropic devices which expanded from a disc into a dome-shaped device, answering RQ9. The rate of the device was controlled with a PDMS coating, and the effect of γ-irradiation on the swelling behaviour was minimised by washing the residual molecules out of the P(MMA-co-NVP) before compression. It was shown that the devices maintained their dome shape during *in vivo* expansion, and that new, healthy tissue was generated in response to this device.

The findings of this thesis provide a greatly improved understanding of the relationship between the manufacturing, and processing routes used to make anisotropically expanding, hydrogel tissue expanders, and the swelling behaviour of these devices. This means that devices can be more effectively designed to meet the clinical needs, thus improving the surgical outcomes. Improvements to the swelling rate of devices (by application of PDMS coatings), have also been made, which show potential in reducing the complication rates experienced during expansion. Finally, the non-prismatic devices show significant clinical promise, and have paved the way for a new area of research in this field.

CHAPTER 8:

Further Work

8 Further Work

In order to build upon the work presented in this thesis, the following further work is recommended. The suggested investigations have been split into three categories, focussing on the P(MMA-co-NVP), the PDMS coating, and the animal models respectively. Each of these will be discussed in turn.

- The P(MMA-co-NVP) hydrogel
    - The current manufacturing limits of anisotropic hydrogel devices were discussed in section 3.4. Future studies may be useful in order to determine how to increase these limits, in order to produce a wider range of devices. For example, it would be of interest to determine the effect of the ratio of NVP to MMA in the co-polymer on the maximum compression ratio, or to investigate different methods of cross-linking.
    - As discussed in section 3.4.1, Figure 3.19 and Figure 3.20 predict that by extending the P(MMA-co-NVP) pellet, thus generating a compression ratio $C < 1$, biaxial expansion will be generated. In order to determine whether this occurs, and the limits of such a device, pellets could be extended via extrusion.
    - The further development of non-prismatic, anisotropic tissue expanders would also be of great interest. The key focus of this work should be determining the limits of the complexity of the shapes. A possible avenue of investigation would be to consider whether it is possible to synthesise the P(MMA-co-NVP) directly into a complex shape mould — in order to remove the difficulty of machining the P(MMA-co-NVP) into more complex shapes.

- Controlling the rate of expansion
    - As a number of potential flaws in dip coating were highlighted in section 5.4 (such as increased risk of defect or thinned region), an alternative method of

applying the PDMS coating could be considered. It is possible that a mould could be developed, where the PDMS is cast directly on to the sample surface.

- Finally, it would be of great use to determine a reliable method of increasing the final height of coated devices. As the required thickness of coating is likely to increase with volume, this will not be a trivial task. However, it would be of great value as it would allow for a wider range of devices available for surgeons.

- Animal models
  - In order to validate, and extend the results of the animal model, a greater number of samples, and sample shapes, must be tested. In addition to the monitoring and characterisation techniques used in section 6.2.4, histology and atomic force microscopy (AFM) could be used to determine the effect of different shapes on the tissue produced. For example, it would be useful to be able to compare the collagen alignment at different positions on the surface of the devices. This is shown for domes compared to cylinders in Figure 8.1.

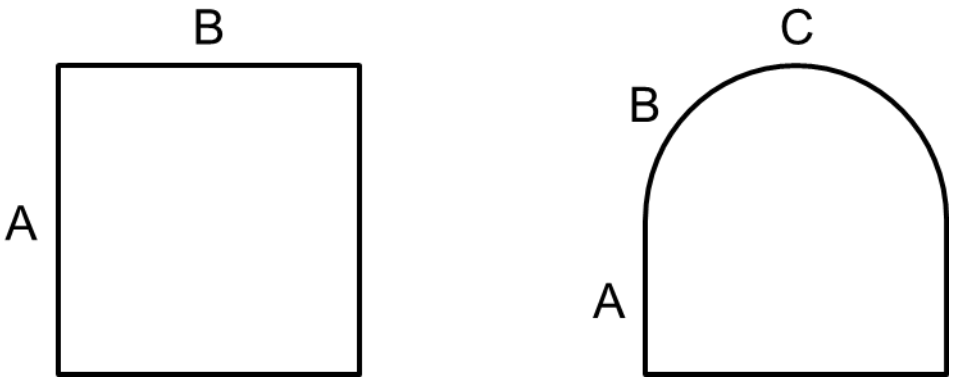

Figure 8.1 A schematic showing the locations of where histology samples could be taken in future animal model studies in order to improve the understanding of how the domed shape effects the structure of the harvested skin

CHAPTER 9:

References

9 References

1. Elshahat A. Management of burn deformities using tissue expanders: A retrospective comparative analysis between tissue expansion in limb and non-limb sites. Burns. 2011;37(3):490–4.

2. Elias DL, Baird WL, Zubowicz VN. Applications and complications of tissue expansion in pediatric patients. J Pediatr Surg. 1991;26(1):15–21.

3. Bozkurt A, Groger A, O'Dey D, Vogeler F, Piatkowski A, Fuchs PC, et al. Retrospective analysis of tissue expansion in reconstructive burn surgery: Evaluation of complication rates. Burns. 2008;34(8):1113–8.

4. Argenta LC, Marks MW, Pasyk KA. Advances in tissue expansion. Clin Plast Surg. 1985;12(2):159–170.

5. Swan MC, Bucknall DG, Goodacre TEE, Czernuszka JT. Synthesis and properties of a novel anisotropic self-inflating hydrogel tissue expander. Acta Biomater. 2011;7(3):1126–32.

6. Swan M, Bucknall D, Czernuszka J, Pigott D, Goodacre T. Development of a novel anisotropic self-inflating tissue expander: in vivo submucoperiosteal performance in the porcine hard palate. J Plast Reconstr Surg. 2012;129(1):79–88.

7. Zoellner AM, Tepole AB, Kuhl E. On the biomechanics and mechanobiology of growing skin. J Theor Biol. 2012;297:166–75.

8. Silver F, Siperko L, Seehra G. Review Mechanobiology of force transduction in dermal tissue. Ski Res Technol. 2003;9:3–23.

9. Zollner A, Holland M, Honda K, Gosain A, Kuhl E. Growth on Demand: Reviewing the Mechanobiology of Stretched Skin. J Mech Behav Biomed Mater. 2013;28:495–509.

10. Beauchene J, Chambers M, Peterson A, Scott P. Biochemical, biomechanical, and physical changes in the skin in an experimental animal model of therapeutic tissue expansion. J Surg Res. 1989;47(6):507–14.

11. De Filippo RE AA. Stretch and growth: the molecular and physiologic influences of tissue expansion. 2002; 109 (7): 2450–2462. Plast Reconstr Surg. 2002;109(7):2450–62.

12. Kippenberger S, Bernd A, Loitsch S, Guschel M, Muller J, Bereiter-Hahn J, et al. Signaling of mechanical stretch in human keratinocytes via MAP kinases. J Investagative Dermatology. 2000;114(3):408–12.

13. Takei T, Rivas-Gotz C, Delling C, Koo J, Mills I, McCarthy T, et al. Effect of strain on human keratinocytes in vitro. J Cell Physiol. 1997;173:64–72.

14. Marcelo Sacramento Cunha Marisa Roma Herson, José Carlos Faes, Rolf Gemperli and Marcus Castro Ferreira. Tissue expander complications in plastic surgery, a 10-year experience Rev Hosp Clin Fac Med Sao Paulo. 2002;57(3).

15. Huang X, Qu X, Li Q. Risk Factors for Complications of Tissue Expansion: A 20-Year Systematic Review and Meta-Analysis. Plast Reconstr Surg. 2011 Sep;128(3):787–97.

16. Wiese KG. Osmotically induced tissue expansion with hydrogels: a new dimension in tissue expansion? A preliminary report. J Cranio-Maxillofacial Surg. 1993;21(7):309–13.

17. Berge D, Wiese K, von Lindern J, Niederhagen B, Appel T, Reich R. Tissue Expansion Using Osmotically Active Hydrogel Systems for Direct Closure of the Donor Defect of the Radial Forearm Flap. J Plast Reconstr Surg. 2001;105:1–5.

18. Anwander T, Schneider M, Gloger W. Investigation of the expansion properties of osmotic expanders with and without silicone shells in animals. Plast Reconstr Surg. 2007;120:590–5.

19. Percival NJ, Sykes PJ. Syndactyly: A review of the factors which influence surgical treatment. J Hand Surg Br Eur Vol. 1989;14(2):196–200.

20. Moss ALH, Foucher G. Syndactyly: Can web creep be avoided? J Hand Surg Br Eur Vol. 1990;15(2):193–200.

21. Ottenio M, Tran D, Ní Annaidh A, Gilchrist MD, Bruyère K. Strain rate and anisotropy effects on the tensile failure characteristics of human skin. J Mech Behav Biomed Mater. 2015;41:241–50.

22. Kopf AW, Bart RS, Hennessey P. Congenital nevocytic nevi and malignant melanomas. J Am Acad Dermatol. 1979;1(2):123–30.

23. Neath P. Soft Tissue Sarcomas in Canines. Oxtex Osmotic Expanders Seminar. 2012.

24. Kent JN, Finger IM, Quinn JH, Guerra LR. Hydroxylapatite alveolar ridge reconstruction: Clinical experiences, complications, and technical modifications. J Oral Maxillofac Surg. 1986;44(1):37–49.

25. Bird TM, Hobbs CA, Cleves MA, Tilford JM, Robbins JM. National rates of birth defects among hospitalized newborns. Birth Defects Res Part A-Clinical; 2006 Nov;76(11):762–9.

26. Bister D, Set P, Cash C, Coleman N, Fanshawe T. Incidence of facial clefts in Cambridge, United Kingdom. Eur J Orthod. 2011;33(4):372–6.

27. Bos A, Prahl C. Oral health-related quality of life in Dutch children with cleft lip and/or palate. Angle Orthod: 2011 Sep;81(5):865–71.

28. Munz SM, Edwards SP, Inglehart MR. Oral health-related quality of life, and satisfaction with treatment and treatment outcomes of adolescents/young adults with cleft lip/palate: an exploration. Int J Oral Maxillofac Surg. 2011;40(8):790–6.

29. Ize-Iyamu IN, Saheeb BD. Feeding intervention in cleft lip and palate babies: a practical approach to feeding efficiency and weight gain. Int J Oral Maxillofac Surg. 2011 Sep;40(9):916–9.

30. Witsenburg B. The Reconstruction of Anterior Residual Bone Defects in Patients with Cleft-Lip, Alveolus and Palate - a Review. J Maxillofac Surg. 1985;13(5):197–208.

31. Zigiotti GL, Messerotti GF, Cavaliere F. Cleft palate surgery from its beginnings until today. Minerva Med. 1983;74(1-2):59–68.

32. Bartzela TN, Katsaros C, Bronkhorst EM, Rizell S, Halazonetis D, Kuijpers-Jagtman AM. A two-centre study on facial morphology in patients with complete bilateral cleft lip and palate at nine years of age. Int J Oral Maxillofac Surg. 2011;40(8):782–9.

33. Kablar B, Rot I. Mechanical and biochemical relationship between the developing muscle and the palate. Dev Biol. 2011 Aug 1;356(1):222–3.

34. Duits EHAMS, Molenaar JDS, van Rappard JHAMD. The Modeling of Skin Expanders. Plast Reconstr Surg. 1989;83(2).

35. Mustoe TAMD, Bartell THMD, Garner WLMD. Physical, Biomechanical, Histologic, and Biochemical Effects of Rapid versus Conventional Tissue Expansion. Plast Reconstr Surg. 89(84):3.

36. Silver F, Freeman J, DeVore D. Viscoelastic properties of human skin and processed dermis. Ski Res Technol. 2001;7:18–23.

37. Purslow P, Wess T, Hukins D. Collagen orientation and molecular spacing during creep and stress-relaxation in soft connective tissues. J Exp Biol. 1998;201:135–42.

38. Zeng YJ, Huang K, Xu CQ, Zhang J, Sun GC. Biorheological characteristics of skin after expansion. Biorheology. 2001;38(5-6):367–78.

39. Ruvolo Jr. EC, Stamatas GN, Kollias N. Skin viscoelasticity displays site- and age-dependent angular awnisotropy. Skin Pharmacol Physiol; 2007;20(6):313–21.

40. Gallagher A, Ni Anniadh A, Bruyere K, Ottenio M, Xie H, Gilchrist M. Dynamic Tensile Properties of Human Skin. IRCOBI. 2012. p. 494–502.

41. Zeng YJ, Liu YH, Xu CQ, Xu XH, Xu H, Sun GC. Biomechanical properties of skin in vitro for different expansion methods. Clin Biomech. 2004 Oct;19(8):853–7.

42. Danby FW. Nutrition and aging skin: sugar and glycation. Nutr Ski Part I. 2010;28(4):409–11.

43. Alexander H, Cook T. Variations with age in the mechanical properties of human skin in vivo. J Tissue Viability. Department of Mechanical Engineering, Stevens Institute of Technology, Castle Point Station, Hoboken, New Jersey 07030, USA.; 2006;16(3):6–11.

44. Verhaegen PD, Schouten HJ, Tigchelaar-Gutter W, van Marle J, van Noorden CJ, Middelkoop E, et al. Adaptation of the dermal collagen structure of human skin and scar tissue in response to stretch: An experimental study. Wound Repair Regen; 2012;20(5):658–66.

45. Kobus KF. Cleft palate repair with the use of osmotic expanders: a preliminary report. J Plast Reconstr Aesthetic Surg. 2007;60(4):414–21.

46. Rees L, Morris P, Hall P. Osmotic tissue expanders in cleft lip and palate surgery: a cautionary tale. J Plast Reconstr Aesthetic Surg. 2008;61:119–20.

47. Swan MC, Goodacre TEE, Czernuszka JT, Bucknall DG. Cleft palate repair with the use of osmotic expanders: a response. J Plast Reconstr Aesthetic Surg. 2008;61(2):220–1.

48. Boettcher-Haberzeth S, Kapoor S, Meuli M, Neuhaus K, Biedermann T, Reichmann E, et al. Osmotic expanders in children: No filling - no control - no problem? Eur J Pediatr Surg. 2011;21(3):163–7.

49. Chummun S, Addison P, Stewart KJ. The osmotic tissue expander: A 5-year experience. J Plast Reconstr Aesthetic Surg. 2010;63(12):2128–32.

50. Obdeijn MC, Nicolai J-PA, Werker PMN. The osmotic tissue expander: a three-year clinical experience. J Plast Reconstr Aesthetic Surg. 2009;62(9):1219–22.

51. Mertens C, Thiele O, Engel M. The use of self-inflating soft tissue expanders prior to bone augmentation of atrophied alveolar ridges. Clin Implant Dent Relat Res. 2015;17(1):44–51.

52. Anwander M. Gloger, W. Reich, RH. Appel, T. Martini, M. Wenghoefer, M. Merkx, M. Bergé, S. TS. Investigation of the expansion properties of osmotic expanders with and without silicone shell in animals. Plast Reconstr Surg. 2007;Sep;120(3):590–595

53. Hoffman AS. Hydrogels for biomedical applications. Advanced Drug Delivery Reviews. 2012. p. 18–23.

54. Mathur A, Moorjani S, Scranton A. Methods for Synthesis of Hydrogel Networks: A Review. Polym Rev. 2006;36(2):405–30.

55. Kopecek J. Hydrogel biomaterials: A smart future? Biomaterials. 2007;28(34):5185–92.

56. Lee K, Mooney D. Hydrogels for Tissue Engineering. Chem Rev. 2001;101(7):1869–79.

57. AS. H. Hydrogels for biomedical applications. 2002; 54 (1): 3–12. Adv Drug Deliv Rev. 2002;54(1):3–12.

58. Drury J, Mooney D. Hydrogels for tissue engineering: scaffold design variables and applications. Biomaterials. 2003;24(24):4337–51.

59. Tan H, Marra KG. Injectable, biodegradable hydrogels for tissue engineering applications. Materials (Basel). 2010;3:1746–67.

60. Nguyen KT, West JL. Photopolymerizable hydrogels for tissue engineering applications. Biomaterials. 2002;23:4307–14.

61. Qiu Y, Park K. Environment-sensitive hydrogels for drug delivery. Advanced Drug Delivery Reviews. 2012. p. 49–60.

62. Hoare TR, Kohane DS. Hydrogels in drug delivery: Progress and challenges. Polymer. 2008. p. 1993–2007.

63. Bhattarai N, Gunn J, Zhang M. Chitosan-based hydrogels for controlled, localized drug delivery. Advanced Drug Delivery Reviews. 2010. p. 83–99.

64. Freeman A, Mayhew E. Targeted drug delivery. Cancer. 2006;58(S2):573–83.

65. Wilson AN, Guiseppi-Elie A. Bioresponsive hydrogels. Adv Healthc Mater. 2013;2:520–32.

66. Ganji F, Vasheghani-Farahani S, Vasheghani-Farahani E. Theoretical Description of Hydrogel Swelling: A Review. Iran Polym J. 2010;19(5):375–98.

67. Arap W, Pasqualini R, Ruoslahti E. Cancer Treatment by Targeted Drug Delivery to Tumor Vasculature in a Mouse Model. Science (80-). 1998;279(337-380).

68. Maeda H, Bharate G, Daruwalla J. Polymeric drugs for efficient tumor-targeted drug delivery based on EPR-effect. Eur J Pharm Biopharm. 2009;71(3):409–19.

69. Chourasia M, Jain S. Pharmaceutical approaches to colon targeted drug delivery systems. J Pharm Sci. 2003;6(1):33–66.

70. Vinogradov S, Bronich T, Kabanov A. Nanosized cationic hydrogels for drug delivery: preparation, properties and interactions with cells. Adv Drug Deliv Rev. 2002;54(1):135–47.

71. Kickhofen B, Wokalek H, Scheel D, Ruh H. Chemical and physical properties of a hydrogel wound dressing. Biomaterials. 1986;7(1):67–72.

72. Jones A, Vaughan D. Hydrogel dressings in the management of a variety of wound types: A review. J Orthop Nurs. 2005;9:S1–11.

73. Eisenbud D, Hunter H, Kessler L, Zulkowski K. Hydrogel wound dressings: where do we stand in 2003? Ostomy Wound Manag. 2003;49:52–7.

74. Cable B. Hydrogel Dressings. J Hum Lact. 2001;17:295.

75. Bucknall DG, Czernuszka JT, Goodacre TEE, Meakins J, Swan MC. A self-inflating anisotropic composition, methods of manufacturing said composition and uses thereof. WO2007080391 A3, 2008.

76. Davis T, Huglin M. Effect of crosslinker on properties of copolymeric N-vinyl-2-pyrrolidone/methyl methacrylate hydrogels and organogels. Macromol Chem Phys. 2003;191(2):331–43.

77. Ahmad MB, Huglin M. DSC Studies on States of Water in Crosslinked Poly(methyl methacrylate-co-N-vinyl -2- pyrrolidone) Hydrogels. Polym Int. 1993;33:273–7.

78. Davis T, Huglin M. Properties of poly(N–vinyl–2– pyrrolidone) hydrogels crosslinked with ethyleneglycol dimethacrylate. Polymer (Guildf). 1988;29(4):701–6.

79. Davis T, Huglin M. Studies on co–polymeric hydrogels of N–vinyl– 2–pyrrolidone with 2–hydroxyethyl methacrylate. Macromolecules. 1989;22(6):2824–9.

80. Ahmad MB, Huglin MB. Dsc Studies on States of Water in Cross-Linked Poly(methyl Methacrylate-Co-N-Vinyl-2-Pyrrolidone) Hydrogels. Polym Int. 1994;33(3):273–7.

81. Amsden B. Solute Diffusion within Hydrogels. Mechanisms and Models. Macromolecules. 1998;31:8382–95.

82. Ahmad MB, Huglin MB. States of Water in Poly(methyl Methacrylate-Co-N-Vinyl-2-Pyrrolidone) Hydrogels during Swelling. Polymer (Guildf). 1994;35(9):1997–2000.

83. Knorgen M, Arndt KF, Richter S, Kuckling D, Schneider H. Investigation of swelling and diffusion in polymers by H-1 NMR imaging: LCP networks and hydrogels. J Mol Struct. 2000;554(1):69–79.

84. Pal K, Banthia A, Majumdar D. Polymeric hydrogels: characterization and biomedical applications. Des monomers. 2009;12:197–220.

85. Alfrey T Lloyd WG. GEF. Diffusion in glassy polymers. J Polym Sci Part C – Polym Lett. 1966;12:249–61.

86. Frisch H. Sorption and transport in glassy polymers: review. Polym Eng Sci. 1980;20(1):2–13.

87. Franson N, Peppas N. Influence of co–polymer composition on non–Fickian water transport through glassy co–polymers. J Appl Polym Sci. 1983;28(4):1299–310.

88. Biren D, Kabra B, Gehrke S. Effect of initial sample anisotropy on the solvent sorption kinetics of glassy poly(2–hydroxyethyl methacrylate). Polymer (Guildf). 1992;33(3):554–61.

89. Chou K, Han C, Lee S. Water transport in crosslinked 2– hydroxyethyl methacrylate. Polym Eng Sci. 2000;40(4):1004–14.

90. Brazel C, Peppas N. Dimensionless analysis of swelling of hydrophilic glassy polymers with subsequent drug release from relaxing structures. Biomaterials. 1999;20(8):721–32.

91. Lucantonio A, Nardinocchi P, Teresi L. Multiphysics Modeling of Swelling Gels. 2012 COMSOL Conference in Milan. 2012. p. 1–4.

92. Zhang J, Zhao X, Suo Z, Jiang H. A finite element method for transient analysis of concurrent large deformation and mass transport in gels. AIP J Appl Phys. 2009;105:105–15.

93. Korsmeyer R, Peppas N. Solute and penetrant diffusion in swellable polymers III: drug release from glassy poly(HEMA–co–NVP) co– polymers. J Control Release. 1984;1(2):89–98.

94. Malak M, Hill D, Whittaker A. Water sorption into poly[(2– hydroxyethyl methacrylate)–co–(1–vinyl–2–pyrrolidone] at 310 K. Polym Int. 2003;52(11):1740–4748.

95. Crank J. The mathematics of diffusion. 2nd ed. 1975.

96. Gehrke S, Biren D, Hopkins J. Evidence for Fickian water transport in initially glassy poly(2–hydroxyethyl methacrylate). J Biomater Sci. 1994;6(4):375–90.

97. Loffler R, Finkelmann H. Amphiphilic Liquid-Crystalline Elastomers. Macromol Rapid Commun. 1990;11:321–8.

98. Meng H, Li G. A review of stimuli-responsive shape memory polymer composites. Polymer (Guildf). 2013;54:2199–221.

99. Chen M, Zhu J, Qi G, He C, Wang H. Anisotropic hydrogels fabricated with directional freezing and radiation-induced polymerization and crosslinking method. Mater Lett. 2012;89:104–7.

100. Despang F, Dittrich R, Gelinsky M. Novel Biomaterials with Parallel Aligned Pore Channels by Directed Ionotropic Gelation of Alginate: Mimicking the Anisotropic Structure of Bone Tissue, Advances in Biomimetics. Advances in Biomimetics. 2011. 349-372 p.

101. Mitchell G, Tojeira A. Role of Anisotropy in Tissue Engineering. Procedia Eng. 2013;59:117–25.

102. Davidenko N, Gibb T, Best S, Campbell J, Watson J, Cameron R. Biomimetic collagen scaffolds with anisotropic pore architecture. Acta Biomater. 2011;2:667–76.

103. Despang F, Borner A, Dittrich R, Tomandl G, Pompe W, Gelinsky M. Alginate/calcium phosphate scaffolds with oriented, tube-like pores. Mat-wiss u werkstofftech. 2005;36(12):761–7.

104. Zhang L, Zhao J, Zhu J, He C, Wang H. Anisotropic tough poly(vinyl alcohol) hydrogels. Soft Matter. 2012;8:10439.

105. Wim H, Heidelberg S-VB. Liquid Crystal Elastomers: Materials and Applications. 2012. 106-107 p.

106. Kleinschmidt F, Hickl M, Saalwachter K, Schmidt C, Finkelmann H. Lamellar Liquid Single Crystal Hydrogels: Synthesis and Investigation of Anisotropic Water Diffusion and Swelling. Macromolecules. 2005;38:9772–82.

107. Zhang J, Xie Z, Hill A, She F, Thornton A, Hoang M, et al. Structure retention in cross-linked poly(ethylene glycol) diacrylate hydrogel templated from a hexagonal lyotropic liquid crystal by controlling the surface tension. Soft Matter. 2011;8(7):2087–94.

108. Amigo-Melchior A, Finkelmann H. A concept for bifocal contact- or intraocular lenses: Liquid single crystal hydrogels (LSCH). Polym Adv Technol. 2002;13:363–9.

109. Woltman S, Jay G, Crawford G. Liquid-crystal materials find a new order in biomedical applications. Nature, Mater. 2007;6:929–38.

110. Fischer P, Finkelmann H. Lyotropic liquid-crystallined elastomers. Macromol Rapid Commun. 1998;111:127–34.

111. Liu M, Ishida Y, Ebina Y, Sasaki T, Hikima T, Takata M, et al. An anisotropic hydrogel with electrostatic repulsion between cofacially aligned nanosheets. Nature. 2014;517:68–72.

112. Eguchi M, Angelone M, Yennaware H, Mallouk T. Anisotropic alignment of lamellar potassium hexaniobate microcrystals and nanoscrolls in a static magnetic field. J Phys Chem C. 2008;112:11280–5.

113. Hayakawa M, Onda T, Tanaka T, Tsujii K. Hydrogels Containing Immobilized Bilayer Membranes. Langmuir. 1997;13:3595–7.

114. Dicker M, Rossiter J, Bond I, Weaver P. Biomimetic photo-actuation: sensing, control and actuation in sun-tracking plants. Bioinspiration and Biomimetics. 2014;9:1–12.

115. Dicker M, Weaver P, Rossiter J, Bond I. Hydrogel core flexible matrix composite (H-FMC) actuators: Theory and preliminary modelling. Smart Mater Struct. 2014;23:95021.

116. Ahadian S, Ramon-Azcon J, Estili M, Liang X, Ostrovidov S, Shiku H, et al. Hybrid hydrogels containing vertically aligned carbon nanotubes with anisotropic electrical conductivity for muscle myofiber fabrication. Sci Rep. 2014;4:4271.

117. Kabanemi K, Vailancourt H. Residual stresses, shrinkage, and warpage of complex injection molded products: Numerical simulation and experimental validation. Polym Eng Sci. 1998;38:21–37.

118. Withers P, Bhadeshia G. Residual stress. Part 1 – Measurement techniques. Mater Sci Technol. 2001;17(4):355–65.

119. Rosato D, Rosato M, Publishers KA. Injection Molding Handbook. 2000. 2-7 p.

120. Chen X, Lam Y, Li D. Analysis of thermal residual stress in plastic injection molding. J Mater Process Technol. 2000;101:275–80.

121. Isayev AI, Crouthamel DL. Residual Stress Development in the Injection Molding of Polymers. Polym Plast Technol Eng. Taylor & Francis; 1984;22(2):177–232.

122. Wang T, Young W. Study on residual stresses of thin-walled injection molding. Eur Polym J. 2005;41(10):2511–7.

123. Choi D, Im Y. Prediction of shrinkage and warpage in consideration of residual stress in integrated simulation of injection molding. Compos Struct. 1999;47:655–65.

124. A. I. Isayev CAH. Toward a viscoelastic modelling of the injection molding of polymers . Rheol Acta. 1980;19(2):168–82.

125. Baaijens F. Calculation of residual stresses in injection molded products. Rheol Acta. 1991;30:284–99.

126. Jain A, Firestone G, Yi A. Viscosity Measurement by Cylindrical Compression for Numerical Modeling of Precision Lens Molding Process. J Am Ceram Soc. 2005;88(9):2409–14.

127. Alexandrov S. An analysis of the axisymmetric compression of viscous materials. J Mater Process Technol. 2000;105(3):278–83.

128. Adams M, Briscoe B, Corfield G, Lawrence C, Papthanasiou T. An analysis of the plane-strain compression of viscoplastic materials. J Appl Mech. 1997;64:420–4.

129. Greving D, Rybicki E, Shadley J. Through-thickness residual stress evaluations for several industrial thermal spray coatings using a modified layer-removal method. J Therm spray Technol. 1994;3(4):379–88.

130. Treuting R, Read W. A Mechanical Determination of Biaxial Residual Stress in Sheet Materials. J Appl Phys. 1951;22(130):130–4.

131. Janeschitz-Kriegl H. Injection moulding of plastics: Some ideas about the relationship between mould filling and birefringence. Rheol Acta. 1977;16(4):327–39.

132. Lu X, Khim L. A statistical experimental study of the injection molding of optical lenses. J Mater Process Technol. 2001;113(189-195).

133. Akay M, Ozden S. Measurement of residual stresses in injection moulded thermoplastics. Polym Test. 1994;13(4):323–54.

134. Singh D. Fundamentals of Optics. 2010. 290 p.

135. Isayev AI. Orientation development in the injection molding of amorphous polymers. Polym Eng Sci. 2004;23(5):271–84.

136. Huebsch N, Gilbert M, Healy K. Analysis of sterilizatoin protocols for peptide-modified hydrogels. J Biomed Mater Res Part B Appl Biomater. 2005;74(1):440–7.

137. Sintzel M, Merkli A, Tabatabay C, Gurny R. Influence of Irradiation Sterilization on Polymers Used as Drug Carriers- A Review. Drug Dev Ind Pharm. 1997;23(9):857–78.

138. Clough R, Shalaby S, Society AC. Irradiation of Polymers: Fundamentals and Technological Applications. 1996. 303-312 p.

139. Russell A, Hugo W, Ayliffe G, Science B. Principles and practice of disinfection, preservation and sterilization. 1999.

140. Healy K. Molecular engineering of materials for bioreactivity. Curr Opin solid state Mater Sci. 1999;4:381–7.

141. Raso J, Barbosa-Canovas G. Nonthermal preservation of foods using combined processing techniques. Crit Rev Food Sci. 2003;43:265–85.

142. Bruck S. Sterilization Problems of Synthetic Biocompatible Materials. J Biomed Mater Res. 1971;5:139–58.

143. Clough R, Shalaby S, Society AC. Radiation Effects on Polymers. 1991. 45-47 p.

144. Cleland M, Parks L, Cheng S. Applications for radiation processing of materials. Nucl Instruments Methods Phys Res Sect B Beam Interact with Mater Atoms. 2003;208:66–73.

145. Mark JE, Springer. Physical Properties of Polymers Handbook. 2007. 871 p.

146. Skiens W. Mechanical properties of polymeric packaging films after radiation sterilization. Radiat Phys Chem. 1980;15:47–57.

147. Abd El-Aal S, Hegazy E, AbuTaleb M, Dessouki A. Radiation synthesis of copolymers for adsorption of dyes from their industrial wastes. J Appl Polym Sci. 2005;96(3):753–63.

148. Musat V, Popa M, Gospodinova N. Origin of Color of Poly(N-vinyl Pyrrolidone) Concentrated Aqueous Solutions. Int J Polym Anal Characterisation. 2011;16:442–8.

149. Haaf F, Sanner A, Straub F. Polymers of N-Vinylpyrrolidone: Synthesis, Characterization and Uses. Polym J. 1985;17:143–52.

150. Hassouna F, Therias S, Mailhot G, Gardette J. Photooxidation of poly(N-vinylpyrrolidone) (PVP) in the solid state and in aqueous solution. Polym Degrad Stab. 2009;94(12):2257–66.

151. Grassie N, Scott G. Polymer degradation and stabilisation. Cambridge University Press; 1985. 88 p.

152. Davis J, Senogles E. γ-Irradiation of N-vinylpyrrolidin-2-one and its homopolymer. Aust J Chem. 1981;34(7):1413–21.

153. Benamer S, Mahlous M, Boukrif A, Mansouri S, Larbi Youcef S. Synthesis and characterisation of hydrogels based on poly(vinyl pyrrolidone). Nucl Instruments Methods Phys Res Sect B Beam Interact with Mater Atoms. 2006;248(2):284–90.

154. Rottach D. Effect of Strain History on Stress and Permanent Set in Cross-Linking Networks: A Molecular Dynamics Study. Macromolecules. 2004;37:5468–73.

155. Shyichuk A, White J. Analysis of chain-scission and crosslinking rates in the photo-oxidation of polystyrene. J Appl Polym Sci. 2000;77(13):3015–23.

156. Baxandall L, Edwards S. Deformation-Dependent Properties of Polymer Networks Constructed by Addition of Cross-Links under Strain. Macromolecules. 1987;21:1763–72.

157. Batchelder D. Colour and chromism of conjugated polymers. Contempary Phys. 1988;29(1):3–31.

158. Alsberg H. Gamma Radiation of Styrene-Methyl Methacrylate Copolymers. Radiat Phys Chem. 1980;15:65–70.

159. Korsmeyer RW Peppas NA. VE. Solute and penetrant diffusion in swellable polymers II: verification of theoretical models. J Polym Sci Part B – Polym Phys. 1986;24(2):409–34.

160. Dominick V. Rosato Marlene G. Rosato DVR. Injection Molding Handbook. Kluwer academic publishers; 2000.

161. Blau PJ. Friction Science and Technology: From Concepts to Applications, Second Edition (Dekker Mechanical Engineering). 2012.

162. Roba M, Duncan EG, Hill GA, D SN, Tosatti SGP. Friction Measurements on Contact Lenses in Their Operating Environment. Tribol Lett. 2011;44:387–97.

163. Katta JK, Marcolongo M, Lowman A, Mansmann KA. Friction and wear behavior of poly(vinyl alcohol)/poly(vinyl pyrrolidone) hydrogels for articular cartilage replacement. J Biomed Mater Res A. 2007;83(2):471–9.

164. Kricheldorf H. Handbook of Polymer Synthesis. Part A. CRC Press; 1991. 116 p.

165. Methyl Methacrylate. Pub Chem: National Center for Biotechnology Information; p. CID=6658.

166. Zulfiqar S, Piracha A, Masud K. The themal degradation of poly(allylmethacrylate). Polym Degrad Stab. 1995;52:89–93.

167. Betts J, Dainton F, Ivin K. Kinetics of Decomposition of Azo-Bis-Isobutyronitrile in Dimethylfonnamide in the Presence of Ferric Chloride and Styrene. Trans Faraday Soc. 1961;21:1203–11.

168. Radzi Z. Development of Anisotropic Self-Inflating Tissue Expanders for Clinical Applications. 2014.

169. Chambon F, Winter HH. Stopping of crosslinking reaction in a PDMS polymer at the gel point. Polym Bull. 1985;13:499–503.

170. Ward I, Sweeney J. An introduction to the mechanical properties of solid polymers. Wiley; 2004. 274.

171. Radzi Z. Development of Anisotropic Self-Inflating Tissue Expanders for Clinical Applications. DPhil Thesis, University of Oxford 2014.

172. Swan MC. Anisotropic Self Inflating Tissue Expanders in Reconstructive Plastic Surgery. DPhil Thesis, University of Oxford 2007.

173. Henri J, Uijlenbroek J, Liu Y, He J, Visscher C, van Wass M, et al. Expanding soft tissue with Osmed® tissue expanders in the goat maxilla. Clincal Oral Implant Res. 2011;22(1):121–8.

174. Ross M, Romrell L, Kaye G. Histology A Text and Atlas. Williams and Wilkins; 1995. 95

APPENDIX

I. Appendix

Axi-symmetric pressing in hydrogels

The following model is used to help explain the boundary seen in the aluminium pressed samples, by considering slip-stick deformation; shown in the schematics Figure 3.45 and Figure 3.46.

Equation 9.1 is the Von Mises criteria for yield in plain strain, in uniaxial compression, where K is the yield stress in pure shear and Y is the yield stress of the disc.

$$K = \frac{Y}{\sqrt{3}}$$

Equation 9.1

Figure 3.45 shows the case for sticking friction, by taking an element, a force balance equation can be determined, as shown in Equation 9.2, where h is the sample height and r is the distance from the center.

$$(\sigma_r + \partial\sigma_r)h2\pi r - \sigma_r h2\pi r - 2K\partial r2\pi r = 0$$

Equation 9.2

Assuming that the hot pressing is axi-symmetric, the stresses will be equal to the stress of the press:

$$\sigma_r = \sigma_z = \sigma_\theta = P$$

Equation 9.3

Equation 9.2 can then be simplified, using Equation 9.3 to give Equation 9.4.

$$-h\partial P = 2K\partial r$$

Equation 9.4

Integrating Equation 9.4, as seen in Equation 9.5 gives Equation 9.6.

$$\int_{Y}^{P} \partial P = \int_{r}^{R} \frac{2K}{h} \partial r$$

Equation 9.5

$$P = Y + \frac{2K}{h}(R - r)$$

Equation 9.6

Equation 9.6 can be further simplified to Equation 9.7 by substituting in Equation 9.1.

Equation 9.7 outlines the condition under which sticking occurs.

$$P = Y + \frac{2Y}{\sqrt{3}h}(R - r)$$

Equation 9.7

Secondly, the conditions of slipping then must be considered. Figure 3.46, where μ is constant friction, and all other variables remain the same, shows this case.

By considering the free body diagram, a force balance equation can be determined as seen in Equation 9.8.

$$2\mu Pr\partial r + h\sigma_\theta \partial r - h\sigma_r \partial r - hr\partial\sigma_r = 0$$

Equation 9.8

Again, assuming that the pressing is axi-symmetric, Equation 9.9 can be used.

$$\varepsilon_\theta = \varepsilon_r, \quad \sigma_\theta = \sigma_r, \ \sigma_r + P = Y$$

Equation 9.9

And so Equation 9.8 gives Equation 9.10.

$$2\mu Pr\partial r = -hr\partial P$$

Equation 9.10

Using the boundary conditions $r = R, \quad \sigma_r = 0$ and $P = Y$ gives Equation 9.11.

$$\int_Y^P \frac{\partial P}{P} = -\int_R^r \frac{2\mu}{h} \partial r$$

Equation 9.11

$$P = Yexp[\frac{2\mu}{h}(R - r)]$$

Equation 9.12

Combining Equation 9.7 and Equation 9.12, gives Equation 9.13, which is the equation at the intersection (or boundary) between slip and stick. This can be arranged for μ, as seen in Equation 9.14.

$$Y + \frac{2Y}{h\sqrt{3}}(R - r) = Yexp\left[\frac{2\mu}{h}(R - r\right]$$

Equation 9.13

$$\mu = \frac{h}{2(R - r)} log\left[\frac{2}{h\sqrt{3}}(R - r)\right]$$

Equation 9.14